Semiconductors, Vol. 34, No. 1, 2000, pp. 1–5. Translated from Fizika i Tekhnika Poluprovodnikov, Vol. 34, No. 1, 2000, pp. 3–7.

ATOMIC STRUCTURE AND NONELECTRONIC PROPERTIES OF SEMICONDUCTORS

Holmium Redistribution upon Solid-Phase Epitaxial Crystallization of Amorphized Silicon Layers

O. V. Aleksandrov*, Yu. A. Nikolaev, and N. A. Sobolev****

** St. Petersburg State Electrotechnical University, St. Petersburg, 197376 Russia*
E-mail: aleks_ov@mailbox.alkor.ru
*** Ioffe Physicotechnical Institute, Russian Academy of Sciences, St. Petersburg, 194021 Russia*

Submitted June 3, 1999; accepted for publication June 8, 1999

Abstract—Concentration profiles of Ho were investigated after annealing at a temperature of 620°C of silicon layers implanted with 1-MeV Ho^+ ions to doses of $1–3 \times 10^{14}$ cm^{-2} exceeding the amorphization threshold, as well as with O^+ ions with energies that ensure the coincidence of the concentration maxima of implanted impurities and doses that are greater by an order of magnitude than those of Ho^+. The crystallization of the amorphized silicon layer occurs by the mechanism of solid-phase epitaxy. The main features of the segregation redistribution of Ho are shown to be similar to the previously studied segregation behavior of Er. An increase in the Ho concentration at the initial stage of the solid-phase epitaxial crystallization is explained by the small rate of mass transfer through the amorphous layer–single crystal interface. An analytical expression was obtained to describe the variation of the segregation coefficient in the process of solid-phase epitaxial crystallization, including its initial stage, which allows the calculation concentration profiles of rare-earth elements. © *2000 MAIK "Nauka/Interperiodica".*

INTRODUCTION

In the process of solid-phase epitaxial (SPE) crystallization of silicon layers amorphized by ion implantation of a rare-earth element Er, a significant change is observed in the concentration profile, which is caused by the impurity segregation at the moving interface between the amorphous layer and the silicon single crystal (α/c boundary). Except for the initial stage of SPE crystallization, when a decrease in the concentration of the rare earth is observed, the segregation redistribution of the impurity is described by the quantitative model [5] whose parameters are the width of the transition layer L and the coordinate-dependent segregation coefficient $K(x)$. The model parameters depend on the conditions of the implantation of the rare earth, such as the target temperature, irradiation dose, and energy of the implanted species, as well as on the co-implantation of an impurity oxygen [4]. At large doses ($D \geq 3 \times 10^{14}$ cm^{-2}), when the amorphous layer emerges onto the surface, the crystallization front moves from the α/c boundary to the surface. In this case, the following empirical relation was found for the $K(x)$ dependence [5]:

$$K(x) = K_0 K_m / [K_0 + (K_m - K_0)\exp(-(x_\alpha - x)/L)], \quad (1)$$

where x is the current coordinate measured from the sample surface; x_α is the position of the minimum in the concentration profile after the impurity redistribution; $x_\alpha - x$ is the current thickness of the crystallized layer; and K_0 and K_m are the initial (at $x = x_\alpha$) and maximum values of the segregation coefficient, respectively. Expression (1) describes the concentration profiles at $x < x_\alpha$ without allowance for the initial stage of SPE crystallization. At doses close to the amorphization threshold ($D \approx 5 \times 10^{13}$ cm^{-2}), the amorphization occurs only near the region of the maximum radiation damage with the formation of a buried amorphous layer. The existence of a thin layer of single-crystal silicon near the surface was confirmed by the Rutherford backscattering (RBS) of protons [6]. In the process of the SPE crystallization of the buried amorphous layer, the upper and bottom α/c interfaces move to the center of this layer and in the place of meeting of the crystallization fronts, there is observed a peak of the impurity concentration [6]. Based on the equations that were derived in [5], the authors of [6] suggested a new technique of calculating the coordinate dependence of the segregation coefficient $K_{ex}(x)$ from the experimental concentration profiles over the entire range of SPE crystallization. At doses close to threshold, an extended region of a falloff is observed at the initial stage of crystallization, which is located between the initial α/c interface (point $x_{\alpha 0}$) and the point x_α. The monotonically increasing dependence of the form (1) describes the behavior of $K_{ex}(x)$ only after the crystallization front passes through the point of minimum x_α. We could expect that the segregation redistribution of other rare-earth elements in sili-

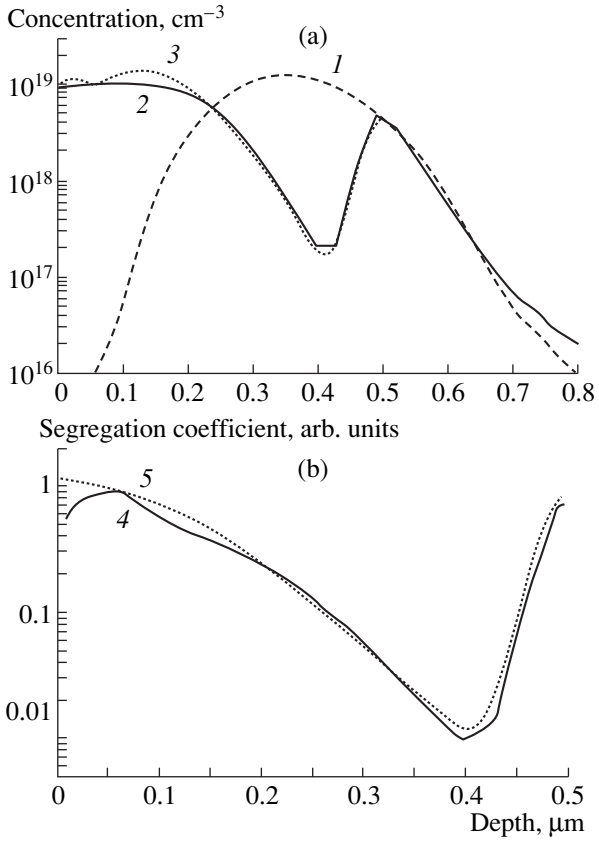

Fig. 1. In-depth profiles of (a) the holmium concentration and (b) the segregation coefficient: (*1*) after implantation of Ho^+ ions (1 MeV, 3×10^{14} cm^{-2}); (*2*) after annealing (620°C, 1 h); (*3*) calculated by formula (8) at $L = 60$ nm, $l = 12$ nm, $K_m = 1.3$; (*4*) calculated by the technique described in [6]; and (*5*) calculated by formula (8).

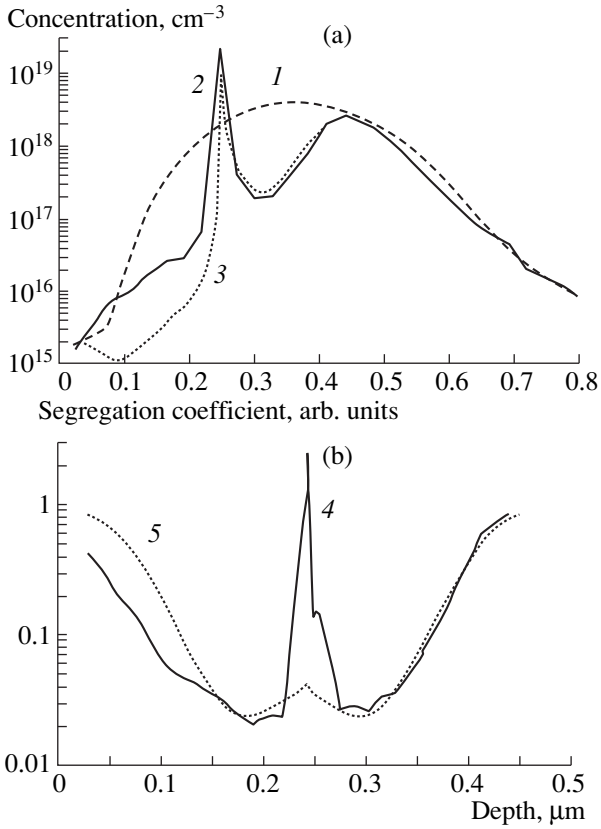

Fig. 2. In-depth profiles of (a) the holmium concentration and (b) the segregation coefficient: (*1*) after implantation of Ho^+ ions (1 MeV, 1×10^{14} cm^{-2}); (*2*) after annealing (620°C, 1 h); (*3*) calculated by formula (8) at $L1 = L2 = 70$ nm, $l1 = l2 = 23$ nm, $K_m = 1.3$; (*4*) calculated by the technique described in [6]; and (*5*) calculated by formula (8).

con would occur in a similar way. Indeed, it was established in [3] that at an energy of 250 keV and doses of $3.5–7 \times 10^{14}$ cm^{-2}, which significantly exceed the amorphization threshold, the segregation and pickup of the impurity of rare-earth element praseodymium, occur similarly to Er at similar concentrations and annealing temperatures, i.e., the concentration profile of Pr is shifted toward the surface, forming a subsurface segregation-induced peak in which the maximum concentration increases with increasing implantation dose.

The aim of this work is to study the behavior of the impurity of a rare-earth element holmium upon solid-phase epitaxial crystallization of silicon layers amorphized during ion implantation and to derive a model of redistribution of rare-earths, including the initial stage of the process.

EXPERIMENTAL

As the initial samples for implantation ("substrates"), we used polished Czochralski-grown B-doped (100) silicon wafers with a resistivity of 20 Ω cm. Ho^+ ions and an energy of 1 MeV were implanted on a High Voltage Engineering Europe K2MV device to doses of $1–3 \times 10^{14}$ cm^{-2}. Some of the samples were additionally implanted with O^+ ions with energies that ensured the same projected range to doses that exceeded by an order of magnitude those of Ho^+. Annealing was performed at 620°C for 1 h in a chlorine-containing atmosphere. The concentration profiles of holmium were determined by second-ion mass spectrometry on a Cameca IMS 4f device.

RESULTS AND DISCUSSION

Annealing of silicon layers implanted with Ho^+ ions to a dose of $D_{Ho} = 3 \times 10^{14}$ cm^{-2} causes a one-sided shift of the concentration profile of Ho toward the surface (Fig. 1a). Near the initial α/c boundary, a region of a falloff of the concentration is observed, whose extension is about 0.08 μm. After implantation to a dose of $D_{Ho} = 1 \times 10^{14}$ cm^{-2}, which is accompanied by the for-

mation of a buried α-layer, the redistribution of holmium occurs on both sides of the profile with the formation of a concentration peak at the place of meeting of the crystallization fronts in the center of the α layer (Fig. 2a), i.e., the velocity of motion of both α/*c* boundaries is the same. The extension of the region of the concentration falloff near the initial position of the lower (farther from the surface) α/*c* interface is 0.14 μm. Upon the combined implantation of Ho^+ ions ($D_{Ho} = 1 \times 10^{14}$ cm^{-2}) and O^+ ions ($D_O = 1 \times 10^{15}$ cm^{-2}), the holmium redistribution, remaining two-directional (two-sided), causes substantially smaller changes (Fig. 3a). Oxygen implantation leads to a shift of the segregation peak of holmium deeper into the sample from the center of the buried α-layer into the region of the mean projected range ($R_p = 0.35$ μm), as in the case of Er [6]. This indicates that the velocity of motion of the α/*c* boundary located farther from the surface decreases in comparison with the velocity of the α/*c* boundary located closer to the surface. Since it is just the lower boundary that passes through the maximum of the distribution of implanted O^+ ions, it is natural to relate the slowing of its motion with the presence of the oxygen impurity, which was previously observed in [7].

Figures 1b–3b (curves *1*) show coordinate dependences of the segregation coefficients $K_{ex}(x)$ calculated from the experimental concentration profiles of holmium using the technique we suggested in [6]. The decrease in the segregation coefficient from ~1 at the beginning of the SPE crystallization to ~0.03 at x_α changes later to a monotonic growth of K_{ex} for both one-sided (Fig. 1b) and two-sided (Figs. 2b, 3b) crystallization. The ascending branch of the variation of the segregation coefficient is described by equation (1), in which, in order to allow for the opposite directions of motion of the upper and lower crystallization fronts, the difference $x_\alpha - x$ is taken as the absolute value. With decreasing holmium implantation dose, the extension of the region of the K_{ex} falloff increases. Implantation of O^+ ions leads to a decrease in the region of the falloff of K_{ex} and the loss of the symmetry of the $K_{ex}(x)$ dependence relative to the point of meeting of the crystallization fronts (Figs. 2b and 3b, curves *1*). From the comparison of the concentration profiles of Ho with those for Er [6] obtained under the same conditions of implantation and annealing, a conclusion can be made on the same mechanism of segregation of these rare-earth impurities with their close atomic masses upon the SPE crystallization of amorphized silicon layers. The common feature in the Ho and Er behavior is, in particular, the presence of extended regions of concentration fall-off near the initial α/*c* boundaries. Previously [6], we suggested that this falloff of K_{ex} is related to the nonequilibrium of the process of segregation at the initial stage of SPE crystallization. This nonequilibrium is connected with the circumstance that at relatively large velocities of motion of the α/*c* boundary, the segregation-related transfer of the impurity through

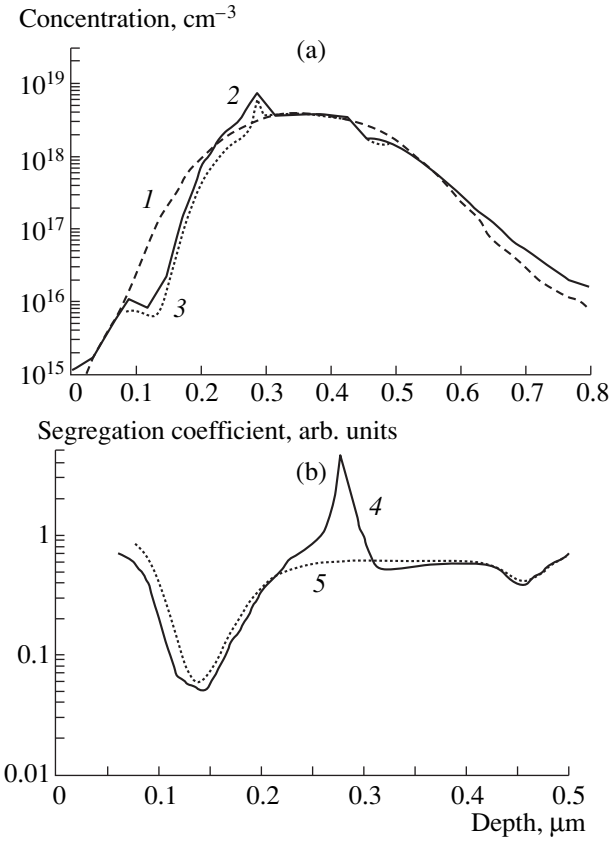

Fig. 3. In-depth profiles of (a) the holmium concentration and (b) the segregation coefficient: (*1*) after co-implantation of Ho^+ ions (1 MeV, 1×10^{14} cm^{-2}) and O^+ ions (0.14 MeV, 1×10^{15} cm^{-2}); (*2*) after annealing (620°C, 1 h); (*3*) calculated by formula (8) at $L1 = 20$ nm, $L2 = 13$ nm, $l1 = 11$ nm, $l2 = 20$ nm, $K_m = 0.6$; (*4*) calculated by the technique described in [6]; and (*5*) calculated by formula (8).

such a boundary is determined by the rate of mass transfer rather than by the difference in the chemical potentials of the phases [8–10].

Let us derive an expression for the variation of the segregation coefficient over the whole process of the SPE crystallization. The segregation flux of impurity through the α/*c* boundary under these conditions is usually described by a first-order kinetic equation [8]

$$F_s = h(C - K_{eq}C_a), \quad (2)$$

where h is the coefficient of mass transfer; C and C_a are the current concentrations of the impurity at the α/*c* boundary on the sides of the single-crystal and amorphous phases, respectively; and K_{eq} is the thermodynamically equilibrium segregation coefficient. In the case of SPE crystallization, the violation of thermodynamic equilibrium appears to occur because of the accumulation of defects and impurities at the moving α/*c* boundary. Therefore, in equation (2) we will con-

sider K_{eq} as a quantity that is not restricted by the rate of mass transfer, i.e., as $K(x)$ obeying dependence (1).

Let the crystallization front in Si advanced a distance Δx for the period Δt, which corresponds to the crystallization of an amorphous layer of thickness $b\Delta x$, where b is the ratio of the atomic volumes of the amorphous and crystalline silicon (according to [11], b = 1.0174). Before crystallization, the amount of the impurity in the α-layer was

$$\Delta Q_a = C_a b \Delta x. \quad (3)$$

After crystallization, the amount of the impurity in the c-layer became

$$\Delta Q_c = C \Delta x, \quad (4)$$

i.e., the resulting change in the amount of the impurity in the crystallized layer is

$$\Delta Q = (bC_a - C)\Delta x. \quad (5)$$

Assuming that the impurity is carried away from the crystallized layer almost wholly via the segregation flux of type (2), we have the following equation for the balance of the impurity at the α/c boundary:

$$\Delta Q = F_s \Delta t \quad (6)$$

or

$$(bC_a - C)\Delta x = h(C - K_{eq}C_a)\Delta t. \quad (7)$$

From equation (7), we obtain the following expression for the effective coefficient of segregation:

$$K_{ef} = C/C_a = (b + K_{eq}h/u)/(1 + h/u), \quad (8)$$

where $u = |\Delta x/\Delta t|$ is the rate of SPE crystallization.

Let us consider limiting cases. At the very beginning of the SPE crystallization, until the mass-transfer coefficient is small ($h \ll u$), there occurs a kinetic pickup of the impurity by the growing crystalline phase ($K_{ef} = b$). Later, at $h \gg u$, the segregation process is no longer limited by mass transfer and the $K_{ef}(x)$ dependence is determined by the $K(x)$ dependence according to (1). The $K_{ef}(x)$ dependence at $h < u$ is determined by the dependence of h on the thickness of the crystallized layer. We assume that at the initial stage of SPE crystallization the coefficient of mass transfer grows exponentially with the thickness of the crystallized layer in the same way as the equilibrium segregation coefficient $K_{eq}(x)$, i.e., in accordance with expression (1)

$$h(x) = h_0 \exp(|x_{\alpha 0} - x|/l), \quad (9)$$

where h_0 is the starting value of the mass-transfer coefficient at the initial α/c boundary (at $x_{\alpha 0}$), and l is the characteristic length for the increase in h.

The calculation of the redistribution of the holmium impurity was carried out using the model developed in [5] with the segregation coefficient $K_{ef}(x)$ defined by (8), K_{eq} defined by (1), and h defined by (9). The calculated concentration profiles are shown in Figs. 1a–3a (curves *3*), and the $K_{ef}(x)$ dependences that yield the best agreement between the calculated and experimental profiles are given in Figs. 1b–3b. The comparison of the calculated and experimental dependences shows their satisfactory agreement. An increase in the dose of implanted Ho^+ ions from 1×10^{14} to 3×10^{14} cm^{-2}, as well as the implantation of O^+ ions, leads to a decrease in the parameters L and K_m, in accordance with the previously found behavior of erbium [4]. Analogous behavior is exhibited by the parameter l, which decreases with increasing holmium implantation dose and upon oxygen implantation. The initial value of the segregation coefficient K_0 and the ratio h_0/u were kept constant during calculation ($K_0 = 2 \times 10^{-3}$ and h_0/u = 0.2). Note that the $K_{ef}(x)$ dependence well agrees with the $K_{ex}(x)$ at all depths, except for the region of the segregation peak, where K_{ex} is significantly greater than K_{ef} (see Figs. 2b, 3b), and the region near the surface, where a falloff of K_{ex} is observed, so that K_{ex} becomes smaller than K_{ef} (see Fig. 1b). Accordingly, the concentration profiles of holmium calculated using $K_{ef}(x)$ differ somewhat from the experimental ones in these regions.

CONCLUSION

Thus, the general rules of the redistribution of the impurity of the rare-earth element holmium upon solid-phase epitaxial crystallization of amorphous silicon were established to be analogous to the corresponding redistribution rules of erbium. The falloff of the rare-earth impurity concentrations at the initial stage of SPE crystallization is due to a decrease in the segregation coefficient because of the decreased rate of mass transfer through the interphase interface. An analytical expression was obtained for the dependence of the effective coefficient of segregation on the thickness of the recrystallized layer; this expression permits one to satisfactorily describe the redistribution of rare-earth impurities upon solid-phase epitaxial crystallization, including its initial stage.

ACKNOWLEDGMENTS

This work was supported in part by the Russian Foundation for Basic Research, project no. 99-02-17750. The authors are grateful to E.O. Parshin for the implantation of the impurities into silicon and Yu.A. Kudryavtsev for measurements of concentration profiles.

REFERENCES

1. D. Moutennet, H. L'Haridon, P. N. Favennec, *et al.*, Mater. Sci. Eng., B **4**, 75 (1989).
2. W. P. Gillin, Z. Jingping, and B. J. Sealy, Solid State Commun. **77**, 907 (1991).
3. J. S. Custer, A. Polman, and H. M. Pinxteren, J. Appl. Phys. **75**, 2809 (1994).
4. O. V. Aleksandrov, Yu. V. Nikolaev, and N. N. Sobolev, Fiz. Tekh. Poluprovodn. (St. Petersburg) **33**, 114 (1999) [Phys.–Semicond. **33**, 101 (1999)].
5. O. V. Aleksandrov, Yu. V. Nikolaev, and N. N. Sobolev, Fiz. Tekh. Poluprovodn. (St. Petersburg) **32**, 1420 (1998) [Phys.–Semicond. **32**, 1266 (1998)].
6. O. V. Aleksandrov, Yu. V. Nikolaev, N. N. Sobolev, *et al.*, Fiz. Tekh. Poluprovodn. (St. Petersburg) **33**, 652 (1999) [Phys.–Semicond. **33**, 606 (1999)].
7. E. F. Kennedy, L. Csepregi, and J. M. Mayer, J. Appl. Phys. **48**, 4241 (1977).
8. D. A. Antoniadis, M. Rodoni, and R. W. Dutton, J. Electrochem. Soc. **126**, 1939 (1979).
9. V. I. Kol'dyaev, V. A. Moroz, and S. A. Nazarov, Avtometriya, No. 3, 46 (1988).
10. O. V. Aleksandrov and N. N. Afonin, Fiz. Tekh. Poluprovodn. (St. Petersburg) **32**, 19 (1998) [Phys.–Semicond. **32**, 15 (1998)].
11. S. Roorda, J. S. Custer, W. C. Sinke, *et al.*, Nucl. Instr. Methods Phys. Res., Sect B **59/60**, 344 (1991).

Translated by S. Gorin

Semiconductors, Vol. 34, No. 1, 2000, pp. 104–107. Translated from Fizika i Tekhnika Poluprovodnikov, Vol. 34, No. 1, 2000, pp. 102–105.

PHYSICS OF SEMICONDUCTOR DEVICES

Light Emitting Diodes for the Spectral Range of λ = 3.3–4.3 μm Fabricated from the InGaAs- and InAsSbP-Based Solid Solutions: Electroluminescence in the Temperature Range of 20–180°C

M. Aĭdaraliev, N. V. Zotova, S. A. Karandashev, B. A. Matveev, M. A. Remennyĭ, N. M. Stus', and G. N. Talalakin

Ioffe Physicothechnical Institute, Russian Academy of Sciences, Politekhnicheskaya ul. 26, St. Petersburg, 194021 Russia
E-mail: bmat@iropt3.ioffe.rssi.ru

Submitted June 7, 1999; accepted for publication June 8, 1999

Abstract—Light emitting diodes (LEDs) with λ_{max} = 3.4 and 4.3 μm (t = 20°C) were studied at elevated temperatures. It is demonstrated that LEDs operating in the temperature range t = 20–180°C can be described using the classical concepts of injection radiation sources and the processes of charge carrier recombination. The temperature dependences of reverse currents in the saturation regions of current–voltage characteristics are consistent with the increase in the intrinsic-carrier concentration according to the Shockley theory. The emission spectra are described on the assumption of the direct band-to-band transitions, spherically symmetric bands, and thermalized charge carriers. The current–power characteristics are proportional to $I^{3/2}$ suggesting that the contribution of the nonradiative Auger recombination is dominant. The radiation power decreases exponentially with the temperature which is characteristic of the CHSH and CHCC processes. *© 2000 MAIK "Nauka/Interperiodica".*

1. INTRODUCTION

Light emitting diodes (LEDs) for the intermediate infrared (IR) spectral range (3–5 μm) with narrow radiation spectra ($\Delta\lambda_{0.5} \sim 0.1\lambda_{max}$) are used in gas detectors for the detection of methane CH_4 (3.3 μm), carbon dioxide CO_2 (4.3 μm), etc. The studies of these LEDs were restricted by the temperature range 4–380 K [1–3], although, for certain purposes LEDs, should operate at higher temperatures.

The purpose of this work is the examination of LEDs for λ_{max} = 3.3 and 4.3 μm (t = 20°C) in the temperature range of 20–180°C.

2. SAMPLES STUDIED AND EXPERIMENTAL TECHNIQUES

Diode heterostructures were grown by liquid-phase epitaxy on (n, p)-InAs(111) substrates with the electron concentration of about 2×10^{16} cm^{-3} at temperatures of 650–680°C and were similar to those described previously [3, 4]. The p–n junction was formed by introducing the zinc or manganese dopants into the melt (the concentration of free carriers was $p \approx 1–2 \times 10^{17}$ cm^{-3}). Epilayers of the n-type were grown without special doping, the electron concentration was $n \approx 1–2 \times 10^{17}$ cm^{-3}. The solid solutions $In_{0.95}Ga_{0.05}As$ (λ = 3.3 μm) and $InAs_{0.87}Sb_{0.12}P_{0.01}$ (λ = 4.3 μm) were used as active layers of LEDs. LEDs had the mesas of 500 μm in diameter. LEDs for λ = 3.3 μm were mounted with the substrate at the bottom (Fig. 1a). In the case of LEDs for λ = 4.3 μm, the substrate and wide-gap layer were partially etched off, and the samples were mounted by the "p" side onto the Si holder (Fig. 1b). The n-InGaAs and p-InAsSbP layers were 5–10 μm in thickness.

Electroluminescence (EL) was measured using a cooled InSb photodiode.

3. EXPERIMENTAL RESULTS AND DISCUSSION

It is known that the p–n junction is formed on condition that the intrinsic-carrier concentration in an active region is lower than the majority-carrier concentration in n- and p-regions, which form the p–n junction. The intrinsic-carrier concentration $n_i = p_i$ is defined by the bandgap energy for the material E_g and temperature T as

$$n_i = p_i = 4.82 \times 10^{15} T^{3/2} \left(\frac{m_e m_h}{m_0^2}\right)^{3/4} \times \exp\left(-\frac{E_g}{2kT}\right) \ [\text{cm}^{-3}], \quad (1)$$

where m_e and m_h are the effective masses of the electron and hole, m_0 is the mass of the free electron, and k is the Boltzmann constant. The temperature dependence of n_i

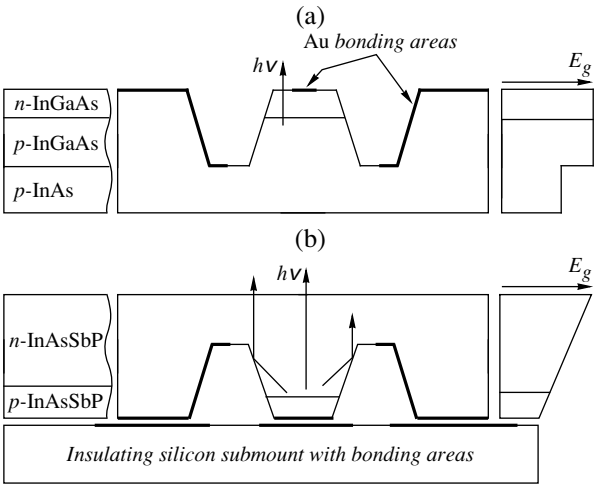

Fig. 1. Design of light emitting diodes with (a) $\lambda = 3.3$ μm and (b) $\lambda = 4.3$ μm.

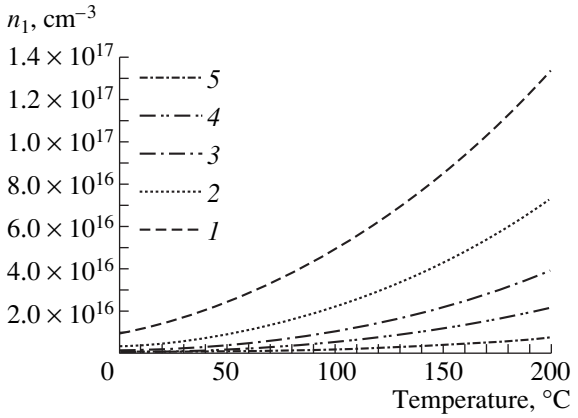

Fig. 2. Temperature dependence of the intrinsic concentration $n_i(T)$ for semiconductors with the composition close to InAs ($m_e = 0.021m_0$, $m_h = 0.41m_0$) for E_g = (*1*) 200, (*2*) 250, (*3*) 300, (*4*) 350, and (*5*) 450 meV.

for semiconductors with a composition close to InAs ($m_e = 0.021m_0$, $m_h = 0.41m_0$, $E_g = 200$–450 meV) is shown in Fig. 2. The majority-carrier concentration in the *p*- and *n*-type epilayers amounts to $p, n \approx 1$–2×10^{17} cm^{-3}. For this reason, one can expect that the condition $p, n > p_i, n_i$ is fulfilled in the materials with $E_g \geq 0.2$ eV ($\lambda \leq 6$ μm), and the *p*–*n* junction exists at temperatures up to 180°C.

The shape of the current–voltage (*I*–*V*) characteristics for InAs at room temperature follows the Shockley theory, which considers the generation and recombination of charge carriers in the *n*- and *p*-regions of the *p*–*n* junction. According to this theory, the reverse currents in the saturation region are proportional to the intrinsic concentration squared [5]. Figure 3a shows the *I*–*V* characteristics for the LED with $\lambda = 4.3$ μm in the temperature range of 20–180°C. The temperature dependences of the reverse current I_s at $U = -1$ V (i.e., in the saturation region at low temperatures) and the intrinsic concentration squared n_i^2 are shown in Fig. 3b. The agreement between the $I_s(t)$ and $n_i^2(t)$ curves demonstrates that the Shockley theory remains valid at elevated temperatures for *p*–*n* junctions, based on solid solutions whose composition is close to InAs.

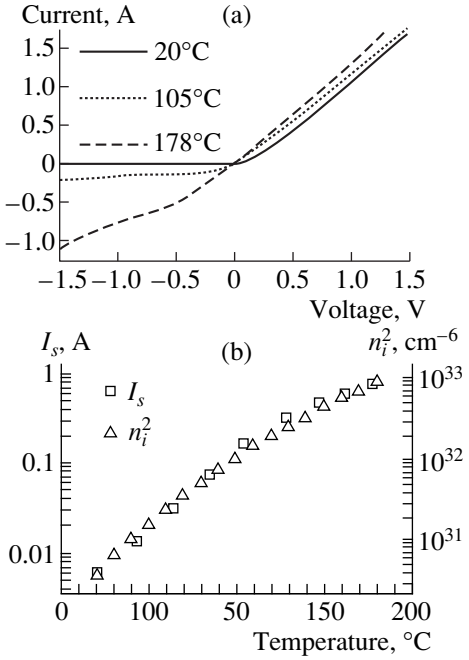

Fig. 3. Current–voltage characteristics (a) for the LED with $\lambda = 4.3$ μm. Temperature dependences (b) of reverse current I_s ($U = -1$ V) and intrinsic concentration squared n_i^2.

The EL spectra for LEDs with $\lambda = 3.3$ μm in the temperature range of 25–180°C are shown in Fig. 4. It was demonstrated [6] that the acceptor level of Zn ($E_a \leq 15$ meV) in long-wavelength LEDs ($\lambda = 5.3$ μm) is depleted even at $T > 175$ K, and the radiative recombination is controlled by transitions between the conduction and valence bands in the *p*-region of the *p*–*n* junction. Because of this, the spectral curves can be processed on the assumption that we have the direct band-to-band transitions, spherically symmetric bands, and thermalized charge carriers. In this case, the EL peak location and short-wavelength shoulder of the spectra are described well by the curve

$$I(E) \sim \left[E_g + \left(1 + \frac{m_e}{m_h}\right)E\right]^2 \sqrt{E} \exp\left(-\frac{m_e}{m_h}\frac{E}{kT}\right) \times \left(\exp\left(\frac{E}{kT}\right) + 1\right)^{-1}, \quad (2)$$

where $E = \hbar\omega - E_g$ is the energy measured from the bottom of the conduction band. The consequence of the

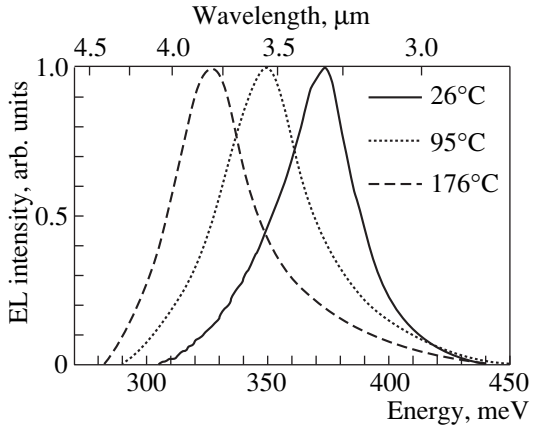

Fig. 4. Electroluminescence spectra for the LED with λ = 3.3 μm.

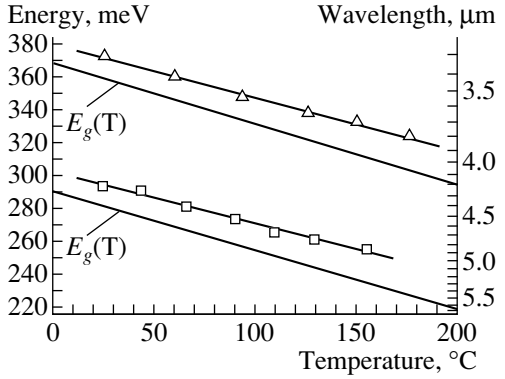

Fig. 5. Temperature dependences of the energy of El peak and the bandgap energy for LEDs with λ = 3.3 and 4.3 μm.

relationship (2) is that the bandgap energy is smaller than the energy of EL peak by the value of $kT/2$:

$$E_g(T) = h\nu_{max}(T) - kT/2. \quad (3)$$

The spectral curve peak shifts to longer wavelengths with an increase in temperature as follows from corresponding band-gap narrowing. The characteristic energy of the short-wavelength slope ε increases proportionally to T. However, the value of ε is smaller than kT. This appears to be caused by the self-absorption of luminescence. The characteristic energy of the long-wavelength slope (~11–15 meV) is approximately the same order as the characteristic energy of the band-edge tailing that is caused by fluctuations of the solid-solution composition [7]. Figure 5 shows the temperature dependences of the EL energy peak and the bandgap energy E_g of the active region for the LED with λ = 3.3 μm; the dependence $E_g(T)$ was and 4.3 μm obtained from relationship (3). The slope of the $E_g(T)$ curves (the temperature coefficient of variation for the bandgap energy dE_g/dT) is equal to 3.6×10^{-4} and 3.5×10^{-4} eV/K for solid solutions $In_{0.95}Ga_{0.05}As$ and $InAs_{0.87}Sb_{0.12}P_{0.01}$, respectively. These values are close to that for InAs (2.8×10^{-4} eV/K), which was reported [8] for the range T = 77–300 K [8].

The power–current characteristics (W–I) for the LED with λ = 3.3 μm in the temperature range 25–180°C and the temperature dependence of the emission power for the pumping current of 2 A are emission in Fig. 6. The W–I characteristics are sublinear and are approximated adequately by the exponential function of the current $W(I) \sim I^{2/3}$ (the solid line). This indicates that the emission originates as a result of bimolecular radiative recombination, with nonradiative Auger recombination being dominant; the rates of the above two recombination processes are proportional to Δn^2 and Δn^3, respectively [9]. The radiation power decreases exponentially with an increase in temperature. This is typical of the CHCC and CHSH Auger recombination processes that are dominant at elevated temperatures in solid solutions close in composition to InAs [10].

The EL spectra for LEDs with λ = 4.3 μm and temperature dependence of the emission power for pumping current of 2 A are shown in Fig. 7. The temperature

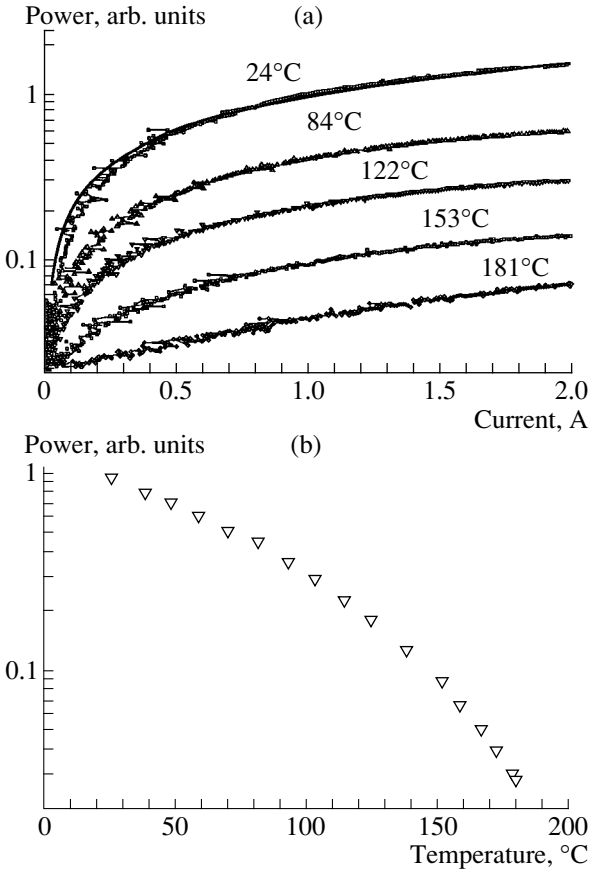

Fig. 6. Power–current characteristics (a) for the LED with λ = 3.3 μm and temperature dependence (b) of emission power for the pumping current of 2 A (10 μs, 500 Hz).

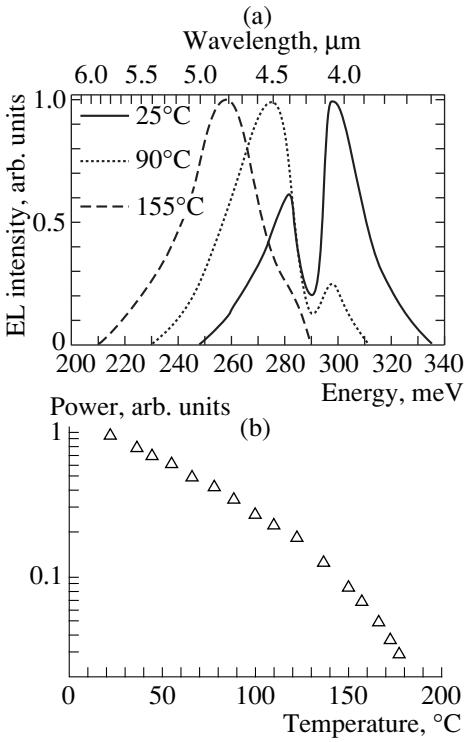

Fig. 7. Electroluminescence spectra (a) for the LED with $\lambda = 4.3$ μm and temperature dependence (b) of emission power for the pumping current of 2 A (10 μs, 500 Hz).

dependence of the spectra is similar to that for LEDs with $\lambda = 3.3$ μm. A decrease in the emission power is sharper than that for LEDs with $\lambda = 3.3$ μm (namely, the ~30-fold decrease to be compared with the ~20-fold decrease). This is caused by the fact that the Auger recombination is more important in the structures with the narrower bandgap.

4. CONCLUSION

Thus, we demonstrated that the operation of the long-wavelength LEDs ($\lambda = 3.3$, 4.3 μm) in the temperature range $T = 20$–180°C can be described using the classical concepts of LEDs and charge carrier recombination. The temperature dependences of reverse currents in the saturation portion of *I–V* characteristics are consistent with the increase in the intrinsic-carrier concentration in the Shockley theory. The emission spectra are described assuming that we have the direct band-to-band transitions, spherically symmetrical bands, and thermalized charge carriers. *W–I* characteristics are proportional to $I^{2/3}$ indicating the dominant role of the nonradiative Auger recombination. The emission power decreases exponentially with temperature, which is typical of the *CHSH* and *CHCC* processes.

ACKNOWLEDGMENTS

This work was supported by the American Civil Research and Development Foundation.

REFERENCES

1. H. J. Gerritsen, C. C. Taylor, S. C. Reuman, *et al.*, in *Proceedings of the Second WVU Conference on Coal Mine Electrotechnology*, Morgantown, USA, (1974), p. 21.
2. N. P. Esina, N. V. Zotova, and D. N. Nasledov, Fiz. Tekh. Poluprovodn. (Leningrad) **3**, 1370 (1969).
3. B. Matveev, M. Aĭdaraliev, G. Gavrilov, *et al.*, Sens. Actuators, B **51**, 233 (1998).
4. M. Aĭdaraliev, N. V. Zotova, S. A. Karandashev, *et al.*, Pis'ma Zh. Tekh. Fiz. **17** (23), 75 (1991).
5. N. P. Esina, N. V. Zotova, and D. N. Nasledov, Radiotekh. Élektron **8**, 1602 (1963).
6. M. Aĭdaraliev, N. V. Zotova, S. A. Karandashev, *et al.*, Pis'ma Zh. Tekh. Fiz. **24** (6), 88 (1998).
7. N. V. Zotova, S. A. Karandashev, B. A. Matveev, *et al.*, Fiz. Tekh. Poluprovodn. (Leningrad) **21** (6), 1079 (1987).
8. O. Madelung, *Physics of III–V Compounds* (Wiley, New York, 1964; Mir, Moscow, 1967).
9. D. Garbuzov, M. Maĭorov, H. Lee *et al.*, Appl. Phys. Lett. **74** (20), 2990 (1999).
10. M. Aĭdaraliev, G. G. Zegrya, N. V. Zotova, *et al.*, Fiz. Tekh. Poluprovodn. (St. Petersburg) **26** (2), 236 (1992).

Translated by N. Korovin

Semiconductors, Vol. 34, No. 1, 2000, pp. 108–114. Translated from Fizika i Tekhnika Poluprovodnikov, Vol. 34, No. 1, 2000, pp. 106–112.

PHYSICS OF SEMICONDUCTOR DEVICES

Current Transport in the Me–*n*–*n*$^+$ Schottky–Barrier Structures

N. A. Torkhov* and S. V. Eremeev**

**NIIP State Research and Production Works, Semiconductor Research Institute, Tomsk, 634045 Russia*
*** Kuznetsov Physicotechnical Institute, Tomsk, 634050 Russia*

Submitted April 1, 1998; accepted for publication June 24, 1999

Abstract—A model of current transport in Schottky-barrier diodes based on the concept of ballistic electron transport through a thin base is proposed. The method of transfer matrix was used in order to obtain tunneling probabilities, which were used in calculation of the forward and reverse current–voltage (*I–V*) characteristics, as well as of the transit time. It is demonstrated that by considering a potential in full form, a good agreement between the experimental and calculated *I–V* characteristics is obtained. It is found that a consideration of the role of a thin base causes the current to decrease; the probability of tunneling through the *n*-base can be close to unity. It is demonstrated that the tunneling probability has a large number of local resonances and that the energy dependence of the transit time is nonmonotonic. This is caused by the influence of the base region. The boundary operating frequency of diodes is evaluated and is found to be 10–100-fold higher than that obtained from the classical concept. *© 2000 MAIK "Nauka/Interperiodica".*

INTRODUCTION

At present, the thermoelectron emission and tunneling of carriers are generally taken into account when calculating the forward and reverse current–voltage (*I–V*) characteristics of Schottky-barrier (SB) diodes and those based on the metal–oxide–semiconductor structures [1–8]. When calculating the tunnel current (tunneling), the tunneling probability is calculated to the Wentzel–Kramers–Brillouin (WKB) approximation. Only the tunneling of carriers is taken into account in the process (the potential region $[X_a, X_b]$; see Fig. 1), whereas the potential at $X > X_b$ is taken to equal zero [9].

The calculation of the reverse-bias regions of *I–V* characteristics is commonly the most difficult problem. In practice, the reverse currents generally exceed the calculated values. Even taking into account the complementary effects affecting the potential barrier height, namely, the lowering of SB height due to the image forces [3] and the lowering of the electrostatic barrier [10], the static *I–V* characteristics could not be described in a wide range of biases.

The transfer-matrix method, which was developed recently [11, 12], allows calculation of the tunneling probability $T(E)$ and transit time $t(E)$ with an adequate accuracy. These quantities characterize the electron motion through the potential barriers of arbitrary shape. The latter are described by the piecewise continuous potentials. Hence, it was reported [13] that, being calculated exactly, the $T(E)$ and $t(E)$ curves can be nonmonotonic.

In this work, the forward and reverse *I–V* characteristics for GaAs-based SB diodes over the entire bias range for weak and heavy currents at different dopant concentrations are calculated for the first time using the transfer matrix for obtaining the $T(E)$ and $t(E)$ dependences. The experimental forward- and reverse-bias regions of the *I–V* characteristics for the SB diode with a thin base are presented. The high-speed performance of diodes is evaluated.

CALCULATION PROCEDURE

To calculate the static *I–V* characteristics for SB diodes, we use the analytical expression [7]

$$J(E) = \frac{4\pi q m^* kT}{h^3} \times \int_0^E T(E) \ln\left[\frac{1 + \exp((E_F - E)/kT)}{1 + \exp((E_F - E - qV)/kV)}\right] dE, \quad (1)$$

where q is the elementary charge, m^* is the effective electron mass, k is the Boltzmann constant, T is temperature, h is the Planck constant, $T(E)$ is the transmission coefficient, E_F is the Fermi level, E is the electron energy, and V is the voltage drop.

The one-dimensional problem of the electron transit through the plane of the metal–semiconductor contact was considered in the context of the effective mass method. To evaluate the transit parameters $T(E)$ and $t(E)$, the recurrence relationships obtained in the context of the transfer-matrix approach were used [11, 12, 14]. For this purpose, a barrier of arbitrary shape is approximated by a system of rectangular potential barriers. It was demonstrated [11] that the transfer-matrix method is characterized by absolute convergence.

In order to calculate the electrical characteristics of the system of rectangular potential barriers in the electric field by the transfer matrix method [14], it is neces-

sary to add the potential step with $l = 0$ to the barrier system (see insert in Fig. 1). In this case, the tunneling probability for electrons passing through the metal–semiconductor contact, i.e. through the system including the rectangular potential barriers and potential step, is calculated from the formula

$$T^{-1} = 1 + \frac{(\sqrt{R} + \sqrt{R_{st}})^2}{TT_{st}} - 4\frac{\sqrt{RR_{st}}}{TT_{st}}\cos^2 F, \qquad (2)$$

where

$$F = \frac{1}{2}\left(I + \Phi + \frac{\pi}{2}\right) + \chi_0 l, \qquad (2a)$$

T and R are the transit and reflection coefficients for the system of rectangular potential barriers, T_{st} and R_{st} are the transit and reflection coefficients for the potential step, I and Φ are the phases of the transmitted and reflected waves, and χ_0 is the electron wave number in the zero-potential region.

The form of the potential $\varphi(x)$ was found from numerical solution of Poisson's equation [15] with allowance made for the image forces [3]. The zero energy level was taken to be the Fermi level location in metal for $V_r < 0$ and in a semiconductor for $V_f > 0$, where V_f is the forward bias and V_r is the reverse bias (Fig. 1). Performing the calculations, the following assumptions were made:

(i) $T(E)$ and $t(E)$ were calculated over the entire region of potential variation from $x = 0$ to $x = W_n$, where W_n is the coordinate of the n–n^+ interface (Fig. 1).

(ii) Processes of scattering in the n-layer were not taken into account. In connection with this, the electron diffusion length was assumed to exceed the width of the diode's thin base.

(iii) It was assumed that, in this case, charge carriers are scattered only by the potential formed in the vicinity of the metal–semiconductor contact.

(iv) The behavior of electrons in metal was not considered, and the electron effective mass in metal was taken to be equal to that in a semiconductor.

(v) The above-barrier transmission of electrons was taken into account by an increase in the limits of integration over the energy from 0 to ∞.

The static electrical characteristics for three diode structures having different SB thickness and charge carrier concentration in epilayer were calculated. The chosen epitaxial n-layer thickness was 0.5 μm for $N_d = 5 \times 10^{17}$ cm^{-3}, 0.52 μm for $N_d = 3.6 \times 10^{16}$ cm^{-3}, and 3 μm for $N_d = 5 \times 10^{15}$ cm^{-3}. The dopant concentration in the n^+ layer was 2×10^{18} cm^{-3}. The potential barrier height φ_{b0} was 0.875 eV at 295 K. The φ_{b0} was specially chosen to be excessive in order to make the barrier height φ_b, (with allowance made for the image forces) consistent with the experimental value. The transit parameters were calculated in the energy range from 0 to 0.9 eV. The potential was divided by 400 points over the space coordinate and by 300 points over energy. The error of calculating the I–V characteristics amounts to 1–3%.

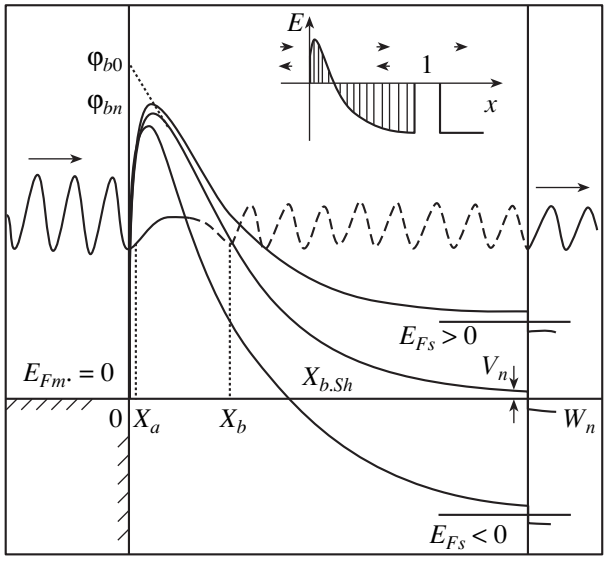

Fig. 1. Schematic energy diagram of the Me–n–n^+ structure. E_{Fm} and E_{Fs} are the Fermi levels for a metal and semiconductor, φ_{b0} is the potential barrier height, φ_b is the potential barrier height with allowance made for the image forces, V_n is the location of the conduction band bottom in the bulk of semiconductors, $X < 0$ is the region of metal–semiconductor contact, $[0, W_n]$ is the n-base region, $X \geq W_n$ is the n-substrate region, $[X_a, X_b]$ is the subbarrier region, $[W_b, W_n]$ is the above-barrier region, and $X_{b\mathrm{Sn}}$ is the SB width for $E = 0$.

The correctness of program execution was verified by calculating $T(E)$ and $t(E)$ for superlattices [16, 17]. The shape of the forward- and reverse-bias portions of the I–V characteristics, as well as the transit parameters, were calculated to the WKB approximation according to the procedure described in [2], but without regard for the electrostatic barrier lowering.

EXPERIMENTAL TECHNIQUE

Static I–V characteristics for the SB diodes were measured using mesas. The GaAs epilayer was 0.52 μm thick. Charge carrier concentration was 3.6×10^{16} cm^{-3} in the epilayer and 2×10^{18} cm^{-3} in the substrate. The (GeNi + Au)-based ohmic contact was formed on the substrate side. The SBs 325 μm in diameter were formed by the electrochemical deposition of the Au film 0.3 μm thick.

The SB height was determined from the capacitance–voltage (C–V) characteristics recorded at a frequency of 1 MHz and, for comparison, from the saturation current in the I–V characteristics. The I–V and C–V characteristics were recorded at 294 K. The SB heights obtained from two independent methods are practically

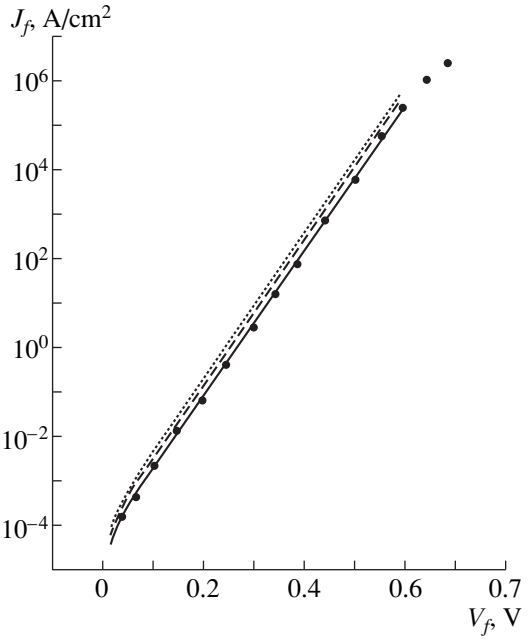

Fig. 2. Forward portions of the *I–V* characteristics. The dots correspond to the experimental values, the ideality factor $n = 1.04$. The lines represent the calculations by the transfer-matrix method with regard to the full form of the potential (the solid line), by the transfer-matrix with allowance made for tunneling only (the dashed line), and by the WKB method (the dotted line). The ideality factors for the curves calculated are 1.039 (the solid line), 1.037 (the dashed line), and 1.035 (the dotted line).

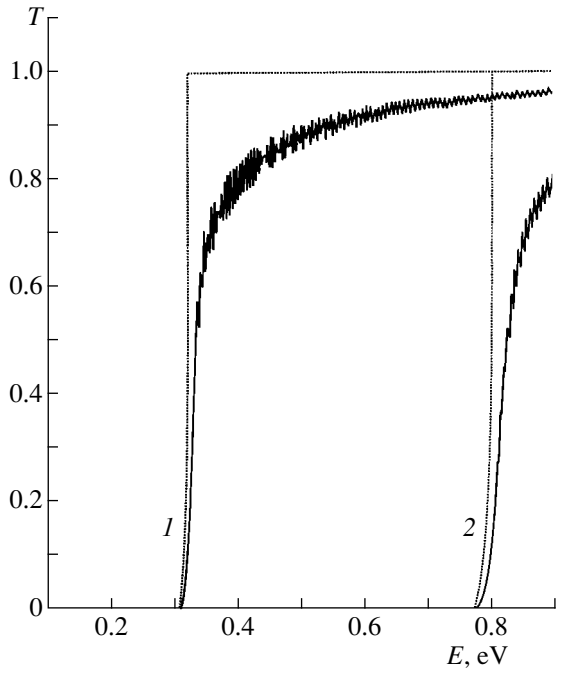

Fig. 3. The tunneling probability T for (*1*) zero bias and (*2*) forward bias $V_f = 0.5$ V calculated by the transfer-matrix method with allowance made for the full form of the potential (solid lines), and by the WKB method (dotted lines).

identical. This indicates that the SB height is fairly uniform over the contact area. In all other cases, the ideality factor for diode structures obtained is close to unity.

The concentration distribution for the ionized shallow donor impurity (concentration profile) $N_d(X)$ was determined from *C–V* characteristics. The uniform impurity distribution along the epilayer thickness was obtained. The effective thickness of the *n*-layer for diodes examined was estimated from the concentration profiles.

RESULTS

The forward-bias portions of the *I–V* characteristics calculated for the diode structure with the concentration $N_d = 3.6 \times 10^{16}$ cm^{-3} at 295 K and average computed values of 0.3 to 0.5 eV for the ideality factor for the energy range are shown in Fig. 2. The $J_f(V_f)$ dependences are in good agreement with the straight lines. The experimental forward *I–V* characteristics are also shown in Fig. 2.

The calculated dependences of the tunneling probability T on the electron energy E for the zero bias and for the forward bias V_f are shown in Fig. 3. The dependences were calculated to the WKB approximation (dotted lines) using the exact recurrence relationships with allowance made for the complete form of the potential barrier (continuous curves). In order to avoid encumbering the figure, the $T(E)$ curves for the case where only the electron tunneling was considered are not shown. We only note that these curves run somewhat below the continuous curves.

The calculated reverse-bias portions of *I–V* characteristics are shown in Fig. 4. They were also calculated for three cases, namely, to the WKB approximation (dotted curve), using the transfer-matrix method (dashed curve), and using the transfer matrix method with allowance made for the complete form of the potential (continuous curve). The experimental reverse *I–V* characteristics are also shown.

The dependences $T(E)$ that were obtained using the transfer-matrix method for the complete form of the potential for reverse biases $V = 0$ (curve *1*), $V_r = -0.5$ V (curve *2*), and $V_r = -5$ V (curve *3*) are shown in Fig. 5. The dependences $T(E)$ that were obtained to the WKB approximation for biases $V_r = -0.5$ V (curve *4*) and $V_r = -5$ V (curve *5*), as well as those calculated by the transfer-matrix method considering the potential only in the $[X_a, X_b]$ region (curve *6*) for the bias $V_r = -5$ V, are also shown in Fig. 5. In the latter case, the $T(E)$ curves for $V_r = -0.5$ V are not shown in order to avoid encumbering the figure. It is seen from Fig. 5 that the curves $T(E)$ become more nonmonotonic with an increase in V_r.

Figure 6 shows the energy dependences of the transit time for the electrons passing through the base region at the biases $V_f = 0.5$ V, $V = 0$, $V_r = -0.5$ V, and $V_r = -5$ V; these dependences were are calculated by the

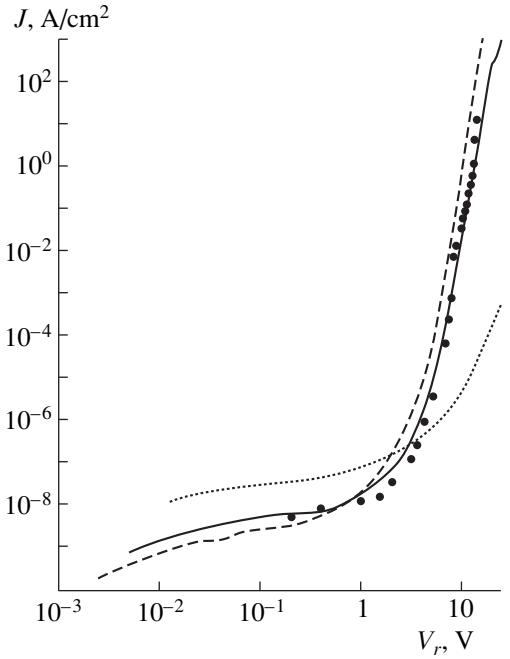

Fig. 4. Reverse portions of *I–V* characteristics. The dots correspond to the experimental values. The lines represent the calculations by the transfer-matrix method with allowance made for the full form of the potential (the solid line), by the transfer-matrix method with regard to tunneling only (the dashed line), and by the WKB method (the dotted line).

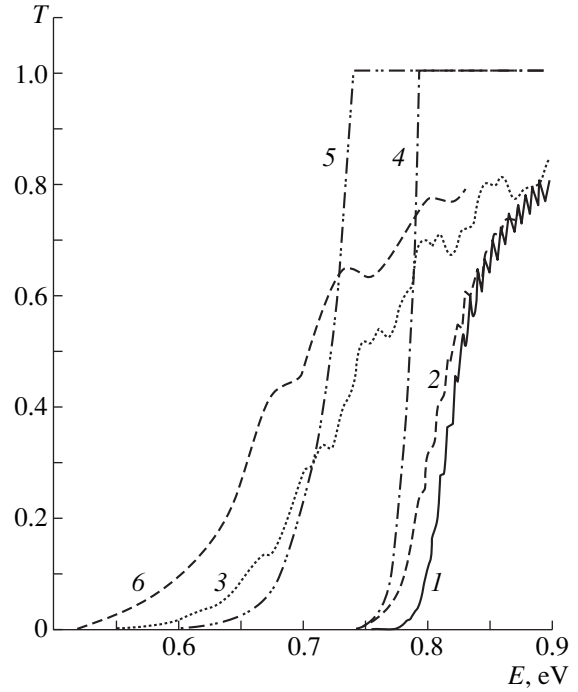

Fig. 5. Calculations of the tunneling probability T for the zero bias (*1*) and for reverse biases $V_r = -0.5$ (*2*, *4*) and –5 V (*3*, *5*, *6*). The calculations were performed by the transfer-matrix method with allowance made for (*1*–*3*) the full form of the potential, (*6*) tunneling only, and (*4*, *5*) by the WKB method.

transfer-matrix method for the case of the potential in full form.

The dependences of the tunnel current density on the electron energy E for certain voltage drops are shown in Fig. 7 (for forward bias, Fig. 7a; for reverse bias, Fig. 7b). As mentioned above, the zero energy level in Fig. 7a coincides with the Fermi level position in semiconductor E_{Fs}, and, in Fig. 7b, coincides with that in metal E_{Fm}.

DISCUSSION OF THE RESULTS OF CALCULATIONS

The forward *I–V* characteristics calculated by different methods have no significant distinctions. Figure 2 demonstrates that the dependence calculated to the WKB approximation corresponds to large currents. The dependences calculated by the transfer-matrix method considering the potential only in the $[X_a, X_b]$ region as well as considering the potential in full form have no significant distinctions. A comparison of the computed values of the ideality factor n for continuous and dashed curves in Fig. 2 demonstrates that the consideration of the full form of the potential somewhat increases the value of n.

Such behavior of the forward *I–V* characteristics can be explained on the basis of the differences in dependences $T(E)$ (Fig. 3). As distinct from the case of calculating the tunneling probabilities to the WKB approximation, the transfer-matrix method yields the dependence $T(E)$ that ceases to be monotone in the vicinity $E \simeq \varphi_b$ and for energies exceeding φ_b. The investigations demonstrated that oscillations of $T(E)$ are caused by the presence of the above-barrier region. It was demonstrated that the behavior of $T(E)$ oscillations changes with variation in the n-layer doping level. The frequency and amplitude of oscillations in the $T(E)$ dependence decrease with an increase in the doping level from $N_d = 5 \times 10^{15}$ to 5×10^{17} cm^{-3}. An increase in the oscillation period in $T(E)$ is related to an increase in the length of the $\varphi(x)$ region, where the electron passes over the barrier with a decrease in N_d. It is also worth noting that even for $E \geq \varphi_b$, as evident from Fig. 3, the tunneling probability $T(E)$ is not equal to unity.

The reverse *I–V* characteristics calculated using different methods have much greater distinctions (see Fig. 4). The characteristics obtained using the transfer-matrix method can be divided into two regions with a lower and higher current as compared to the characteristics obtained using the WKB approximation. One can assume from the shape of the reverse *I–V* characteristics that the calculation of $T(E)$ (see Fig. 5) by the transfer-matrix method yields a steeper current increase.

Thus, the above demonstrates that the shape of the computed *I–V* characteristics for the SB diodes depends strongly on the method of calculating $T(E)$ as

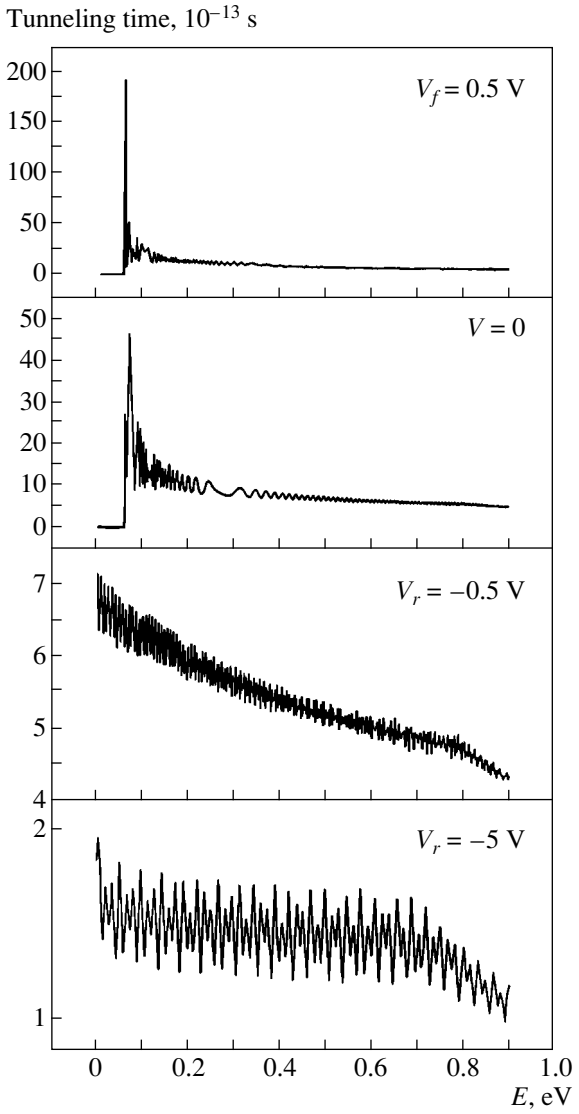

Fig. 6. Tunneling time for the forward bias $V_f = 0.5$ V, for the zero bias and reverse biases $V_r = -0.5$ and -5 V.

well as on the consideration of the above-barrier region in the course of the electron motion.

The dependences $J_f(E)$ for several values of the forward bias are shown in Fig. 7a. It is clearly seen that the maximum of the current density for the forward bias range under investigation (0.1–0.6 V) is located close to the potential-barrier top. For the reverse bias (Fig. 7b), the tunneling-current maximum shifts to the Fermi level for metal with an increase in V_r. For $V_r = 10$ V, the position of the maximum in the dependence $J_r(E)$ actually coincides with $E = E_{\mathrm{Fm}}$. This demonstrates that, at large reverse biases, the current through the structure under investigation is the tunnel one. The maximum of $J_r(E)$ for low V_r corresponds to the potential-barrier top. This fact agrees with the results of [18].

Figure 6 demonstrates that the $t(E)$ dependence is highly nonmonotonic. Once the full form of the potential is taken into account, the electron transit through the n-base for $E > V_n = \varphi(W_n)$ is always influenced by the above-barrier region. Its influence implies that the transmission time is modulated by the electron energy. This is also demonstrated by the fact that the dependence $t(E)$ is smooth only in the case of electron tunneling, which takes place for $E < V_n$. Only when the electron energy exceeds V_n do the oscillations appear in the $t(E)$ curve.

It is generally agreed that the average value of electron saturation velocity in GaAs amounts to about 2.2×10^7 cm/s [2]. Figure 6 ($V = 0$) demonstrates that the average transit time for electrons with energy lower than φ_b is equal to approximately 5×10^{-13} s, which yields an average value of approximately 10^7 cm/s for the electron transport velocity. The transport velocity for electrons with energy higher than φ_b is somewhat larger. Figure 6 demonstrates that, in the case of the reverse bias, it takes less time for electrons to pass through the thin base. Consequently, the average transport velocity for electrons is increased. For example, at $V_r = -5$ V, the average velocity for electrons with energy lower than φ_b is approximately 3.7×10^8 cm/s. For the V_r values close to the breakdown ones (10–15 V), the transit time for electrons with the energy $E < \varphi_b$ is approximately 8×10^{-14} s, which corresponds to a velocity of approximately 10^8–10^9 cm/s.

According to the results obtained (Fig. 6), the transit time for electrons passing through a thin n-base at large reverse-bias voltages can be less than the energy relaxation time for a semiconductor. In this case, the maximum response speed is limited by the energy relaxation time for the n^+-substrate, since it is supposed that the carriers travel through the n-base region ballistically. The transit time for low reverse-bias voltages can exceed the energy relaxation time. In this case, the highest speed of response is limited by the time of travel through the base region.

Actually, the time of travel through the n-base at forward biases always exceeds the energy relaxation time for a metal (Fig. 6). For this reason, the maximum response speed should, in this case, also be limited by the time of travel through the base region.

Thus, the computations demonstrate that the time it takes for electrons to travel through the n-base, especially at high reverse-bias voltages, should be 10–100 times less than was previously believed.

It is difficult to predict the effect of a consideration of the full form of the potential when calculating the I–V characteristics. Expression (2) describing the tunneling probability for a system of rectangular potential barrier and potential step demonstrates that the presence of the region with $\varphi(x) < 0$ can both increase and decrease $T(E)$, and can even give rise to resonances.

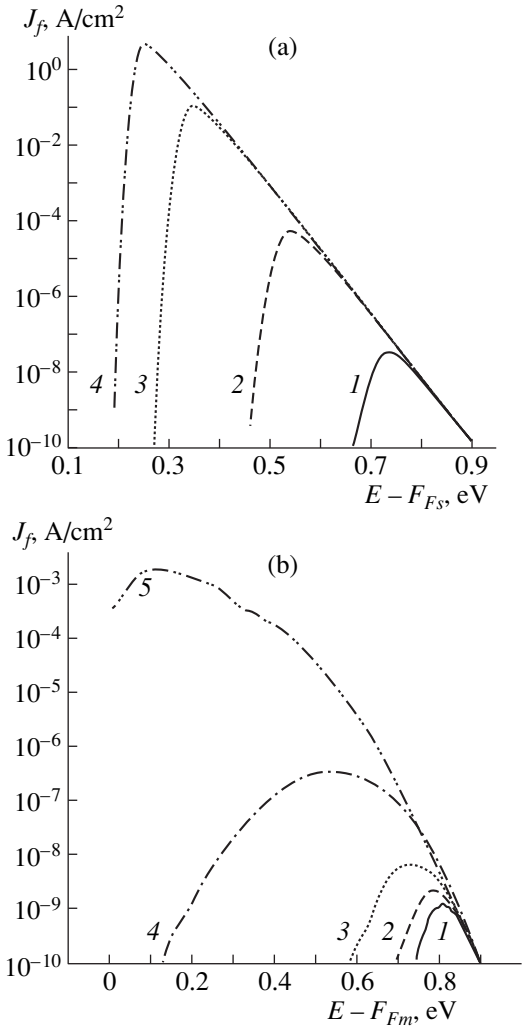

Fig. 7. Current density: (a) the forward current for bias voltages V_f = (*1*) 0.1, (*2*) 0.3, (*3*) 0.5, and (*4*) 0.6 V; and (b) the reverse current for bias voltages V_r = (*1*) –0.5, (*2*) –1, (*3*) –2, (*4*) –5, and (*5*) –10 V.

The results obtained demonstrate that resonances of the potential $\varphi(x)$ formed at a metal–semiconductor contact are absent in a wide range of bias voltages. As this takes place, fast oscillations of the $t(E)$ dependence and local resonances in the $T(E)$ dependence are observed. It is demonstrated that a consideration of the full form of potential when calculating the *I–V* characteristics decreases the current.

Thus, under assumption that electrons are not scattered within a thin base, the base region itself can significantly affect the current through the diode structure. In this case, the current through a thin base can be described adequately within the concept of tunneling. In spite of the micrometer-scale dimensions of this region, the tunneling probability T in the presence of the forward or reverse bias can be quite close to unity.

DISCUSSION OF EXPERIMENTAL RESULTS

As evident from Fig. 2, the computed dependences of the forward-bias portion of the *I–V* characteristics exactly coincide with the experimental ones. The average value of the ideality factor (n = 1.04) in the current range from 10^{-6} to 10^2 A/cm^2 is in a good agreement with the computed value n = 1.039, which was determined from the forward *I–V* characteristics calculated using the transfer-matrix method with regard to full form of the potential. The forward *I–V* characteristics calculated using other methods also are quite similar to the experimental ones. This can be explained by the fact that, at forward-bias voltages, the major current corresponds to the potential barrier top (Fig. 7a) and is not controlled by tunneling.

The reverse *I–V* characteristics are a different matter. The maximum of the $J(E)$ dependence approaches the Fermi level in metal with an increase in the reverse bias. For this reason, the electrons tunneling through the barrier provide the major contribution to the total current. In this case, the shape of the potential substantially affects the motion of electrons, and, consequently, the shape of the reverse *I–V* characteristic. In addition, the influence of the above-barrier region substantially enhances with an increase in the reverse bias. As is seen from Fig. 4, the reverse *I–V* characteristics calculated using the transfer-matrix method are in a good agreement with the experimental values within the rather wide range of reverse currents.

CONCLUSION

The calculations carried out using the transfer-matrix method with regard to the full form of the potential (a system of rectangular potential barrier and potential step) allowed us to uniquely describe the behavior of the forward and reverse *I–V* characteristics of the SB diodes.

The strong influence of the shape of the potential in the n-layer on the current transport in the Me–n–n$^+$ structures with a thin base is demonstrated. Specifically, this is true of the dependences of the tunneling probability T on the electron energy E that are calculated for a system consisting of the rectangular potential barrier and potential step. The reverse *I–V* characteristics that are calculated from these dependences give a steeper (by several orders of magnitude) increase in the reverse currents and are in better agreement with the experimental data. The consideration of a thin base when calculating the *I–V* characteristics yields an appreciable decrease (almost by an order of magnitude) in the reverse current. Calculating the forward portions of the *I–V* characteristics, a slight decrease in forward currents is found, and generally the results are in a good agreement with already-known data.

It is demonstrated that the time t it takes for electrons to pass through a metal–semiconductor contact region and the thin n-base is less than the accepted

"classical" time. In this case, strong oscillations in $t(E)$ dependences are observed in a wide energy range; also local resonances in $T(E)$ dependences appear in the vicinity of the potential barrier top and in the above-barrier region.

It is demonstrated that the potential formed by metal–semiconductor contact, as well as by a superlattice, is a mesoscopic object, and the probability of tunneling through it can be close to unity.

The frequency limitations for operation of the SB diode with a thin base ($N_d = 3.6 \times 10^{16}$ cm^{-3}, $W_n = 0.52$ μm) are evaluated. Depending on the voltage drop across the diode structure, the highest maximum frequency of operation of the diode was from 200 GHz for $V = 0$ to 6 THz for the reverse bias $V_r = -5$ V. It is demonstrated that the maximum operating frequency of the diode is substantially increased with an increase in V_r.

ACKNOWLEDGMENTS

We thank V.G. Bozhkov for his valuable help and N.L. Chuprikov for his fruitful participation in discussions of the results.

This work was supported by the Ministry of Science and Technology under the program "Surface Atomic Structures," project no. 95-1.24.

REFERENCES

1. F. A. Radovani and R. Stratton, Solid-State Electron. **9**, 695 (1966).
2. K. Shenai and R. W. Dutton, IEEE Trans. Electron Devices **35** (4), 468 (1988).
3. S. M. Sze, *Physics of Semiconductor Devices* (Wiley, New York, 1981; Mir, Moscow, 1984).
4. M. I. Veksler, Fiz. Tekh. Poluprovodn. (St. Petersburg) **30** (9), 1718 (1996).
5. V. N. Dobrovolskiĭ, G. K. Nitsidze, and V. N. Petrusenko, Fiz. Tekh. Poluprovodn. (St. Petersburg) **28** (4), 651 (1994).
6. J. Martinez, E. Calleja, and J. Piqueras, Phys. Status Solidi A **60**, 277 (1980).
7. J. Crofton and S. Sriram, IEEE Trans. Electron Devices **43** (12), 2305 (1996).
8. H. C. Card and E. H. Rhoderick, J. Phys. D: Appl. Phys. **4**, 1589 (1971).
9. E. H. Rhoderick, *Metal–Semiconductor Contacts* (Clarendon, Oxford, 1978; Radio i svyaz', Moscow, 1982).
10. J. M. Andrews, J. Vac. Sci. Technol. **11**, 951 (1974).
11. N. L. Chuprikov, Available from VINITI (1991) No. 492–V91.
12. N. L. Chuprikov, Fiz. Tekh. Poluprovodn. (St. Petersburg) **30** (3), 443 (1996).
13. N. A. Torkhov, in *Proceedings of the 4th International Conference on Actual Problems of Electronic Instrument Engineering Proceeding* (APEIE–98) (Novosibirsk, Russia, 1998), Vol. 2, p. 217.
14. N. L. Chuprikov, Fiz. Tekh. Poluprovodn. (Leningrad) **26** (12), 2040 (1992).
15. V. L. Bonch-Bruevich and S. G. Kalashnikov, *Physics of Semiconductors* (Nauka, Moscow, 1990).
16. L. Esaki, IEEE J. Quantum Electron. **22** (9), 1611 (1986).
17. S. D. Collins, D. Lowet, and J. R. Barker, J. Phys. C: Solid State Phys. **20**, 6213 (1987).
18. Yu. A. Gol'dberg, V. V. Zabrodsky, and O. I. Obolensky, Fiz. Tekh. Poluprovodn. (Leningrad) **25** (3), 439 (1991).

Translated by N. Korovin

Semiconductors, Vol. 34, No. 1, 2000, pp. 11–16. Translated from Fizika i Tekhnika Poluprovodnikov, Vol. 34, No. 1, 2000, pp. 13–18.

ELECTRONIC AND OPTICAL PROPERTIES OF SEMICONDUCTORS

Emission Associated with Extended Defects in Epitaxial ZnTe/GaAs Layers and Multilayer Structures

E. F. Venger*, Yu. G. Sadof'ev, G. N. Semenova*, N. E. Korsunskaya*, V. P. Klad'ko*, M. P. Semtsiv*, and L. V. Borkovskaya***

** Institute of Semiconductor Physics, National Academy of Sciences of Ukraine, Kiev, 252028 Ukraine*
Fax: (38044)265-83-42; E-mail: semenova@isp.kiev.ua
*** Lebedev Physical Institute, Russian Academy of Sciences, Leninskii pr. 53, Moscow, 117924 Russia*
Submitted April 22, 1999; accepted for publication May 19, 1999

Abstract—It was shown by the methods of X-ray diffraction and photoluminescence that the use of a thin intermediate recrystallized ZnTe layer between the ZnTe buffer layer obtained by molecular-beam epitaxy and GaAs substrate, as well as an increase in the thickness of the epilayer result in the improvement of the structure (enhancement of the mosaic size) and an increase in the intensity of exitonic bands. It is established that a number of characteristics of the I_1^C bands with $h\nu \approx 2.361$ eV, which are observed in the samples with quantum wells and superlattices, differ from the corresponding features of the emission lines of free and bound excitons and those lines typical of dislocation-related radiation in II–VI single crystals. It is assumed that the I_1^C band is associated with the subblocks boundaries, which comprise the mosaic structure of epitaxial layers. © *2000 MAIK "Nauka/Interperiodica".*

INTRODUCTION

It is known that, during the growth of epilayers of II–VI semiconductors on GaAs substrates, a transition layer with high densities of dislocation and other extended defects [1] is formed; these defects affect the optical properties of epilayers and also stimulate the degradation processes in light-emitting diodes fabricated on the basis of these layers [2]. This makes the problem of the identification of the bands associated with extended defects (dislocations among them) urgent in II–VI epilayers.

It is known that, in photoluminescence (PL) [3] and cathodoluminescence spectra [4] of ZnTe epilayers obtained by various methods, as well as of single crystals [5], an intense emission line I_1^C is often present ($h\nu = 2.357$ eV at 4.2 K) [6]. It is assumed that this line is caused by the radiative recombination of excitons bound either with the isolated neutral acceptor (Si_{Te} [5]), or with the acceptor (V_{Zn}) located near the misfit dislocation (vacancy-dislocation complex) [3, 7]. Thus, the nature of this band has not yet been finally established.

For elucidating the origin of emission centers responsible for the I_1^C band, the influence of buffer ZnTe epilayer on the PL spectra is studied in this work. In particular, we studied the effects of (i) a thin (~5–10 nm) intermediate recrystallized ZnTe layer placed between the buffer layer and (100) GaAs; (ii) the thickness of the buffer layer, as well as (iii) grown quantum-size layers of $Cd_xZn_{1-x}Te$/ZnTe ($x = 0.2$–0.4). In addition, the spatial distribution (over the thickness of the buffer) of the intensity (I) and spectral position (λ_m) of I_1^C band, as well as temperature dependences of I and λ_m were studied. The X-ray diffraction measurements of rocking curves were carried out simultaneously for monitoring the crystal perfection of ZnTe epilayers.

EXPERIMENTAL

All the structures were obtained by the molecular-beam epitaxy (MBE) in a Katun' setup by the evaporation of high-purity elements onto the semiinsulating (100) GaAs substrate. The GaAs surface was cleaned of the oxide layer by heating in a vacuum at a temperature of ~550–580°C; the state of the surface was monitored during the growth by the method of reflection high-energy electron diffraction (RHEED). The growth of ZnTe layers was carried out by two methods. In the first method (process I), after the substrate was cooled to the temperature of 250–280°C, molecular beams of zinc and tellurium were delivered simultaneously with to the substrate the ratio of their equivalent pressures $I_{Zn}/I_{Te} = 1 : 2$. This results in the reconstruction of the surface $a(2 \times 1)$, i.e., to its stabilization by tellurium. After film grew up to tens of nanometers, the temperature was increased up to $T_G \approx 350$°C. The epitaxy was carried out at this temperature and at the ratio of Zn/Te beam intensities to provide a simultaneous coexistence of reconstructions $a(2 \times 1)$ and $c(2 \times 2)$ for the fulfillment of growth conditions close to stoichiometric.

1063-7826/00/3401-0011$20.00 © 2000 MAIK "Nauka/Interperiodica"

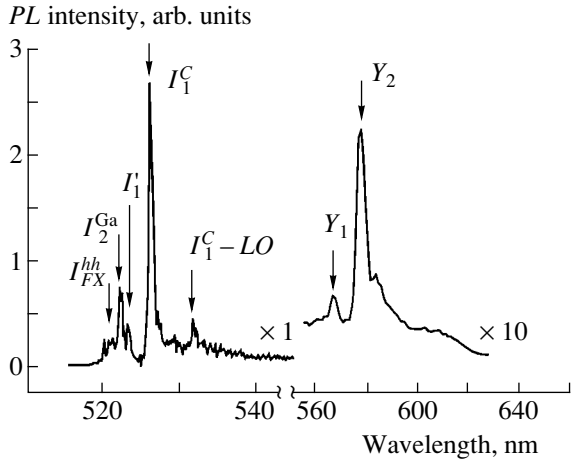

Fig. 1. Photoluminescence spectrum at T = 4.2 K of undoped buffer ZnTe/GaAs epitaxial layer 1.5 μm thick, grown with a thin intermediate recrystallized layer, λ_{exc} = 0.488 μm and P_{exc} = 8.3 W/cm^2.

In the second method, an intermediate amorphous ZnTe layer was deposited onto the substrate to improve the growth conditions [4]; then this layer was crystallized in the Te flow at T = 400–450°C. After crystallization, the substrate was cooled to 250–280°C and afterwards all the growth procedures described for process I were successively carried out.

PL was excited by the Ar^+-laser at the wavelengths λ_{exc} of λ_1 = 0.448 μm and λ_2 = 0.5145 μm and was measured at temperatures 4.2–77 K by the grating spectrometer with a resolution of ~0.5 meV. The layer-by-layer etching (in a solution of Br_2, HCl, and dioxane [8]) was used for studies of the distribution of radiative-recombination centers over the thickness of the layers. Some initial parameters of samples are listed in the table. The X-ray rocking curves were measured for studies of defect structure of layers on a two-crystal diffractometer [8].

EXPERIMENTAL RESULTS

3.1. Dependence of PL Spectra on the Preparation Conditions and Thickness of Layers

A typical spectrum of PL for ZnTe/GaAs buffer epilayer (see table, sample 2) at 4.2 K in the wavelength range of 510–630 nm is shown in Fig. 1. The spectrum involves the emission lines of free exciton (I_{FX}) split by the biaxial tensile stress into the following two components: I_{FX}^{hh} (X_{IS}; $m_j = +3/2$) and I_{FX}^{lh} (X_{IS}; $m_j = +1/2$) [3]. In this case, the line with $h\nu$ = 2.379 eV corresponds to

Parameters of samples under study

The sample no.	Buffer epilayer		Type of quantum-size layers		Position of PL bands for λ_m for λ_{exc} = 488 nm and T = 4.2 K			Half-width of rocking curves (in seconds of arc)	ε
	Thickness, μm	Type of process	Quantum wells	Superlattices	I_2^{Ga}, eV	I_1', eV	I_1^C, eV		
1	2.7	II	–	–	2.3747	2.369	2.357	~312	5.4×10^{-4}
2	1.5	II	–	–	2.3745	2.369	2.357	~360	5.6×10^{-4}
3	1.5	I	–	–	2.3734	2.37	2.356	~570	6.6×10^{-4}
4	1.5	II	$Gd_{0.3}Zn_{0.7}Te$ $L_{Z1} = L_{Z2} = L_{Z3}$ = 2 nm L_B = 30 nm	–	2.3741	2.3691	2.3569	–	6.4×10^{-4}
5	1.5	II	$Cd_{0.2}Zn_{0.8}Te$ L_Z = 5 nm	–	2.374	2.37	2.357	–	6.4×10^{-4}
6	1.5	II	$Gd_{0.3}Zn_{0.7}Te$ L_Z = 5 nm	–	2.3730	2.368	2.3565	–	6.5×10^{-4}
7	1.5	II	$Gd_{0.3}Zn_{0.7}Te$ L_{Z1} = 2 nm L_{Z2} = 4 nm L_{Z3} = 8 nm L_B = 30 nm	–	2.3734	2.368	2.357	–	6.9×10^{-4}
8	1.5	II	–	$Gd_{0.3}Zn_{0.7}Te$15 periods with L_Z = 2 nm L_B = 2 nm	2.3727	2.368	2.3557	–	7.3×10^{-4}

the I_{FX}^{hh} component, and the line with $h\nu$ = 2.374 eV, to I_{FX}^{lh} component; the latter line is likely to be the superposition of I_{FX}^{lh} and the emission line of exciton bound with the neutral donor (I_2^{Ga}) [3]. The line of exciton bound with the neutral acceptor (I_1') (presumably $\mathrm{As_{Zn}}$ [6] or a complex including V_{Zn} [9]) is also observed.

In addition to PL bands described, the intense band I_1^C peaked at $h\nu_m$ = 2.356 eV and accompanied on the long-wavelength side by a nearby band with $h\nu_m$ = 2.352 eV (I_2^C) with lower intensity is observed in the excitonic region of the spectrum (Fig. 1). In the samples with quantum-size layers, on the short-wavelength side from I_1^C, the additional band I_X is observed with $h\nu_m$ = 2.359 eV (see table, samples 8 and 6) (Figs. 2a and 2b, respectively). The band I_1^C is apparently a composite one, because one can observe in some samples a clearly pronounced shoulder on its long-wavelength side (Fig. 2). The bands located placed near I_1^C are accompanied by the phonon satellites with the electron-phonon coupling factor $s \approx 0.2$ (Fig. 1). To the longer wavelengths, fairly less intense (as compared to I_1^C) bands Y_1 ($h\nu_{m1}$ = 2.189 eV at 4.2 K) and Y_2 ($h\nu_{m2}$ = 2.147 eV at 4.2 K) were observed.

The use of the intermediate ZnTe layer (process II), as well as an increase in the epilayer thickness, result in an increase in intensity of all lines in the excitonic region and in a decrease in the intensities of the impurity band (λ = 650 nm) and the bands Y_1 and Y_2. Both these bands are virtually absent for the layer thickness of ~2.7 μm. One should note that the ratios of band intensities $I_2^{\mathrm{Ga}}/I_{FX}^{hh}$ and I_1'/I_{FX}^{hh} remain virtually constant when we pass from sample 1.5 μm thick to sample 2.7 μm thick (λ_{exc} = 0.488 μm), whereas the ratio I_1^C/I_{FX}^{hh} slightly increases [8].

Along with the change of the bands intensities, a shift of their peaks is observed (see table). The positions of band peaks for free I_{FX}^{hh} and bound excitons I_2^{Ga} (I_{FX}^{lh}), I_1', and for I_1^C band are shifted towards lower energies as compared to their position in the bulk material (E = 2.3805 ± 0.0003 eV, 4.2 K [10]); this is caused by the presence of plane tensile stresses ε [3]. In this case, the value of the shift is maximal in the samples obtained without the intermediate layer, and in the samples where the intermediate layer decreases as the epilayer thickness increases, which indicates that the stresses are relieved. Deposition of superlattice results in a noticeable shift of the peaks to lower energies, i.e., in an increase in tensile stresses, the values of which are

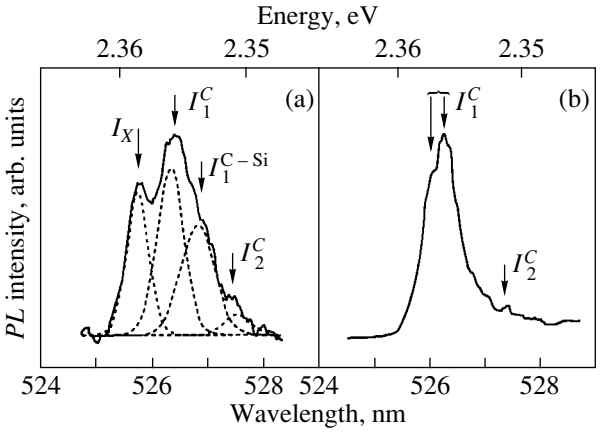

Fig. 2. Detailed PL spectrum in the 524–528 nm range of ZnTe/GaAs epilayer in the samples with a superlattice (a) and a single quantum well (b) at 4.2 K, λ_{exc} = 0.488 μm and P_{exc} = 8.3 W/cm^2.

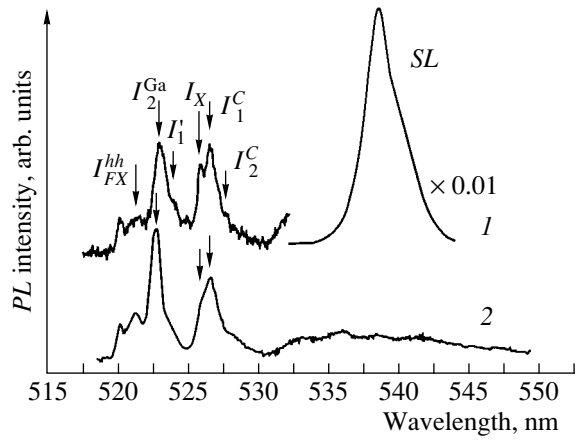

Fig. 3. PL spectrum of undoped buffer ZnTe/GaAs layer 1.5 μm thick with a superlattice prior (*1*) and after (*2*) etching off of the layer ~0.1 μm thick at λ_{exc} = 0.488 μm, P_{exc} = 8.3 W/cm^2, T = 4.2 K.

given in the table. The deformation-potential constants and the formulas given in [11] were used in calculations. It is noteworthy that the peaks of I_2^{Ga} and I_1' bands shift with the stress increase almost similarly, whereas the peak of the band I_1^C shifts to a lesser extent, which agrees with data from [11].

In [3], the band with I_1^C was assigned to an exciton bound with V_{Zn} near the dislocation, and it was assumed that the corresponding radiation comes predominantly from the GaAs–ZnTe interface region; therefore, we studied the distribution of I_1^C over the depth of the epilayer using the layer-by-layer etching of samples with the step of ~0.1 μm.

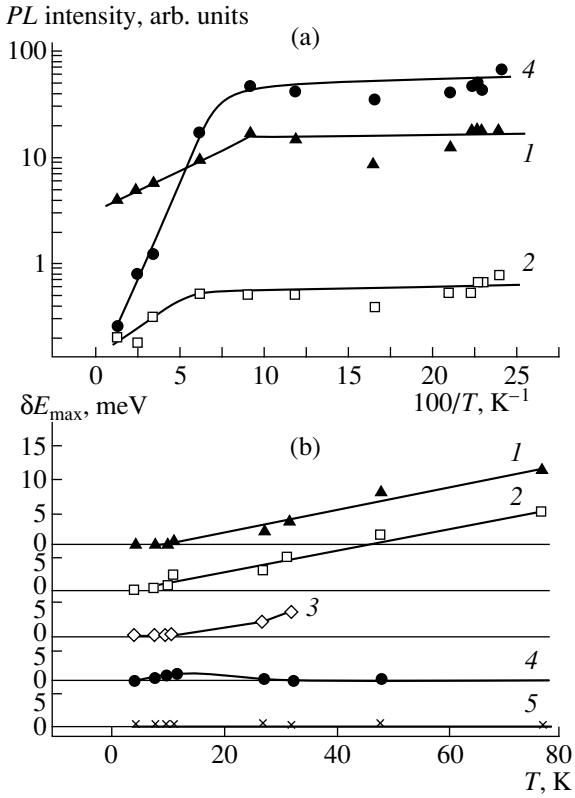

Fig. 4. Temperature dependences of intensity (a) and spectral shift of PL bands (b) in the 4.2–80 K range for ZnTe/GaAs epilayer with a single quantum well. The bands I_2^{Ga}, I_{FX}, I_1', I_1^C, and I_X are designated by *1–5*, respectively.

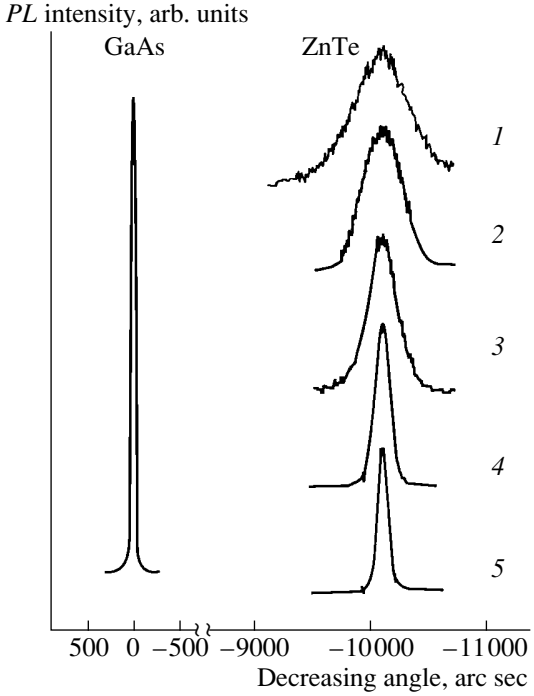

Fig. 5. Two-crystal X-ray diffraction rocking curves for ZnTe/GaAs epilayers of various thicknesses: (*1*, *2*) 1.5 μm; (*3*, *4*, and *5*) 2.7, 3.2, and 5.7 μm, respectively. For comparison, a GaAs substrate is shown (W = 36″). The rocking curves are arbitrarily shifted along abscissas for clarity. The (004) reflection and Cu$K_{\alpha 1}$ radiation was used.

As is seen from Fig. 3, the etching off of the layer ≈0.1 μm thick (see table, sample 8) results in a decrease in the relative intensities of bands I_2^{Ga}/I_{FX}^{hh}, I_1'/I_{FX}^{hh}, I_1^C/I_{FX}, and I_X/I_{FX}^{hh}. In this case, the band I_2^{Ga} was shifted to shorter wavelengths, which was caused by a decrease in the magnitude of strain. The successive etching off of the layer ≈0.2 μm thick resulted in a decrease in the ratios I_2^{Ga}/I_{FX}^{hh}, I_1'/I_{FX}^{hh}, I_1^C/I_{FX}, and I_X/I_{FX}^{hh}. The shift of I_X and I_1^C bands was not observed.

3.2. Temperature Dependence of the PL Spectrum

Figures 4a and 4b show the temperature dependences of intensities and temperature shifts of band peaks ($\Delta E_{max} = h\nu_{4.2} - h\nu_T$, where $h\nu_T$ is the peak position of the corresponding band at temperature T) in the excitonic part of the spectrum for sample 5 (see table). As the temperature increases above 15 K, the intensity of all these bands begins to diminish. The intensity of I_2^{Ga} band varies similarly to the intensity of I_{FX}^{hh} band in this case. At the same time, the slope of temperature dependence for I_1^C in this temperature region (>15 K) is noticeably steeper and corresponds to the activation energy $\Delta E_a \sim 0.008$ eV (Fig. 4a). Along with a decrease in the intensity of PL bands as the temperature is elevated, the spectral positions of free exciton I_{FX}^{hh} and bound exciton (I_2^{Ga} and I_1') emission lines are shifted to longer wavelengths with a thermal shift coefficient $dE/dT \sim 0.16$ meV/K in the temperature range of 20–80 K (Fig. 4b). At the same time, position of I_1^C and I_X lines practically do not change up to the temperature of 80 K.

3.3. Changes in X-ray Diffraction

The two-crystal rocking curves are shown in Fig. 5 for ZnTe epilayer of various thicknesses with the intermediate layer (curves *2–5*) and without it (curve *1*). The half-width of rocking curves (W) for ZnTe epilayer 1.5 μm thick without the recrystallized layer is ≈570″ (curve *1*, Fig. 5). The use of a thin recrystallized layer and an increase in the epilayer thickness from 1.5 to 5.7 μm resulted in a noticeable decrease in W from 312″ (curve *2*) to 90″ (curve *5*), respectively. It is known that for ZnTe/GaAs epilayer with a large mismatch of the layer and substrate lattice parameters

($f \sim 7.9\%$) for thicknesses exceeding critical values, the relaxation of stresses occurring by the introduction of misfit dislocations is followed by the formation of a mosaic structure [12]. The sizes of mosaic blocks (regions of coherent scattering) were increased from 0.065 (curve *1*) up to 0.75 μm (curve *5*).

DISCUSSION OF RESULTS

As is evident from the results presented, a number of characteristics of the bands I_1^C and I_X differ from those of both free and bound excitons. This difference manifests itself in the absence of a shift for the peaks of these bands in the temperature range of 4.2–80 K, and in a smaller, as compared to I_{FX}^{hh} and I_2^{Ga}, shift of λ_m when the strains are changed. The latter effect is evidenced by the dependence of positions of I_1^C and exciton lines on the presence or absence of the intermediate layer and epilayer thickness as well as by the shift of I_1^C and I_X bands as a result of the layer-by-layer etching of samples. One should note that a slight shift of the position of I_1^C with an increase in the epilayer thickness was observed also in [3] and was explained by assuming that the emission centers corresponding to this band are located predominantly in deeper layers adjacent to the ZnTe/GaAs interface. This made it possible [3] to relate the centers responsible for I_1^C band to defects in the neighborhood of misfit dislocations. However, as our experiments with the layer-by-layer etching of the epilayer show, the intensity of I_1^C band diminishes with the depth of the layer, which contradicts the assumption that the corresponding centers and misfit dislocations are related. It is important that the magnitudes of elastic strains decrease with an increase in the epilayer thickness, whereas the intensity of the I_1^C band increases. Such an anticorrelation of I_1^C and ε can indicate that this band is related to some extended defects, but not to the misfit dislocations. Another argument in favor of the relation of I_1^C and I_X bands to extended defects is the similarity of their characteristics with those of PL bands appearing in a number of II–VI single crystals after the low-temperature plastic deformation (so-called dislocation-related emission [13, 14]). Actually, as is shown in [13, 14], the plastic deformation of CdS, CdSe, and CdTe single crystals affects the bands in PL and optical absorption spectra. As in the case of the bands studied by us, the positions of the peaks of dislocation-related emission bands do not follow the temperature change of the forbidden gap width (the shift is absent up to ~40 K [13]), and also responds weaker to the mechanical stresses than the line positions for the free and bound excitons. The aforementioned similarity I_1^C and I_X to dislocation-related emission bands can be regarded as evidence for their common nature. A fairly large value of the Huang-Rhys factor $s \sim 0.2$, is apparently caused by the acceptor character of the state responsible for the I_1^C and I_X bands [13].

However, one should note that the dislocation-related emission in the bulk II–VI materials practically disappeared if they were kept at room temperature [13], whereas the I_1^C and I_X bands are the PL spectra of ZnTe epilayers which were retained without a time limit. This difference can be easily explained by the fact that the defects (impurities) mobile at room temperature are present in bulk materials and decorate the dislocations, which result in a decrease in the intensity of dislocation-related bands. At the same time, undoped ZnTe epilayers grown by MBE are much purer than single crystals. Such an explanation is consistent with the fact that the doping of the ZnTe epilayer by acceptor (nitrogen) and donor impurities (chlorine) significantly reduces the I_1^C band intensity, and this band is not detected at all for the impurity concentration $N > 10^{15}$ cm^{-3} [6].

In conclusion, we dwell on the detailed interpretation of I_1^C band as assigned to an exciton bound with the double-charged acceptor $\mathrm{Si_{Te}}$ [5]. The presence of a doubly charged acceptor was established by the Zeeman effect studies in the bulk of ZnTe single crystals [5]; the emission line 524.96 nm (E = 2.36308 eV) at 5 K corresponds to this acceptor. In the case of ZnTe epilayers obtained by various methods, MBE among them, the line I_1^C peaked at 526 nm (E = 2.3574 eV) is usually identified with the line 524.96 nm in the bulk material. The shift of its spectral position is explained in this case by the presence of mechanical stresses, and the position itself is calculated from the shifts of the free-exciton lines. However, a deformation-related shift of I_1^C band does not coincide with the deformation shift of the free-exciton line (see table) and, consequently, the line I_1^C cannot correspond to the line peaked at 524 nm in the bulk material. At the same time, one cannot rule out the presence of doubly charged acceptors (e.g., silicon or carbon, which are the typical residual impurities) in the layers studied. Therefore, the line I_1^C can be a superposition of lines of excitons bound with the doubly charged acceptor and the line of dislocation-related emission. This assumption is supported by a complex structure of this line well-pronounced in Fig. 2 and by an increase in the distance between the components of the line with an increase in strain.

The X-ray diffraction studies we have carried out allow us to suggest the following qualitative model that explains the appearance and nature of the I_1^C line:

Since its intensity increases with an increase in the mosaic size, we may assume that the centers, which caused this band, are related to the defects inside the misoriented blocks, probably with the boundaries of subblocks, which are composed of the mosaic and produce the acceptor levels in the forbidden gap. The transition I_1^C can be related to the radiative recombination of exciton bound with dislocations.

CONCLUSION

It is shown that the change of the MBE growth of the epitaxial buffer ZnTe/GaAs layers (i) by using a thin recrystallized buffer ZnTe layer ($d \sim 10$ nm), as well as (ii) by increasing the buffer layer thickness, results in the improvement of the epilayer structure (a decrease in the rocking curve half-width and an increase in the mosaic sizes), in the enhancement of the total overall intensity of PL bands in the excitonic region of the spectrum, and in a decrease in intensity at longer wavelengths.

We obtained additional information about the nature of I_1^C and on the band found nearby (I_X). The difference between the temperature and strain dependences of the positions of these bands and the corresponding characteristics of the exciton emission lines, as well as the enhancement of their intensity as the strain was decreased, allowed us to relate these bands to extended defects. This conclusion is confirmed by the similarity of their behavior and the behavior of dislocation-related emission bands in II–VI single crystals. It is assumed on the basis of these data and results of X-ray diffraction measurements that the centers responsible for I_1^C band are related to the subblock boundaries in the mosaic structure.

REFERENCES

1. J. Petruzello, D. J. Olego, X. Chu, *et al.*, J. Appl. Phys. **63**, 1783 (1988).
2. S. Guha, J. M. DePuydt, M. A. Haase, *et al.*, Appl. Phys. Lett. **63**, 3107 (1993).
3. G. Kudlek and J. Gutowski, J. Lumin. **52**, 55 (1992).
4. V. I. Kozlivsky, A. B. Krysa, and Yu. G. Sadof'ev, in *Proceedings of the X-th International Conference on MBE*, Cannes, France (1998).
5. P. J. Dean, M. J. Kane, N. Magnea, *et al.*, J. Phys. C: Solid-State Phys. **18**, 6185 (1985).
6. H. P. Wagner, W. Kuhn, W. Gebhardt, *et al.*, J. Cryst. Growth **101**, 199 (1990).
7. A. Naumov, K. Wolf, T. Reisinger, *et al.*, J. Appl. Phys. **73**, 2581 (1993).
8. E. F. Venger, Yu. G. Sadof'ev, G. N. Semenova, *et al.*, SPIE PROC., 1999 (in press).
9. J. L. Dessus, Le Si Dang, A. Nahmani, *et al.*, Solid-State Commun. **37**, 689 (1981).
10. V. I. Gavrilenko, A. M. Grekhov, D. V. Korbutyak, *et al.*, *Optical Properties of Semiconductors* [in Russian] (Naukova Dumka, Kiev, 1987).
11. G. Kudlek, N. Presser, J. Gutowski, *et al.*, Semicond. Sci. Technol. **6**, A90 (1991).
12. B. T. Jonker, S. B. Qadri, J. J. Krebs, *et al.*, J. Vac. Sci. Technol., A **7**, 1360 (1989).
13. N. I. Tarbaev and G. A. Shepel'skiĭ, Fiz. Tekh. Poluprovodn. (St. Petersburg) **32**, 646, (1998).
14. V. D. Negrii, Yu. A. Osipyan, and N. V. Lomak, Phys. Status Solidi A **126**, 49 (1991).

Translated by T. Galkina

Semiconductors, Vol. 34, No. 1, 2000, pp. 115–118. Translated from Fizika i Tekhnika Poluprovodnikov, Vol. 34, No. 1, 2000, pp. 113–116.

PHYSICS OF SEMICONDUCTOR DEVICES

Capacitance Measurements for Diodes in the Case of Strong Dependence of the Diode-Base Series Resistance on the Applied Voltage

A. A. Lebedev, Jr., A. A. Lebedev†, and D. V. Davydov

Ioffe Physicotechnical Institute, Russian Academy of Sciences, Politekhnicheskaya ul. 26, St. Petersburg, 194021 Russia

Submitted June 22, 1999; accepted for publication June 28, 1999

Abstract—Epitaxial–diffused 6*H*-SiC diodes incorporating a high-resistivity interlayer in the base were studied; the resistance of this interlayer varied when the forward-bias voltage was applied. It is shown that, in spite of the absence of direct indications of the effects of the series resistance (the capacitance is independent of frequency and the value of capacitive cutoff voltage is small), the capacitance measurements for such structures may be incorrect. *© 2000 MAIK "Nauka/Interperiodica".*

INTRODUCTION

In the past 10–15 years, capacitance-measurement methods (the capacitance spectroscopy) have been actively developed and used to study various semiconductors and semiconductor devices. We may state that capacitance spectroscopy amounts to the determination of material parameters by detecting the variations in capacitance of a *p–n* structure or a Schottky diode under the influence of various factors (illumination, temperature, and the applied voltage) or their combination. The basic advantages of the capacitance-measurement methods include a high sensitivity, the availability of a unified theory when dealing with various semiconducting materials, the possibility of studying both the devices and initial semiconducting materials, and the fact that these methods are nondestructive.

However, the capacitance-measurement methods (as any other methods) have certain restrictions imposed on their applicability. One of these restrictions is related to a large series resistance (R_b) of the sample under study. The question of how the resistance R_b influences the capacitance measurements has been repeatedly studied [1–5]. However, it has been assumed that the value of R_b does not vary in the course of measurements. In this work, we studied the *p–n* structures in which the value of R_b depended strongly on the applied voltage.

THE SAMPLES

We studied the epitaxial–diffused 6*H*-SiC p^+–*n* (SiC:B) structures [6, 7] obtained by sublimation epitaxy. Pulsed diffusion of boron was performed through the p^+ emitter into these structures after the *p–n* junction had been formed by sublimation. This diffusion was used to increase the bulk-breakdown voltage and reduce the probability of the surface breakdown. Following the doping with boron, two types of deep acceptor centers are formed in SiC: a boron-related center with a relatively shallow level located at E_v + 0.35 eV and the so-called *D* center with a level at E_v + 0.58 eV [8, 9]. The latter center is an effective trap for holes and acts as the center activating the 6*H*-SiC luminescence whose intensity peak falls in the yellow region of the visible spectrum (2.14 eV) [10]. However, a compensation of the base region by acceptor centers increases also the series resistance of the diode.

THE EXPERIMENT

Although the conditions of diffusion were the same for all the samples, the original spread in the doping level of the *n*-base resulted in a certain difference in the properties of the epitaxial–diffused structures obtained. The majority of the studied structures featured *C–V* characteristics close to those shown in Fig. 1 (diode 7). In the vicinity of the technological boundary of the *p–n* junction (region *A*), the dopant-distribution profile related to the compensation of the base region due to boron diffusion was observed in the base. Uniform distribution of impurities was observed deep inside the base region (portion *B*, Fig. 1), and the value of $N_d - N_a$ was equal to that determined in the layer prior to boron diffusion. A weak frequency dependence of the measured capacitance was also observed for certain samples.

In addition, we measured the *C–V* characteristics of another type (see Fig. 2) represented by diode 15. These *C–V* characteristics had two well-pronounced regions, the value of $N_d - N_a$ for which differed by more than two orders of magnitude (see table). In this case, the value of the measured capacitance (C_M) was inde-

† Deceased.

1063-7826/00/3401-0115$20.00 © 2000 MAIK "Nauka/Interperiodica"

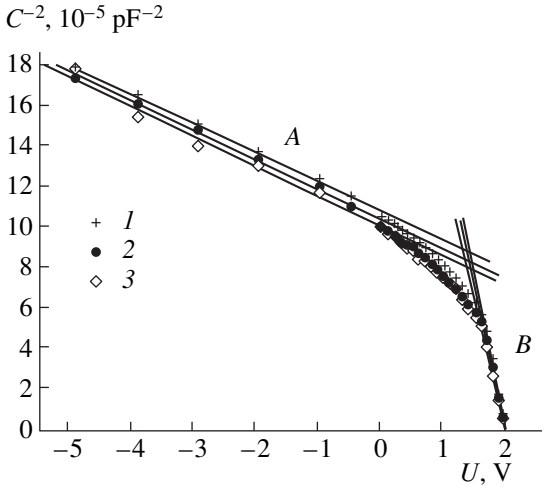

Fig. 1. The *C–V* characteristics of diode 7 as measured at the frequencies of f = (*1*) 100, (*2*) 10, and (*3*) 1 kHz.

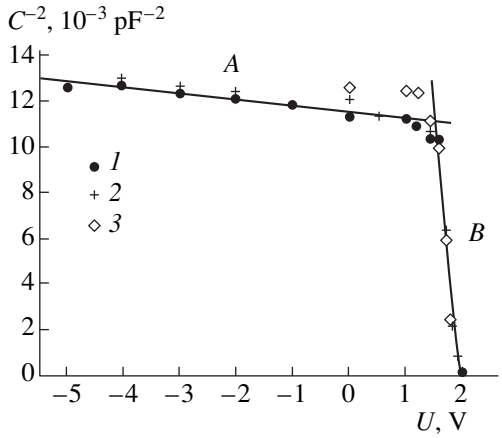

Fig. 2. The *C–V* characteristics of diode 15 as measured at the frequencies of f = (*1*) 10, (*2*) 3, and (*3*) 1 kHz.

pendent of frequency down to the minimal values of the frequencies used (f = 1 kHz). Another special feature of these structures was an abrupt emergence of yellow-region electroluminescence for the voltages corresponding to the demarcation line between the two regions of *C–V* characteristics (i.e., for $U \simeq 1.5$ eV).

Although the *C–V* characteristics of the samples similar to diode 15 did not show (according to [3, 4]) any indications that the condition for the absence of the dependence $C_M = f(\omega)$ was violated and featured a "conventional" value of capacitive cutoff ($U_C < 3$ V), the impurity-distribution profile calculated on the basis of these characteristics was unusual. First, such an abrupt change of concentration as a result of diffusion was unexpected. Second, the value of concentration $N_d - N_a$ in the vicinity of the *p–n* junction was found to be equal to about 6×10^{13} cm^{-3}, which would have been very hard to obtain by compensating the original epitaxial layer with concentration $N_d - N_a \simeq 5 \times 10^{16}$ cm^{-3}. Third, the value of $N_d - N_a$ deep inside the base region (region *B*) was almost an order of magnitude smaller than that in the layer prior to diffusion.

The value of N_d–N_a (in cm^{-3}) determined from two different portions of the *C–U* characteristic

Portions of the *C–U* characteristic	Temperature, °C			
	25	150		300
	f = 10 kHz	f = 10 kHz	f = 100 kHz	f = 10 kHz
B	6.3×10^{13}	3.9×10^{15}	8.8×10^{13}	9.7×10^{15}
A	8.5×10^{15}	4.4×10^{16}	4.5×10^{17}	4.8×10^{16}

If the observed *C–V* characteristics were nevertheless distorted by a large value of R_b, one might expect that, with an increase in temperature, this characteristic would change because the value of R_b increases as temperature is elevated; this is due to a large value of ionization energy for impurity in SiC. Therefore, we measured the *C–V* characteristics of diode 15 at temperatures of up to 300°C (see table and Fig. 3). As is evident from Fig. 3, the measured value of $N_d - N_a$ increased with an increase in temperature, and the impurity-distribution profile became less steep and more closely resembled a conventional diffusion-induced distribution.

As the frequency f was increased to 100 kHz, the *C–V* characteristic measured at T = 150°C became identical with the *C–V* characteristic measured at room temperature at a lower frequency f (Fig. 4). Thus, we demonstrated that the samples studied feature a large value of R_b and the room-temperature measurements of the capacitance were incorrect.

DISCUSSION OF THE RESULTS

As a rule, a parallel equivalent circuit for capacitance is used in measuring systems (Fig. 5a). In the case where the value of R_b is appreciable, the equivalent circuit typically used to represent a diode is shown in Fig. 5b. During the experiment, we determine the value of C_M that can be easily expressed in terms of the equivalent-circuit parameters as

$$C_M = \frac{C_d}{(1 + R_b/R_d) + \omega^2 R_b^2 C_d^2}, \qquad (1)$$

where $\omega = 2\pi f$ and C_d is the capacitance of the diode under study. As has been shown, correct measurements are possible if the ranges of frequencies and series resistances are such that

$$(R_b \omega C_d^2) \ll 1. \qquad (2)$$

It was also shown [3, 4] that a distinctive indication of violation of condition (2) is an emergence of frequency dependence of the capacitance, which brings about an increase in the capacitive cutoff U_C in the mea-

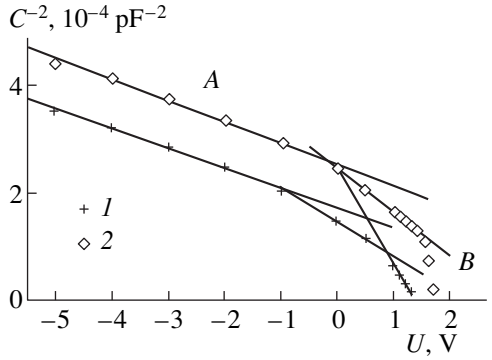

Fig. 3. The *C–V* characteristics of diode 15 as measured at the temperatures of (*1*) 300 and (*2*) 150°C. The capacitance was measured at a frequency *f* of 10 kHz.

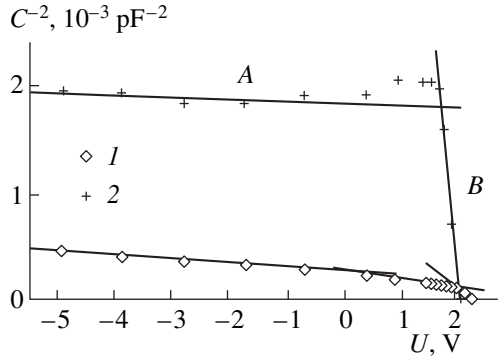

Fig. 4. The *C–V* characteristics of diode 1 as measured at a temperature of 150°C; the capacitance was measured at the frequencies *f* of (*1*) 10 and (*2*) 100 kHz.

sured dependence $C_M^{-2} = f(U)$ and, as a result, a decrease in the ionized-impurity concentration determined from this dependence.

Usually, it is assumed that $R_b \ll R_d$; therefore, in the case where $(R_b\omega C_d)^2 > 1$, expression (1) may be written as

$$C_M \simeq \frac{C_d}{\omega^2 R_b^2 C_d^2}. \quad (3)$$

It follows from expression (3) that the capacitance C_M varies proportionally to ω^{-2} and, thus, tends to zero as the operating frequency increases. At the same time, the minimal value of capacitance for the structures we studied was about 10 pF, and the value of C_M was independent of frequency (portion *A* of the curve shown in Fig. 2). This suggests that, in this case, we should use a more detailed equivalent circuit of the diode, which will make it possible to describe more correctly the experimental dependences observed. Apparently, in the case of the very large series resistance under consideration, we should take into account the base capacitance (C_b) when analyzing portion *A* of the *C–V* characteristic; the equivalent circuit of the diode then takes the form shown in Fig. 5c. In this case, the quantity C_M is given by

$$C_M = \{(R_b/R_d + 1)(C_d + (R_b/R_d)C_b) - R_b/R_d(C_d + C_b) + \omega^2 R_b^2 C_b C_d(C_b + C_d)\}/\{(1 + R_b/R_d)^2 + \omega^2 R_b^2 (C_d + C_b)^2\}. \quad (4)$$

Assuming that $R_b \simeq R_d$ and $(R_b\omega C_d)^2 \gg 1$, we arrive at

$$C_M \simeq \frac{C_d C_b}{C_d + C_b}. \quad (5)$$

Since $C_d \gg C_b$, expression (5) yields $C_M \simeq C_b$; i.e., for $R_b \simeq R_d$, the capacitance C_M is equal to the capacitance of two capacitors connected in series, with its magnitude tending to the value of C_b (that is, to several picofarads). In this case, the capacitance is independent of frequency.

ANALYSIS OF EXPERIMENTAL DATA

We now return to the SiC:B structures studied in this work. There is certain evidence that the *D* centers [11, 12] are largely formed at the edge of diffusion-induced boron distribution; therefore, in the case under consideration, it is these centers that are most likely responsible for compensation of the *n*-base. For smaller values of $N_d - N_a$ in the *n*-base, the formation of *D* centers can even result in overcompensation of the *n*-base in the vicinity of the technological boundary of the *p–n* junction (i.e., in formation of an interlayer with the π type of conductivity). Electrical conductivity of such an interlayer is defined by ionization of *D* centers (generation of holes); the probability of this process is very low at room temperature. Thus, a layer with π-type conductivity can be formed in the vicinity of the *p–n* junction; this layer is almost devoid of free charge carriers at room temperature.

We now consider the effect of such a high-resistivity interlayer on the results of measurements of capacitance in the structures under study.

Portion A of the *C–V* characteristic. At room temperature and for reverse bias, the resistance of the interlayer is large ($R_b \simeq R_d$). According to expressions (4) and (5), we have

$$C_M \simeq \frac{C_d C_b}{C_d + C_b} \simeq C_b.$$

The capacitance measured is independent of frequency and is small in magnitude. The *C–V* characteristic plotted for this range of applied voltages cannot be used to determine the value of $N_d - N_a$ in the case of $R_b \simeq R_d$.

Portion B of the *C–V* characteristic. At the point of inflection of this characteristic, the applied forward bias is found to be sufficient for the injected charge carriers to modulate the high-resistivity interlayer. The

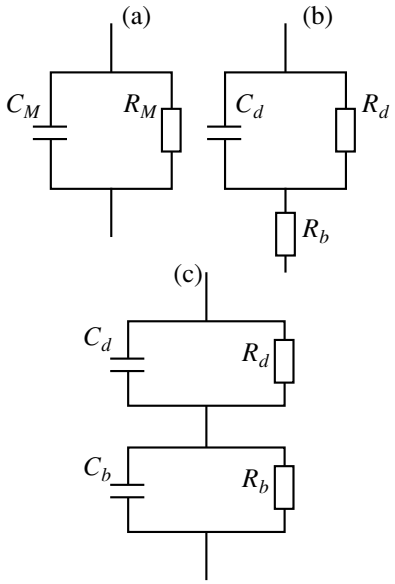

Fig. 5. Equivalent circuits of diode in measurements of the capacitance: (a) parallel equivalent circuit; (b) a more sophisticated equivalent circuit; and (c) equivalent circuit of the diode with allowance made for the presence of a thin high-resistivity interlayer.

burst of yellow-region electroluminescence indicates that the diode becomes conductive. As a result, the resistance of the base begins to decrease drastically; i.e., we now have $R_b < R_d$, and expression (3) may be used to describe the dependence $C_M = f(U)$. However, it should be taken into account that a specific value of R_b corresponds to each value of U, and the net dependence is given by

$$C_M = \frac{C_d}{1 + \omega^2 [R_b(U)]^2 C_d^2}. \quad (6)$$

As a result of a drastic decrease in the value of R_b, the capacitance C_M varies from C_b to C_d in region B. Therefore, the measured dependence $C_M^{-2} = f(U)$ is found to be much steeper (and the calculated value of $N_d - N_a$ happens to be much smaller) than it is in reality. If $U \longrightarrow U_C$, where U_C is the cutoff voltage, $C_M \longrightarrow C_d$; therefore, the voltage U_C determined from the C–V characteristic has the value typical of such SiC p–n structures ($U_C \simeq 2.5$ V for $T = 300$ K).

The temperature dependence. As the temperature increases, the probability of thermal generation of charge carriers from D centers increases. As a result, the concentration of equilibrium charge carriers in the π-conductivity region increases, and the resistance of the interlayer decreases. The C–V characteristic recovers its undistorted shape. An increase in frequency again brings about the violation of condition (2), and the C–V characteristic becomes distorted.

Thus, on the basis of the assumption that a thin high-resistivity layer is formed in the base of an SiC diode after the diffusion of boron, it is possible to interpret all the experimental results obtained.

CONCLUSION

We studied the SiC diodes with a high-resistivity interlayer in the base whose resistance was modulated when the diode was forward-biased. It is shown that, in spite of the absence of typical indications of the effects of the series resistance (independence of the capacitance of frequency and a small value of capacitive cutoff), capacitance measurements in such structures may be incorrect.

ACKNOWLEDGMENTS

This work was supported by INCO-COPERNICUS Foundation, grant. no. 96-0211.

REFERENCES

1. A. A. Lebedev and N. A. Sobolev, Fiz. Tekh. Poluprovodn. (Leningrad) **16**, 1874 (1982).
2. L. S. Berman and A. A. Lebedev, *Deep-Level Transient Spectroscopy in Semiconductors* [in Russian] (Nauka, Moscow, 1981).
3. O. V. Konstantinov and O. A. Merzin, Fiz. Tekh. Poluprovodn. (Leningrad) **17**, 305 (1983).
4. Yu. A. Gol'dberg, O. V. Ivanova, T. V. L'vova, *et al.*, Fiz. Tekh. Poluprovodn. (Leningrad) **17**, 1068 (1983).
5. E. V. Astrova, A. A. Lebedev, and A. A. Lebedev, Fiz. Tekh. Poluprovodn. (Leningrad) **19**, 1382 (1985).
6. S. Ortolland, C. Raynald, J. P. Chante, *et al.*, J. Appl. Phys. **80**, 5464 (1996).
7. A. A. Lebedev, M. M. Anikin, M. G. Rastegaeva, *et al.*, Fiz. Tekh. Poluprovodn. (St. Petersburg) **29**, 1635 (1995).
8. M. M. Anikin, A. A. Lebedev, A. L. Syrkin, *et al.*, Fiz. Tekh. Poluprovodn. (Leningrad) **19**, 69 (1985).
9. W. Suttrop, G. Pensl, and P. Laning, Appl. Phys. A **51**, 231 (1991).
10. M. M. Anikin, N. I. Kuznetsov, A. A. Lebedev, *et al.*, Fiz. Tekh. Poluprovodn. (Leningrad) **24**, 1384 (1990).
11. A. I. Veĭnger, Yu. A. Vodakov, Yu. Kulev, *et al.*, Pis'ma Zh. Tekh. Fiz. **6**, 1319 (1980).
12. V. S. Balandovich and E. N. Mokhov, in *Proceedings of Second International High-Temperature Electronics Conference* (Charlotte, USA, 1994), Vol. 2, p. 181.

Translated by A. Spitsyn

Semiconductors, Vol. 34, No. 1, 2000, pp. 119–121. Translated from Fizika i Tekhnika Poluprovodnikov, Vol. 34, No. 1, 2000, pp. 117–120.

PHYSICS OF SEMICONDUCTOR DEVICES

A Spatially Single-Mode Laser for a Range of 1.25–1.28 μm on the Basis of InAs Quantum Dots on a GaAs Substrate

S. S. Mikhrin*, A. E. Zhukov*, A. R. Kovsh*, N. A. Maleev*, V. M. Ustinov*, Yu. M. Shernyakov*, I. N. Kayander*, E. Yu. Kondrat'eva*, D. A. Livshits*, I. S. Tarasov*, M. V. Maksimov*, A. F. Tsatsul'nikov*, N. N. Ledentsov*, P. S. Kop'ev*, D. Bimberg, and Zh. I. Alferov***

** Ioffe Physicotechnical Institute, Russian Academy of Sciences, Politekhnicheskaya ul. 26, St. Petersburg, 194021 Russia*
*** Institut für Festkörperphysik Technische Universität Berlin, D-10623 Berlin, Germany*

Submitted September 20, 1999; accepted for publication September 23, 1999

Abstract—Spatially single-mode lasing in the wavelength range of 1.25–1.28 μm was accomplished in injection lasers on GaAs substrates. The peak output power is 110 mW at room temperature, and the differential quantum efficiency amounts to 37%. The active region of the laser is formed by an array of self-organizing InAs quantum dots. © *2000 MAIK "Nauka/Interperiodica".*

At present, a serious challenge is to develop inexpensive lasers designed for the region of 1.3 μm, formed on GaAs substrates, and intended to replace the existing InP-based lasers in fiber-link communication systems. Furthermore, it is expected that a more profound localization of charge carriers in the active region would make it possible to appreciably improve the device's performance [1]. Recently it has been found that the operating range of a GaAs laser can be extended to the wavelengths of 1.24–1.31 μm by using an array of self-organizing (In, Ga)As quantum dots (QDs) in the active region [2–5]. The lowest so far threshold-current density (26 A/cm^2) [3], high temperature stability (T_0 = 160 K) [4], and high differential quantum efficiency (50%) and output power (2.7 W) [5] were demonstrated. However, these promising characteristics were attained in multimode lasers with a stripe width of 50–200 μm, whereas, as far as we know, the development of spatially single-mode QD-based lasers for the region of 1.3 μm required for fiber-optic communication links has not been reported as yet.

In order to solve this problem, it is required to form narrow-stripe structures (with the width of the stripe $W < 10$ μm). In this case, internal losses increase owing to a more pronounced scattering of the light wave by inhomogeneities of the stripe boundary. The search for an increase in the differential quantum efficiency in the case of increased internal losses and for attain a higher yield of laser diodes per epitaxial wafer necessitate a decrease in the stripe length. A corresponding increase in optical losses can render impossible the attainment of long-wavelength lasing via the ground state of QD as a result of insufficient gain.

In this work, we study the spatially single-mode QD laser diodes formed on the GaAs substrates and emitting at a wavelength of 1.25 μm. The epitaxial structure was grown in the configuration of a double AlGaAs/GaAs heterostructure with separate confinement; the layers were deposited onto the *n*-GaAs(100) substrate by molecular-beam epitaxy in a RIBER-32P system. The active region of the laser structure consisted of three rows of QDs InAs filled with an $In_{0.13}Ga_{0.87}As$ solid solution with a thickness of 5.5 nm and separated by GaAs spacer layers 33 nm thick. The waveguide thickness (in the growth direction) was 0.4 μm. The details of epitaxial growth were reported elsewhere [5]. The epitaxial structure was used in fabricating laser diodes in comb configuration, with the width of the stripe being W = 7 μm. The residual thickness of the upper emitter in the etched-off region was 0.6 μm. For an insulator forming the stripe contact, we used a 0.2-μm-thick SiO_2 layer deposited by magnetron sputtering of an Si target in an oxygen atmosphere. The stripe length was varied in a range of 0.55–2.6 mm. The cavity faces were not protected by any coating. The diodes were soldered by their *p*-contact to a copper heat sink. All the device characteristics were studied under continuous excitation at 22°C unless otherwise specified.

Figure 1 shows the dependences of threshold current density J_{th} and the laser-emission wavelength λ on the stripe length L. It is evident that the lasing via the ground state of QD (λ = 1.253 μm) is realized in long-stripe diodes ($L \geq 2$ mm). The lowest J_{th} was equal to 250 A/cm^2 for L = 2.55 mm. As the stripe length decreases ($L \leq 1.25$ mm), a transition to lasing via the first excited state of QD is observed (λ = 1.18 μm) and

1063-7826/00/3401-0119$20.00

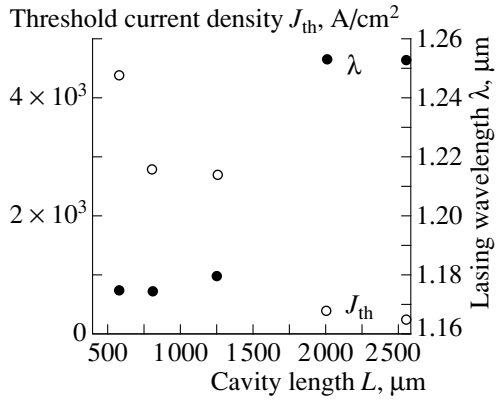

Fig. 1. Dependences of the threshold current density (nonshaded circles) and the lasing wavelength (shaded circles) on the stripe length.

is accompanied by a sharp increase in J_{th}. In order to attain the lasing via the ground state of QD, the following condition should be satisfied:

$$\alpha_i + \frac{1}{2L}\ln\left(\frac{1}{R_1 R_2}\right) \le g^{sat}. \qquad (1)$$

Here, α_i are the internal losses, $R_{1,2}$ are the coefficients of reflection from the cavity faces (equal to 0.32 in the case under consideration), and g^{sat} is the saturated (i.e., the highest attainable) gain. Internal losses in thin stripes being studied were determined from the analysis of the dependence of external differential quantum efficiency on the stripe length and were found to be 5.2 cm^{-1}, with the internal quantum efficiency being equal to $\eta_i = 70\%$. This makes it possible to evaluate the saturated gain for the ground state of QD as equal to 10.9 cm^{-1}. This value is in excellent agreement with $g^{sat} = 11$ cm^{-1} determined from the analysis of characteristics of wide-stripe diodes ($W = 200$ μm) [5]. It is noteworthy that, in the latter case, the transition to lasing via the excited state of QD was observed in the diodes with shorter stripes ($L \sim 1.2$ mm) as a consequence of lower internal losses (1.5 cm^{-1}). Thus, the relatively low saturated gain inherent in this active region with three rows of QDs imposes a limitation on the minimal stripe length. The use of a larger number of rows of QDs would make it possible to attain the lasing via the ground state in shorter stripes and, thus, increase the differential quantum efficiency.

Figure 2 shows the output power P_{out} (in continuous-wave mode) as a function of pump current for the laser with the stripe length of 2 mm. In this case, the threshold current I_{th} is 60 mA and the differential quantum efficiency $\eta_D = 37\%$. The dependence of emission intensity on the observation angle in the plane of *p–n* junction for several values of the pump current is shown in the insert. The shape of the far-field patterns for the pump currents lower than 350 mA is close to that of a Gaussian function, which indicates that the emission of this laser is spatially single-mode. For the pump currents exceeding 350 mA, a hybrid mode emerges, which is accompanied by a decrease in the detected output power. The peak power attainable with this structure for the single-mode continuous-wave lasing is 110 mW (Fig. 2).

Figure 3 shows the laser-emission spectra measured for several values of output optical power. Each spectrum involves a large number of longitudinal modes;

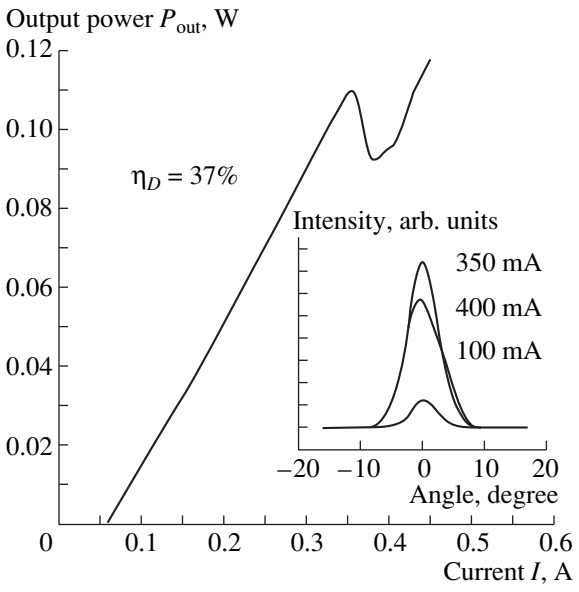

Fig. 2. The output optical power as a function of pump current. The external differential quantum efficiency (η_D) is equal to 37%. Dependence of the emission intensity on the observation angle for different pump currents (100, 350, and 400 mA) is shown in the insert.

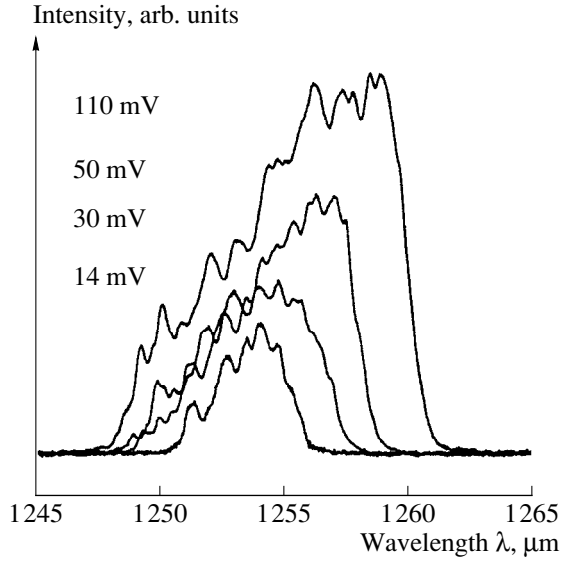

Fig. 3. Spectra of laser emission measured for several levels of output optical power (14–100 mW).

i.e., the lasers being studied do not belong to the single-frequency type. As the pump current increases, the spectral peak shifts to longer wavelengths owing to the fact that the active region is heated in the continuous-wave mode of lasing. Spectral width of the emission line δ increases with an increase in pump current I and attains a value of 8 nm for I = 330 mA (100 mW).

Taking into account the surface density of QDs ($N_{QD} = 5 \times 10^{10}$ cm^{-2} in each layer) and geometric size of the cavity (7 μm × 2 mm), we can evaluate the total number of QDs involved in lasing,

$$n_{las} = \frac{\delta}{\Delta} WLNN_{QD}, \quad (2)$$

as approximately equal to 3.4×10^6. In (2), N is the number of rows of QDs and Δ is the value of inhomogeneous broadening determined from the photoluminescence spectrum as being equal to 42 meV (50 nm). Consequently, each QD emits approximately p_{QD} = 30 nW of output optical power, which corresponds to 56 nW of overall emitted power [$(\eta_i/\eta_D p_{QD}$]. This significantly exceeds the corresponding value (p_{QD} = 12.5 nW) calculated for a laser emitting in the region of 1.1 μm and having an active region based on self-organizing InGaAs QDs in GaAs matrix [6].

We believe that the large value of output power is caused by more rapid trapping of charge carriers in the ground states of QDs residing in the outer quantum well [3]. The power emitted by a single QD is equal to the energy of an emitted photon (approximately 1 eV in the case under consideration) multiplied by the stimulated-recombination rate (1/τ). Thus, for an output optical power equal to 100 mW, the value of τ amounts approximately to 2.5 ps. In the lasing mode, an increase in the optical power is caused by the corresponding decrease in τ. However, when τ becomes comparable to the time needed to populate the state involved in lasing, the power emitted into a given spectral mode becomes saturated. Thus, the time needed to populate the ground state of the QD array being studied and estimated as the lower limit of τ is equal to 2.5 ps.

Figure 4 shows the temperature dependences of the threshold current and the emission wavelength for a diode 2 mm in length. Lasing via the ground state is observed up to 54°C. At this temperature, the wavelength of radiation attains the value of 1.28 μm, and the threshold current is 163 mA. The characteristic temperature T_0 is estimated as equal to 35 K in this range. It is noteworthy that (as we found by studying the wide laser diodes fabricated from the same epitaxial wafer) the temperature dependence of threshold current is significantly affected by the ratio between the threshold laser gain and the saturated gain of an active medium, g^{th}/g^{sat} [7]. The smaller is the ratio g^{th}/g^{sat}, the higher is T_0 at room temperature. Thus, the value of T_0 = 160 K was obtained for a laser with four cleaved faces [4]. The interrelation between the threshold gain and the temperature dependences was also discussed in [8, 9]. Thus, the use of a larger number of rows of QDs in the laser's active region would probably make it possible to increase the value of T_0.

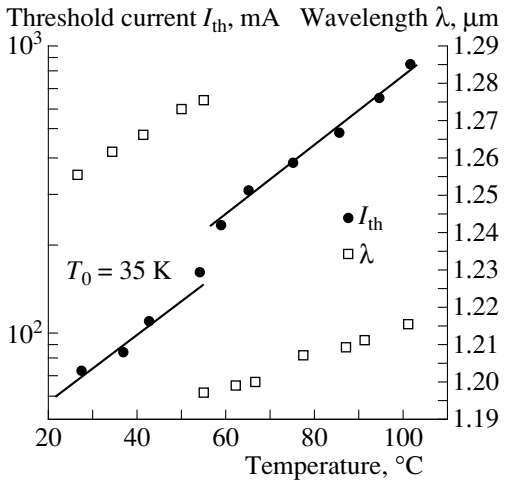

Fig. 4. Temperature dependences of the threshold current and the laser-radiation wavelength. Characteristic temperature (T_0) is equal to 35 K.

Thus, in this work, we studied the injection lasers with active regions based on three rows of self-organizing InAs QDs located in the outer InGaAs quantum well. We, for the first time, achieved spatially single-mode lasing at wavelength in the range of 1.25–1.28 μm in the structures on GaAs substrates. The peak output power is 110 mW, with the external differential quantum efficiency being 37%. The time needed to populate the ground state of a QD is evaluated as equal to 2.5 ps. The use of a larger number of the QD rows would make it possible to decrease the spectral width of the emission line, achieve a higher differential quantum efficiency, and also enhance the temperature stability of threshold current.

REFERENCES

1. K. Nakahara, M. Kondow, T. Kitatani, *et al.*, IEEE Photon. Technol. Lett. **10**, 487 (1998).
2. G. Park, D. L. Huffaker, Z. Zou, *et al.*, IEEE Photon. Technol. Lett. **11**, 301 (1999).
3. L. F. Lester, A. Stinz, H. Li, *et al.*, IEEE Photon. Technol. Lett. **11**, 931 (1999).
4. Yu. M. Shernyakov, D. A. Bedarev, E. Yu. Kondrat'eva, *et al.*, Electron. Lett. **35**, 898 (1999).
5. A. E. Zhukov, A. R. Kovsh, V. M. Ustinov, *et al.*, IEEE Photon. Technol. Lett. (1999) (in press).
6. M. Grundmann, F. Heinrichsdorf, N. N. Ledentsov, *et al.*, Jpn. J. Appl. Phys. (1999) (in press).
7. A. E. Zhukov, A. R. Kovsh, N. A. Maleev, *et al.*, Appl. Phys. Lett. **75** (13), (1999) (in press).
8. H. Temkin, D. Coblenz, R. A. Logan, *et al.*, Appl. Phys. Lett. **62**, 2402 (1993).
9. S. Seki, H. Oohasi, H. Sugiura, *et al.*, J. Appl. Phys. **79**, 2192 (1996).

Translated by A. Spitsyn

Semiconductors, Vol. 34, No. 1, 2000, pp. 17–20. Translated from Fizika i Tekhnika Poluprovodnikov, Vol. 34, No. 1, 2000, pp. 19–22.

ELECTRONIC AND OPTICAL PROPERTIES OF SEMICONDUCTORS

Evolution of Photoluminescence Spectra of Stoichiometric CdTe: Dependence on the Purity of Starting Components

A. V. Kvit, Yu. V. Klevkov, S. A. Medvedev, V. S. Bagaev, A. V. Perestoronin, and A. F. Plotnikov

Lebedev Physical Institute, Russian Academy of Sciences, Leninskii pr. 53, Moscow, 117924 Russia
E-mail: bagaev@sci.lebedev.ru

Submitted February 8, 1999; accepted for publication May 25, 1999

Abstract—A new sublimation method of material purification in a vacuum based on the crystal–vapor–crystal phase transformation is outlined. A basic design of growth reactor and the main parameters of CdTe fine purification are given. With the use of low-temperature photoluminescence (PL), the purification dynamics are revealed. This process is characterized by a complete decomposition of various complexes and by a sharp decrease in the concentration of both shallow- and deep-level residual impurity. At the final stage of purification, a polycrystalline CdTe with stoichiometric composition is obtained, and the impurity-related emission is entirely absent in PL spectra that involve only excitonic lines. The necessity of the fine purification for starting components is experimentally confirmed. Similar results are obtained for ZnTe and ZnSe. © *2000 MAIK "Nauka/Interperiodica".*

INTRODUCTION

The fundamental properties of II–VI compounds and their applications have attracted a great deal of attention. The main efforts were focused upon the development of detectors of ionizing radiation as well as of the efficient light sources operating in the short-wavelength region of the visible spectrum. The attempts at using the bulk crystals grown from the melts, solution–melts or by the vapor-phase methods in devices did not yield desired results. In these processes, the thermal-equilibrium growth and high temperatures are inherent.

Now, it becomes evident that the growth at low temperatures and high purity of starting materials are the main prerequisites for the subsequent reproducible growth of device-garde CdTe single crystals. For preparation of the high-quality II–VI compounds, the low-temperature technologies of purification adequate to the physicochemical properties of these compounds, in particular, of CdTe are required.

When developing the adequate purification technologies of non-stoichiometric II–VI compounds, their following properties were taken into account: (i) high values of the formation heat of these compounds; (ii) high vapor pressures at temperatures well below their melting points; (iii) the compounds of this class are the phases of variable composition; (iv) the point defects can be ionized and form complexes with impurities; and (v) the concentrations of impurities and point defects are interrelated.

The method described in this paper is classified as a sublimation method of material purification in a vacuum and is based on the crystal–vapor–crystal phase transformation [1]. This method has been developed as an analogue of the zone melting specially for sublimating non-stoichiometric compounds. The preliminary synthesized compound is subjected by small portions to the numerous sublimations and crystallizations, which are continuously following one after another; i.e., a cyclic reiteration of crystal–vapor–crystal phase transformation is used with simultaneous shifting of the constant temperature gradient. As a result of purification, the composition of the compound approaches the composition of the minimum pressure (the so-called point P_{min}) with a simultaneous removal of the excess component and residual impurities [1, 2]. The influence of the purity of the components used for the synthesis on the efficiency of the method of CdTe purification is assessed on the basis of PL spectra evolution.

EXPERIMENTAL

The purification of compounds (Fig. 1) is performed in an evacuated cylindrical reactor with a diameter of 0.1 m and a length of 2 m. This reactor consists of the operating (*1*) and ancillary (*2*) parts. The operating part is an annular cavity consisting of two coaxial silica tubes that are hermetically welded with each other from one side. The inner tube is closed by a blind the side of the ancillary part. The open end of the ancillary portion serves to charge the purified material into the reactor (*3*) and is equipped with a cryopump (*4*). After charging the compounds to be purified, a cup (*5*) was welded to the open end of the reactor, with the cooled finger (*6*) of the cup serve as a collector for the purified material. After the reactoring was connected to the vacuum system (an evacuated outlet is not shown in Fig. 1) and evacuated down to 10^{-5} torr, it is sealed and placed into a resistance furnace with two independent heating

1063-7826/00/3401-0017$20.00 © 2000 MAIK "Nauka/Interperiodica"

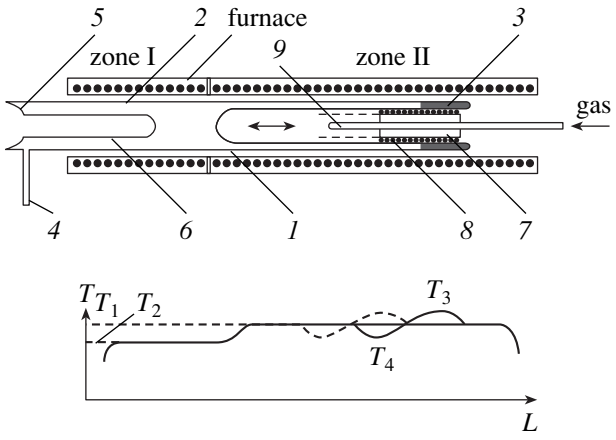

Fig. 1. Schematic sketch of the apparatus (at the top) and the distribution of T along its length (at the bottom).

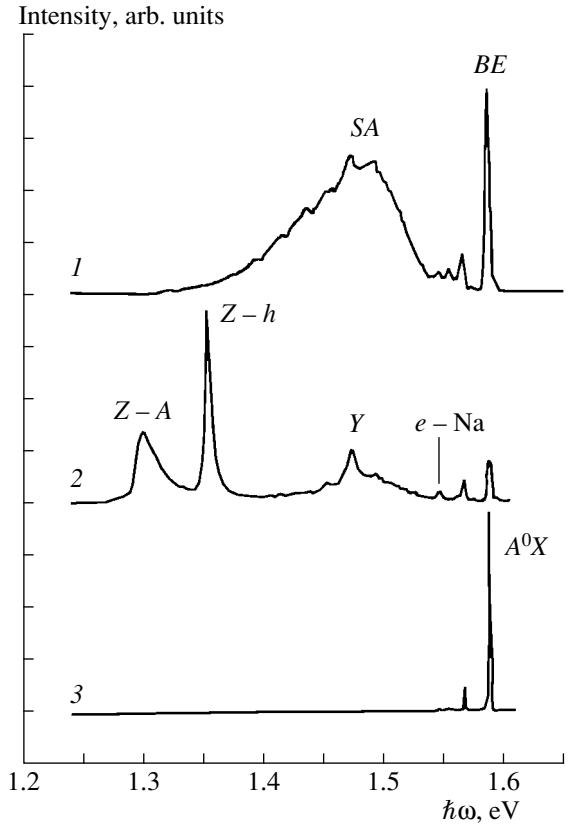

Fig. 2. Changes in the CdTe low-temperature PL spectra with an increase in the purification degree. (*1*) for CdTe synthesized from the commercial starting components (99.99%); (*2*) for CdTe synthesized from the purified components; and (*3*) for CdTe after the final purification.

zones. Zone II, where the operating part of the reactor is then placed, is heated up to a temperature T_1 and provides a background heating of the operating part. Zone I, where the cooled finger is placed, provides the temperature of deposition of material to be purified (T_2). A local gradient ($\Delta T = T_3 - T_4$) is formed with the use of a heater/cooler system (*7*) consisting of a small electrical furnace (*8*) and a nozzle (*9*) for the gas inlet into the space immediately ahead of the furnace (*8*). As a result of evaporation of the first portion CdTe, a deposit of material is formed at the inner surface of the annular cavity in the region cooled by the injected gas. This deposit (with a width of about 8–12 cm and 0.5–1.5 mm thick) is moved together with the local gradient of the system heater/cooler along the operating part of reactor with the help of a driving mechanism (not shown in Fig. 1) with a given velocity. In the course of this operation, the material is subjected repeatedly to sublimation and crystallization. Finally, when the heater/cooler system reaches the blind of the inner tube of the reactor, the cooler is switched off, and the deposit of material brought into the extended temperature field of the electrical furnace (*8*) evaporates and then is condensed at the cooled finger. The heater/cooler system returns back to the initial position (to the place where the charge was loaded), and the next portion of material is subjected to purification. The number of runs for the system transport is determined by the mass of the charge.

The starting CdTe, which was subjected to final purification, was synthesized by a direct reaction of the components of various degrees of purity at a temperature below 680°C. The low temperature of synthesis allowed us to obtain a more homogeneous material with a minimum stoichiometric deviation; this material is able to sublimate at a rather high rate.

Since all the processes of CdTe synthesis and final purification were carried out at the same temperatures, the efficiency and reproducibility of the purification method were related to the degree of purity of the starting components of Cd and Te. Before the synthesis of the compound, we purified the components by the standard methods of vacuum distillation.

The main characteristic parameters of the final purification method are as follows: $T_1 \approx 590$–610°C, $T_3 \approx 630$–650°C, $T_4 \approx 540$–560°C; the velocity of translation of heater/cooler is 6 cm/h; and the amount of material subjected to purification for a single run of the system is 50–70 g, and for one total cycle of the process it is as large as 0.5–0.8 kg.

With the help of the method proposed, compact polycrystalline ingots of high-purity CdTe were obtained at $T_2 = 560$–580°C. The grain size was as large as 5 mm. The typical results of mass-spectrometry analysis of CdTe prepared from the purified components after the final purification of compounds are shown in the table. The total purity of CdTe was 99.9997 wt % (H, N, O, C, Cl, F, and S are excluded from this estimate according to the Johnson–Matthey catalog).

The PL spectra were measured at temperatures of 4.2 and 77 K under Ar^+-laser excitation (power density $P_{exc} \sim 0.5$ W/cm^2).

RESULTS AND DISCUSSION

We have detected the changes in the low-temperature PL spectra with an increase in the purity degree of the starting components. Since all the purification processes were carried out at the same temperatures, there are strong grounds for believing that the concentrations of non-stoichiometric defects correspond to the composition at the P_{min} point for all the samples. PL spectra (one of them is shown in Fig. 2, spectrum *1*) are typical of CdTe samples synthesized from the starting components commercially available at present (99.99%). The self-activation (SA) band is dominant in the spectra; this band is overlapped by the band $\hbar\omega = 1.45$ eV. After the first process of purification of the starting initial components, the intensity of these bands decreases (spectrum *2*), and the emission of the so-called *Z* centers appears. Such a tendency is retained with an increase in the number of cycles of purification of the starting components.

The initial purification stages of the starting components mentioned above are most likely efficient for the removal of shallow-level residual donors. It is a decrease in the shallow-donor concentration in CdTe that results in a decrease in the intensity for the band $\hbar\omega = 1.45$ eV, because the shallow donors are involved in the formation of emitting complexes [3, 4].

This reasoning is confirmed by the analysis of the PL spectra for the excitonic region. The line of an exciton bound with the neutral donor (*BE*) disappears. A unique feature of the excitonic part of the spectrum is characterized by the lines of free exciton and exciton bound with the neutral acceptor (the line A^0X with $\hbar\omega = 1.59$ eV).

By using the series of purification stages for starting components, a final purification of material itself begins to be efficient: it results in a noticeable and constant decrease in the *Z*-center concentration. At the final stage of material purification, we have observed a quenching of both the *Z* and *Y* bands. The spectrum acquires a shape typical of the high-purity compounds; i.e., the PL exciton lines are absolutely dominant (Fig. 2, spectrum *3*).

It was shown previously that the *Z* band (*Z–A*) $\hbar\omega = 1.3$ eV is caused by the donor–acceptor recombination, where *Z* is a deep donor, and the acceptor is shallow (Li_{Cd}, Na_{Cd}, or K_{Cd} [5]). Owing to the fact that the purification process is more efficient for *Z* impurity than for Li, K, and Na, in the intermediate stages, an increase in the intensity of the bands related to these shallow acceptors (1.55 and 1.54 eV) can be observed. However, in the final stage, these emission lines disappear too. The low-temperature PL spectrum *3* (Fig. 2) characterizes the level of purity attained now by improving the apparatus design and enhancing the purification efficiency at the final stage. Similar results are obtained also for other II–VI compounds (ZnSe, ZnTe, and CdS).

Impurity content in the high-purity CdTe

Element	Concentration, ppm	Element	Concentration, ppm	Element	Concentration, ppm
H	Is not detected	Zn	0.04	Pr	<0.01
Li	0.009	Ga	<0.05	Nd	<0.02
Be	<0.0002	Ge	<0.008	Sm	<0.04
B	<0.0002	As	<0.02	Eu	<0.02
C	4	Se	1	Gd	<0.03
N	Is not detected	Br	<0.006	Tb	<0.01
O	5	Rb	<0.06	Dy	<0.02
F	0.02	Sr	<0.008	Ho	<0.01
Na	<0.006	Y	<0.01	Er	<0.02
Mg	<0.02	Zr	<0.01	Tm	<0.01
Al	0.01	Nb	<0.02	Yb	<0.02
Si	0.03	Mb	<0.03	Lu	<0.03
P	<0.01	Ru	<0.01	Hf	<0.02
S	0.05	Rh	<0.008	Ta	Is not detected
Cl	0.04	Pd	<0.02	W	<0.03
K	<0.01	Ag	<0.02	Re	<0.05
Ca	<0.03	Cd	Matrix	Os	<0.08
Sc	<0.01	In	<0.009	Ir	<0.03
Ti	<0.02	Sn	<0.04	Pt	<0.08
V	<0.005	Sb	<0.02	Au	<0.07
Cr	<0.04	Te	Matrix	Hg	<0.06
Mn	Is not detected	I	<0.03	Tl	<0.06
Fe	Is not detected	Cs	<0.009	Pb	<0.05
Co	<0.002	Ba	<0.04	Bi	<0.02
Ni	<0.002	La	<0.01	Th	<0.02
Cu	Is not detected	Ce	<0.01	U	<0.02

One should note that the CdTe under study had a *p*-type conduction and the concentration ~10^{13} cm^{-3} and a high mobility (>100 cm^2/V s) at 300 K. At the intermediate purification stages of the starting components, the samples have a high resistivity (up to 10^9 Ω cm) that is likely caused with the pinning of the chemical potential level by deep traps, which are produced by the impurity complexes. However, after the final purification, the resistivity drops again up to the level of 10^3–10^4 Ω cm that, as we assume, is evidence for a weak compensation of the material. The data of electrophysical measurements agrees fairly well with the results of the luminescence analysis.

Thus, we have developed a novel method and built an apparatus for the fine purification of II–VI semicon-

ductor compounds. The purification efficiency of these compounds increases with the number of purification cycles of the starting components. Correlation of the purity of the starting components with changes in PL spectra is illustrated. Both the stage-by-stage reduction of shallow donor/acceptor concentrations, and, more importantly, a decrease in the deep *Z*- and *Y*-center of concentrations are observed.

Despite the fact that, with an increase in purity the starting components, a tendency for the removal of many adverse residual impurities from the material is clearly pronounced, the efficiency of the final purification method of the compound itself is yet to be studied.

ACKNOWLEDGMENTS

This work was supported by the Russian Foundation for Basic Research, project nos. 97-02-177747, 97-02-16721, and 98-02-16980; by the grant "Leading Schools of Russia", no. 96-15-96341, and by the Programme of the Ministry of Science of RF, project no. 97-1045.

REFERENCES

1. S. Medvedieff, U.S. Patent No. 5201985 (13 April 1993).
2. S. Medvedieff and Yu. Klevkov, Application No. PCT/RU 96/00176.
3. Y. Marfaing, Progr. Cryst. Growth Charact. **4**, 317 (1981).
4. A. V. Kvit, Yu. V. Klevkov, S. R. Oktyabrsky, *et al.*, Semicond. Sci. Technol. **9**, 1805 (1994).
5. A. V. Kvit, Yu. V. Klevkov, S. R. Oktyabrsky, *et al.*, Mater. Sci. Eng., B **26**, 1 (1994).

Translated by T. Galkina

Semiconductors, Vol. 34, No. 1, 2000, pp. 21–26. Translated from Fizika i Tekhnika Poluprovodnikov, Vol. 34, No. 1, 2000, pp. 23–27.

ELECTRONIC AND OPTICAL PROPERTIES OF SEMICONDUCTORS

Formation of Photoluminescence Centers During Annealing of SiO_2 Layers Implanted with Ge Ions

G. A. Kachurin*, L. Rebohle, I. E. Tyschenko*, V. A. Volodin*, M. Voelskow**, W. Skorupa**, and H. Froeb*****

** Institute of the Physics of Semiconductors, Siberian Division, Russian Academy of Sciences, pr. akademika Lavrent'eva 13, Novosibirsk, 630090 Russia*
E-mail: kachurin@isp.nsc.ru
*** Rossendorf Research Center, Dresden, D-01314 Germany*
**** Technical University of Dresden, Dresden, D-01062 Germany*
Submitted December 17, 1998; accepted for publication June 8, 1999

Abstract—Photoluminescence (PL), Raman scattering, and the Rutherford backscattering of α-particles were used to study the formation of the centers of radiative-recombination emission in the visible region of the spectrum on annealing of the SiO_2 layers implanted with Ge ions. It was found that the Ge-containing centers were formed in the as-implanted layers, whereas the stages of increase and decrease in the intensities of PL bands were observed following an increase in the annealing temperature to 800°C. The diffusion-related redistribution of Ge atoms was observed only when the annealing temperatures were as high as 1000°C and was accompanied by formation of Ge nanocrystals. However, this did not give rise to intense PL as distinct from the case of Si-enriched SiO_2 layers subjected to the same treatment. It is assumed that, prior to the onset of Ge diffusion, the formation of PL centers occurs via completion of direct bonds between the neighboring excess atoms, which gives rise to the dominant violet PL band (similar to the PL of O vacancies in SiO_2) and a low-intensity long-wavelength emission from various Ge-containing complexes. The subsequent formation of centers of PL with $\lambda_m \sim 570$ nm as a result of anneals at temperatures below 800°C is explained by agglomeration of bonded Ge atoms with formation of compact nanocrystalline precipitates. The absence of intense PL following the high-temperature anneals is believed to be caused by irregularities in the interfaces between the formed Ge nanocrystals and the SiO_2 matrix. © *2000 MAIK "Nauka/Interperiodica".*

INTRODUCTION

The development of efficient emitters of light would be extremely valuable for silicon-based microelectronics, because it would make possible the integration of circuits for electrical and optical processing of information. Recently, the prospects for solving this problem by using the quantum-size effects in Si nanocrystals became evident. Intense emission in the spectral range near the demarcation line between the red and IR regions of the spectrum was obtained after high-temperature anneals of SiO_2 layers containing an excess of Si [1–6]. Formation of silicon nanocrystals was observed simultaneously with the emergence of intense photoluminescence (PL); this made it possible to relate the PL to the quantum-size effect, although the mechanism of the emission is not clearly understood at present. Another indirect-gap semiconductor of Group IV of the periodic table of elements (namely, Ge) has also attracted much attention. Germanium nanocrystals in SiO_2 layers are bound to exhibit the PL with a larger blue shift as a result of a large radius of exciton in Ge [7]. However, in this case, the data on the correlation between the formation of nanocrystals and that of the centers of intense PL are highly contradictory. In an early publication [7], it was reported that crystals about 6 nm in size were formed in SiO_2:Ge layers as a result of an annealing at a temperature of 800°C; simultaneously, a broad PL band peaked at $\lambda_m = 570$ nm emerged. In [8], the SiO_2:Ge samples were annealed at temperatures of 300–800°C, and an increase in the size of Ge crystallites from ≤4 to > 14 nm was observed. The precipitates with sizes of < 4 nm did not possess the diamond-like structure; however, it was these precipitates that were responsible for PL with $\lambda_m \cong 540$ nm after an annealing at 300°C. In [9], it was reported that fine nonocrystalline Ge precipitates were present in SiO_2 after annealings at temperatures T_a below 800°C. The number of these precipitates increases as T_a increases, but only for T_a approaching 800°C are they transformed into nanocrystals. It was the Ge clusters ≤2 nm in size, rather than the nanocrystals, that were related to the red PL in [10]. At the same time, in a number of publications [11–13], Ge nanocrystals were regarded as the source of PL in the range of 500–800 nm, and the possible influence of their sizes on the emission was assessed. Meanwhile, in [14], such a correlation between PL in the range of 600–800 nm and the sizes of Ge nanocrystals was not observed. In [15], a violet PL band assigned to the defects at the interfaces between Ge nanocrystals with the matrix was observed. In none of the aforementioned publications were there

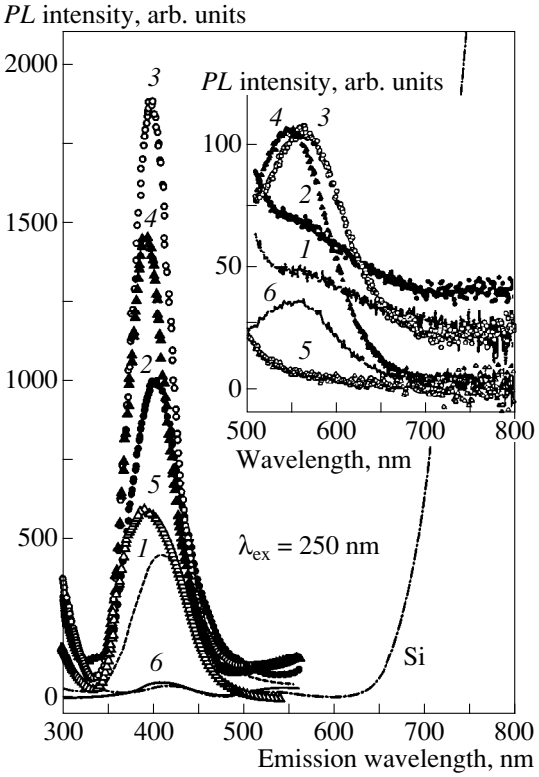

Fig. 1. Changes in PL spectra of SiO_2:Ge layers as a result of isochronal anneals for 30 min: (*1*) as-implanted; T_a = (*2*) 400, (*3*) 600, (*4*) 800, (*5*) 1000, and (*6*) 1200°C. The insert shows the long-wavelength region of the spectra. The spectrum for SiO_2:Si after an anneal at 1200°C is shown by the dot-and-dash line.

any indications that the high-temperature annealings of SiO_2:Ge layers resulted in intense PL, as is characteristic of SiO_2 implanted with Si ions.

Thus, by now, not only the relation of PL to Ge nanocrystals but also the details of the process of formation of PL centers in the course of annealing remain poorly understood. In particular, it is basically important to determine whether Ge nanocrystals are formed at a certain stage of annealing (similarly to the case of Si in SiO_2) that is accompanied by the emergence of high-intensity PL. In this work, in order to elucidate the questions posed, we annealed isochronally the SiO_2 layers implanted with Ge ions and monitored both the PL spectra in the entire visible region and Ge precipitation. For the sake of comparison, we also annealed under identical conditions the SiO_2 layers implanted with Si to the same level of doping. The conditions of excitation and detection of PL were identical for all the samples.

EXPERIMENTAL

SiO_2 layers 500 nm thick were grown thermally on Si(100) substrates. In order to obtain a thick implanted layer, Ge^+ ions were first implanted with an energy of 450 keV and a dose of 3×10^{16} cm^{-2} and then with an energy of 230 keV and a dose of 1.8×10^{16} cm^{-2}. In order to obtain a similar distribution of the implant in the reference samples, we implanted Si^+ ions first with an energy of 200 keV and a dose of 3×10^{16} cm^{-2} and then with an energy of 100 keV and a dose of 1.8×10^{16} cm^{-2}. Henceforth, the corresponding implanted layers are referred to as the SiO_2:Ge and SiO_2:Si layers, respectively. The samples were annealed for 30 min in N_2 atmosphere with a step of 200°C in the temperature range of 400–1200°C. The PL spectra were measured at room temperature, with the level of excitation by radiation with λ_e = 250 nm kept constant. The PL excitation spectra were also taken at room temperature. The intensities of all the spectra presented in what follows are given in the same units, which facilitates a comparison of the spectra. The extent of possible diffusion of Ge atoms in relation to T_a was evaluated from the data of Rutherford backscattering (RBS) of He^+ ions with an energy of 1.5 MeV. The sensitivity of RBS with respect to Ge was about 10^{19} cm^{-3}, and the depth resolution was ~10 nm. The emergence of Ge nanocrystals as the temperature T_a was elevated was detected by the Raman scattering measured at 20°C, with the pump provided by 488-nm radiation of the Ar laser and detected by a photomultiplier in the photon-counting mode. We used the *Z*(*XY*)*Z* quasi-backscattering configuration, where the axes *X*, *Y*, and *Z* corresponded to the crystallographic directions of (100), (010), and (001). Such a choice of configuration stemmed from the necessity of eliminating the signal that originated at the Si(100) substrate and was caused by two-photon scattering at transverse acoustic phonons in crystalline silicon.

RESULTS

The changes in PL spectra of SiO_2:Ge layers in the range of λ_m = 300–800 nm as caused by a gradual increase in T_a from 400 to 1200°C are illustrated in Fig. 1. The following deserves attention: The centers of luminescence peaked at about 400 nm are formed in the layers even prior to annealing. A low-intensity PL is also distinct in the longer wavelength region that is shown on an enlarged scale in the insert in Fig. 1. The annealing proceeds in several stages. Initially (T_a < 600°C), the PL intensity increases both in the region of the peak and in the long-wavelength portion of the spectrum. As the annealing temperature approaches T_a = 600°C, the intensity of the violet band with λ_m ~ 400 nm continues to increase; however, the intensity of the long-wavelength edge becomes lower, and, simultaneously, the yellow band becomes distinguishable. For T_a = 800°C, the band is more pronounced and is peaked at λ_m ~ 570 nm. In this case, the intensity of the violet band becomes significantly lower. The next characteristic stage of annealing occurs at T_a = 1000°C. Here, the long-wavelength PL becomes virtually quenched, and the intensity of the violet band continues to decrease.

Finally, after an annealing at T_a = 1200°C, a low-intensity yellow band peaked at $\lambda_m \sim 570$ nm emerges. In this respect, the SiO_2:Ge layers are radically different from the reference SiO_2:Si samples; in the latter, an annealing at 1200°C gave rise to a high-intensity PL band that was peaked at about 830 nm (see Fig. 1) and significantly exceeded in magnitude all the other peaks. It was such bands that were previously related to silicon nanocrystals [1–6].

For the sake of comparison, Fig. 2 shows the spectra of PL excitation in SiO_2:Ge and SiO_2:Si layers at the emission wavelengths of ~400 and ~460 nm, respectively. It is noteworthy that, first, the response of the SiO_2:Ge and SiO_2:Si systems to annealing is similar, and, second, there exists a correlation between variations in the intensity of emission (Fig. 1) and the excitation intensity (Fig. 2). The first of the aforementioned special features testifies to the fact that the processes occurring during the annealing of the layers implanted with Ge and Si ions are similar. The second special feature testifies that it is the PL-center formation and transformation which occur in the course of annealing, rather than an emergence or disappearance of certain competing (for example, nonradiative) recombination centers. The excitation maximum is observed after annealings at 400–600°C; following an annealing at 800°C, a decrease in intensity is already distinct, and the short-wavelength bands in both systems are virtually nonexcited when the annealing temperature is in the range of 1000–1200°C.

The extent of Ge diffusion during the annealings can be assessed from the RBS data obtained with α-particles (Fig. 3). The channels corresponding to scattering from the inner and outer boundaries of the amorphous SiO_2 layers are indicated by arrows in Fig. 3 in order to specify the depth scale. Initial distribution of Ge is close to the calculated one (see the insert in Fig. 3). Although the PL intensity (according to the data given in Figs. 1 and 2) had the opportunity to increase and decrease as the annealing temperature increased to 800°C, a redistribution of Ge for T_a < 1000°C was not observed. For T_a = 1000°C, the profile remains almost unchanged in the central part of the SiO_2 layer; however, accumulation of impurity occurs at the Si–SiO_2 boundary, which indicates that the diffusion is significant. Following an annealing at T_a = 1200°C, changes in the central part of the impurity profile become distinct as well (Fig. 3). Germanium accumulates in the vicinity of the absolute concentration maximum at a depth of ~200 nm, which indicates that there are stable sinks at this depth. The region between two peaks is depleted of Ge, and these peaks become more pronounced. The near-surface layer is also significantly depleted of Ge, and a decrease in accumulation of Ge at the Si–SiO_2 boundary is accompanied by diffusion of Ge into the Si substrate.

The Raman scattering studies (Fig. 4) showed that the peak located in the vicinity of 300 cm^{-1} and characteristic of crystalline Ge is not formed when the annealing temperature T_a is lower than 900°C. However, when T_a is increased to 1000°C, this peak becomes distinct, with its position almost consistent with that for bulk material. In addition to the emergence of the well-pro-

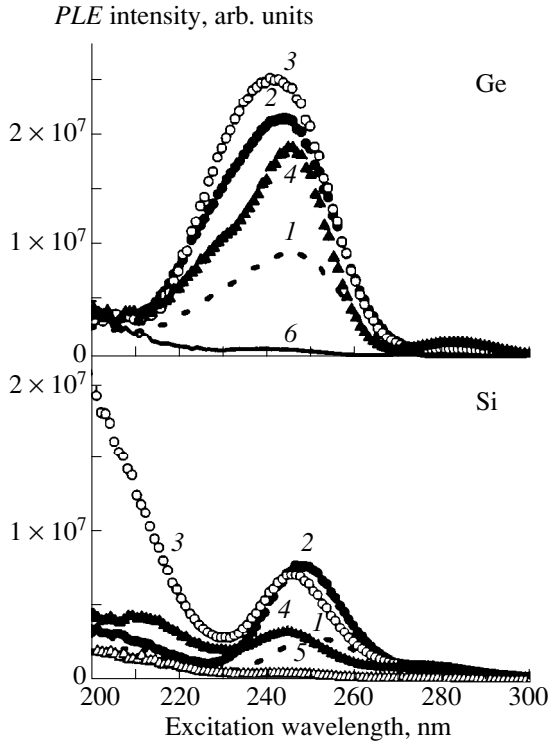

Fig. 2. Excitation spectra of ultraviolet PL for Ge and blue PL for Si in (*1*) as-implanted SiO_2 and after anneals at T_a = (*2*) 400, (*3*) 600, (*4*) 800, (*5*) 1000, and (*6*) 1200°C.

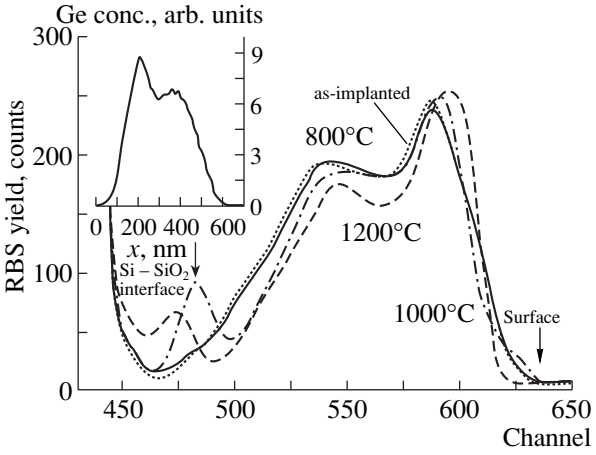

Fig. 3. The spectra of Rutherford backscattering (RBS) of He^+ ions from the as-implanted SiO_2:Ge layers and after anneals at 800, 1000, and 1200°C. The in-depth Ge distribution computed using the TRIM-95 code is shown in the insert.

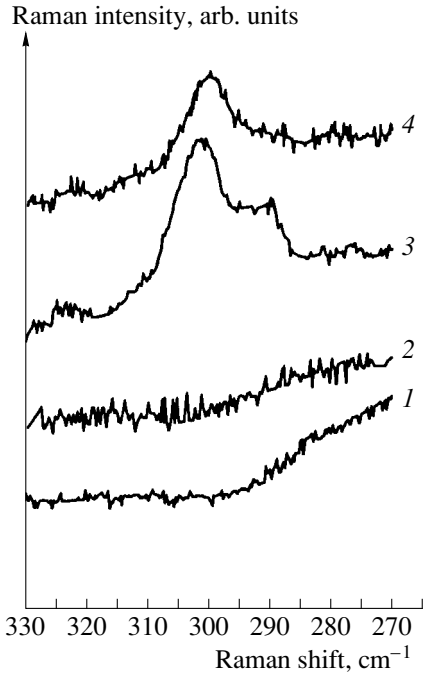

Fig. 4. The Raman spectra of (*1*) as-implanted SiO_2:Ge layers and the layers subjected to anneals at T_a = (*2*) 900, (*3*) 1000, and (*4*) 1200°C.

nounced peak at 300 cm^{-1} as T_a is increased from 900 to 1000°C, a shoulder appears in the range of wave numbers from 300 to 270 cm^{-1} and includes the line at 280-cm^{-1} corresponding to amorphous germanium. The part of the shoulder in the range of 285–295 cm^{-1} is the most evident. The low-frequency shoulder becomes significantly depressed after an annealing at 1200°C although a low-intensity scattering by amorphous Ge in the vicinity of 280 cm^{-1} is still detectable at the ultimate sensitivity of the setup.

DISCUSSION

It follows from the results reported above that, in the course of annealing of the SiO_2:Ge layers, the PL centers are formed at the early stages of decomposition of the supersaturated solid solution, well before a diffusive redistribution of Ge, and without formation of nanocrystals. Since the SiO_2:Ge and SiO_2:Si systems are much alike and, as the experiments show, the processes occurring in these systems have similar features, the mechanism of formation of PL centers is apparently the same in both cases. On the basis of the results reported in [16–21], we may state that the violet and blue bands emerge as a result of direct interaction of excess atoms of Group IV with formation of bonds of the type of Si–Si, Ge–Ge, or Ge–Si. Such bonds are similar to those corresponding to O vacancies in SiO_2, whose absorption and activation energies are well known. In the SiO_2:Si system, these energies are 5 and 2.7 eV [18, 19], respectively; in the SiO_2:Ge system, they are 5 and 3.1 eV [20, 21]. These data are consistent with the parameters observed by us for the blue and violet bands (Figs. 1, 2). In the absence of diffusion, a large-scale formation of such "vacancy" pairs may be expected in the case where the average distance between the implanted atoms becomes smaller than 1 nm. Concentration of Ge in SiO_2 in our experiments corresponded to this condition; therefore, the violet PL centers could form even before annealing. The moderate-temperature annealings help to expel Ge from the oxide, which accounts for the initial increase in the intensity of emission and excitation of short-wavelength PL (Figs. 1, 2). It is reasonable to relate the emergence and initial increase in intensity of the poorly pronounced long-wavelength PL (see the insert in Fig. 1) to the formation of more complex precipitates of Ge. This PL is not caused by radiation defects in the oxide [17]. Since the centers are formed well before the onset of Ge diffusion, they are formed most likely by completing the bonds inside the groups of neighboring expelled atoms and constitute the chains and branching clusters.

The yellow PL centers are formed for $T_a \cong$ 600–800°C in the absence of diffusion-caused redistribution of Ge. We observed a significant diffusion of Ge atoms at the same temperatures as in the case of Si diffusion [22]. If we rely on the data reported in [22], the diffusion length for Ge is bound to amount to 0.03–0.3 nm at 600–800°C. This length is too small to account for the diffusion-limited growth of precipitates; however, in this case, motion of Ge over the interatomic distances is possible. We assume that, in the above range of T_a, germanium branching clusters agglomerate to form compact noncrystalline nanoprecipitates [5, 6]. This assumption is supported by the fact that formation of the peak in the vicinity of λ_m = 570 nm is accompanied by suppression of PL in the region of longer wavelengths. Against the diffusion-limited growth of Ge precipitates and in favor of the agglomeration mechanism is also the fact that, in a number of publications, the reported sizes distributions of precipitates were not consistent with the results of calculations according to Lifshits and Slezov [23]. It follows from [23] that, in the case of diffusion-limited growth, the precipitate size distributions are bound to have a steep cutoff for particle sizes above average. In contrast, distributions with an appreciable number of large precipitates were observed experimentally in many cases after an annealing at T_a < 800°C [8, 9, 24]. Such distributions are possible if the precipitates emerge owing initially to formation of branching clusters with subsequent agglomeration of them into denser particles.

Formation of Ge nanocrystals at $T_a \sim$ 1000°C was accompanied by a quenching of yellow PL and by evident diffusion of Ge atoms to sinks (Figs. 1, 3). Both of these facts can be easily accounted for if we assume that the centers of PL with $\lambda_m \sim$ 570 nm are the precursors of nanocrystals and that the Ostwald ripening contributes to crystallization. The latter assumption is sup-

ported by the features of redistribution of Ge in the course of high-temperature anneals. Germanium atoms leave the regions where their concentration and the probability of forming stable precipitates are lower. On the other hand, germanium accumulates in the vicinity of the concentration peak (Fig. 3). A significant increase in the average size of Ge precipitates on annealings was observed in [8, 12, 24]. As is evident from Fig. 3, comparatively small differences in initial concentrations of Ge at the depth of ~200–400 nm significantly affect the destiny of precipitates in the course of anneals. This agrees well with the aforementioned hypotheses that nucleation of PL centers critically depends on the initial concentration of germanium.

The absence of intense PL in SiO_2 containing Ge nanocrystals after high-temperature anneals is apparently related to the Ge–SiO_2 boundary. Previously, an important role of the boundary between Si nanocrystals and SiO_2 matrix has been repeatedly emphasized when analyzing the PL in these nanocrystals [1, 4, 6]. It is reasonable to assume that the perfect Si–SiO_2 boundary meets the requirements for an efficient PL, whereas the Ge–SiO_2 boundary does not. The presence of the low-frequency shoulder (in addition to the peak corresponding to crystalline Ge; see Fig. 4) in the Raman spectra after an anneal at 1000°C is direct evidence of relaxation of Ge atoms in the vicinity of the crystallites' boundaries [25, 26]. On the other hand, these spectral features may be a consequence of the simultaneous existence of fine amorphous and larger crystalline nanoprecipitates. As the temperature T_a is elevated to 1200°C and Ostwald ripening sets in, the average particle sizes increase and the role of interfaces becomes less important (Fig. 4). However, visible PL is impossible in the case of large crystallites because the size restrictions are lifted. In the case of fine precipitates remaining after an anneal at 1200°C, the Ge–SiO_2 boundary becomes more perfect; however, these precipitates cannot preserve the crystallinity owing to the destabilizing effect of the surface [27]. The emergence of long-wavelength PL after a high-temperature anneal was also reported in [28]; in this case, the intensity of this PL was lower by a factor of about 30 than that of the violet PL. We believe that the low-intensity 570-nm PL after an anneal at 1200°C is related to fine nonocrystalline Ge precipitates. At present, it is hard to tell whether the nature of the yellow PL centers is the same after the anneals at 800 and 1200°C.

CONCLUSION

In SiO_2 implanted with high doses of Ge ions, the visible-PL centers are formed even before an anneal, with a violet-PL band with $\lambda_m \sim 400$ nm dominant. The evolution of PL emission and excitation spectra as a result of anneals is similar to that for a SiO_2:Si system; moreover, changes in the PL spectra are observed well before the temperatures corresponding to diffusion-related Ge redistribution are reached. This makes it possible to assume that, in the case of Ge implantation as well, the emergence of primary centers of PL for low T_a occurs initially via the formation of direct bonds between the neighboring excess atoms (i.e., the oxygen vacancies giving rise to the band peaked at $\lambda_m \sim$ 400 nm) and the development of clusters bringing about a broad spectrum of low-intensity PL. Transformation of the above band into the band with $\lambda_m \sim$ 570 nm on the annealings at temperatures up to ~800°C is accounted for by agglomeration of branching clusters into compact noncrystalline Ge precipitates rather than by diffusion-limited growth of precipitates. The diffusion-caused redistribution of Ge becomes evident only when the annealing temperature T_a is as high as ~1000°C; it is only then that Ge nanocrystals are formed. As distinct from the case of Si nanocrystals, the formation of Ge nanocrystals is not accompanied by the emergence of high-intensity PL caused by the size restrictions. The absence of such PL is apparently caused by the fact that the Ge–SiO_2 boundary is imperfect.

REFERENCES

1. T. Shimizu-Iwayama, K. Fujita, S. Nakao, *et al.*, J. Appl. Phys. **75**, 7779 (1994).
2. H. A. Atwater, K. V. Scheglov, S. S. Wong, *et al.*, Mater. Res. Soc. Symp. Proc. **316**, 409 (1994).
3. P. Mutti, G. Ghislott, S. Bertoni, *et al.*, Appl. Phys. Lett. **66**, 851 (1995).
4. T. Shimizu-Iwayama, Y. Terao, A. Kamiya, *et al.*, Nucl. Instrum. Methods Phys. Res., Sect. B **112**, 214 (1996).
5. G. A. Kachurin, I. E. Tyschenko, K. S. Zhuravlev, *et al.*, Nucl. Instrum. Methods Phys. Res., Sect. B **112**, 571 (1997).
6. G. A. Kachurin, I. E. Tyschenko, W. Skorupa, *et al.*, Fiz. Tekh. Poluprovodn. **31**, 730 (1997).
7. Y. Maeda, N. Tsukamoto, Y. Masumoto, *et al*., Appl. Phys. Lett. **59**, 3168 (1991).
8. Y. Kanemitsu, H. Uto, Y. Masumoto, *et al.*, Appl. Phys. Lett. **61**, 2187 (1992).
9. M. Fujii, S. Hayashi, and K. Yamamoto, Jpn. J. Appl. Phys. **30**, 687 (1991).
10. S. Hayashi, J. Kanazawa, M. Kataoka, *et al.*, Z. Phys. D: At., Mol. Clusters **26**, 144 (1993).
11. J. Maeda, Phys. Rev. B: Condens. Matter **51**, 1658 (1995).
12. C. M. Yang, K. V. Scheglov, K. J. Vahala, *et al.*, Nucl. Instrum. Methods Phys. Res., Sect. B **106**, 433 (1995).
13. A. K. Dutta, Appl. Phys. Lett. **68**, 1189 (1996).
14. K. S. Min, K. V. Scheglov, C. M. Yang, *et al.*, Appl. Phys. Lett. **68**, 2511 (1996).
15. M. Zacharias and P. M. Fauchet, Appl. Phys. Lett. **71**, 380 (1997).
16. L.-S. Liao, X.-M. Bao, X.-Q. Zheng, *et al.*, Appl. Phys. Lett. **68**, 850 (1996).
17. G. A. Kachurin, L. Rebohle, W. Skorupa, *et al.*, Fiz. Tekh. Poluprovodn. **32**, 439 (1998).

18. R. Tohmon, J. Shimogaichi, H. Mizuno, *et al.*, Phys. Rev. Lett. **62**, 1388 (1989).
19. H. Nishikawa, T. Shiroyama, R. Nakamura, *et al.*, Phys. Rev B: Condens. Matter **45**, 586 (1992).
20. H. Hosono, Y. Abe, D. L. Kinser, *et al.*, Phys. Rev. B: Condens. Matter **46**, 11445 (1982).
21. M. Gallagher and U. Osterberg, Appl. Phys. Lett. **63**, 2987 (1993).
22. L. A. Nesbit, Appl. Phys. Lett. **46**, 38 (1985).
23. I. M. Lifshits and V. V. Slezov, Zh. Éksp. Teor. Fiz. **35**, 479 (1958).
24. J. G. Zhu, C. W. White, L. D. Budai, *et al.*, J. Appl. Phys. **78**, 4386 (1995).
25. S. Hayashi, M. Ito, H. Kanamori, *et al.*, Solid State Commun. **44**, 75 (1983).
26. V. A. Gaĭsler, I. G. Neizvestnyĭ, M. P. Sinyukov, *et al.*, Pis'ma Zh. Éksp. Teor. Fiz. **45**, 347 (1987) [JETP Lett. **45**, 441 (1987)].
27. Z. Iqbal, S. Veprek, A. P. Webb, *et al.*, Solid State Commun. **37**, 993 (1981).
28. J.-Y. Zhang, X.-L. Wu, and X.-M. Bao, Appl. Phys. Lett. **71**, 2505 (1997).

Translated by A. Spitsyn

Semiconductors, Vol. 34, No. 1, 2000, pp. 27–31. Translated from Fizika i Tekhnika Poluprovodnikov, Vol. 34, No. 1, 2000, pp. 28–32.

ELECTRONIC AND OPTICAL PROPERTIES OF SEMICONDUCTORS

Special Features of Electrical Activation of ^{28}Si in Single-Crystal and Epitaxial GaAs Subjected to Rapid Thermal Annealing

V. M. Ardyshev*, M. V. Ardyshev, and S. S. Khludkov****

** Tomsk Polytechnical University, Tomsk, 634004 Russia*

*** Siberian Institute of Physics and Technology, Tomsk State University, pl. Revolyutsii 1, Tomsk, 634050 Russia*

Submitted March 29, 1999; accepted for publication June 8, 1999

Abstract—Concentration profiles of ^{28}Si implanted in single-crystal and epitaxial GaAs were determined by measuring the *C–V* characteristics after the postimplantation rapid thermal annealings for 12 s at T = 825, 870, and 905°C. The temperature dependence of Hall mobility of electrons in the Si-implanted layers subjected to the same annealings was determined by the Van der Pauw method within the range of 70–400 K. As distinct from conventional thermal annealing (for 30 min at 800°C), the rapid thermal annealing brings about a diffusive redistribution of silicon to deeper layers of GaAs for the materials of both types, with the diffusivity of silicon being twice as high in single-crystal GaAs as that in GaAs epitaxial layers. Analysis of temperature dependence of electron mobility in ion-implanted layers following a rapid thermal annealing indicates a significantly lower concentration of the defects limiting the mobility as compared to the case of a conventional thermal annealing for 30 min. © *2000 MAIK "Nauka/Interperiodica".*

INTRODUCTION

It was shown in [1–3] that, in the case of radiation-induced annealing of GaAs, the role of nonthermal effects is important in the processes of diffusion and electrical activation of impurity. The rates of the above processes are largely controlled by imperfections in the initial material.

In connection with this, the objective of this work was to study the behavior of ^{28}Si implanted in single-crystal and epitaxial GaAs in relation to the temperature of the rapid thermal annealing (RTA), with the implanted surface being protected by a dielectric film; we also studied the residual defects in ion-implanted layers, which controlled the mobility of electrons.

EXPERIMENTAL

We studied the samples of initially undoped, (100)-oriented wafers of GaAs single crystals with chromium concentration $N_{Cr} < 10^{16}$ cm^{-3}, dislocation density $N_D \le 5 \times 10^4$ cm^{-2}, and resistivity $\rho > 10^7$ Ω cm; the epitaxial GaAs films that were grown by gaseous-phase epitaxy, had the background-impurity concentration $N_{res} < 10^{14}$ cm^{-3}, and were 5–7 μm thick were also studied.

After the wafers were treated in a $H_2SO_4 : H_2O_2 : H_2O = 1 : 1 : 10$ etchant, they were implanted with ^{28}Si ions, first with an energy of E_1 = 50 keV and a dose of $F_1 = 6.25 \times 10^{12}$ cm^{-2} and then with an energy of E_2 = 75 keV and a dose of $F_2 = 1.875 \times 10^{12}$ cm^{-2}. Care was taken to eliminate the axial and planar channeling during the implantation [3]. The RTA of the samples with the surface protected by Sm-doped SiO_2 film was performed in an Impul's-5 setup at the temperatures T = 825, 870, and 905°C in a flow of nitrogen with a dew point no higher than –65°C; the duration of RTA was 12 s. Reference samples were annealed thermally in a furnace for 30 min at T = 800°C. After the annealing, the SiO_2 film was removed and the surface of the samples was cleaned. The Schottky barriers 100×100 μm^2 in area were then formed, with metallization being based on an AuGe + 14%Ni alloy; the *C–V* characteristics of these barriers were measured to determine the concentration profiles of electrons. The Van der Pauw method was used to measure the temperature dependence of the Hall mobility of electrons within the temperature range of 80–400 K.

RESULTS AND DISCUSSION

Figures 1 and 2 show the experimental concentration profiles for electrons $n(x)$ as measured after an RTA of single-crystal and epitaxial GaAs, respectively; the calculated profile of ion-implanted silicon is also shown. Figure 1 also shows the electron-concentration profile measured after a conventional thermal annealing (TA) for 30 min at 800°C. The calculated profile was plotted with the use of the first two moments of the ^{28}Si projected-range distribution measured by the secondary-ion mass spectroscopy [4]; these moments are R_p (the projected range itself) and ΔR_p (the corresponding standard deviation).

1063-7826/00/3401-0027$20.00 © 2000 MAIK "Nauka/Interperiodica"

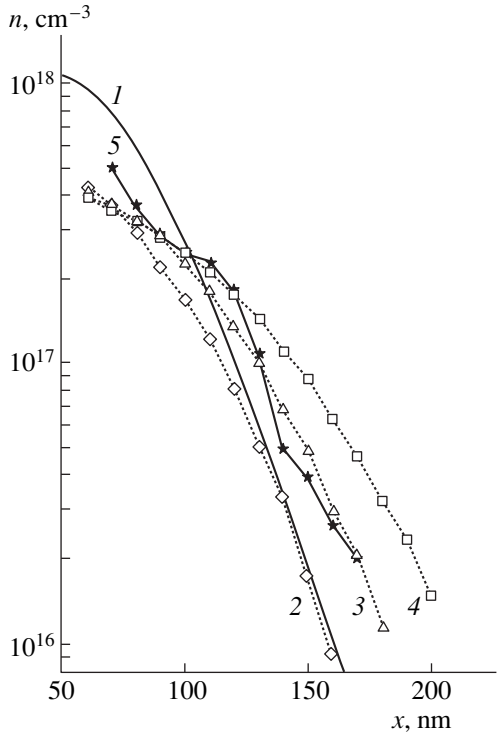

Fig. 1. The concentration profiles for implanted silicon: (*1*) the result of calculation for the implantation parameters of $E_1 = 50$ keV and $F_1 = 6.25 \times 10^{12}$ cm^{-2} combined with $E_2 = 75$ keV and $F_2 = 1.88 \times 10^{12}$ cm^{-2}; the electron-concentration profiles $n(x)$ measured after a rapid thermal annealing of GaAs single crystals for $t = 12$ s at the temperatures T_{ann} of anneal of (*2*) 825, (*3*) 870, and (*4*) 905°C; and the concentration profile (*5*) $n(x)$ measured after a conventional thermal anneal for $t = 30$ min at $T_{ann} = 800$°C.

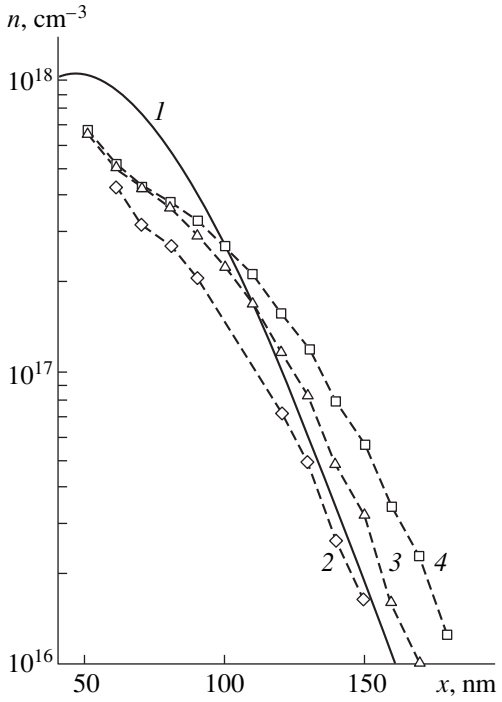

Fig. 2. The same concentration profiles as in Fig. 1 (except for the curve *5*) are shown, but the curves *2–4* here were obtained for epitaxial GaAs film after anneals at the same (as in Fig. 1) temperatures.

We assume that the experimental profile can be described by the formula

$$n(x) = n_{max}\exp\left[-\frac{(x-R_p)^2}{2\sigma^2}\right], \qquad (1)$$

where $n_{max} = \eta F/(2\pi)^{1/2}\sigma$;

$$\sigma^2 = \Delta R_p^2 + 2Dt;$$

η is the fraction of electrically active silicon; D is the diffusion coefficient; F is the dose of implanted ^{28}Si; and t is the duration of annealing. We then used the above formulas and experimental data to determine the values of σ^2, n_{max}, D, and η (see Table 1).

It is evident from Figs. 1 and 2 that a broadening of the electron-concentration profiles (Figs. 1, 2; curves *2–4*) as compared to the calculated profile

Table 1. The values of diffusion-related parameters and the fraction of electrically active silicon in GaAs single crystals and epitaxial films subjected to rapid thermal annealing

Type of material, type of annealing, temperature of annealing, duration of annealing	σ^2, 10^{-11} cm^2	n_{max}, 10^{17} cm^{-3}	D, 10^{-15} cm^2 s^{-1}	η
Single crystal, TA, 800°C, 30 min	2.10	6.10	2.0	0.860
Single crystal, RTA, 825°C, 12 s	1.86	4.25	144.5	0.564
Single crystal, RTA, 870°C, 12 s	2.50	4.20	411.2	0.646
Single crystal, RTA, 905°C, 12 s	3.70	3.80	911.2	0.711
Epitaxial, RTA, 825°C, 12 s	1.70	4.58	73.7	0.581
Epitaxial, RTA, 870°C, 12 s	2.00	4.80	202.8	0.661
Epitaxial, RTA, 905°C, 12 s	2.60	4.65	452.8	0.730

Note: TA stands for conventional thermal annealing, and RTA stands for rapid thermal annealing.

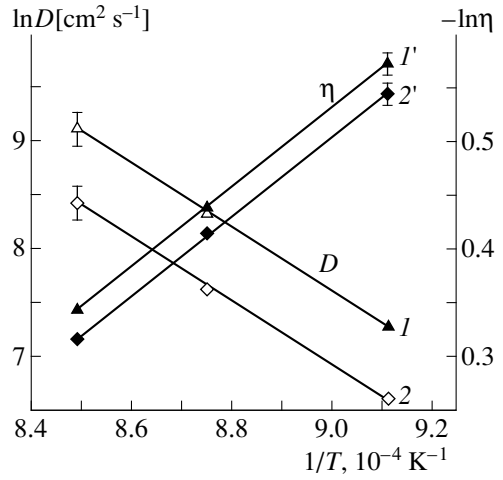

Fig. 3. Dependences of (*1*, *2*) the diffusion coefficient *D* and (*1*', *2*') the level of electrical activation η of silicon on reciprocal absolute temperature for GaAs (*1*, *1*') single crystals and (*2*, *2*') epitaxial films.

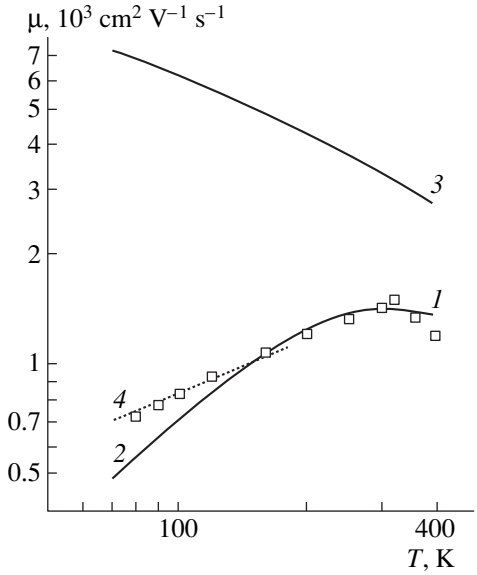

Fig. 4. Temperature dependences of (*1*) the Hall mobility of electrons in GaAs single crystal after a thermal annealing; (*2*) the mobility calculated with formula (4); and (*3*) the mobility calculated with formula (5). The dashed line *4* corresponds to $\mu \sim T^{1/2}$.

(Figs. 1, 2; curves *1*) is observed in both single crystals and epitaxial films of GaAs. The profiles obtained after an RTA have a smooth slope, whereas, in the case of profiles measured after a TA, a dispersion of the electron-concentration gradient in depth is observed, so that the profile features the points of inflection. The diffusion coefficient (Table 1) in single-crystal GaAs is four times greater than that in epitaxial GaAs, whereas the fraction of electrically active Si is somewhat smaller in the case of epitaxial GaAs for each of the annealing temperatures. In the case of RTA, on average, the values of *D* are two orders of magnitude larger than those in the case of TA. An anomalously high level of electrical activation of ^{28}Si is also observed in the case of TA, which is apparently related to the effect of electrons generated as a result of TA-induced cessation of compensation of background donors present in initial material.

Figure 3 shows the dependences of the diffusion coefficient and the level of electrical activation of ^{28}Si on reciprocal temperature for single crystals and epitaxial films of GaAs. Assuming that *D* and η are given by

$$D = D_0 \exp\left[-\frac{E_{AD}}{kT}\right] \quad (2)$$

and

$$\eta \sim \exp\left[-\frac{E_{A\eta}}{kT}\right], \quad (3)$$

we use the tangent of the slope of straight lines $\ln D(1/T)$ and $\ln\eta(1/T)$ to estimate the activation energies of diffusion and electrical activation of ^{28}Si (E_{AD} and $E_{A\eta}$, respectively) and also the pre-exponential factor D_0. For GaAs single crystals, we found that E_{AD} = (2.58 ± 0.05) eV, $E_{A\eta}$ = (0.32 ± 0.01) eV, and $D_0 \cong 9.5 \times 10^{-2}$ cm^2 s^{-1}. For epitaxial GaAs, we obtained E_{AD} = (2.55 ± 0.05) eV, $E_{A\eta}$ = (0.32 ± 0.01) eV, and $D_0 \cong 3.6 \times 10^{-2}$ cm^2 s^{-1}.

It is evident that the values of E_{AD} and $E_{A\eta}$ almost coincide for the materials of both types; however, the factor D_0 is almost three times larger in the case of single crystals of GaAs than in the case of epitaxial GaAs. The obtained values of E_{AD} and $E_{A\eta}$ for RTA are smaller than those for TA (3.3 eV [6] and 0.5 eV [7], respectively). Thus, in the course of rapid thermal annealing of GaAs single crystals and epitaxial films, a decrease in the height of potential barriers for diffusion and electrical activation of silicon is observed as compared to a long-term conventional thermal annealing.

Figure 4 shows the experimental temperature dependence of the Hall mobility of electrons in GaAs single crystals after a TA (curve *1*) and the resulting calculated dependence μ(*T*) (curve *2*) determined from the formula

$$\mu_\Sigma = \left[\frac{1}{\mu_{PO}} + \frac{1}{\mu_{AC}} + \frac{1}{\mu_{PIEZO}} + \frac{1}{\mu_{ION}} + \frac{1}{\mu_W}\right]^{-1}, \quad (4)$$

where μ_{PO} is the mobility controlled by scattering by polar optical phonons, μ_{AC} is the mobility controlled by acoustic phonons, μ_{PIEZO} is the mobility controlled by piezoelectric scattering, μ_{ION} is the mobility controlled by scattering by ionized impurity, and μ_W is the mobility controlled by scattering from additional agglomerates of defects. The components of mobility controlled by the lattice scattering were calculated as in [8], whereas those of mobility controlled by scattering from

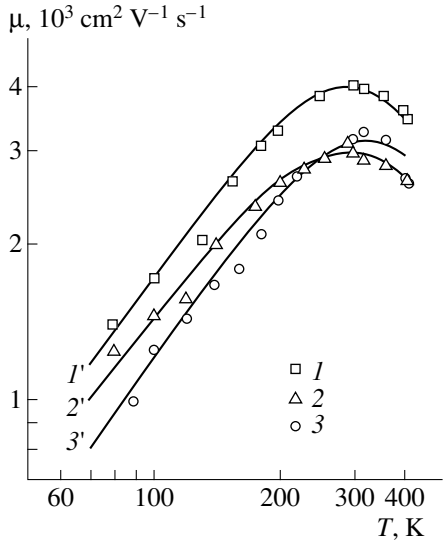

Fig. 5. Temperature dependences of electron mobility in GaAs subjected to a rapid thermal annealing: (*1*, *1*', *2*, *2*') in epitaxial GaAs and (*3*, *3*') in GaAs single crystals. Curves *1*–*3* correspond to experimental Hall mobility, whereas curves *1*'–*3*' describe the results of calculations using formula (4). The annealing temperature T_{ann} was (*1*, *3*) 825 and (*2*) 905°C.

the ionized impurity and defects were calculated as in [9]. The value of μ_W was determined following the Weisberg model [10] as

$$\mu_W = \frac{e}{N_S S\sqrt{2m_n KT}}, \quad (5)$$

where N_S and S are the concentration and the scattering cross section for the agglomerates of defects, respectively; and m_n is the effective mass of electron. Assuming that the inner radius of the defects' agglomerates is much smaller than the screening radius, we used (5) to calculate the dependence $\mu(T)$ shown in Fig. 4 (curve *3*). It is evident that the largest contribution of additional agglomerates of defects to mobility is observed at elevated temperatures.

Table 2. Parameters characterizing the degree of perfection of ion-implanted layers in GaAs single crystals and epitaxial films subjected to rapid thermal annealing

Type of material, type of annealing, temperature of annealing, duration of annealing	N_I, 10^{17} cm^{-3}	N_S, 10^{16} cm^{-3}
Single crystal, TA, 800°C, 30 min	9.4	6.6
Single crystal, RTA, 825°C, 12 s	6.8	0
Epitaxial, RTA, 825°C, 12 s	5.4	2.6
Epitaxial, RTA, 905°C, 12 s	5.5	2.0

Note: TA stands for conventional thermal annealing, and RTA stands for rapid thermal annealing.

The best agreement between experimental and calculated data for $T > 150$ K (see Fig. 4; curves *1*, *2*) is observed for $N_I = 9.4 \times 10^{17}$ cm^{-3} (here, N_I is the concentration of ionized impurity and defects) and for $N_S = 6.6 \times 10^{16}$ cm^{-3}. For $T < 150$ K, the experimental mobility $\mu \sim T^{1/2}$ (Fig. 4; the dashed curve *4*), which is characteristic of scattering by dipoles [11]. Consequently, after a thermal annealing, the complexes of defects with a concentration of 6.6×10^{16} cm^{-3} and also the defects of supposedly dipole type are present in GaAs.

Figure 5 shows the experimental (curves *1*–*3*) and calculated (curves *1*'–*3*') dependences $\mu(T)$ for electrons in epitaxial GaAs after the RTA at 825°C (curves *1*, *1*') and at 905°C (curves *2*, *2*'), and also for electrons in GaAs single crystals after RTA at 825°C (curves *3*, *3*'). The parameters N_I and N_S used in deriving the dependences represented by curves *1*'–*3*' are listed in Table 2. We may infer the following from Fig. 5 and Table 2:

(i) Additional scattering centers of the type of complexes of defects (the Weisberg model) are not observed in the ion-implanted layers of Gas single crystals following an RTA at 825°C (Fig. 5; curves *3*, *3*'); in contrast, such centers are present in epitaxial GaAs layers, although their concentration is low, after an RTA at the same temperature (Fig. 5; curves *1*, *1*').

(ii) An RTA at 905°C brings about a significant degradation of ion-implanted layers in epitaxial GaAs (Fig. 5; curves *2*, *2*'); as a result of this annealing, the concentration of complexes of defects increases by almost an order of magnitude as compared to that after an RTA at 825°C.

(iii) After an RTA (Fig. 5), as distinct from a long-term conventional TA (Fig. 4), the dipole-related "tail" is not observed in the dependence $\mu(T)$ at low temperatures.

CONCLUSION

(I) As distinct from the case of long-term TA, an RTA causes a diffusion-related redistribution of Si to deeper layers in both GaAs single crystals and epitaxial films. The diffusion coefficient of Si in GaAs single crystals is about two times larger, and the level of electrical activation is somewhat lower than those in epitaxial GaAs films. The diffusion coefficient D for Si is larger, on average, by two orders of magnitude in the case of RTA than that in the case TA. The activation energies for diffusion and electrical activation of Si are lower in the case of RTA than those in the case of TA, which indicates that the potential barriers for diffusion and electrical activation of Si are lowered for RTA as compared to purely thermal processes occurring in the case of TA.

(II) In GaAs single crystals subjected to RTA at 825°C, additional scattering centers (of the type of agglomerates of defects) are not observed; in contrast, such centers are present (although their concentration is

low) in epitaxial GaAs subjected to RTA at the same temperature. An RTA of epitaxial GaAs at 905°C brings about an appreciable degradation of the material; namely, the concentration of agglomerates of defects increases by almost an order of magnitude as compared to that after an RTA at 825°C. A "tail" at low temperatures evident in the dependence $\mu(T)$ after TA and supposedly caused by scattering by dipoles is not observed in the case of RTA.

REFERENCES

1. V. M. Ardyshev and M. V. Ardyshev, Fiz. Tekh. Poluprovodn. (St. Petersburg) **10**, 1153 (1998).
2. V. M. Ardyshev and M. V. Ardyshev, Izv. Vyssh. Uchebn. Zaved., Fiz., No. 7, 89 (1998).
3. V. M. Ardyshev and M. V. Ardyshev, Izv. Vyssh. Uchebn. Zaved., Fiz., No. 11, 78 (1998).
4. A. V. Burenkov, F. F. Komarov, M. A. Kumakhov, and M. M. Temkin, *Tables of Parameters of Spatial Distribution of Ion-Implanted Impurities* [in Russian] (Beloruss. Gos. Univ., Minsk, 1980).
5. *Process and Device Simulation for MOS–VLSI Circuits*, Ed. by Paolo Antognetti, Dimitri A. Antoniadis, Robert W. Dutton, and William G. Oldham (Martinus Nijhoff, Boston, 1983; Radio i Svyaz', Moscow, 1988).
6. T. T. Lavrischev and S. S. Khludkov, in *Gallium Arsenide* [in Russian] (Tomsk Gos. Univ., Tomsk, 1974).
7. B. M. Goryunov and E. I. Zorin, in *Gallium Arsenide* [in Russian] (Tomsk Gos. Univ., Tomsk, 1974).
8. B. Pödor and N. Nador, Acta. Phys. Acad. Sci. Hung. **37** (4), 317 (1974).
9. F. J. Blatt, Solid State Phys. **4**, 1999 (1957); *Mobility of Electrons in Semiconductors*, (Fizmatgiz, Moscow, 1963).
10. L. R. Weisberg, J. Appl. Phys. **33**, 1817 (1962).
11. R. Stratton, J. Phys. Soc. Jpn. **23**, 1011 (1962).

Translated by A. Spitsyn

Semiconductors, Vol. 34, No. 1, 2000, pp. 32–34. Translated from Fizika i Tekhnika Poluprovodnikov, Vol. 34, No. 1, 2000, pp. 33–35.

ELECTRONIC AND OPTICAL PROPERTIES OF SEMICONDUCTORS

Electrophysical Properties of $Hg_{1-x}Cd_xTe$ Crystals under Hydrostatic Pressure

I. V. Virt, V. D. Prozorovskiĭ, and D. I. Tsyutsyura

Drogobych I. Franko State Pedagogical University, Drogobych, 293720 Ukraine

Submitted May 25, 1999; accepted for publication June 9, 1999

Abstract—The electrophysical properties of $Hg_{1-x}Cd_xTe$ crystals subjected to hydrostatic pressure were studied by a noncontact method. It is shown that there exists the effect of irreversible change in the state of native lattice defects. A decrease in hole (acceptor) concentration and an increase in electron mobility are observed in the samples subjected to pressure. © *2000 MAIK "Nauka/Interperiodica".*

The effect of hydrostatic pressure on the state of defect structure, on the physical properties of $Hg_{1-x}Cd_xTe$ solid solutions in particular, has not been adequately studied so far. Nevertheless, irreversible changes in defect structure under the action of hydrostatic pressure in semiconductors take place [1]. For example, in [2] it is shown that hydrostatic compression induces ordering in the distribution of dislocations. As is known [3, 4], $Hg_{1-x}Cd_xTe$ solid solutions, having appreciable plasticity, are characterized by a high density of growth dislocations, by various types of point defects, and inhomogeneity of the composition.

This work is devoted to the study of the effect of the residual hydrostatic compression on the electrophysical properties of narrow-band HgCdTe semiconductors.

The hydrostatic compression of $Hg_{1-x}Cd_xTe$ (x = 0.17–0.20) samples was accomplished in a separate chamber at room temperature. The disk-shaped plane-parallel samples 1.2–0.8 mm in thickness and 5–6 mm in diameter were employed in the experiments. An oil–kerosene mixture was used as a pressure-transmitting medium. The compression was performed by the cycles (1–3 cycles) within the range of pressures P = 0–2 GPa with a pressure-increase rate of 1.5–2.0 GPa/s. The samples were kept for 10–60 minutes under each pressure.

The measurements of electric properties were carried out with the use of a noncontact technique of helicon interferometry The samples were coupled to a resonator through a diaphragm with the experimentally tuned coupling opening. The dependences $dR/dH = f(T)$, where R is the reflection coefficient and H is the static magnetic field, were determined in a temperature range of T = 1.6–150 K with the use of a radiospectrometer working at the frequencies of 36.04 and 26.10 GHz with a circular polarization of the microwave field of the resonator.

The method of determining the effective mass of free carriers and kinetic coefficients from the oscillations (resulting from the interference of helicon waves in the sample) of the reflection-coefficient derivative with respect to the magnetic field $dR/dH = f(H)$ is described in [5]. According to this method, the fitting of the calculated curve $dR/dH = f(H)$ to the experimental points is performed by varying the desired parameters, i.e. by minimizing the functional $\Phi = \sum_k (H_{k1} - H_{k2})$. Here H_{k1} and H_{k2} are the experimental and calculated values of magnetic field, at which dR/dH take the extreme value. The charge carrier concentration and their mobilities were determined from the relations [6] $n \sim N_n^2/\omega_{rn}$, $p \sim N_p^2/\omega_{rp}$; $\mu_n = 2Q_n/H_{k1}$, and $\mu_p = 2Q_p/H_{k1}$. Here N_n and N_p are the orders of resonance for electrons and holes, ω_{rn} and ω_{rp} are the corresponding values of the resonance frequencies, and Q_n and Q_p are the electron and hole components of the helicon-resonance quality factor.

The reliability of the parameters thus obtained is confirmed by satisfactory agreement between the curves taken at the frequency of 26.10 GHz, for which the parameters calculated from the $dR/dH = f(H)$ curve at 36.04 GHz were used.

After performing the cycled treatment, prior to electrophysical measurements, the samples underwent polishing etching in a Br_2–HBr reagent. We also used concomitant samples whose surface had been selectively etched in order to study the effect of hydrostatic compression on the dislocation structure (network).

EXPERIMENTAL RESULTS AND THEIR DISCUSSION

It is established by the method of selective etching that after compression, in some parts of the single-crystal samples with a low density of dislocation the arrangement of dislocations becomes ordered, with the dislocations forming "walls". This occurs even at pressures of 0.3–0.4 GPa. As observed visually, the disloca-

1063-7826/00/3401-0032$20.00 © 2000 MAIK "Nauka/Interperiodica"

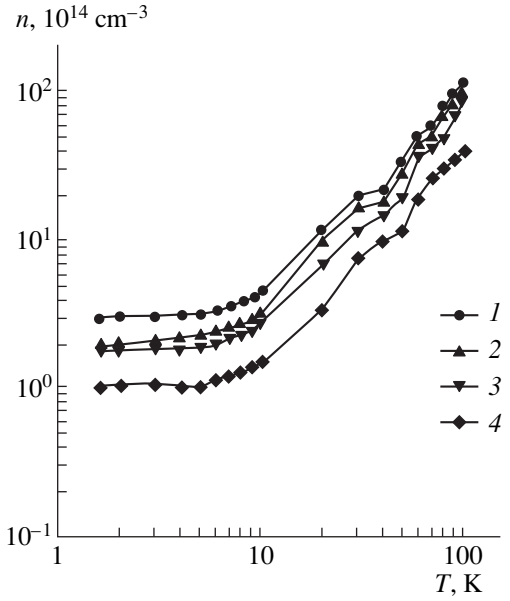

Fig. 1. Temperature dependences of electron concentration in (1) an as-grown n-$Hg_{0.83}Cd_{0.17}Te$ sample and in the same sample subjected to hydrostatic pressure (*2*) 0.3 GPa for 20 min, (*3*) 0.6 GPa for 20 min, and (*4*) 0.6 GPa for 40 min.

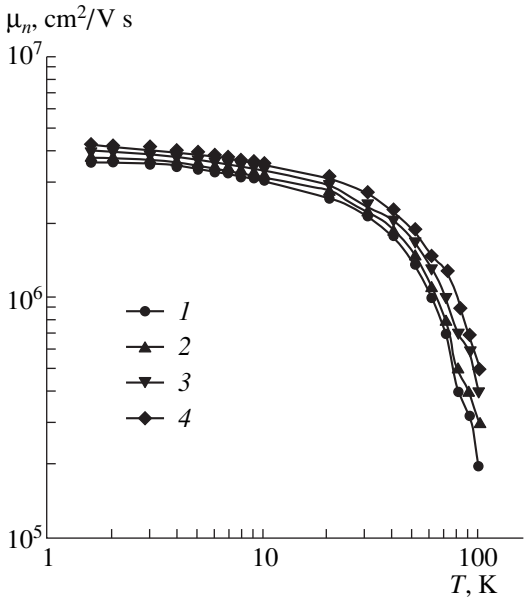

Fig. 2. The temperature dependences of electron mobility in n-$Hg_{0.83}Cd_{0.17}Te$ sample subjected to various hydrostatic pressures. The designations are the same as in Fig. 1.

tion network in the crystals with dislocations pinned by extended defects is less rearranged even at high pressures.

The typical irreversible changes of electron concentration as a function of temperature for the sample $Hg_{1-x}Cd_xTe$ (x = 0.17) after compression at various pressures are illustrated in Fig. 1. As seen in the figure, the electron concentration decreases with increasing pressure in the entire range of temperatures. The limiting change of concentration in this sample is attained at the pressure of 0.6 GPa. Such an effect of irreversible change of the electron concentration is observed in all narrow-gaps of $Hg_{1-x}Cd_xTe$ samples studied. A decrease in electron concentration depends both on the amplitude of pressure and on the duration of pressure action (compare curves *3* and *4* in Fig. 1). Variations in electron concentration are accompanied by the changes in electron mobility μ_n (Fig. 2), with these changes being more pronounced at temperatures of 20–100 K. For the composition with x = 0.2, the concentrations of electrons (n) and holes (p) were determined separately at 100 K both in initial samples and in the samples subjected to compression. The corresponding pressure dependences are shown in Fig. 3. As seen in the figure, the residual hydrostatic compression differently affects the concentrations of electrons and holes. A decrease in hole concentration is much more pronounced. In the low temperature region (~4 K), the change in carrier concentration in this sample is less significant.

On the basis of the results obtained in studies of electrophysical properties of $Hg_{1-x}Cd_xTe$ single crystals subjected to the hydrostatic pressure (compression), we may conclude that the hydrostatic compression is responsible for the irreversible rearrangement of both point and extended defects. The process seems to induce a certain decrease in concentration of crystal defects. This manifests itself mainly in an increase in electron mobility as well as in a decrease in electron

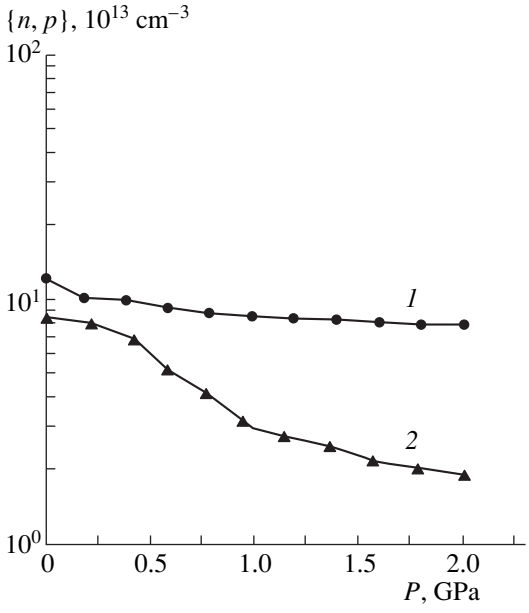

Fig. 3. Dependences of (*1*) electron and (*2*) hole concentrations in n-$Hg_{0.80}Cd_{0.20}Te$ sample on hydrostatic pressure. The temperature of measurement is T = 100 K.

and hole concentrations. The change in hole concentration reflects the process of a decrease in density of electrically active acceptor defects, which may be due to the filling of mercury vacancies in a crystal lattice by interstitial mercury atoms. The interstitial mercury atoms are present in the crystals with *n*-type conductivity after homogenizing annealing; however, their electrical activity is insignificant [7].

CONCLUSION

Thus, the hydrostatic pressure (compression) on $Hg_{1-x}Cd_xTe$ single crystals produces irreversible changes in the crystal defect structure. These changes affect electrophysical properties: the electron and hole concentration in crystals decreases (the latter to a larger extent), with an increasing carrier mobility.

REFERENCES

1. V. I. Zaĭtsev, *Physics of Plasticity of Hydrostatically Compressed Crystals* [in Russian], Kiev (1983).
2. J. B. Yung, Philos. Mag. **43**, 1057 (1981).
3. S. G. Gasan-zade, E. A. Sal'kov, and G.A. Shepel'skiĭ, Fiz. Tekh. Poluprovodn. (Leningrad) **17**, 1913 (1983).
4. M. G. Andrukhiv, I. S. Virt, D. I. Tsyutsyura *et al.*, Fiz. Tekh. Poluprovodn. (Leningrad) **23**, 1263 (1989).
5. V. D. Prozorovskiĭ, I. Yu. Reshedova, Yu. A. Bratashevskiĭ, *et al*., Fiz. Tekh. Poluprovodn. (Leningrad) **17**, 1325 (1983).
6. E. V. Kuchis, *Galvanomagnetic Effects and the Methods of Their Study* [in Russian], Moscow (1990).
7. I. N. Tsidil'kovskiĭ, G. I. Kharus, and N. G. Shelushinina, *Inpurity States and Transport Phenomena in Zeo-Gap Semiconductors* [in Russian], Sverdlovsk (1987).

Translated by A. Zalesskiĭ

Semiconductors, Vol. 34, No. 1, 2000, pp. 35–39. Translated from Fizika i Tekhnika Poluprovodnikov, Vol. 34, No. 1, 2000, pp. 36–40.

ELECTRONIC AND OPTICAL PROPERTIES OF SEMICONDUCTORS

Band Structure and Spatial Charge Distribution in $Al_xGa_{1-x}N$

V. G. Deĭbuk*, A. V. Voznyĭ, and M. M. Sletov

Fed'kovich State University, ul. Kotsyubinskogo 2, Chernovtsy, 274012 Ukraine
** E-mail: vdei@chdu.cv.ua*

Submitted June 13, 1999; accepted for publication June 21, 1999

Abstract—The band structure of $Al_xGa_{1-x}N$ substitutional solid solution is calculated by the method of local model pseudopotential in the modified virtual-crystal approximation. This provides an opportunity to explain both the dependence of the energy gap value (E_g) on AlN concentration (x) and on temperature and the $E_g(x)$ bending. The dynamics of chemical bonds in this compounds is studied by analyzing the spatial distribution of valence electron charge. The results of calculations are in a good agreement with the experimental data. © *2000 MAIK "Nauka/Interperiodica".*

As distinct from binary semiconductors with zinc blende structure, III–V compounds with a wurtzite structure have recently attracted much attention both from the experimental and theoretical points of view. This increased interest is related to the use of these compounds in semiconductor lasers and photodiodes based on AlGaN/GaN and InGaN/GaN heterostructures and intended for the ultraviolet-violet range [1, 2]. There are publications concerned with the production of bipolar transistors based on the GaN/AlGaN heterostructure [3]. At the same time, such fundamental properties as $Al_xGa_{1-x}N$ energy gap nonlinear dependence on the composition of solid solution, rearrangement of chemical bonds, and spatial charge distribution of valence electrons are of great scientific interest. In this paper, we report the results of our studies of these problems.

EXPERIMENTAL

Undoped GaN, AlGaN, and AlN epitaxial layers of 0.5–20 μm thickness were grown by pyrolytic deposition on the (0001) sapphire substrates from complex ammonium compounds of Ga and Al halides [4]. Electron diffraction and X-ray diffraction studies confirm that as-grown structure is single-crystal. The composition of solid solution is determined by X-ray diffraction analysis using a JXA microanalyzer. The energy gap (E_g) of the samples is found from the optical absorption long-wavelength edge. The dependence of optical absorption coefficient α on the photon energy $h\nu$ is approximated by the well-known relation for direct interband transitions

$$\alpha(h\nu) = \alpha_0(E_g - h\nu)^{1/2}, \quad (1)$$

where α_0 is the parameter which does not depend on $h\nu$. According to (1), the dependence of $\alpha^2(h\nu)$ is linear within six orders of magnitude, and extrapolation of α^2 until it intersects the energy axis yields the values of E_g which are in reasonably good agreement with well-known published data.

THEORY

Well-known $Al_xGa_{1-x}N$ band structure calculations are performed by the methods of orthogonalized linear combinations of atomic orbitals [5], by linear-muffin-tin-orbitals [6], by the first-principle pseudopotential calculation based on the theory of density functional [7], and by other methods.

In this paper, by the band structure of GaN and AlN is calculated by the local model pseudopotential method. A modified virtual crystal approximation [8] accounting for the existence of antisite defects created during the formation of substitutional solid solution is used to explain the nonlinear concentration dependence of the energy gap. Temperature dependence of the energy gap is considered in the context of the Brooks-U theory [9]. The dynamics of the chemical bond in the compounds is investigated by analyzing the spatial distribution of the valence electron charge.

Our calculations are based on the local model pseudopotential method [9] developed in [10, 11] for hexagonal binary compounds. One-electron pseudopotential Hamiltonian is expressed by the relation

$$\hat{H} = -\frac{\hbar^2}{2m}\nabla^2 + V(\mathbf{r}), \quad (2)$$

where $V(\mathbf{r})$ is total crystal pseudopotential, which is written for periodic lattice as

$$V(\mathbf{r}) = \sum_{G \le G_0} V(\mathbf{G})\exp(i\mathbf{G}\cdot\mathbf{r}), \quad (3)$$

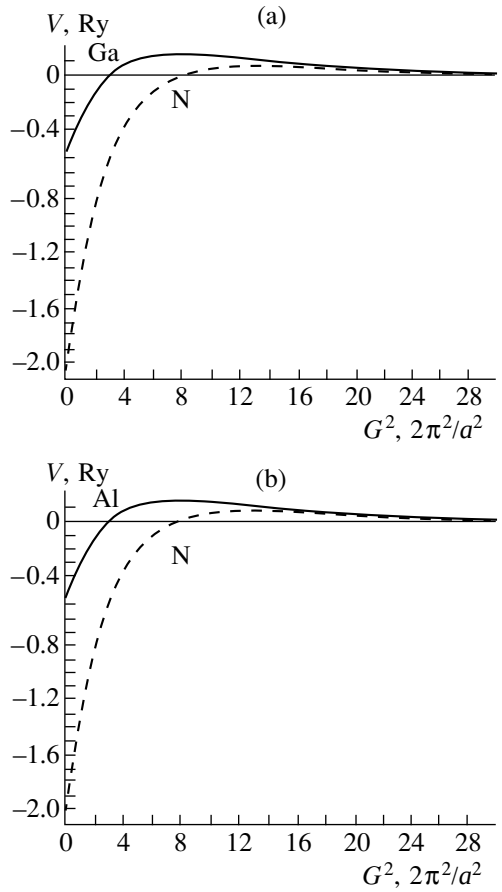

Fig. 1. Model screened pseudopotentials of (a) Ga and N in GaN compound, and (b) Al and N in AlN compound.

$$V(\mathbf{G}) = S^S(\mathbf{G})V^S(\mathbf{G}) + iS^A(\mathbf{G})V^A(\mathbf{G}). \quad (4)$$

Structure factors for wurtzite [9] are given by

$$\begin{aligned} S^S(\mathbf{G}) &= \cos[2\pi(l/6 + m/6 + n/4)]\cos(\pi nu), \\ S^A(\mathbf{G}) &= \cos[2\pi(l/6 + m/6 + n/4)]\sin(\pi nu), \end{aligned} \quad (5)$$

where u is the wortzite parameter; the vectors of the reciprocal lattice are given by

$$\mathbf{G} = 2\pi(l\mathbf{a}^* + m\mathbf{b}^* + n\mathbf{c}^*). \quad (6)$$

Here $\mathbf{a}^*$, $\mathbf{b}^*$, and $\mathbf{c}^*$ are primitive translation vectors of the reciprocal lattice, and l, m, n are integers.

Table 1. Model pseudopotential parameters a_0, a_1, a_2, a_3 used in the calculations

Atoms	a_0	a_1	a_2	a_3
Ga in GaN	28	4.095	203.4	0.2
N in GaN	23	7.3	85	0.2745
Al in AlN	7.8	3.4	46	0.215
N in AlN	21	8.23	85	0.2262

Symmetric and antisymmetric pseudopotential form factors are

$$\begin{aligned} V^S(\mathbf{G}) &= [V_A(\mathbf{G}) + V_B(\mathbf{G})]/2, \\ V^A(\mathbf{G}) &= [V_A(\mathbf{G}) - V_B(\mathbf{G})]/2. \end{aligned} \quad (7)$$

Band structure is determined from the solution of secular equation

$$\det\{H_{GG'}(\mathbf{k}) - E_n(\mathbf{k})\delta_{GG'}\} = 0, \quad (8)$$

where

$$\begin{aligned} H_{GG'}(\mathbf{k}) = \frac{\hbar^2}{2m}(\mathbf{k} + \mathbf{G})^2\delta_{GG'} + V_S(|\mathbf{G} - \mathbf{G}'|)S^S(\mathbf{G} - \mathbf{G}') \\ + iV^S(|\mathbf{G} - \mathbf{G}'|)S^S(\mathbf{G} - \mathbf{G}'). \end{aligned} \quad (9)$$

Spin–orbital interaction was not considered due to the lightness of the elements.

Atomic pseudopotentials V_{Ga}, V_{Al}, V_{N} were modeled in the form [12] of

$$V(k) = a_0\frac{(k^2 - a_1)}{a_2\exp(a_3k^2) - 1}. \quad (10)$$

Parameters a_0, a_1, a_2, a_3 were obtained by the approximation procedure on the basis of well-known form factors [11]. The parameters are finally determined by matching the calculated band structure to peaks in experimental reflection spectrum in high-symmetry points of the Brillouin zone (Table 1). The model pseudopotentials used in the calculations are presented in Fig. 1. Calculated GaN and AlN band structures are shown in Fig. 2. The calculated and experimental values of distances between the energy levels in some high-symmetry points of Brillouin zone are given in Table 2. Secular matrix dimension was taken equal to 135.

According to the well-known virtual crystal approximation (VCA) and Vegard's law [14], in $\mathrm{Al}_x\mathrm{Ga}_{1-x}\mathrm{N}$ solid solution, the lattice constant and pseudopotentials are determined as linear combinations of appropriate values for AlN and GaN components

$$\begin{aligned} a_{SS} &= A_{\mathrm{AlN}}x + a_{\mathrm{GaN}}(1 - x), \\ V_{SS} &= V_{\mathrm{AlN}}x + V_{\mathrm{GaN}}(1 - x), \end{aligned} \quad (11)$$

where a_{SS} and V_{SS} are substitutional lattice constant of solid solution and pseudopotential form factors, respectively. Equations (11) are valid if Ga atoms are substituted by Al atoms or vice versa. However, due to the fact that synthesis of the solid solution occurs in thermodynamically nonequilibrium conditions, the atoms of one kind may occupy the site of another kind of atom, creating antisite defects. The influence of antisite lattice defects on $\mathrm{Al}_x\mathrm{Ga}_{1-x}\mathrm{N}$ band structure is studied in modified virtual-crystal approximation [8]. In this approximation, pseudopotential form factors of solid solution depend on the probability for each kind of

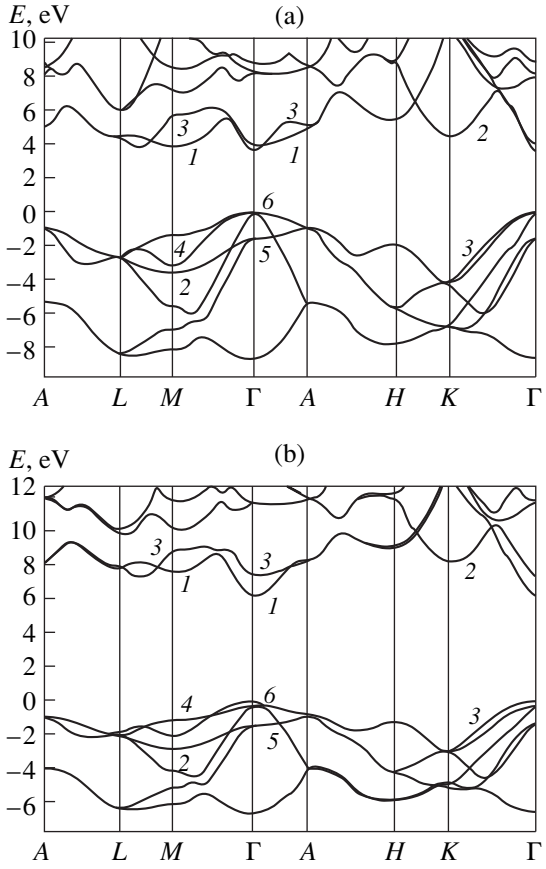

Fig. 2. Calculated band structures of (a) GaN and (b) AlN.

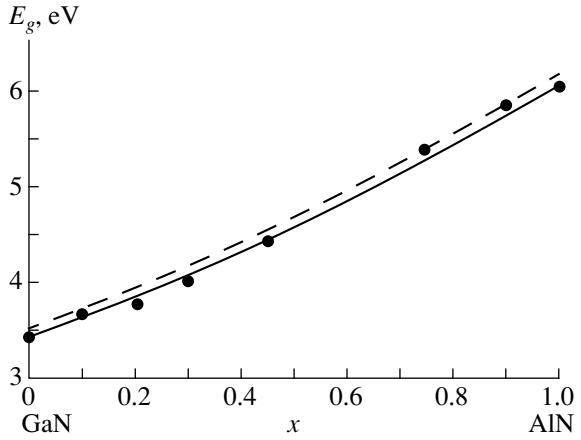

Fig. 3. Energy gap dependence on the composition of $Al_xGa_{1-x}N$ solid solution (calculation and experiment) at different temperatures: calculation at $T = 0$ (dashed line), calculation at $T = 300$ K (solid line), and experimental data at $T = 300$ K (points).

atom to occupy a certain site in the lattice. In this case, symmetric form factors do not change. Antisymmetric form factors may be expressed as

$$V_{SS}^A = [1 - 8\beta x(1-x)][V_{\mathrm{AlN}}^A x + V_{\mathrm{GaN}}^A(1-x)]. \quad (12)$$

In deriving (12), we assumed that the dependence of the probability of antisite-defect creation is a quadratic function of AlN concentration (x); i.e., we have

$$1 - W_{\mathrm{Ga}} = 1 - W_{\mathrm{Al}} = 1 - W_{\mathrm{N}} = 4\beta(1-x)x, \quad (13)$$

where β is the probability of antisite-defect formation for $x = 0.5$. Because disordering in the solid solution for this x is at its maximum, β has the maximum value. We use in our calculations β equal to 0.005.

The influence of temperature on solid-solution band structure is considered in the context of the Brooks-U theory [9]. If at zero temperature, electron energies are calculated as the functions of atomic pseudopotential form factors

$$E(\mathbf{k}) = E(\mathbf{k}, \{V_j(\mathbf{G})\}), \quad (14)$$

then at $T = 0$, each Fourier component of jth atomic pseudopotential is corrected by the Debye–Waller factor $M_j(\mathbf{G}, T)$ as

$$E(\mathbf{k}, T) = E[\mathbf{k}, \{V_j(\mathbf{G})\exp[-M_j(\mathbf{G}, T)]\}]. \quad (15)$$

The Debye–Waller factor for cubic crystals is equal to

$$M_j(\mathbf{G}, T) = \frac{|\mathbf{G}|^2}{6}\langle U_j^2(T)\rangle, \quad (16)$$

where mean-square displacement of the jth atom $\langle U_j^2(T)\rangle$ is described by the Debye equation

$$\langle U_j^2(T)\rangle = \frac{3\hbar^2}{m_j k_B \Theta_j^2}\frac{T}{}\left[\Phi\left(\frac{\Theta_j}{T}\right) + \frac{1}{4}\frac{\Theta_j}{T}\right]. \quad (17)$$

Here m_j are the ion masses, Θ_j is the Debye temperature for each kind of atom, and Φ is the Debye integral of the first kind. We take in our calculations the following Debye temperature values: $\Theta_{\mathrm{Ga}} = 240$ K, $\Theta_{\mathrm{Al}} = 400$ K, and $\Theta_{\mathrm{N}} = 80$ K [15]. Lattice thermal expansion is taken into account in the temperature dependences of lattice constants [16]. The results of calculation of energy gap dependences on temperature and semiconductor solid-solution composition and the experimental results

Table 2. Comparison of calculated interband transition energies (in eV) in GaN and AlN with the experimental values [8, 12, 13]

Transition	GaN			AlN	
	Calculation	Experiment [12]	Experiment [13]	Calculation	Experiment [8]
G_{6v}–G_{1c}	3.503	3.6	3.503	6.21	6.20
G_{5v}–G_{3c}	5.28	5.3		8.63	8.92
M_{2v}–M_{1c}	7.13	7.0–7.1		10.24	8.21
M_{4v}–M_{3c}	6.8	7.0–7.1		9.7	–
K_{3v}–K_{2c}	8.29	8.3–8.7		10.84	7.90

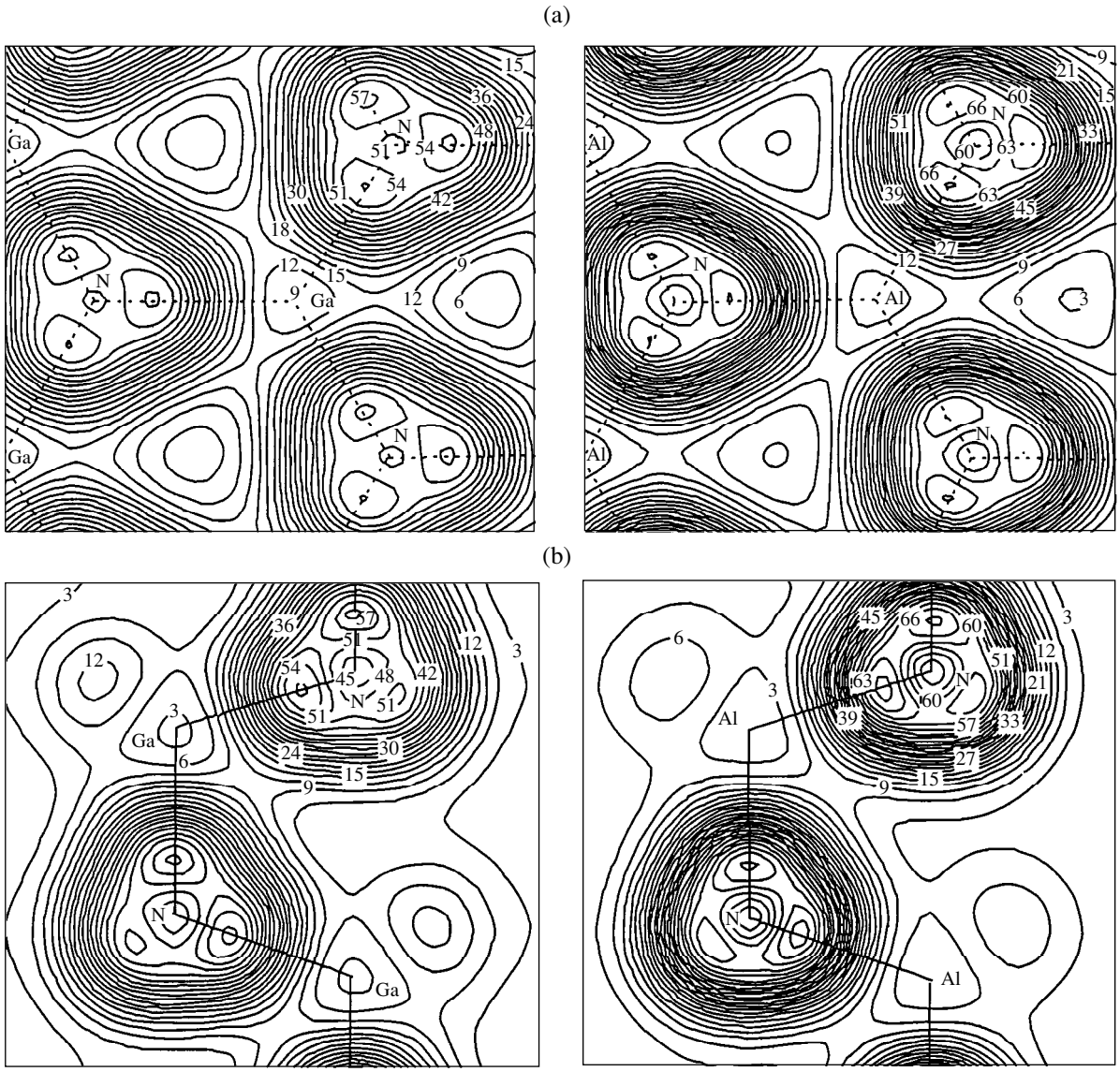

Fig. 4. Charge density distribution in GaN (on the left) and AlN (on the right) in (a) (001) and (b) (110) planes. The numbers on the contour line are indicated in *e*/atomic volume units.

obtained from the optical absorption data [17] are shown in Fig. 3. As follows from the calculations, the bending parameter is equal to 0.609. This correlates with the experimental value $b = 0.6$ [18] obtained from the well-known empirical relation

$$E_g(x) = E_g(\mathrm{GaN}) + (c - b)x + bx^2, \qquad (18)$$

where $c = E_g(\mathrm{AlN}) - E_g(\mathrm{GaN})$. Thus, together with local stresses, one of the factors causing the bending of $E_g(x)$ dependence in $Ga_{1-x}Al_xN$ alloys is the presence of antisite defects.

The calculated band structure makes it possible to theoretically determine $Ga_{1-x}Al_xN$ charge density. Charge density of the *n*th band is equal to

$$\rho_n(\mathbf{r}) = e\sum_k^{BZ} \Psi^*_{n,k}(\mathbf{r})\Psi_{n,k}(\mathbf{r}). \qquad (19)$$

Total charge density is expressed as

$$\rho(\mathbf{r}) = \sum_n \rho_n(\mathbf{r}), \qquad (20)$$

where the summation is performed over the valence bands. Summation over the Brillouin zone (*BZ*) was performed at six special points [19]. The distribution of

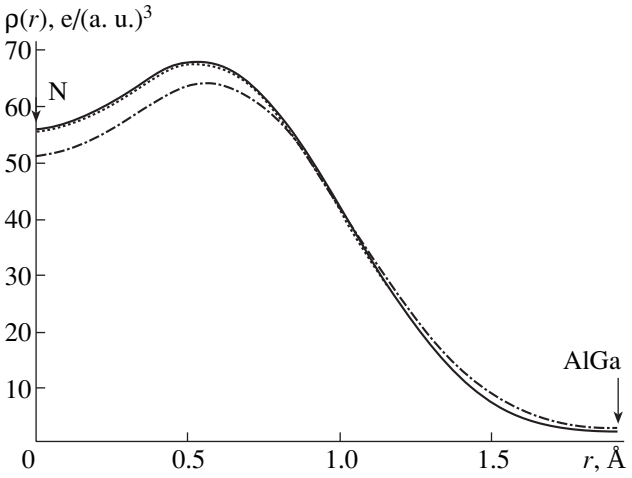

Fig. 5. Charge density distribution ρ along the N–(Ga, Al) bond in $Al_xGa_{1-x}N$ compound ($x = 0.5$) for different values of antisite defect probability formation: $\beta = 0$ (solid line), $\beta = 0.005$ (dashed line), and $\beta = 0.05$ (dot-and-dash line).

valence-electron charge density in the (110) and (001) planes is presented in Fig. 4. We can see that the maximum charge density of valence electrons that gives the main contribution to the formation of chemical bond is shifted to the anion side when Al concentration in the alloy is increased. It corresponds to an increase in ionicity of the alloy. As one can see from Fig. 5, the consideration of antisite defects in modified virtual crystal approximation gives rise to a decrease in the charge-density maximum and to an increase in alloy covalency. Let us note also that there is a channel along the *z* axis with a very low charge density. It provides the diffusion of atoms in the crystal along this direction. According to the charge density (Fig. 5), the probability of diffusion is increased when *x* in the compound is increased.

REFERENCES

1. S. Nakamura and G. Fasol, *The Blue Laser Diode* (Springer, Berlin, 1997).
2. B. Monemar, J. Cryst. Growth **189–190**, 1 (1998).
3. F. Ren, C. R. Abernathy, J. M. Van Hove *et al.*, MRS Internet J. Nitride Semicond. Res. **3**, 41 (1998).
4. A. V. Dobrynin, M. M. Sletov, and V. V. Smirnov, Zh. Prikl. Spektrosk. **55**, 861 (1991).
5. Yong-Nian Xu and W. Y. Ching, Phys. Rev. B: Condens. Matter **48**, 4335 (1993).
6. E. A. Albanesi, W. R. L. Lambrecht, and B. Segall, Phys. Rev. B: Condens. Matter **48**, 17841 (1993).
7. M. Malachowski, I. R. Kityk, and B. Sahraoui, Phys. Status Solidi B **207**, 405 (1998).
8. A. P. Dmitriev, N. V. Evlakhov, and A. S. Furman, Fiz. Tekh. Poluprovodn. (St. Petersburg) **30**, 106 (1996).
9. M. L. Cohen and J. R. Chelicowsky, *Electronic Structures and Optical Properties of Semiconductors* (Springer, Berlin, 1998).
10. S. Bloom, J. Phys. Chem. Solids **32**, 2027 (1971).
11. M. Schluter, J. R. Chelikowsky, S. G. Lui, *et al.*, Phys. Rev. B: Condens. Matter **12**, 4200 (1975).
12. S. Bloom, G. Harbeke, E. Meier, *et al.*, Phys. Status Solidi B **66**, 161 (1974).
13. B. Monemar, Phys. Rev. B: Condens. Matter **10**, 676 (1974).
14. T.-F. Huang, J. S. Harris, Jr., Appl. Phys. Lett. **72**, 1158 (1998).
15. N. W. Ashcroft and N. D. Mermin, *Solid State Physics* (Holt Saunders, Philadelphia, 1976).
16. S. Strite and H. Markoc, J. Vac. Sci. Technol., B **10**, 1237 (1992).
17. Y. Koide, H. Itoh, M. R. Khan, *et al.*, J. Appl. Phys. **61**, 4540 (1987).
18. G. Steude, D. M. Hofmann, B. K. Meyer, *et al.*, Phys. Status Solidi. B **205**, R7 (1997).
19. D. J. Chadi and M. L. Cohen, Phys. Rev. B: Condens. Matter **8**, 5747 (1973).

Translated by I. Kucherenko

Semiconductors, Vol. 34, No. 1, 2000, pp. 40–44. Translated from Fizika i Tekhnika Poluprovodnikov, Vol. 34, No. 1, 2000, pp. 41–45.

ELECTRONIC AND OPTICAL PROPERTIES OF SEMICONDUCTORS

Field Dependence of the Rate of Thermal Emission of Holes from the $V_{Ga}S_{As}$ Complex in Gallium Arsenide

S. V. Bulyarskiĭ, N. S. Grushko, and A. V. Zhukov

Ul'yanovsk State University, Ul'yanovsk, 432700 Russia

Submitted February 2, 1999; accepted for publication June 24, 1999

Abstract—An algorithm is proposed for evaluating the field dependence of the emission rate based on the form-function of optical transition. Experiment and calculations are carried out for the $V_{Ga}S_{As}$ complex in a gallium arsenide crystal. The model proposed is compared with theoretical studies based on one-coordinate approximation. It is concluded that the one-coordinate model can be used to describe the field dependence of hole emission rate from the $V_{Ga}S_{As}$ center. *© 2000 MAIK "Nauka/Interperiodica".*

INTRODUCTION

The important role in nonradiative transitions is played by multiphonon processes [1–4]. The electron–phonon interaction leads to the temperature dependences of capture coefficient and to an increase in thermal emission rate in strong electric fields. In particular, both experimentally [5] and theoretically it is shown [6–14] that the probability of such transitions in strong electric fields increases exponentially with the squared electric field strength. Therefore, for more accurate calculations of the parameters in optoelectronic and high-power semiconductor devices related to the generation, recombination and tunneling processes with the involvement of deep levels, one needs to have the information about the parameters of the electron–phonon interaction characterizing a particular electron-transition.

The one-coordinate model [6–14] is known to be most commonly used in practical applications. This model imposes fairly rigid requirements on the characteristics of oscillations in the system and requires the verification in every particular case.

The degeneracy of electron states of the crystal with an impurity center leads to the invalidity of the adiabatic approximation and to the oscillatory mixing of the electron levels. In this case, the one-coordinate model may turn out to be inapplicable to the calculation of the field dependences.

In this work, an algorithm is proposed for the calculation of field dependences of the thermal emission rates; this algorithm is based on the form-function of the optical transition calculated from the emission spectrum. The results obtained in this way are compared with the experiment and calculations based on the one-coordinate model.

1. SAMPLES AND MEASUREMENTS

Gallium arsenide doped with sulfur was chosen as a material for the experimental verification of the model. The impurities of Group VI of the periodic table occupy arsenic sites and become donors forming shallow levels near the conduction band bottom. Furthermore, it is known [15–17] that they form the complexes consisting of gallium vacancy and donor at the arsenic sites ($V_{Ga}D_{As}$). These complexes give rise to broad bands in the photoluminescence spectrum with peaks at a photon energy of 1.18–1.25 eV. The symmetry and electron structure of these complexes were studied in [15–17]. It is also known that in the excited state, a hole trapped by the complex interacts with incompletely symmetrical oscillations of surrounding V_{Ga} atoms; i.e. the Jahn–Teller effect takes place.

The samples of GaAs:S were grown by the gaseous-phase epitaxy with the concentration of dopant (N) ranging from 4.7×10^{17} to 1.5×10^{18} cm^{-3}. The spectral characteristics of photoluminescence $I(\varepsilon)$ were measured within the photon-energy range of $\varepsilon = 0.8$–1.6 eV and at temperatures (T) from 100 to 200 K with the use of an SDL-2M system.

The spectra obtained for all samples have two characteristic bands; one of them, has a peak corresponding the photon energy, to 1.48–1.49 eV, whereas the other band (a broader one) peaked at 1.22–1.24 eV. The first luminescence peak is determined by the band-to-band emission in GaAs, the second peak is caused by the emission of $V_{Ga}S_{As}$ complexes (Fig. 1a). If one takes into account that the complex consisting of gallium vacancy and the neighboring sublattice site gives rise to deep levels in the forbidden band of GaAs near the top of the valence band, the luminescence band with the maximum at 1.22–1.24 eV should correspond to the radiative recombination of electrons from the state near the bottom of the conduction band with a hole localized at the deep center under investigation.

1063-7826/00/3401-0040$20.00

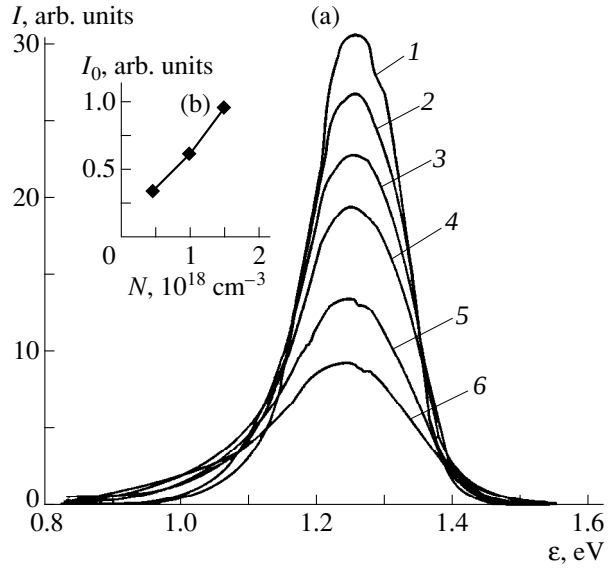

Fig. 1. (a) Emission spectra of the $V_{Ga}S_{As}$ complexes at temperatures of (*1*) 100, (*2*) 118, (*3*) 137, (*4*) 161, (*5*) 180, and (*6*) 200 K. (b) The integrated emission intensity (I_0) of the same complexes as a function of the dopant concentration.

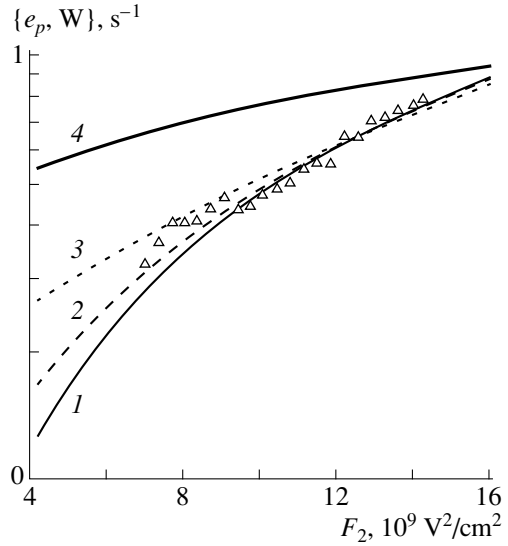

Fig. 2. The field dependence of the probability for the transition of a hole from the deep level corresponding to the ground state of the $V_{Ga}S_{As}$ complex to the localized state near the top of the valence band. Points correspond to the experiment, lines represent the results of calculations (*1*) by formula (2), (*2*) according to [12], (*3*) according to [8, 9], and (*4*) according to [6, 7].

The study of the dependence of integrated intensity (I_0) of luminescence of the complexes on the concentration of dopants (N) shows that the intensity is actually proportional to the sulfur concentration in the samples, which confirms the chosen complex model (Fig. 1b). It is also revealed that the emission-band shape (the band dispersion in particular) at constant temperatures does not depend on the concentration of dopant, and seems to be determined by the electron–phonon interaction rather than by the doping effect. The measurements performed at various temperatures (Fig. 1a) confirm this assumption. With increasing temperature, a shift towards lower energies and broadening of the emission band occur. The shape of the spectra and their temperature dependence allow one to conclude that the electron–phonon interaction takes an important part in these processes.

Using the electrochemical deposition of nickel on gallium arsenide, the metal–semiconductor contacts were formed on the samples studied. The investigation of the electrical properties of the contacts showed that the carrier transport is described by the thermoelectron emission. Thus, the contacts serve as Schottky barriers with the potential barrier height equal to 1 eV. On thus prepared structures, the field dependences of thermal emission rates of the holes from the deep level introduced by the $V_{Ga}S_{As}$ complex were studied. The experiment was performed at $T = 77$ K in the following way. The photoionization of the centers was accomplished with the use of AL-106 light-emitting diodes operating in the IR region with the emission peak at the wavelength of $\lambda = 914$ nm (the photon energy $\varepsilon = 1.36$ eV), which approximately corresponds to the maximum in absorption spectrum of the $V_{Ga}S_{As}$ center. The kinetics of the photo-induced capacitance was measured after the switching on and off of the light.

The analysis of the results is based on a simple kinetic equation, which, provided the electron and hole trapping is absent, in the field of space-charge region (SCR), takes the form

$$\frac{dn_t}{dt} = -(Jq_n + e_n)n_t + (Jq_p + e_p)(N_t - n_t), \qquad (1)$$

where J is a photon flux in SCR, $q_{n(p)}$ is the cross section of photoionization of electrons and holes, $e_{n(p)}$ is the rate of emission of electrons and holes from the level, N_t is the concentration of complexes, and n_t is the concentration of electrons at the complexes. The emission rate includes the combination of all thermal and field processes. Then the time constant of a decrease in capacitance after the light was switched off is given by $\tau^{-1} = e_n + e_p$.

Taking into account that the level is located closer to the valence band, and the energy distances to the bands are larger than 10 kT, we may assume that the recharging of the level after switching off the light is completely determined by the hole emission and, consequently, the time constant of the process is equal to $\tau^{-1} = e_p$. The experiment was repeated at various voltages of reverse bias, which allowed us to determine the field dependence of the thermal emission rate. The typical dependences of the emission rate on the squared field in SCR (F) are shown in Fig. 2.

2. CALCULATIONS OF THE FIELD DEPENDENCE OF THERMAL EMISSION RATE BASED ON THE EXPERIMENTAL FORM-FUNCTION OF THE OPTICAL TRANSITION

The calculations of field dependences were based on the results obtained in [18] where it was rigorously shown that the probability of quantum-mechanical transition with an allowance made for electron–phonon interaction may be generally expressed by the convolution equation

$$W = \sum_{i,j} \int_{-\infty}^{\infty} W_{0(i,j)}(E_{t(i,j)} - \varepsilon) f_{i,j}(\varepsilon) d\varepsilon, \qquad (2)$$

where $W_{0(i,j)}(E_{t(i,j)} - \varepsilon)$ is the probability of pure electron transition, and $f_{i,j}(\varepsilon)$ is the expression for the form-function of the optical transition from the ith sublevel of the multiplet of the initial state of the center to the jth sublevel of the multiplet of the final state. Actually, $f_{i,j}(\varepsilon)$ represents the contribution of the electron-phonon interaction to the transition probability.

The probability of pure electronic transition can be calculated using Franz's formula [19]:

$$W_{0(i,j)}(E_{t(i,j)} - \varepsilon) = A \frac{eF}{2\sqrt{2m^*(E_{t(i,j)} - \varepsilon)}} \exp\left(-\frac{4}{3}\frac{\sqrt{2m^*}(E_{t(i,j)} - \varepsilon)^{3/2}}{e\hbar F}\right), \qquad (3)$$

where A is a normalization factor, F is the electric field strength, m^* is the effective mass, and $E_{t(i,j)}$ is the energy of pure electronic transition from the ith sublevel of the multiplet of the initial state of the center to the jth sublevel of the multiplet of the final state.

In order to calculate the field dependence of the transition probability by formula (2), it is necessary to know the form-function of the spectrum of electron excitation from the localized state near the valence band to the level. We shall seek this form-function in the following way. First, we calculate the form-function of the radiative transition, then we find its moments. We then transform the latter on the basic of the model of the complex and the symmetry of the wave functions.

According to [20], if one knows the emission spectrum of the electron transition, it is possible to calculate its form-function using the formula

$$f(\varepsilon) = I(\varepsilon)/(M_0\varepsilon^4). \qquad (4)$$

Here, $I(\varepsilon)$ is the luminescence intensity, ε is photon energy, and M_0 is the zero moment of the emission band proportional to the oscillator strength

$$M_0 = \int I(\varepsilon) d\varepsilon.$$

Now, let us examine the sum in (2) related to the degeneracy of electron terms.

According to the model proposed for $V_{Ga}Te_{As}$ complex in [15–17], a lowering of the symmetry of the complex in the excited state of the complex occurs due to the Jahn–Teller effect; in this case, each defect continues to exist in one of three equivalent configurations corresponding to three possible orientations of the Jahn–Teller distortion. In each of these configurations, there exists the {110} symmetry plane that includes the initial axis of the complex and thus contains the lattice sites corresponding to the initial position of both components of the complex. The reorientation of the Jahn–Teller distortions of the complex is reduced to the rotation of this plane around the initial axis through the angle $\varphi = \pm 2\pi/3$. As vigorously shown in [21], the adiabatic potentials of three terms for the excited states in this case are equivalent in energy and geometry to the equilibrium configuration of the complex in the ground state. Thus, we can take this probability out from the summation sign in formula (2), putting this sign directly in front of form-functions:

$$W = \int_{-\infty}^{\infty} W_0(E_t - \varepsilon) \sum_{i,j} f_{i,j}(\varepsilon) d\varepsilon. \qquad (5)$$

Then

$$\sum_{i,j} f_{i,j}(\varepsilon) = f(\varepsilon).$$

This quantity can be calculated from the experimental data by the use of (4).

Thus, formula (5) contains the form-function obtained from the experimental emission spectra (the form-function of the transition from the local state that is close to the conduction band bottom and corresponds to the excited state of the $V_{Ga}S_{As}$ complex to the ground state) which allows one to perform the numerical integration and determine the transition probability.

In order to calculate the form-function for the transition from the local state close to the top of the valence band to the deep level corresponding to the ground state of $V_{Ga}S_{As}$ center (for which the field dependences of thermal emission rates were measured), we use the following reasoning.

The models of the electron–vibrational interaction, strictly speaking, are valid for intracenter transitions [22]. With this in mind, we assume that the wave function is determined solely by the recombination-center states.

According to [16], the center under study has a nondegenerate ground state, the wave function of which has the symmetry of s type (we designate the wave function of this state as $|s\rangle$), and the degenerate excited state which is formed from the wave functions of p-type symmetry as ($|p\rangle$). Let us consider two transitions: one (with the emission) from the localized state that is close to the conduction band bottom and corresponds to the excited state of the center to the ground state, and the

other transition (with absorption) from the localized state near the top of the valence band to the deep level corresponding to the ground state of the center. Taking into account that there exists a sufficiently strong electron–phonon interaction in the system (the experiment yields a Stokes' losses value equal to ~0.12 eV), and that both initial states (near the bottom of the conduction band and near the top of the valence band) correspond to the same excited state of the complex, we may consider the wave functions of these states as equal to each other $|p\rangle = |p'\rangle$. The energy spectrum of the system studied consists of a single s level corresponding to the ground state of the center with the energy E_s and two groups of close levels p_i and p_i' with energies E_{pi} and $E_{p'i}$.

According to [22, 23], the form-functions of the emission band at the transition from $|p\rangle$ state to $|s\rangle$ state and those of the absorption band at the transition from $|p'\rangle$ state to $|s\rangle$ state may be written correspondingly as

$$f^e(\varepsilon) = \frac{1}{z_p}\sum_i\sum_{s,p}\left|\langle s|\widehat{M}|p_i\rangle\right|^2 \times \exp\left(-\frac{E_{pi}}{kT}\right)\delta(E_s - E_{pi} + \varepsilon), \quad (6)$$

$$f^a(\varepsilon) = \frac{1}{z_{p'}}\sum_i\sum_{s,p'}\left|\langle s|\widehat{M}|p_i'\rangle\right|^2 \times \exp\left(-\frac{E_{p'i}}{kT}\right)\delta(E_s - E_{p'i} - \varepsilon), \quad (7)$$

where $\sum_{s,p(p')}$ signifies the summation over vibrational states of s and p (p') terms,

$$z_{p(p')} = \sum_i \exp(-E_{p(p')}/kT)$$

is the partition function of the group of levels $p(p')$, and $\widehat{M}$ is the perturbation operator inducing the transition.

Considering that $|p\rangle = |p'\rangle$ and $E_{p'i} = E_{pi} - E_g$, where E_g is the forbidden-band width, we may rewrite the expression (7) as

$$f^a(\varepsilon) = \frac{1}{z_p}\sum_i\sum_{s,p}\left|\langle s|\widehat{M}|p_i\rangle\right|^2 \times \exp\left(-\frac{E_{pi}}{kT}\right)\delta(E_s - E_{pi} - \varepsilon + E_g). \quad (8)$$

As can be seen, expression (8) completely coincides with (6), if a new variable $\varepsilon' = -\varepsilon + E_g$ used in (8).

Thus, by the mirror imaging of our experimental emission form-function with respect to the axis $\varepsilon = 0$ and shifting it to higher energies by the value of E_g, we obtain the form-function of the absorption band corresponding to the transition from the localized state near the valence band top, to the deep level representing the ground state of the center.

Now, this form-function can be substituted into (2), and, taking into account (5), we obtain the dependence of the probability of hole emission from the deep level of $V_{Ga}S_{As}$ complex on the average field in SCR. This dependence is shown in Fig. 2 (curve *1*). The factor A was varied to obtain the best fit of the calculated dependence to the experiment in the high-field region.

Thus, the calculated field dependence has been obtained without any assumptions related to the one-coordinate model. The calculation is based on the experimental form-function, which naturally accounts for the complex electron–vibrational interactions. In connection with this, the proposed procedure of the calculations of field dependences is preferable in comparison with the methods based on the one-coordinate model.

3. CALCULATION OF THE FIELD DEPENDENCES OF THE THERMAL EMISSION RATE IN ONE-COORDINATE APPROXIMATION

In this section, we analyze the applicability of the one-coordinate model to the description of the center under discussion. As mentioned above, the one-coordinate model is widely used in the theory of multiphonon processes. For this model several formulas have been obtained describing the field dependences of the probability of carrier emission from deep impurity centers [6–14]. In order to use these formulas, it is necessary to know the parameters of the one-coordinate model (of electron–phonon interaction). These parameters were calculated with the formulas reported in [20–23] from the moments of the form-functions of the optical transition. For the $V_{Ga}S_{As}$ complex, we have the following values of the parameters in the one-coordinate model: $E_0 = 1.3$ eV at 100 K, $\hbar\omega_u = 0.017$ eV, $\hbar\omega_g = 0.025$ eV, $S = 3$ (here $\hbar\omega_u$ is the phonon energy describing the adiabatic potential of the excited state, $\hbar\omega_g$ is the phonon energy describing the adiabatic potential of the ground state, S is the Huang–Rhys factor, E_0 is the energy of a pure electron transition from the localized state near the conduction-band bottom to the deep level of the ground state of the center). According to the calculated parameters, the level of the ground state of the center under discussion is spaced by $E_t = E_g - E_0 \approx 0.2$ eV (at 100 K) from the valence band top.

The above parameters were used for the calculation of the field dependences of the emission rates with the use of the best known models.

In Fig. 2 (curve *4*) the field dependence of the tunnel ionization rate of a deep center is given; this dependence was calculated according to the theory of Pons, Makram-Ebeid and Lannoo [6, 7]. For $\hbar\omega$ in this

model, the intermediate value between $\hbar\omega_u$ and $\hbar\omega_g$—$\hbar\omega = 0.21$ eV was chosen; the emission rate in a zero field was calculated by the formulas given in [14], and was found to be equal to $e_{n0} = 0.045$ s^{-1}. The fact that the theory is in poor agreement with the experiment, to our opinion, can be associated with the inaccuracy of the formulas for weak and intermediate fields (for the center in gallium arsenide under discussion, $F_c = 2.2 \times 10^5$ V/cm). The experimental data in [7], where $F > 2 \times 10^6$ V/cm, seem to belong to the range of strong fields.

As distinct from the theory [6, 7], the results obtained by Timashov [8, 9] more adequately describe the field dependences of emission rates in weak and intermediate fields. In [5], the rates of emission from the deep levels were studied in Au–InP:Fe structures in the fields $F < 7 \times 10^4$ V/cm by capacitance spectroscopy. A good agreement with the theory [8, 9] was found. As to our experiment, a good agreement with the theory was also obtained in the entire range of fields (Fig. 2, curve *3*; for $e^t_{n(p)}(0) = 0.045$ eV, $\hbar\omega = 0.21$ eV, and $\sigma^2 = 2.8 \times 10^{-3}$ at 77 K we obtained $\gamma = 0.00195$ cm$^{1/2}$/V$^{1/2}$ and $\nu = 4.56 \times 10^{-11}$ cm^2/V^2 at 77 K).

The more general theoretical analysis of multiphonon generation in the electric field was reported in [10–14]. By choosing the most popular model [1] for the description of multiphonon transitions, the authors of [10–14] examined the processes in the context of the multiband model, which enabled them to obtain the dependences for the ionization cross sections for electron and holes for the same center [13]. The theory developed, with the allowance made for these processes, simultaneously allows one to explain both an increase in the probability of the thermal emission in the electric field and an increase in probability of tunneling, with the electron–phonon interaction taken into consideration. Curve *2* in Fig. 2 represents the result of calculation by the formulas reported in [12]. It is seen that this curve is the best fit to the experimental points.

CONCLUSION

It is noteworthy that various analytical expressions for the field-dependent probability of the ionization for deep centers, which show a good agreement with the experiment in the range of high fields, fail to agree with the experiment in weak and intermediate fields. The analysis made here shows that our experimental data can be well accounted for by the expression $e_p \propto \exp\{\alpha F^2\}$, with the coefficient α coinciding with ν in formulas given in [8, 9]. This confirms the applicability of the one-coordinate approach to the description of the field dependences of the rates of the carriers' emission from the deep level of $V_{Ga}S_{As}$ complex. In this case, it is preferable to use the scheme based on the experimental value of the form-function and on the numerical calculation based on formula (2), since this calculation can be made, on the one hand, without any assumptions about the nature of electron–phonon interaction in the system, and, on the other hand, it does not require cumbersome computations (such as the determination of parameters of the electron–phonon interaction in the one-coordinate model).

REFERENCES

1. K. Huang and A. Rhys, Proc. R. Soc., Sect. A **204**, 406 (1950).
2. S. I. Pekar, Usp. Fiz. Nauk **50**, 197 (1953).
3. V. A. Kovarskiĭ, *Kinetics of Nonradiative Processes* [in Russian], Kishinev (1968).
4. C. H. Henry and D. V. Lang, in *Proceedings 12th International Conference on the Physics of Semiconductors* (1974), p. 584.
5. S. V. Bulyarskiĭ, N. S. Grushko, and A. A. Gutlin, Fiz. Tekh. Poluprovodn. (Leningrad) **9**, 287 (1975).
6. D. Pons and S. Makram-Ebeid, J. Phys. (France) **40**, 1168 (1979).
7. S. Makram-Ebeid and M. Lannoo, Phys. Rev. **25**, 6406 (1982).
8. S. F. Timashov, Fiz. Tverd. Tela (Leningrad) **14**, 2621 (1972).
9. S. F. Timashov, Fiz. Tverd. Tela (Leningrad) **14**, 171 (1972).
10. V. Karpus and V. I. Perel', Pis'ma Zh. Éksp. Teor. Fiz. **42**, 403 (1985).
11. V. Karpus, Pis'ma Zh. Éksp. Teor. Fiz. **44**, 344 (1986).
12. V. Karpus and V. I. Perel', Zh. Éksp. Teor. Fiz **91**, 2319 (1986).
13. V. N. Abakumov, I. A. Merkulov, V. I. Pelrel', *et al.*, Zh. Éksp. Teor. Fiz. **89** (4), 1472 (1985).
14. V. N. Abakumov, O. V. Kurnosova, A. A. Pakhomov *et al.*, Fiz. Tverd. Tela (Leningrad) **30**, 1793 (1988).
15. N. S. Averkiev, A. A. Gutkin, and E. B. Osipov, Fiz. Tekh. Poluprovodn. (St. Petersburg) **25** (1), 50 (1992).
16. N. S. Averkiev, A. A. Gutkin, E. B. Osipov, *et al.*, Fiz. Tekh. Poluprovodn. **25** (1), 57 (1992).
17. A. A. Gutkin, M. A. Reshchikov, and V. E. Sedov, Fiz. Tekh. Poluprobvodn. (St. Petersburg) **31** (9), 1062 (1997).
18. Yu. B. Rozenfel'd, S. V. Bulyarskiĭ, and E. P. Evseev, *Abstracts of Papers, 23th All-Union Meeting on the Theory of Semiconductors* [in Russian] (Erevan, 1987).
19. W. Franz, in *Handbuch der Physik* (Springer-Verlag, Berlin, 1956; IL, Moscow, 1961).
20. K. K. Rebane, A. P. Purga, and O. N. Sil'd, Tr. Inst. Fiz. Astron., Akad. Nauk Estonian SSR, No. 14, 31 (1961).
21. K. K. Rebane and O. I. Sil'd, Opt. Spektrosk. **9**, 521 (1960).
22. Yu. E. Perlin and B. S. Tsukerblat, *Effects of Electron–Vibrational Interaction in Optical Spectra of Impurity Paramagnetic Ions* [in Russian] (Shtiintsa, Kishenev, 1974).
23. K. K. Rebane, E. D. Trifonov, and V. V. Khizhnyakov, Tr. Inst. Fiz. Astron., Akad. Nauk Estonian SSR, No. 27, 3 (1964).
24. K. K. Rebane, A. P. Purga, and O. I. Sil'd, Tr. Inst. Fiz. Astron., Akad. Nauk Estonian SSR, No. 20, 48 (1963).

Translated by A. Zalesskiĭ

Semiconductors, Vol. 34, No. 1, 2000, pp. 45–55. Translated from Fizika i Tekhnika Poluprovodnikov, Vol. 34, No. 1, 2000, pp. 46–56.

ELECTRONIC AND OPTICAL PROPERTIES OF SEMICONDUCTORS

Electron Spin Resonance in the Vicinity of Metal–Insulator Transition in Compensated *n*-Ge:As

A. I. Veĭnger, A. G. Zabrodskiĭ, and T. V. Tisnek

Ioffe Physicotechnical Institute, Russian Academy of Sciences, Politekhnicheskaya 26, St. Petersburg, 194021 Russia

Submitted June 25, 1999; accepted for publication June 28, 1999

Abstract—Electron spin resonance (ESR) is investigated in the vicinity of metal–insulator transition in compensated *n*-Ge:As. It is found that the 10-GHz signal is observed from both sides of the transition up to a temperature of 100 K. ESR spectrum in metallic samples looks like a single line of the Dyson type, with the line shape varying with temperature. The Dyson line in the insulating samples transforms into the Lorentz line which splits into two lines at temperatures below 4.1 K. One line has an ordinary shape, the other has an anomalous step-like shape in the magnetic field, increasing with decreasing temperature. This effect has not been satisfactorily explained so far. Two mechanisms are proposed for the spin relaxation observed, one of which is related to donor–acceptor pairs and the other, to phonons. The Pauli and Curie paramagnetism is found in metallic and insulator samples, respectively. *© 2000 MAIK "Nauka/Interperiodica".*

1. INTRODUCTION

The magnetic properties of doped semiconductors on the insulator side of the metal–insulator (MI) transition and in the vicinity of the transition itself, are less studied in comparison with their electrical properties. According to the existing ideas (see, for example, [1]), with an increase in the doping level of an electron semiconductor, the paramagnetism of individual donors should give way to antiferromagnetism of interacting electrons, which, in turn, should be replaced by Pauli paramagnetism at the transition of the semiconductor into the metallic state.

The first assumption is confirmed by ESR measurements in electron semiconductors Si [2], Ge [3], and SiC [4]. According to these data, well before MI transition, an increase in donor concentration transforms the ESR spectrum belonging to separate atoms and consisting of 2S + 1 lines (S is the spin of the donor atom) into the ESR spectrum of interacting atoms with a single exchange-narrowed line. It is found that in some semiconductors, such as Si:P [5–8] and Si:As[5], on further increase in donor concentration in the insulator state, the concentration of spins involved in ESR absorption saturates, and in SiC:N [9, 10] it even decreases. This is explained by the antiferromagnetic interaction of localized spins. Simultaneously, according to [9], instead of exchange-narrowing, the broadening line is observed. All this occurs against the background of an increase in conductivity of the samples at low temperatures related to a gradual loss of localization as the MI transition is approached. The ESR investigations under the conditions of passing through the point of transition into metallic state in Si [11, 12] show that appreciable weakening of temperature dependence of the signal occurs in the critical region of the transition, as one would expect when Curie paramagnetism changes into Pauli paramagnetism.

In comparison with the silicon well-studied by ESR, germanium represents a much more challenging object. This is primarily related to the fact that the interaction of spins with lattice in germanium is much more intense, and the ESR lines become, by an order of magnitude, broader than in Si, which hampers the ESR study. The ESR signal in Ge has not even been found near the MI transition [13, 14]. For slightly compensated Ge:As [15], the ESR signal in the MI transition region was observed at the frequency of 63.2 MHz. The signal decreases towards ultralow temperatures and increases under uniaxial compression.

In [16], we found that ESR absorption is clearly observable in the Ge:As samples with natural isotopic composition at conventional conditions on both sides of MI transition induced by the introduction of a compensating impurity of Ga. This work is devoted to the description and analysis of this effect, as well as to its relation to other properties of electron germanium near the MI transition.

2. EXPERIMENTAL AND RESULTS

The ESR measurements were made with the use of an E-112 Varian ESR spectrometer at a frequency near 10 GHz with an ESR-9 cryostat manufactured by Oxford Instruments. This allowed us to perform measurements in the temperature range from 3 K up to room temperature. The standard accuracy of temperature control in the ESR-9 cryostat was about 0.1 K. However, in practice, the thermocouple junction and the sample were located at different sites of the cryostat, and a varying difference in temperatures might

Parameters of compensated Ge : As samples

Sample	n, 10^{17} cm^{-3}	N_D, 10^{17} cm^{-3}	N_A, 10^{17} cm^{-3}	$K = N_A/N_D$
1	5.75	5.75	0	0
2	4.5	6.28	1.78	0.28
3	4.15	6.43	2.28	0.35
4	3.85	6.56	2.71	0.41
5	3.3	6.80	3.50	0.51
6	0.7	7.90	7.21	0.91

occur between the junction located closer to the helium coolant-flow than to the sample. This required a special analysis of the error in temperature measurements. The calibration of the thermometer by the reference points for the superconducting transitions of tin and indium showed that below 4.2 K the correspondence in temperatures between the thermocouple junction and the sample was maintained to within 0.005 K, and the temperature could be measured by the helium vapor pressure in cryostat [17]. The measurements with an additional thermocouple, which was placed instead of the sample, showed that above 30 K the error is also negligible. The largest error was found to occur within the range of 4–30 K, where it was minimized by the optimal choice of helium flow through the cryostat [18].

The ESR studies were carried out on the series of *n*-Ge:As samples with a controlled compensation by the Ga acceptor impurity; the starting samples were obtained from an ingot of "metallic" *n*-Ge:As with the electron concentration (arsenic concentration) equal to 5.75×10^{17} cm^{-3}. For a controlled decrease of electron concentration, the samples were compensated by the Ga acceptor impurity introduced by neutron-transmutation doping.[1] The advantage of this method is that the spatial distribution of transmutation-induced donors and acceptors turned out to be uncorrelated (random). The samples with electron concentration from $n = 5.75 \times 10^{17}$ to 7×10^{16} cm^{-3} were studied. Their parameters are shown in the table. The temperature dependences of resistivity for five typical Ge:As samples are shown in Fig. 1 (reproduced from [19]). It is seen that four of them have a metallic type of temperature dependence of resistivity, while the fifth one, the most highly compensated, shows the insulator behavior. Sample no. 6 has the heaviest compensation ($n = 7 \times 10^{16}$ cm^{-3}) in comparison with sample no. 5. At low temperatures $T < 10$ K, the insulator samples show the hopping conductivity with the variable hop length over the Coulomb gap states [19, 20]. The gap vanishes as a result of MI transition [19, 20]. At high temperatures $T > 50$ K the charge transport proceeds by the free electrons at the threshold of mobility [20].

The samples for ESR measurements had the shape of parallelepipeds with the thickness of about 1 mm and differed slightly in other dimensions. The ESR was observed on both sides of MI transition in all samples. The highest intensity of the spectrum was observed in the initial sample no. 1. The ESR line for this sample at $T = 3.2$ K is shown in Fig. 2. It is seen that the line has an asymmetric shape (Dyson's shape [21]): its left-side wing is more "compressed" in comparison with the right-side one and is characterized by the appreciably larger derivative of the absorption signal ($A > B$ in Fig. 2). It should be remembered that the signal of the derivative represents only the most intense part of the ESR line (its positive part). This is the reason why the field H_0, which determines the position of the center of the undistorted line, is located approximately at the half-height of the positive part of the derivative [22] rather than at the point where $dP/dH = 0$. For the same reason, the linewidth in this case is determined by a doubled width measured at the half-height of its positive part rather than by the distance between the extreme points of the derivative. The Dyson's shape is known to be typical when the skin depth δ is much less than the sample thickness [21]. In fact, the estimation of the skin depth from the data shown in Fig. 1 yields $\delta \approx 0.07$ mm, which is much less than the thickness of the sample.

In the samples on the metallic side of MI transition ("metallic" samples), no appreciable shift in ESR line position with temperature is observed. However, on the insulator side of MI transition ("insulator" samples) at the temperatures below 4.1 K we observed the splitting of the ESR line into the ordinary line and the anomalous one (Fig. 3).[2] The latter is characterized only by the positive derivative $dP/dH > 0$; i. e., the $P(H)$ has a step-like shape and rapidly shifts towards the stronger fields. It is also worth noting that the ESR signal is observed against the background of the slow change in the derivative of microwave absorption due to magnetoresistance effect.

The temperature change of the line half-width for all samples studied is shown in Fig. 4. It strongly depends on the concentration of compensating impurities. For example, in uncompensated sample no. 1, the linewidth rather slowly increases with increasing temperature, while in metallic samples, even in the presence of slight compensation, the linewidth first decreases, and only above 30–50 K does it begin to increase and approaches at high temperatures the dependence typical of the uncompensated sample. At low temperatures, as seen in Fig. 4, the line steadily broadens with compensation. For the most highly compensated sample, nos. 5 and 6,

[1] In the process of neutron doping of germanium, as a result of transmutation of ^{70}Ge and ^{74}Ge isotopes, the acceptor (Ga) and donor (As) impurities are introduced in the ratio of 3:1, as well as a small amount of deep doubly charged donors arising from the ^{76}Ga isotope. The details of preparation of Ge:As samples for the investigation of MI transition are given in [19, 20].

[2] The temperature $T < 4.1$ K for these samples corresponds to the mechanism of hopping with variable hop length over the Coulomb gap states [19, 20].

the linewidth increases by a factor of approximately 20. This is the first experiment in which the variation of the ESR signal in Ge could be traced up to 100 K.

The temperature dependence of the maximum of the positive part of the derivative A is shown in Fig. 5. This dependence also turns out to be substantially different for compensated and uncompensated samples. In the former case, the amplitude decreases with increasing temperature in the entire range of its variation, but in the latter case this occurs only at high temperatures, whereas at low temperatures the amplitude of derivative increases. In the low-temperature region, the introduction of comparatively small amounts of compensating impurity strongly reduces the value of derivative dP/dH.

3. ANALYSIS AND DISCUSSION OF EXPERIMENTAL RESULTS

Let us dwell consecutively on the above features of the ESR line parameters and on their relation to the physical processes in the vicinity of MI transition.

3.1 ESR Linewidth Analysis

Let us begin with the analysis of concentration and temperature dependences of the linewidth δH. The linewidth is directly related to the spin relaxation time T_2 by the following formula:

$$T_2 = h/(g\mu_B\delta H). \quad (1)$$

Here, μ_B is the Bohr magneton, g is the electron g-factor, and h is the Planck constant.

The mechanism of interaction between the spin system and lattice can be inferred from the temperature dependence of EPR linewidth (or T_2). For example, in lightly doped Si [23, 24] the spin–lattice relaxation time is very large, but it rapidly decreases with increasing temperature, which corresponds to the direct spin–phonon interaction. The spin–lattice relaxation time also decreases with the emergence of free electrons as a result of illumination or heavy doping corresponding to the insulator–metal transition, which is indicative of efficiency of the energy transfer from the spin system to the lattice via free electrons. This process is intensified when the interaction of free or weakly bound electrons with charged centers (as a result of the introduction of compensating impurities) becomes more important.

In all samples studied, as follows from Fig 4, the relaxation time decreases with temperature much slower than is known from the literature for lightly doped Ge [3]. In compensated samples in the low-temperature region, the relaxation time increases with increasing temperature: the higher the compensation, the larger is this increase. It is reasonable to associate this region with the relaxation of spins at charged impurities. Such mechanisms have not yet been studied, though in [22–24] it was emphasized that they should

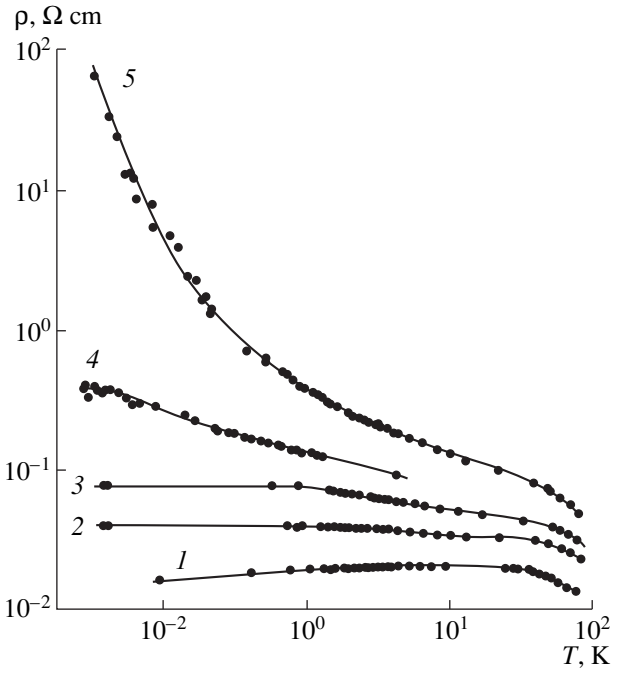

Fig. 1. Temperature dependence of resistivity of n-Ge:As in the region of MI transition. The numbers correspond to the samples in the table.

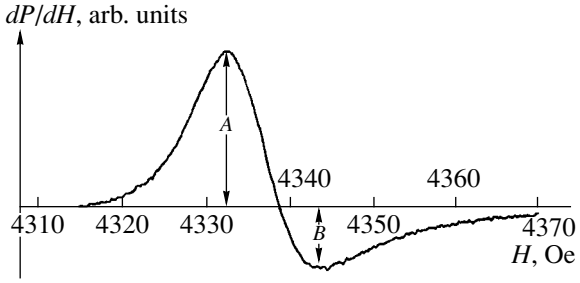

Fig. 2. ESR derivatives (dP/dH) for noncompensated metal sample no. 1 at T = 3.2 K. The A and B arrows show the Dyson line shape parameters.

be dominant at high concentrations of charge carriers in semiconductors.

Let us turn to the quantitative analysis of dependences in Fig. 4. It turns out that the corresponding curves for T_2 can be satisfactorily rectified on the log–log scale, i. e. they have the exponential character both at low and high temperatures (see Fig. 6).[3] The low-temperature region is most pronounced for highly compensated sample no. 5, while the high-temperature region is more pronounced in original uncompensated sample no. 1. It is interesting that compensation affects the slope of the curves differently at low and high tem-

[3] For sample nos. 2 and 6 the dependences are actually the same as for sample nos. 3 and 5, respectively.

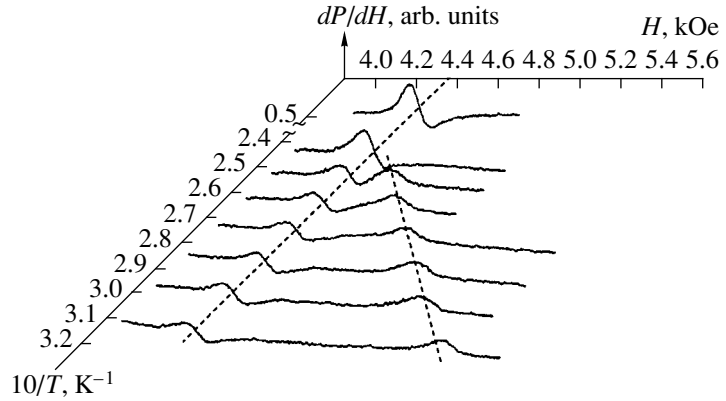

Fig. 3. ESR spectra for compensated insulator sample no. 5 as a function of inverse temperature; the vertical scale for the line at 20 K is reduced by a factor of 2.5.

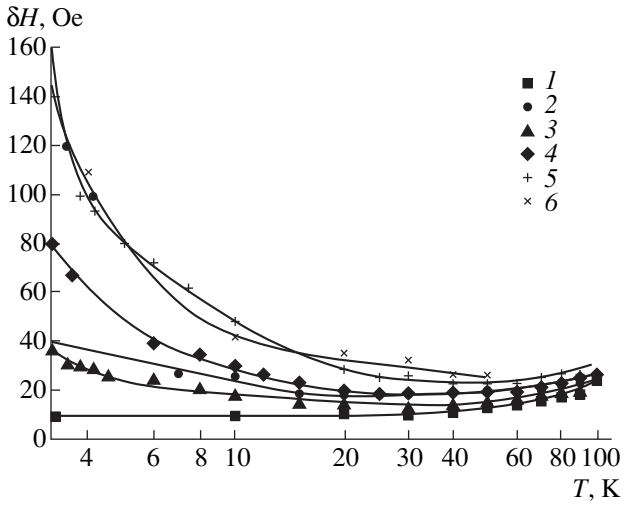

Fig. 4. Temperature dependence of the half-width of the ESR derivative (δH) for the Ge:As samples. The number corresponds to the samples in the table.

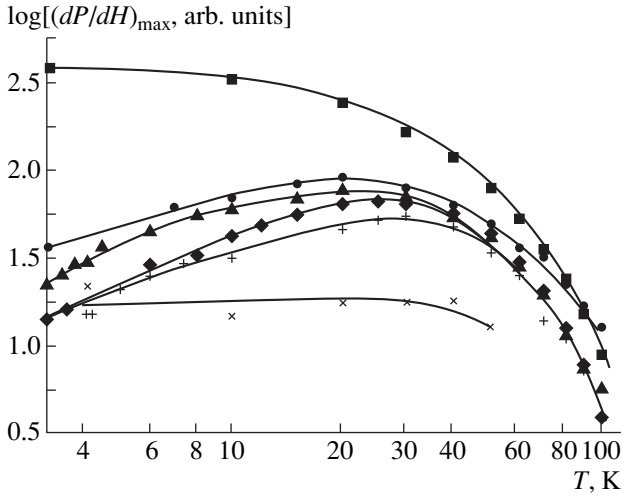

Fig. 5. Temperature dependence of the amplitude of the positive part of the ESR line derivative for the samples Ge:As; the designations of the experimental data are the same as in Fig. 4.

peratures, increasing it in the former case, and decreasing it in the latter case. For both regions, we have

$$T_2 \sim T^{\alpha}, \tag{2}$$

where $\alpha = 0.48$–0.79 for the low-temperature region, and $\alpha = -(0.45$–$0.7)$ for the high-temperature one.

An increase in relaxation time with temperature indicates that the relaxation occurs at charged centers of attraction, i. e. at donors, the electrons of which are trapped by the acceptors, or at more complex aggregations containing also the neighboring negatively charged acceptor. As is known [25], in the processes that are determined by the interaction of a particle with a center of attraction, the observed temperature dependence of interaction allows one to determine the spatial distribution of the potential. Let us use this idea in further estimations.

The potential energy of the center at which the relaxation occurs can be written as

$$E_P = e^2/\varepsilon r^n, \tag{3}$$

where ε is the dielectric constant, e is the elementary charge, and the exponent n depends on the type of attractive potential. The value on n can be determined by assuming that the cross section of the interaction $\sigma = \pi r^2$ is determined by the distance from the center r at which the potential energy E_P is equal to the kinetic energy $E_K = kT$. Thus, we obtain

$$\sigma \sim T^{-2/n}. \tag{4}$$

If the spin–lattice relaxation time is determined by the scattering of free electrons by the charged donors with the concentration N_+, then, taking into account (4) and

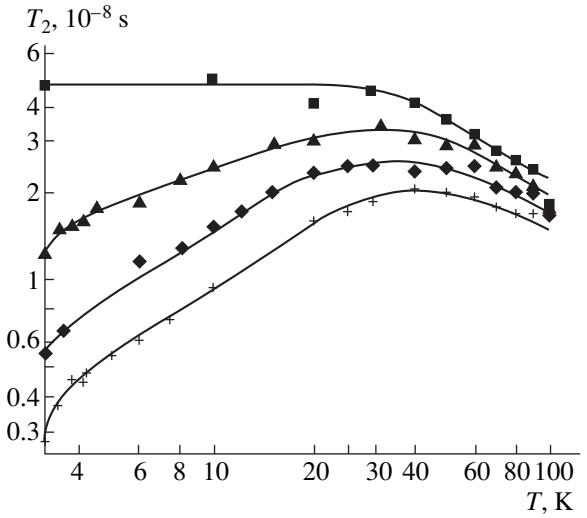

Fig. 6. Temperature dependence of spin—lattice relaxation time T_2 for samples nos. 1, 3, 4 and 5; the designations of the experimental data are the same as in Fig. 4.

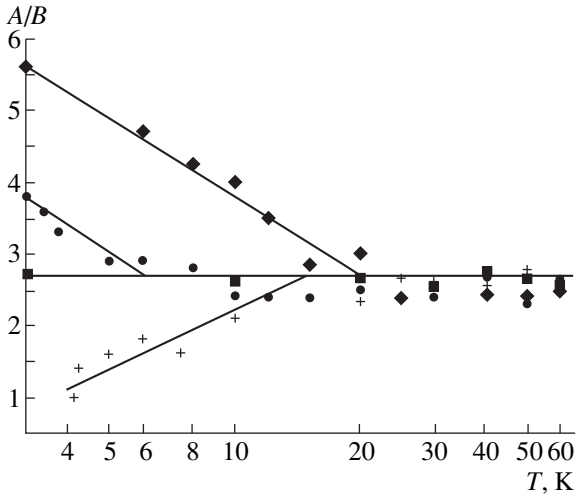

Fig. 7. Temperature dependence of the ratio A/B for samples nos. 1, 3, 4 and 5; the designations of the experimental data are the same as in Fig. 4.

the fact that the thermal velocity of electron $\nu \sim T^{1/2}$, we obtain

$$T_2 = (\sigma \nu N_+)^{-1} \sim T^{2/n - 1/2}. \quad (5)$$

Equating the exponent at T to the experimental value, we arrive at the relation

$$2/n - 1/2 = \alpha. \quad (6)$$

It follows from (6) that, for $\alpha = 0.48$–0.79, we have $n = 2$–1.55. Such values of the exponent are closer to the dipole potential rather than to the potential of an attractive Coulomb center. It is easy to identify the origin of these dipoles. Indeed, when the compensating acceptors are introduced into the material with *n*-type of conductivity, these acceptors trap electrons from donors. Thus, all acceptors with the concentration N_A become negatively charged, and the equal number of donors N_D^+ become positively charged. Moreover, it is the donors located close to acceptors that become charged. Therefore, we may assume that donor–acceptor pairs [26] are formed. Apparently, it is at such pairs with dipole potential that effective relaxation of excited spins occurs.

In this case, the experimentally observed increase in the exponent α in (*2*) with the increase in the compensation level could be explained by assuming that, for the spin relaxation, the electrons should move towards the attraction center to the distance equal, by the order of magnitude, to the distance l between donor and acceptor forming a dipole, in which case the potential could not be considered to be purely a dipole one. The further analysis of the spin relaxation cross section shows that the pairs with closely located charges (i. e. with small l in comparison with the average distance between charges) turn out to be primarily responsible for the relaxation process.

The cross section of spin relaxation at the charged centers was obtained for helium temperatures from formula (5) as

$$\sigma = (T_2 \nu N_+)^{-1} \simeq 10^{-15}\ \text{cm}^2. \quad (7)$$

This value is equal by the order of magnitude to atomic dimensions, if we assume that the relaxation occurs at all donor–acceptor pairs $N_D^+ = N_A$ that are formed as a result of compensation. At the same time, the average value of l in our case is equal to $l \simeq 10^{-6}$ cm. In order to make the electron "feel" the potential as a dipole potential, the electron must be located at a distance larger than l; i. e., the relaxation cross-section should be no less than 10^{-12} cm^2.

To attain a better fit for the value of σ to the value obtained from the simple considerations, we should assume that the spin relaxation does not involve all donor-acceptor pairs but only the nearest ones with $l \ll 10^{-6}$ cm. If we assume that this distance is on the order of 10^{-7} cm, the number of these pairs should be much less than the total concentration of acceptors. Assuming the Poisson distribution, the concentration of such pairs is estimated to be by three orders of magnitude less than the total concentration of donor–acceptor pairs (10^{14} and 10^{17} cm^{-3}, respectively). For the concentrations of nearest-neighbor donor–acceptor pairs of such an order as this, the substitution of T_2 and thermal rate into (8) yields $\sigma \simeq 10^{-12}$ cm^2. Thus, the assumption that the spin relaxation occurs at nearest-neighbor pairs allows us to obtain an appropriate value of the cross section.

With the increase of compensation, the concentration of such pairs should increase proportionally to the

squared concentration of charged centers, because the concentration of pairs is proportional to the product of the acceptor concentration and the concentration of charged donors. Accordingly, the spin–lattice relaxation time should decrease proportionally to the squared concentration of such centers. Assuming this, let us consider the concentration dependences of the spin–lattice relaxation time. As seen in Fig. 6, the slope of the curves at low temperatures is slightly increased with an increase in the level of compensation. Consequently, the dependence of T_2 on N_+ at various temperatures should have a different slope decreasing with increasing temperature. In view of this, we represented the dependence of T_2 on N_+ as

$$T_2 \sim N_+^{-\beta} \tag{8}$$

and determined the value of β at three temperatures: $\beta = 1.61 \pm 0.72$ for $T = 4$ K, $\beta = 1.2 \pm 0.6$ for $T = 10$ K, and $\beta = 0.9 \pm 0.5$ for $T = 20$ K. The dependences were derived for the metal samples nos. 2–4, and for the insulating sample no. 5 with properties close to the MI transition. Because of the small number of samples, the value β was determined with low accuracy. However, one can clearly see that the value β increases with decreasing temperature and approaches 2. This supports the above assumption that the spin–lattice relaxation in compensated Ge:As at low temperatures occurs at closely spaced donor–acceptor pairs, the concentration of which is significantly lower than the total concentration of acceptors. The similar mechanism of relaxation was proposed in [24] for the conduction electrons in Si. However, it was assumed in [24] that the relaxation occurred at pairs of closely spaced neutral donor atoms or at the same pairs, but with a single charged center. Our experiments show that the spin loss in the field of the nearest-neighbor donor–acceptor pairs is most likely responsible for the relaxation in compensated semiconductors. However, for spin transfer, there should exist a bound electron, to which the excitation is transferred. The electron localized at the neighboring donor (neutral center), or the electron localized at the acceptor of the donor–acceptor pair may serve as such an additional electron.

Below 4 K in compensated samples the tendency to a more rapid decrease of spin-lattice relaxation time, with a decrease in temperature, is observed. The transition to another mechanism of relaxation mechanism seems to be taking place. A possible relaxation mechanism in this case may be the scattering by the electrons localized at donors. The degree of localization in this case increases with a decrease in temperature. However, the ESR studies at lower temperatures are necessary to make more definite conclusions.

At higher temperatures, the above mechanism becomes ineffective because the carriers cannot any longer "feel" the attractive Coulomb potential. At these temperatures, the spin–lattice relaxation is determined by another mechanism which provides the reduction of relaxation time with an increasing temperature. The dominant mechanism in this temperature region seems to be the direct interaction with phonons, although the theory of this process developed for lightly doped silicon [23, 24] yields a stronger dependence on temperature. Additional experimental studies and the development of the theory are necessary in order to determine conclusively the mechanism of spin-lattice relaxation of free spins.

3.2 Analysis of Line Shape

The ESR line-shape distortion in metals has been explained by Dyson by assuming that the electron diffusing through the skin-depth layer periodically finds itself in the external electromagnetic field of various amplitudes and the field acting on this electron becomes modulated by the frequency on the order of inverse time of electron diffusion through the skin-depth layer t_D^{-1} [21]. Then the line asymmetry depends on how fast the electron transfers the spin excitation to the lattice in comparison with the diffusion time through the skin-depth layer; i.e., it depends on the ratio of T_2 and t_D: for $t_D \ll T_2$, the electron "feels" the modulation of the electromagnetic field amplitude in full measure, whereas for $t_D \gg T_2$, this effect is much smaller. For the semiconductors with degenerate electron gas that have a conductivity much lower than that of metals, and, consequently, the skin depth is larger, one can expect the fulfillment of the latter inequality. Feher and Kip [22] used Dyson's results [21] to determine the relationship between the ratio of the wing amplitudes A and B (parameters A and B were defined in Fig. 2) of the ESR line, or of its derivative, and the ratio of times $(t_D/T_2)^{1/2}$ and illustrated this relationship graphically. From these graphs it follows that, for $t_D/T_2 \longrightarrow \infty$, the ratio $A/B = 2.7$.

The temperature dependences of the A/B ratio for the same four samples as in Fig. 6 are shown in Fig. 7. It can be seen that for an uncompensated sample this ratio is temperature-independent and for all relevant temperatures is close to 2.7. This means that the inequality $t_D \gg T_2$ holds for all relevant temperatures. The validity of this inequality is confirmed by numerical estimations. In fact, using the above obtained value of the skin depth, estimating the value of diffusion coefficient D from Fig. 1, and using the formulas $\mu = \sigma/en$ and $D = \mu kT/e$ (μ is the mobility and n is the electron concentration), we obtain $t_D = \delta^2/D \simeq 2 \times 10^{-4}$ s. At the same time, as follows from the preceding section, $T_2 \simeq 10^{-8}$ s $\ll t_D$.

The results for compensated samples are found to be quite different. As can be seen in Fig. 7, for the temperature of 3.2 K and for the most compensated metallic sample no. 4, the ratio $A/B \approx 5.6$ which corresponds [22] to $t_D \simeq 0.25T_2$. At the same time, as a result of compensation due to diffusion through the skin-depth layer, the inequality $t_D \gg T_2$ can only strengthen

because of a decrease in mobility. Consequently, some other mechanisms responsible for the distortion of the ESR line in this case.

Dyson considered the distortion of the line for metals with large Fermi energy. In this case the structure of the conduction-band bottom does not affect the charge-carrier motion. In semiconductors, even with metallic conductivity but with a weak degeneracy, the carriers must be very sensitive to the potential profile of the conduction band bottom, which is determined by the distribution of charged impurities and by the mechanism of screening of the arising electrostatic field. As a result, similar to the case considered by Dyson, not only the external electromagnetic field at the frequency ω is acting on the moving carrier, but also the electric field with the frequency reciprocal to the time it takes for the charge carrier to travel the distance by the order of magnitude equal to the period of variation in the potential. In connection with this, it can occur that the characteristic time, which determines the line shape, might be the time of charge carrier diffusion over the distance on the order of magnitude equal to the characteristic spatial scale of the variations in potential λ rather than the time of diffusion of carrier over the skin depth layer. The calculations by the above formulas yield for sample no. 4 the values $D = 0.042$ cm^2/s and $T_2 = 5 \times 10^{-9}$ s. Using these values, we estimate the value of λ as

$$\lambda = (0.25DT_2)^{1/2} = 7 \times 10^{-6} \text{ cm}. \quad (9)$$

This value is considerably larger than the mean distance between the charged donors $l_+ = N_{D^+}^{-1/3} \simeq 1.8 \times 10^{-6}$ cm (sample no. 4). Thus, we can relate the obtained above value λ to the scale of the fluctuation potential of statistical origin.

According to the above conclusions we may consider that at relatively high temperatures the time of diffusion which determines the ratio of derivative wings, corresponds, as in Dyson's case, to the time of diffusion through the skin-depth layer. Thus, the ratio may be taken as $A/B = 2.7$. As the temperature decreases, two independent low-temperature processes of interaction of electrons with the charged impurity centers become effective. On the one hand, the electron spins begin to relax at closely located donor–acceptor pairs; on the other hand, they begin to experience the action of the fluctuations of the conduction band bottom. An increase in the ratio A/B indicates that these processes have different temperature dependence. The time t_D decreases with decreasing temperature because the spins begin to interact with progressively smaller fluctuations. This process goes more rapidly than the decrease in T_2, which leads to an increase in line distortion (i.e. to the increase of the ratio A/B).

The line shape of insulator samples behaves quite differently. At low temperatures they have high resistance, and the microwave field remains uniform through the entire volume of the sample. In connection with this, the line shape transforms from the Dyson's type into a Lorentz one, and the ratio A/B becomes equal to unity. However, as the temperature increases, the resistance of these samples decreases, and the skin effect comes into being. This effect occurs at a temperature such that the fluctuation potential of charged centers does not affect the electrons. Because of this, the ratio A/B increases with an increase in temperature from 1 to 2.7, which is clearly seen in Fig. 7. It also follows from Fig. 7 that the modulation of electron motion by the potential profile of the conduction band bottom does not manifest itself in insulator samples in the way it does in metal samples (by an increase in the line distortion). It is known that in the fine particles of normal metals where the skin depth is larger than the particle dimensions, the symmetrization of the line takes place [22]. However, there are no grounds to believe that such interaction ceases to exist in the interaction of electrons with potential profile of the conduction band bottom in transition to the insulator state. The possible evidence for such an interaction will be considered below in the analysis of the ESR spectrum in an insulating state.

3.3 Analysis of the Concentration of Resonant Centers

The dependence of the maximum value of the positive part of the derivative with respect to temperature for six samples, in which the ESR signal was observed, shown in Fig. 5. The maximum of the derivative itself does not give any interesting physical information about the concentration of paramagnetic centers, which, on the insulator side of the MI transition, can be less than the electron concentration because of antiferromagnetic coupling. Such information can be obtained from the area under the absorption-line curve; this area is proportional to the concentration of paramagnetic centers, provided the microwave field penetrates the entire sample. This is valid for dielectrics and lightly doped semiconductors; however, in the case of metals and heavily doped semiconductors, only a small fraction of paramagnetic centers is involved in absorption, because in the highly conducting media, due to the skin effect, the microwave field penetrates only into the near-surface layer and affects the centers within this layer. This is the reason why the ESR signal in highly conducting materials is usually small.

As was mentioned in the Introduction, the transition from the Curie paramagnetism, which is characteristic of nondegenerate systems, to the Pauli paramagnetism in degenerate systems takes place in the vicinity of MI transition. In the region of Pauli paramagnetism, the temperature dependence of paramagnetic susceptibility remains pronounced but differs from that of the Curie paramagnetism. To clarify the origin of paramagnetism in compensated Ge:As samples, we should study the temperature variations of resonant-center concentra-

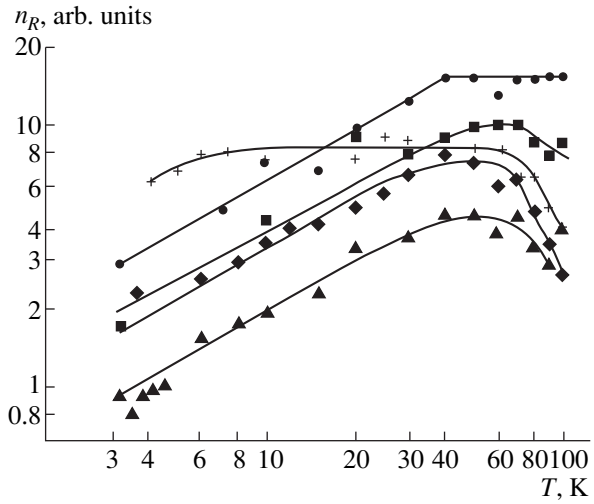

Fig. 8. Temperature dependence of the concentration of the resonant centers n_R for sample nos. 1–5; the designations of the experimental data are the same as in Fig. 4.

tions. In order to do this, we should solve some problems of experimental data processing.

First, in order to obtain the quantity proportional to the concentration of the resonant centers n_R from the measured first derivative of the ESR line, we should calculate the second integral of the derivative of the ESR absorption line; this integral is proportional to the value of paramagnetic susceptibility:

$$I \sim \int dH \int (dP/dH)dH. \tag{10}$$

Since the line shape remained unchanged at relevant temperatures and was the same for all samples, for simplicity in construction of the temperature dependences, we replaced the double integral (10) by a simple estimate

$$I \simeq (dP/dH)_{\max}(\Delta H_{1/2})^2, \tag{11}$$

where $(dP/dH)_{\max}$ is the maximum value of the positive part of the derivative of the absorption line and $(\Delta H_{1/2})$ is the width of this part of the derivative at half height.

Furthermore, taking into account that the ESR signal amplitude for the constant concentration of paramagnetic centers is proportional to $1/T$, we should have in mind that $n_R \sim IT$ in determining the temperature variation of n_R. The obtained dependences of $\log n_R = f(\log T)$ for five samples are shown in Fig. 8. The Curie paramagnetism in such coordinates corresponds to the horizontal lines, and the Pauli paramagnetism corresponds to the straight lines with a slope equal to unity. It is seen in Fig. 8 that the relation

$$n_R \sim T^{\gamma}, \tag{12}$$

with $\gamma \simeq 2/3$, holds for the samples with degenerate electron gas, in which case the conductivity varies only slightly with temperature and the skin depth may be regarded as temperature-independent.

This increase in concentration of resonant spins with increasing temperature seems to be indicative of Pauli paramagnetism in the samples with degenerate electron gas existing up to the temperatures of 40–50 K. Above these temperatures the degeneracy is removed, and the concentration n_R begins to decrease owing to a rapid increase in spin relaxation rate. It should be noted that, in the case of Pauli paramagnetism, the concentration of the resonant centers in metals is temperature-independent; consequently, in the limit of a strong degeneracy, the exponent γ must be close to unity. In the case of slight degeneracy, an increase in the density of states at the Fermi level with increasing temperature seems to play an essential role and is responsible for the weakening of temperature dependence in (12).

Unfortunately, we failed to obtain the dependences of n_R on the concentration of uncompensated donors in these samples since, at the present stage of research, we could not correctly take into account the simultaneous change in the skin depth and in the Q-factor of the resonator in the course of detection of the ESR signal in the samples with different levels of compensation. More precise measurements are needed to resolve this problem.

The samples with nondegenerate electron gas show dependence typical of Curie paramagnetism in a wide temperature range. However, it should be taken into account that the measured conductivity of insulator samples increases with temperature by at least an order of magnitude. This reduces both the skin depth and the Q-factor of the resonator. For this reason, the dependences for sample no. *5* in Fig. 8 can be considered only as a rough approximation illustrating the change in dependence in comparison with the samples with degenerate electron gas. For the confirmation of the occurrence of antiferromagnetism in Ge on the insulator side of the MI transition from the temperature variations of ESR parameters, further consideration of the above factors is needed.

3.4 Analysis of Position and the Type of ESR Spectrum

The metallic samples show very weak dependence of the position of the center of ESR line on temperature. Within the accuracy of our measurements of the g-factor, it remained independent of temperature and compensation and equal to the value of the g-factor of the electron bound with the donor center. Within this accuracy, the position of the line does not change both with the change in temperature and with compensation. Such behavior of the line correlates with the known results [2] for Si and Ge where it is shown that the g-factor for electrons bound with a shallow donor differs very slightly from that for the electrons in a conduction band.

However, in the two most heavily compensated samples which were already on the insulator side of the MI transition, at temperatures below 4 K we found quite a new effect: the splitting of a single line into two lines one of which is anomalously shaped and rapidly shifts to stronger fields with further decrease of temperature. These spectra for sample no. 5 are shown in Fig. 3. The temperature dependence of the distance between the main and the anomalous split-off line is clear from Fig. 3. This distance is proportional to the inverse temperature. The similar dependence is observed in the insulator sample no. 6. The only distinction between them is that the amplitude of the split-off line for sample no. 6 is substantially less than for sample no. 5. The position of the split-off line does not depend either on the compensation at the insulator part of the MI transition or on crystallographic direction. It is also of importance to emphasize the unusual shape of the split-off line. It has no wing with a negative derivative; i.e., an increase in microwave absorption with increasing field is described by a step function. Such behavior of the ESR spectrum and line shape have not yet been observed in any paramagnetic systems. This effect cannot be explained even qualitatively in the context of existing ESR models. The observed shape of split-off line may be attributed to the abrupt change of resistance. A similar effect is known to exist at the collapse of superconductivity [7]. Although the direction of the step shift corresponds to a similar shift in superconductors, we could not find any adequate model for the description of the steplike increase in resistance in the samples studied. In connection with this, we restrict our explanations of the effect henceforth to the context of ESR models.

Hypothetically, the possible reasons for the splitting and the shift of one of the lines to stronger fields can be considered by using the basic condition for ESR:

$$h\nu = g\mu_B H, \tag{13}$$

where ν is the frequency of the external alternating magnetic field. From (13) it follows that the shift of one of the lines can be related either to the temperature-variable internal magnetic field or to the temperature-dependent change in the alternating field acting on the resonant spin. Let us discuss the difficulties arising when each of the above reasons is used to explain the observed effect of line splitting.

1. It is conceivable that some macroscopic regions with internal magnetic field B determining the true value of the resonance magnetic field emerge in the sample with an increase in the level of compensation at low temperatures. In this case, the following relation must exist between the external and internal fields H and B:

$$B = \mu H, \tag{14}$$

where μ is permeability. For the line to be shifted to stronger fields, it is necessary that the internal field responsible for the resonance be less than the external field; i. e., the permeability should be appreciably less than unity. For T = 3.2 K, H = 5500 Oe and B = 4300 Oe. This means that the macroscopic regions with internal fields should be diamagnetic. First, their permeability must be of a magnitude much smaller than that observed in nature for nonsuperconducting materials, $\mu = B/H = 0.78$, and second, the permeability must decrease with lowering temperature.

2. The macroscopic diamagnetic regions are absent, but each spin experiences the action of the magnetic field generated by the neighboring spin and directed opposite to the external field. However, in this situation we should also observe the line from the spins subjected to the action of the field generated by the neighboring spin and directed along the external field. This line must be located at lower fields in comparison with the nonsplit line. As seen in Fig. 2 this line is absent. In addition, it is not clear how the field from the neighboring atom could increase with lowering temperature.

3. In order to make the mechanism described in item 2 closer to the experiment, one may suppose that simultaneously with an increase in the field from the neighboring spin, a decrease in the g-factor with lowering temperatures occurs. This does not eliminate the contradictions related to the appearance of the internal magnetic field; however, if this field exists and increases with decreasing temperature, then the conservation of the spectrum symmetry requires a decrease in the g-factor simultaneously with an increase in the internal field, so that the low-field line is not shifted and the high-field line is shifted to stronger fields. Since the g-factor is determined by the effective mass of carriers [27], the abrupt change in mobility should occur simultaneously with the shift of the g-factor. However, as seen in Fig. 1, no appreciable change in mobility for sample no. 5 is observed in this range of temperatures.

4. We can try to relate the line splitting at low temperatures to the interaction of the spin with the electric field of impurities. As shown above, the free spins in the samples with degenerate electron gas respond to the impurity electric field, which results in the change of the shape of Dyson's line with lowering temperatures and with an increase in the level of compensation. The reason is that the moving electron experiences the action of an additional alternative field of the frequency

$$\nu_1 = v_d/r_s, \tag{15}$$

where v_d is the electron diffusion speed and r_s is the transverse dimension of the fluctuation.

At the transition into insulator state, a forbidden band (of Coulomb or Hubbard type) comes in to existence in the sample. The electrons with energy higher than this forbidden band remain free. The rest of the electrons become bound. The free electron diffuse through the crystal experiencing the action of the impurity electric field of the frequency ν_1. As follows from the item 3.2 above, the moving electrons responds to smaller and smaller fluctuations as their energy or the

temperature decreases. Therefore, the frequency ν_1 must increase with decreasing temperature. In this case, the frequency of the field acting on free electrons is the sum of the frequencies ν of the external field and $\nu_1(T)$. The bound electrons do not move through the crystal and do not experience the action of the impurity electric field. Therefore, free electrons resonate in a stronger field in comparison with the bound electrons. The resonance is determined by the relation

$$h[\nu + \nu_1(T)] = g\mu_B[H + \Delta H(T)], \qquad (16)$$

where $\Delta H(T)$ is the difference between the resonance magnetic fields for shifted and nonshifted lines, which depends on temperature. Again, the difficulties emerge in explanation. First, the external alternating field is magnetic, whereas the impurity field is electric. The examples are known in the literature of the electric-field effects on the ESR line (see, for example, [28–30]). It is shown that at certain conditions the constant electric fields can split the ESR line, and the alternating electric fields excite the resonance transitions. The theory of such effects is given in [28, 29], and the most illustrative experiment is described in [30]. In our case, the spin is subjected simultaneously to the magnetic component of the external field and the electric component of the impurity field. What kind of effect results from this is not yet clear. Second, no adequate explanation can be found for the change in the effect of the electric field when we turn from the samples with degenerate electron gas to the samples with nondegenerate gas. It is not clear why in the former case the action of the impurity field changes the line shape, while in the latter case the line splitting occurs. Finally, it is not clear why the magnitude of the anomalous line does not decrease as the temperature lowers, although the ratio of free electron concentration to the concentration of localized electrons decreases. Thus, this new effect cannot be satisfactory explained at present.

Finally, let us discuss the unusual line shape of the anomalous line. As distinct from the fairly symmetric nonshifted line, the shifted line has only a positive part of the derivative. If the assumption about the origin of this line (as a result of the interaction of the moving electron with the potential profile of the conduction-band bottom) is correct, then such a shape of the derivative can be explained by the spread in energy of moving electrons. In fact, the moving electrons have the energy with the lowest value limited by the upper edge of the gap (of Coulomb or Hubbard type), and with unlimited value from the upper side; i. e., the electrons are distributed over the energies within the interval of kT. Let us compare these energies. As seen in Fig. 3, the distance between the normal and anomalous lines at $T = 3.2$ K is $\Delta E = 1215$ G $= 10^{-5}$ eV $\simeq 0.05kT$. The experimental half-width, which we attribute to free electrons, is $\Delta E_H = 150$ Oe $\simeq 0.005kT$. Thus, all observed splittings are much smaller than kT, and the line amplitude determined by the free electrons has to decrease very slowly in the scale of the ESR spectrum. Consequently, the derivative of this part must be very small in magnitude and should not reveal itself in experimental signals similar to the case of Dyson-like line shape where the low-field part of the absorption line does not reveal itself in the derivative [21, 22].

4. CONCLUSION

1. The ESR signal at the frequency of 10 GHz is observed in Ge:As in the temperature range up to 100 K on both sides of the metal—insulator transition induced by compensation

2. In the samples with the metal conductivity, the ESR spectrum in the entire temperature range (3–100 K) consists of a single Dyson-type line with parameters varying with temperature. In the samples on the insulator part of the transition, the Dyson-type shape of the single line with a decrease in temperature transforms into a Lorentz shape, then the line splits into two lines: a normal and anomalous one.

3. Two mechanisms of spin-lattice relaxation in Ge:As can be distinguished depending on the compensation degree and the temperature: the relaxation at the donor–acceptor pairs (the case of compensated samples and low temperatures) and at phonons (high temperatures).

4. The change of parameters for the Dyson-type line shape with temperature in the compensated samples on the metal side of the transition can be accounted for by considering that free electrons at motion at low temperatures interact with fluctuations in the potential profile of the conduction-band bottom governed by the charged impurities (donors and acceptors).

5. The Pauli paramagnetism manifests itself in the samples of Ge on the metal side of the transition at temperatures below 50 K.

6. The Curie paramagnetism manifests itself in the samples of Ge on the insulator side of the transition in the range of temperatures from 4.1 to 50 K.

7. On the insulator part of the metal-insulator transition at the temperatures $3.2 \lesssim T \lesssim 4.1$ corresponding to the hopping conductivity with variable hop length over the Coulomb gap states, a new effect has been observed: the splitting of the ESR line into a normal line (of conventional shape in a fixed magnetic field) and anomalous line (with a step-like shape in the field increasing proportional to inverse temperature). No satisfactory explanation for this effect has been found at present.

ACKNOWLEDGMENTS

The authors thank A. Finkelstein from Weizmann Institute (Israel) and the participants of the Seminars of the Laboratory of Nonequilibrium Processes in Semiconductors and of the Sector of Physical Kinetics of Ioffe Physicotechnical Institute for helpful discussion.

This study was supported by the Russian Foundation for Basic Research, project no.98-02-17353.

REFERENCES

1. N. F. Mott, *Metal-Insulator Transitions* (Tailor & Francis, London, 1974; Nauka, Moscow, 1979).
2. G. Feher, Phys. Rev. **114**, 1219 (1959).
3. D. K. Wilson, Phys. Rev. A: Gen. Phys. **134**, 265 (1964).
4. A. I. Veĭnger, Fiz. Tekh. Poluprovodn. (Leningrad) **1**, 20 (1967).
5. B. G. Zhurkin and N. A. Penin, Fiz. Tverd. Tela (Leningrad) **6**, 1143 (1964).
6. S. Maekawa and N. Kinoshita, J. Phys. Soc. Jpn. **20**, 1447 (1965).
7. H. Ue and S. Maekawa, Phys. Rev. B: Condens. Matter **3**, 4232 (1971).
8. K. Morigaki and S. Maekawa, J. Phys. Soc. Jpn. **32**, 462 (1972).
9. M. V. Alekseenko, A. I. Veĭgner, A. G. Zabrodskiĭ, *et al.*, Pis'ma Zh. Éksp. Teor. Fiz. **39**, 255 (1984).
10. A. G. Zabrodskiĭ, M. V. Alekseenko, V. A. Il'in, *et al.*, in *Proceeding 16th International Conference on Physics of Semiconductors* (Stockholm, Sweden, 1986), p. 283.
11. J. D. Quirt and J. R. Marko, Phys. Rev. B: Condens. Matter **7**, 3842 (1973).
12. M. A. Paalanen, S. Sachdev, and R. N. Bhatt, in *Proceedings 16th International Conference on Physics of Semiconductors*, Stockholm, Sweden (1986), p. 1249.
13. K. Morigaki and T. Mitsushima, J. Phys. Soc. Jpn. **20**, 62 (1965).
14. K. Morigaki and M. Onda, J. Phys. Soc. Jpn. **33**, 103 (1972).
15. D. P. Tungstall, P. J. Mason, A. N. Ionov, *et al.*, J. Phys.: Condens Matter **9**, 403 (1997).
16. A. I. Veĭgner, A. G. Zabrodskiĭ, and T. B. Tisnek. In *Abstacts of 31st Meeting on Low-Temperature Physics* (Moscow, Russia, 1998), p. 48.
17. A. S. Kheifets and A. I. Veĭnger, Physica C (Amsterdam) **165**, 491 (1990).
18. S. I. Goloshchapov, A. I. Veĭnger, and S. G. Konnikov, Prib. Tekh. Éksp., No. 3, 232 (1993).
19. A. G. Zabrodskiĭ and K. H. Zinov'eva, Zh. Éksp. Teor. Fiz. **86**, 727 (1984).
20. A. G. Zabrodskiĭ, Fiz. Tekh. Poluprovodn. (Leningrad) **14**, 1130 (1980).
21. F. J. Dyson, Phys. Rev. **98**, 349 (1955).
22. G. Feher and A. F. Kip, Phys. Rev. **98**, 337 (1955).
23. G. Feher and E. A. Gere, Phys. Rev. **114**, 1245 (1959).
24. A. Honig and E. Stapp, Phys. Rev **117**, 69 (1960).
25. L. D. Landau and E. M. Lifshits, *Theoretical Physics, Mechanics* [in Russian] (Nauka, Moscow, 1979).
26. B. I. Shklovskiĭ and A. L. Éfros, *Electronic Properties of Doped Semiconductors* [in Russian] (Nauka, Moscow, 1979).
27. L. M. Roth, Phys. Rev. **114**, 1534 (1960).
28. *Electric Effects in Radiospectroscopy: Electron Spin Resonance, and Double Electron-Nuclear and Paraelectric Resonances*, Ed. by M. F. Deĭgen (Nauka, Moscow, 1981).
29. A. B. Roĭtsin, Fiz. Tverd. Tela (Leningrad) **5**, 151 (1961).
30. M. D. Sturge, F. R. Merrit, J. C. Hensel, *et al.*, Phys. Rev. **180**, 402 (1969).

Translated by A. Zalesskii

Semiconductors, Vol. 34, No. 1, 2000, pp. 56–60. Translated from Fizika i Tekhnika Poluprovodnikov, Vol. 34, No. 1, 2000, pp. 57–61.

SEMICONDUCTORS STRUCTURES, INTERFACES, AND SURFACES

Ellipsometric Study of Ultrathin $Al_xGa_{1-x}As$ Layers

M. V. Sukhorukova*, I. A. Skorokhodova*, and V. P. Khvostikov**

** St. Petersburg State Institute of Precise Mechanics and Optics (Technical University), St. Petersburg, 197101 Russia*
*** Ioffe Physicotechnical Institute, Russian Academy of Sciences, St. Petersburg, 194021 Russia*
E-mail: ms@mail.wplus.net

Submitted April 8, 1999; accepted for publication April 20, 1999

Abstract—A method for rapid monitoring of the parameters of thin-layer semiconductor structures by ellipsometry is proposed. The results of ellipsometric analysis of the material thickness and composition distribution in $Al_xGa_{1-x}As$ films grown by low- temperature liquid-phase epitaxy (LPE) are presented. The ellipsometric data are compared to those obtained by the Raman scattering spectroscopy. © *2000 MAIK "Nauka/Interperiodica".*

Using heterostructures composed of ultrathin (50–500 Å) layers, it is possible to improve the main characteristics of various semiconductor devices including lasers, photodetectors, transistors, etc. An important task encountered in the process of creation and perfection of technologies for the growth of such heterostructures consists in the corresponding development of methods for monitoring properties of the growing crystalline layers. An effective technique for the analysis of various thin-layer structures can be based on ellipsometry [1], a highly sensitive optical method ensuring nondestructive testing of samples.

Below we describe a rapid ellipsometric procedure for studying the features of growth in quantum-sized AlGaAs films, which provides illustrative diagrams of distribution of the film parameters (thickness and composition of the AlGaAs solid solution) over the sample area.

EXPERIMENTAL

Ellipsometric measurements were performed using light with a wavelength of $\lambda = 632.8$ nm incident at an angle of $\varphi = 70°$. The measurements were carried out with a Rudolf Research Auto EL-III automated ellipsometer and an automated Stokes ellipsometer designed and constructed at the Institute of Precise Mechanics and Optics on the basis of a serial manual ellipsometer of the LEF-3M-1 type. The incidence angle ($\varphi = 70°$) was selected slightly below the Brewster's angle ($\varphi < \varphi_B$) for $Al_xGa_{1-x}As$ in order to provide for a high sensitivity of measurements [2].

The film samples were grown by low-temperature LPE technique (at T_g = 580–620°C) on (100)-oriented GaAs substrates ($n \sim 10^{18}$ cm^{-3}) with dimensions 20×32 mm^2. The sample structures comprised *n*-GaAs underlayers and $Al_xGa_{1-x}As$ films of various compositions ($x > 0.7$) and thicknesses (d_x = 250–750 Å). The *n*-GaAs film with a thickness of $d \simeq 5$–7 μm was grown on the GaAs(Sn) substrate and served as a buffer layer for the subsequent deposition of an $Al_xGa_{1-x}As$ solid solution. The growth time τ of the AlGaAs layers was varied within 0.5–60 s. The sample structures were grown using a cassette sample holder of the piston type. Since the *n*-GaAs layer thickness was markedly greater than the penetration depth of UV and visible light, this layer can be considered as a semiinfinite substrate for the probing radiation with $\lambda = 632.8$ nm.

With the LPE technology employed, there appears a transition layer featuring composition gradient

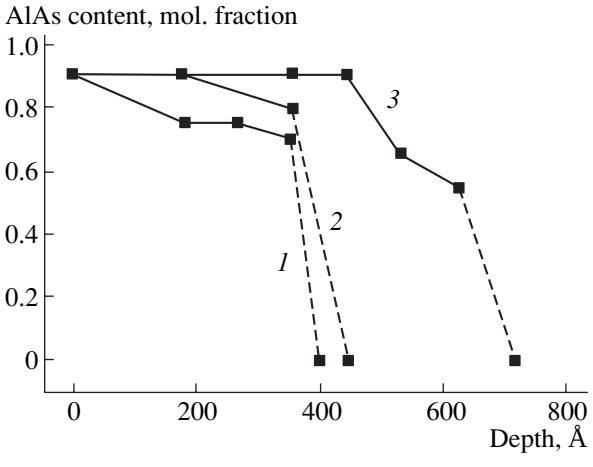

Fig. 1. Profiles of AlAs concentration distribution in depth of an $Al_xGa_{1-x}As$ heterostructure plotted by the Raman spectroscopy data: (*1*) sample 5 (solid solution crystallization time τ = 60 s); (*2*) sample 2 (τ = 2 s); (*3*) sample 6 (τ = 4 s). Here, τ is the crystallization time for solid solution.

1063-7826/00/3401-0056$20.00 © 2000 MAIK "Nauka/Interperiodica"

between the GaAs and $Al_xGa_{1-x}As$ layers. This is confirmed by profiles of the AlAs concentration distribution in depth of the heterostructures presented in Fig. 1. The method of depth–concentration profile determination consisted in conducting the Raman spectroscopic measurements in the course of layer-by-layer etching of a sample [3]. The high-precision thinning of the sample structures was performed by the method of anodic oxidation, whereby the uppermost surface layer of the heterostructure is converted into oxide. The oxide layer has a thickness proportional to the applied anodic voltage and can be removed by chemical etching. After every sequential removal of an AlGaAs layer (50–100 Å at each step), the Raman spectrum was registered and analyzed to determine the solid solution composition. The Raman spectra were measured with a DFS-52 automated spectrometer using an Ar laser excitation source (2.41 eV).

ELLIPSOMETRIC MODEL

The AlGaAs structures with sufficiently high Al content, occurring in contact with real atmosphere, are subject to rapid uncontrolled oxidation of the surface layer. Therefore, in modeling these systems it is necessary to take into account the natural oxide formation. The natural oxide film on a AlGaAs surface comprises a mixture of Al_2O_3, As_2O_3, and Ga_2O_3. The optical properties of this system are insufficiently studied. For this reason, it is a usual practice to restrict the consideration to Al_2O_3 and describe the transition from AlGaAs to environment by a four-phase model of the type "AlGaAs–mixed layer (AlGaAs + Al_2O_3)–Al_2O_3–ambient medium" [4]. Our investigation was performed within the framework of a model with sharp transitions, because the thickness and composition of AlGaAs films are analyzed primarily with the purpose of studying variations (gradients) of these parameters in the lateral direction. Indeed, a necessary condition for the fabrication of related devices with perfect characteristics is the constancy and homogeneity of their parameters in the plain of heterostructures. The values of thicknesses and chemical compositions determined within the framework of a model with sharp transitions between layers agree with the values expected for the film growth technology employed.

Thus, within the framework of our problem, the GaAs–$Al_xGa_{1-x}As$ structures can be quite adequately described using a two-layer model of the epitaxial solid solution in a system of the type "substrate–solid solution layer–natural oxide layer-ambient medium" with sharp interfaces, the possible transition layers on the outermost and inner (substrate) surfaces being ignored (Fig. 2). For the model justified above, a functional dependence of the ellipsometric angles Ψ and Δ on the

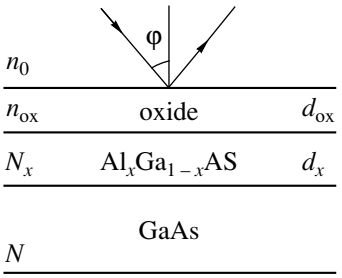

Fig. 2. Schematic diagram of a model structure "GaAs substrate– $Al_xGa_{1-x}As$ solid solution layer–oxide layer–ambient medium."

experimental conditions (λ, φ) and the system parameters can be described by an equation of the type

$$\tan\Psi \exp(i\Delta) \equiv \rho(N_0, N_{ox}, N_x, N, d_{ox}, d_x, \lambda, \varphi). \quad (1)$$

In the general case, assuming the refractive index of the medium n_0 to be known, this expression contains seven unknown quantities: index of refraction n_{ox}, oxide thickness d_{ox}, complex index of refraction of the solid solution $N_x = n_x - ik_x$, solid solution layer thickness d_x, and complex index of refraction of the substrate $N = n - ik$.

In solving the task of monitoring the solid solution layer parameters, it was necessary to select an initial approximation for the unknown parameters based on the analysis of data reported in the literature. The presently available experimental data on the complex indices of refraction for GaAs and $Al_xGa_{1-x}As$ with various compositions exhibit a considerable scatter [4–8]. This variance is apparently related to errors in modeling the surface of objects, rather than to some features of the compositions studied. The main difficulty consists in making a correct allowance for the natural oxide. In this context, the results reported in [4], where the n and k values for GaAs and the n_x and k_x values for various $Al_xGa_{1-x}As$ systems were studied in a broad spectral range using samples prepared on thoroughly cleaned surfaces, seem to be most reliable. The values $n = 3.856$ and $k = 0.198$ reported for GaAs $\lambda = 632.8$ nm were used in our calculations.

Our special attention in this work was paid to characterization of the natural oxide, because uncertainty in the parameters of this layer leads to considerable errors in parameters of the underlying layer. Preliminary measurements and calculations, performed in order to evaluate the natural oxide parameters for the technology employed, showed that the natural oxide thickness falls within $d_{ox} = 5$–60 Å. The results of calculations indicated that, in this range of oxide thicknesses, variation of the oxide index of refraction within 1.6–2.2 does not significantly affect the dependence of ellipsometric angles on the layer parameters. Therefore, no greater

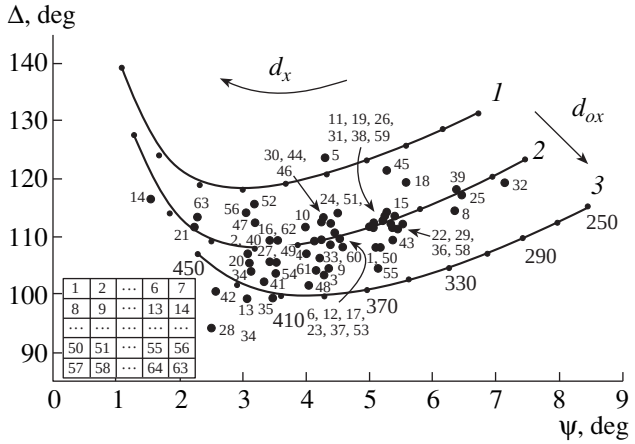

Fig. 3. Ψ–Δ nomogram relating the ellipsometric angles Ψ and Δ to the oxide thickness d_{ox} and AlGaAs layer thickness d_x (φ = 70°). Solid curves were calculated within the framework of a two-layer model for the AlGaAs index of refraction $N_x = 3.321 - i0.0$ ($x = 0.73$); $n_{ox} = 1.8$; $d_{ox} = 5$ (*1*), 30 (*2*), 60 Å (*3*); marks correspond to $d_x = 250$–450 Å. Symbols represent the experimental data for sample 5 (τ = 60 s), the numbers corresponding to the sites of measurement on the sample surface (according to the scheme on inset).

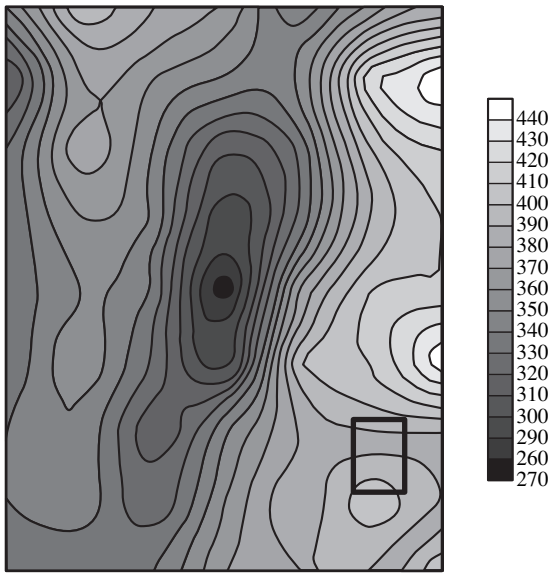

Fig. 4. A map showing variation of the thickness (in Å) of a layer of solid solution AlGaAs over the surface of sample 5 (τ = 60 s). Frame indicates the region analyzed by Raman spectroscopy.

precision in determining n_{ox} was required and we took $n_{ox} = 1.8$.

Using the two-layer model and the initial approximation selected, we have calculated nomograms in the Ψ–Δ plane (direct ellipsometric problem) and plotted the experimentally determined values of Ψ and Δ. An

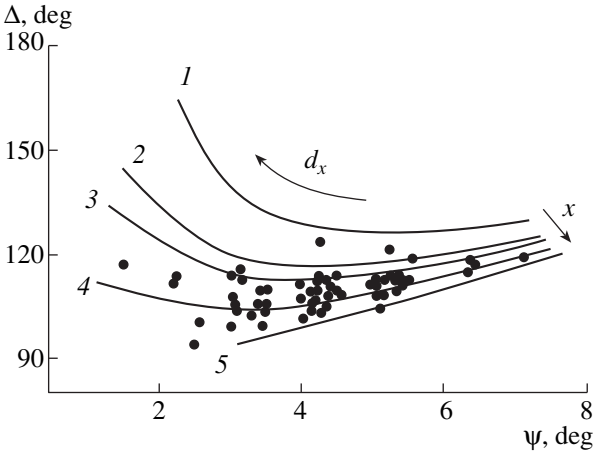

Fig. 5. Ψ–Δ nomogram relating the ellipsometric angles Ψ and Δ to the thickness d_x and composition x of the $Al_xGa_{1-x}As$ layer (φ = 70°); $x = 0.65$ (*1*), 0.70 (*2*), 0.72 (*3*), 0.75 (*4*), 0.78 (*5*). Solid curves were calculated within the framework of a two-layer model; symbols represent the experimental data for sample 5 (τ = 60 s).

analysis of coincidence between the experimental points and calculated Ψ–Δ nomograms allows one to make conclusions concerning correctness of the model and the initial approximation selected.

Thus, the task of monitoring the two-layer model parameters can be reduced to a rapid procedure based on the analysis of Ψ–Δ nomograms relating two system parameters [(d_{ox}, d_x) for monitoring of the solid solution layer thickness d_x, or (x, d_x) for monitoring of the composition homogeneity (i.e., x for the other parameters fixed)] to the ellipsometric angles Ψ and Δ:

$$\tan\Psi \exp(i\Delta) \sim f(d_x, d_{ox}), \quad x = \text{const}, \tag{2}$$

$$\tan\Psi \exp(i\Delta) \sim f(x, d_x), \quad d_{ox} = \text{const}. \tag{3}$$

Since we are interested in the planar properties, that is, in relative variations of the layer thickness and composition in the lateral direction, this sequential fixation of one of the system parameters is quite permissible. Taking into account the results of preliminary investigations using this method for a series of samples differing by the growth time τ, we have studied the thicknesses and compositions of the surface layers of $Al_xGa_{1-x}As$. The experimentally measured ellipsometric angles Ψ and Δ determined at various points on the sample surface were plotted on the nomogram relating the Ψ and Δ values to the thickness d_x and composition x of the solid solution $Al_xGa_{1-x}As$ calculated within the framework of the above two- layer model system confined between a semiinfinite substrate and ambient medium.

Table 1. Parameters of $Al_xGa_{1-x}As$ layers

Sample No.	Growth time τ, s	AlAs content, x	Layer thickness d_x, Å
1	0.5	0.87 ± 4.6%	360 ± 80
2	2.0	0.8	520 ± 120
3	1.0	0.75	590 ± 160
4	60.0	0.80 ± 12.5%	350 ± 50
5	60.0	0.73 ± 6.8%	360 ± 90
6	4.0	0.7	540 ± 160
7	1.0	0.7	520 ± 100
8	60.0	0.7	550 ± 150
9	1.0	0.77	590 ± 130

Table 2. Parameters of $Al_xGa_{1-x}As$ layers (comparison of data obtained by ellipsometry and Raman spectroscopy)

Sample No.	Growth time τ, s	AlAs content, x		Layer thickness d_x, Å	
		Ellipsometry	Raman spectroscopy	Ellipsometry	Raman spectroscopy
2	2.0	0.8	0.8–0.9	380–470	360–450
3	1.0	0.75	0.75–0.9	450–650	540–630
4	60.0	0.78	0.75–0.9	360–390	360–405
6	4.0	0.7	0.55–0.9	630–700	630–720
9	1.0	0.77	0.5–0.9	460	360–540

RESULTS AND DISCUSSION

Figure 3 shows a nomogram calculated for determination of the thickness of a layer of $Al_xGa_{1-x}As$ solid solution, where the variable parameters are the oxide thickness d_{ox} and the $Al_xGa_{1-x}As$ layer thickness d_x. The points in this figure represent the pairs Ψ and Δ experimentally measured for sample 5 (τ = 60 s), and the point numbers correspond to a diagram indicating of their mutual arrangement over the sample surface. The scatter of experimental points along the directions selected for monitoring of the sample thickness variation allows one to judge on the degree of planarity (nonplanarity) of the $Al_xGa_{1-x}As$ layer. In particular, an analysis of the data presented in Fig. 3 reveals the pattern of variation of the solid solution layer thickness in two mutually perpendicular directions, which is depicted in Fig. 4. For the given sample, the scatter of the solid solution layer thickness d_x over the surface was ±80 Å at an average thickness of 420 Å.

Figure 5 shows a calculated Ψ–Δ nomogram for determination of the composition distribution over the same sample, where the variable parameters are the $Al_xGa_{1-x}As$ layer thickness d_x and the AlAs content x. An analysis of this nomogram indicates that inhomogeneity of the composition amounts to ±6.8% at an average value of x = 0.73 (Fig. 6).

The results of investigation of a series of $Al_xGa_{1-x}As$ samples using the proposed rapid procedure are summarized in Table 1. In order to verify correctness of the results provided by this method, the d_x and x parameters of some samples were checked by the Raman spectroscopy technique in the course of a stepwise anodic oxidation process described above. The Raman spectra were measured only on a separate region of the sample surface (indicated by a frame in Figs. 4 and 6). As seen, the results of investigation of the same heterostructure by two methods, based on ellipsometry and Raman spectroscopy, are in good agreement. For sample 5, the values of parameters determined from experimental ellipsometric data are d_x = 370–410 Å, x = 0.78 (Figs. 4 and 6) while the Raman spectroscopy gives d_x = 360–405 Å, x = 0.75–0.9 (Fig. 1, curve *1*).

Table 2 presents a comparison of data obtained for a series of $Al_xGa_{1-x}As$ samples by the methods of ellipsometry and Raman spectroscopy.

Thus, a rapid method proposed for monitoring of the parameters of epitaxially grown layers is convenient for the LPE growth and some other technologies used for the fabrication of analogous structures. The advantages of ellipsometry are manifested both in high sensitivity

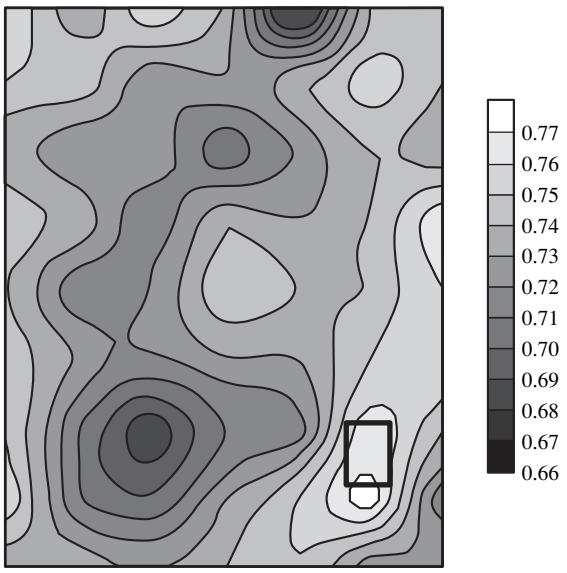

Fig. 6. A map showing variation of the AlAs content x in a solid solution $Al_xGa_{1-x}As$ over the surface of sample 5 (τ = 60 s). Frame indicates the region analyzed by Raman spectroscopy.

with respect to small sample thickness variations and in a small time required for the monitoring.

REFERENCES

1. P. Azzam and N. Bashara, *Polarized Light* (North-Holland, Amsterdam, 1977; Mir, Moscow, 1981).
2. G. B. Porus, G. F. Lymar', and R. R. Rezvyĭ, Elektron. Tekhn., Ser. 2. Poluprovodn. Prib., No. 6(203), 27 (1989).
3. V. M. Andreev, V. R. Larionov, A. M. Mintairov, T. A. Prutskikh, V. D. Rumyantsev, K. E. Smekalin, and V. P. Khvostikov, Pis'ma Zh. Éksp. Teor. Fiz. **16** (9), 7 (1990).
4. D. E. Aspnes and S. M. Kelso, J. Appl. Phys. **60**, 754 (1986).
5. H. Burkhard, H. W. Dinges, and E. Kuphal, J. Appl. Phys. **53**, 655 (1982).
6. V. I. Gavrilenko, A. M. Grekhov, and D. V. Kobulyak, *Optical Properties of Semiconductors. A Handbook* [in Russian] (Naukova Dumka, Kiev, 1987).
7. A. V. Lyashenko, F. I. Gromov, and Yu. F. Tarantov, Opt. Spektrosk. **53**,1035 (1982).
8. N. L. Dmitruk and V. N. Antonyuk, Poverkhnost: Fiz. Khim. Mekh., No. 12, **49** (1985).

Translated by P. Pozdeev

Semiconductors, Vol. 34, No. 1, 2000, pp. 6–10. Translated from Fizika i Tekhnika Poluprovodnikov, Vol. 34, No. 1, 2000, pp. 8–12.

ATOMIC STRUCTURE AND NONELECTRONIC PROPERTIES OF SEMICONDUCTORS

Elastic Strain and Composition of Self-Assembled GeSi Nanoislands on Si(001)

N. V. Vostokov*, S. A. Gusev*, I. V. Dolgov*, Yu. N. Drozdov*, Z. F. Krasil'nik*, D. N. Lobanov*, L. D. Moldavskaya*, A. V. Novikov*, V. V. Postnikov*, and D. O. Filatov**

** Institute of the Physics of Microstructures, Russian Academy of Sciences, Nizhniĭ Novgorod, 603600 Russia*
*** Regional Center of Scanning-Probe Microscopy, Nizhegorodsk State University, Nizhniĭ Novgorod, 603600 Russia*
E-mail: mmold@ipm.sci-nnov.ru

Submitted June 17, 1999; accepted for publication August 18, 1999

Abstract—The growth of self-assembled Ge islands on Si(001) surface and changes in the island structure parameters in the course of subsequent annealing were studied. Island structures possessing a small (~6%) scatter with respect to lateral dimensions and heights of the islands were obtained. The Raman spectra and X-ray diffraction data show evidence that silicon dissolves in the islands. The atomic fraction of Si in the resulting Si_xGe_{1-x} solid solution was determined and the elastic strain in the islands was measured. It was found that annealing of the heterostructures with islands is accompanied by increasing Si fraction in the islands, which leads to changes in the island shape and size. © *2000 MAIK "Nauka/Interperiodica".*

INTRODUCTION

GeSi-based heterostructures with self-organized (self-assembled) nanoislands and quantum dots are promising systems for the optoelectronic applications of Si-based technologies. At present, despite a large number of works devoted to the investigation of GeSi island structures, there are still many questions concerning the growth mechanism and composition of islands, as well as the elastic strains developed in these islands. A considerable interest in the study of self-organization (self-assembly) processes on the growth surface in elastically strained heterosystems is related to the possibility of obtaining nanoobjects using methods obviating considerable difficulties encountered in the lithography of very small objects.

Below we present the results of investigation of the growth of self-assembled Ge nanoislands on Si(001) at 700°C and a change in their parameters during subsequent annealing, studied by the atomic-force microscopy (AFM) and electron microscopy techniques. The growth conditions providing for the formation of island structures possessing a small scatter with respect to lateral dimensions and heights of the islands were established. The elastic strains and compositions of the islands were determined from the results of X-ray diffraction and Raman scattering measurements. We have also studied effects of the subsequent annealing on the composition, shape, and dimensions of the islands.

EXPERIMENTAL

The sample structures were grown on Si(001) substrates by the method of molecular-beam epitaxy (MBE) at 700°C using a Balzers MBE system. Silicon and germanium beams were generated using electron-beam evaporators. The deposition rates were 0.16 and 0.015 nm/s for Si and Ge, respectively. The substrates were cleaned from oxide by heating to 800°C in a weak flow of silicon atoms. After cleaning, the substrates were coated with a buffer Si film with a thickness of approximately 2000 Å. A layer of germanium with an equivalent thickness (d_{Ge}) from 1 to 11 monoatomic layers (ML = 1.4 Å) was deposited above the buffer film. Some structures upon the Ge layer deposition were annealed at a temperature equal to the growth temperature. The structures were studied by microprobe techniques using the Solver P4 and Topometrix TMX-2100 atomic-force microscopes. The AFM measurements were performed in air using both contact and contactless modes. The electron-microscopic measurements were performed in the secondary-electron imaging mode on a Jeol JEM-2000EX microscope. The Raman scattering spectra and X-ray diffraction patterns were obtained at room temperature using the DFS-52 spectrometer and DRON-4 diffractometer, respectively.

RESULTS AND DISCUSSION

1. Growth of Self-Assembled Islands

According to the AFM data, the formation of Ge islands under the growth conditions studied in this work begins when the Ge layer thickness exceeds 4 ML. The island growth begins with the formation of pyramidal hut clusters with {105} type facets [1]. The base edges of the pyramidal clusters are oriented along [100] and [010] directions. When the equivalent germanium layer thickness increases to $d_{Ge} \geq 5.5$ ML, dome-shaped islands possessing no clearly pronounced faceting but having definite lateral dimensions appear in

1063-7826/00/3401-0006$20.00 © 2000 MAIK "Nauka/Interperiodica"

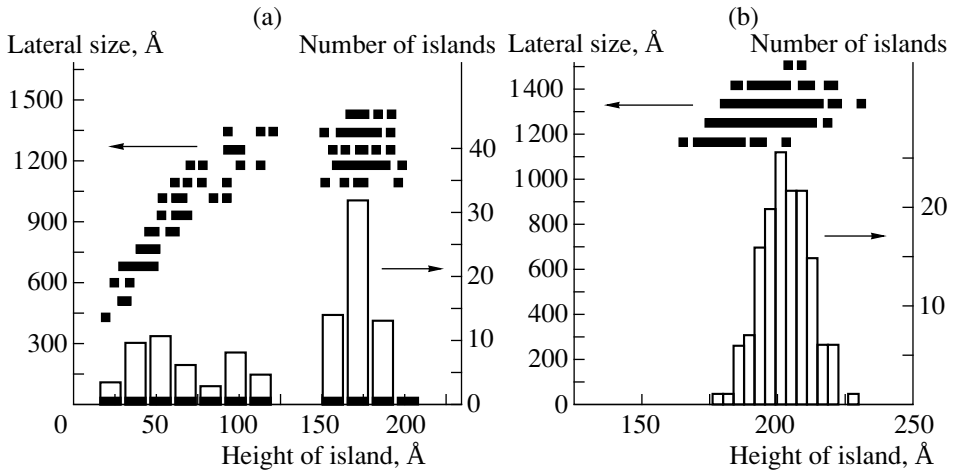

Fig. 1. The plots of lateral island size D versus island height H and histograms of the island height distribution constructed using the results of processing of the AFM images of an island heterostructure with d_{Ge} = 5.5 ML (a) and 11 ML (b).

addition to the pyramidal clusters. The results of *in situ* scanning tunneling microscopy investigation [2] showed that the dome-shaped islands have faces of the {113}, {102}, and {105} types.

A relationship between the lateral size D and the height H of the islands and a histogram of the island height distribution for a sample with d_{Ge} = 5.5 ML (Fig. 1a) clearly demonstrate a bimodal character of the island size distribution previously reported in some works [2–4]. A linear portion of the $D(H)$ plot reflects the growth of pyramidal clusters, whereby both the lateral size and height of the islands exhibit a proportional increase while the island shape remains unchanged. The subsequent horizontal portion is related to the growth of dome-shaped islands, in which the base remains unchanged while the height gradually increases. Using the $D(H)$ plot for the sample with d_{Ge} = 5.5 ML, we may estimate the maximum (critical) lateral size (D_c) and height (H_c) of the pyramidal cluster. According to Ross *et al.* [4], the maximum size of the pyramidal clusters corresponds to the critical volume V_c at which the pyramidal clusters begin to transform into dome-shaped islands. This transformation is energetically favorable, since the energy of a dome-shaped island with $V > V_c$ is smaller than that of a pyramidal cluster with the same volume [4].

As the effective amount of deposited Ge increases from 5.5 to 11 ML, the surface density of islands increases 1.5–2 times and all pyramidal clusters gradually convert into the dome-shaped islands. Since the size of the dome-shaped islands in the growth plane is fixed, their scatter with respect to lateral dimensions becomes small (standard deviation below 10%) on reaching d_{Ge} = 8 ML, while the scatter with respect to height is initially still significant (standard deviation 15–20%). Further increase in the amount of deposited Ge markedly reduces the scatter of islands with respect to height as well. For d_{Ge} = 11 ML, the islands exhibit equal standard deviations (~6%) with respect to both height and lateral size (Fig. 1b). Such a narrow distribution can be related either to the presence of a local minimum in the surface energy of the dome-shaped islands or to the existence of an energy barrier for the nucleation of dislocations in the island. It must be noted that finite dimensions and a special shape of the atomic-force microscope point hinder exact determination of the lateral size of islands. Electron-microscopic observations showed the lateral size of the islands for d_{Ge} = 11 ML to be 20–30 nm smaller as compared to the estimates provided by AFM.

2. Elastic Strain and Composition of Nanoislands

Due to the highly homogeneous distribution of island dimensions in the sample with d_{Ge} = 11 ML, it was possible to determine the content of Ge(x) in these islands and to measure elastic strains (ε) developed in their structures, using the data of Raman scattering and X-ray diffraction measurements. Figure 2a shows X-ray diffractograms measured in the $\theta/2\theta$ scan mode for the initial Si(001) substrate (curve *3*) and a sample with d_{Ge} = 11 ML (curve *1*). A signal observed in the region of 66°–67° in the diffractogram of the Ge-coated sample was attributed to the diffraction from nanoislands. It should be noted that this signal, irrespective of the ε value, does not fall within the region of scattering from a layer containing 100% Ge (Fig. 2a). This fact suggests that Si dissolves in the islands. The x and ε variables cannot be separated using one-dimensional single-reflection X-ray diffraction patterns measured in the $\theta/2\theta$ scan mode. In order to estimate the particular x and ε values, we have constructed two-dimensional reciprocal lattice cross-sections in the region of two X-ray diffraction peaks: (004) and (224). The content of Ge and the elastic strains in the islands determined

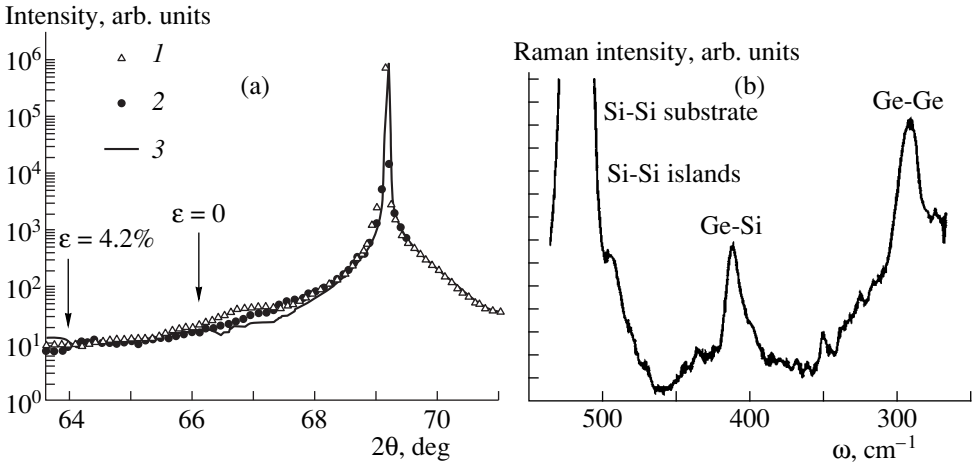

Fig. 2. Experimental data on the strain and composition of island heterostructures: (a) X-ray diffraction patterns (θ/2θ scan mode) from Ge islands in the region of (004) reflection for (*1*) a sample with d_{Ge} = 11 ML without silicon overlayer, (*2*) the same sample with Si overlayer, and (*3*) a clean substrate (arrows indicate peak positions for the strained (ε = 4.2%) and strain-relaxed (ε = 0) layer of pure Ge; (b) Raman spectrum of a sample with d_{Ge} = 11 ML.

from the two-dimensional reciprocal lattice cross-sections using the elastically strained layer approximation were $x = 0.5 \pm 0.05$ and $\varepsilon = (-0.7 \pm 0.05)\%$.

The elastic strains and compositions of the islands can be also determined using the Raman scattering spectrum of the sample with d_{Ge} = 11 ML (Fig. 2b). This spectrum contains, besides an intense signal from Si substrate (at $\omega = 520.5$ cm^{-1}) three lines related to the vibrational modes Ge–Ge (ω_{GeGe} = 294 cm^{-1}), Ge–Si (ω_{GeSi} = 412 cm^{-1}), and Si–Si (ω_{SiSi} = 495 cm^{-1}) for atoms in the islands [5]. Using these three peaks, we constructed the corresponding linear relationships of the $\varepsilon(x)$ type [6]:

$$\begin{aligned} \omega_{SiSi} &= 520.5 - 62x - 815\varepsilon, \\ \omega_{GeSi} &= 400.5 + 14.2x - 575\varepsilon, \\ \omega_{GeGe} &= 282.5 + 16x - 385\varepsilon. \end{aligned} \qquad (1)$$

The point of intersection for any pair of these straight lines gives the particular ε and x values. The contents of germanium and elastic strains determined by this method coincide to within the experimental error with the values obtained from the X-ray diffractograms.

Analysis of the X-ray diffraction and Raman scattering data showed that the self-assembled islands formed in the samples with d_{Ge} = 11 ML under the growth conditions studied represent weakly strained $Si_{0.5}Ge_{0.5}$ alloy. A large content of silicon in the islands can hardly be explained by the bulk diffusion of Si atoms, the more so that the samples exhibited no uppermost silicon layer. A possible mechanism of the alloy formation is the surface diffusion of Si from a region near the island base. As is known, the region of maximum strain occurs in the island base [7]. The elastic strain field existing in the base induces a flow of atoms outgoing from this region [8].

We suggest that the island growth leads to accumulation of the elastic strain in the island base, which is accompanied by gradual decrease in the thickness of a contact layer of Ge atoms in this region. At a certain size of the island, the contact Ge layer in the base disappears to expose the surface of the silicon substrate. Beginning with this moment, a silicon solution in the island begins to form by the surface diffusion of Si atoms from the island base region. The proposed mechanism of alloy formation in the islands is confirmed by the presence of small dips having the shape of grooves at the base of dome-shaped islands observed in the AFM images. The depth of these grooves reaches 0.8–1.5 nm, which is greater than the contact layer thickness. Note that the groove formation is not caused by interaction of the atomic force microscope point with the island, as confirmed by AFM observations of the structures upon annealing (see below).

It must be noted that overgrowth of the GeSi islands leads to further decrease in the atomic fraction of Ge in the islands as a result of mutual diffusion and segregation processes [9]. This is confirmed by X-ray diffractograms of the samples with d_{Ge} = 11 ML, showing the presence of an uppermost silicon layer (Fig. 2a, curve *2*). As seen, the presence of the Si overlayer results in smearing of the diffraction peak from the island and shifts this signal toward smaller x values (provided ε is unchanged).

3. Evolution of the Parameters of Islands in the Course of Annealing

Annealing of the heterostructures with nanoislands at 700°C was accompanied by significant changes in

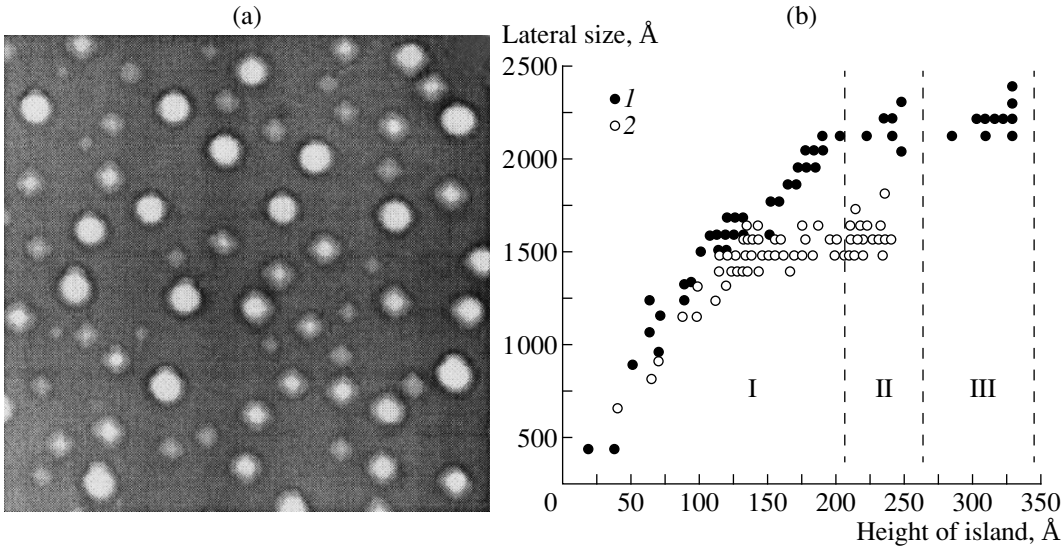

Fig. 3. AFM data: (a) image of a 2.5×2.5 μm^2 area of a heterostructure with d_{Ge} = 7.5 ML upon a 10-min annealing; (b) $D(H)$ plot for (*1*) annealed and (*2*) unannealed samples with d_{Ge} = 7.5 ML.

the shape, size, and surface density of islands. Figure 3a shows a typical AFM image of a sample with d_{Ge} = 7.5 ML upon annealing. Figure 3b presents the plots of lateral size versus height of islands on the sample with d_{Ge} = 7.5 ML before and after annealing. Both the AFM image and the $D(H)$ plot show that annealing leads to the appearance of pyramidal clusters with dimensions greater than the critical D_c and H_c values. In addition, there appear large islands (D = 220–250 nm, H = 30–35 nm) having no clearly pronounced faceting, while the total surface density of islands decreases by a factor of 1.5–2.

The $D(H)$ plot for the annealed sample can be conventionally divided into three regions (Fig. 3b). Region I, where D is a linear function of H, is related to the growth of pyramidal clusters. We believe that the appearance of pyramidal clusters with the height $H > H_c$ is due to continuation of the silicon diffusion into islands in the course of annealing [10]. According to the X-ray diffraction data, the atomic fraction of Si in the islands upon a 10-min annealing increased from 50 to 70%. An increase in the atomic fraction of Si in the islands results in the drop of elastic strain which, in turn, induces the reverse transformation of dome-shaped islands into pyramidal clusters with dimensions greater than D_c and H_c. This change in the island shape leads to a decrease in the additional surface energy of the islands, which is related to the island height to base size ratio being lower for the pyramidal cluster than for the dome-shaped island. The reverse transformation from pyramidal to dome-shaped island takes place at the expense of increasing lateral size of the dome-shaped islands and forming facets of the {105} type.

Region II corresponds to the appearance of formations intermediate between pyramidal clusters and dome-shaped islands. Apparently, the annealing duration (5 min) in this sample was insufficient for all dome-shaped islands to transform completely into pyramidal clusters. The islands exhibit 2–3 developed facets of the {105} type. Region III reflects the so-called super-dome islands [10], the growth of which proceeds both by Si diffusion and by the Ostwald ripening mechanism, whereby atoms are detached from one island and built-up into another island. The latter mechanism ensures the growth of some islands at the expense of the disappearance of the other ones. Partial dissipation of the islands leads to a decrease in the total surface density of islands upon a 20-min annealing to 1/3 of the initial value. The surface of annealed samples retained traces of the dissociated islands in the form of circular grooves. The diameter of these circles was approximately equal to the lateral size of the dome-shaped islands existing before annealing, with the groove depth not exceeding 1 nm. The presence of these grooves upon dissociation of the islands confirms the existence of grooves around the islands before annealing.

CONCLUSION

This work established parameters providing the formation of self- assembled nanoislands characterized by a small scatter of both lateral size and height (with a standard deviation of ~6%). The X-ray diffraction and Raman scattering measurements were used to determine the composition of islands and the elastic strain developed in their structure. For a Ge layer with an equivalent thickness of 11 ML, the self-assembled islands represent a weakly strained alloy $Ge_{0.5}Si_{0.5}$. A mechanism of the alloy formation in the course of the island growth is proposed. Evolution of the island parameters in the course of annealing was studied. The reverse transformation of islands from dome-shaped to

pyramidal is related to the diffusion of silicon into islands during the annealing.

ACKNOWLEDGMENTS

This work was supported by the Russian Foundation for Basic Research (project no. 99-02-16980), the Russian Academy of Sciences' Program of Support for Young Researchers, the BRHE Program (Grant CRDGF RESC-02), and the Programs of the Ministry of Policy in Science and Technology of the Russian Federation "Physics of Solid-State Nanostructures" (project 02.04.1.1.16.E1) and "Promising Technologies and Instruments for Micro- and Nanoelectronics" (project no. 99-0247).

REFERENCES

1. Y. M. Mo, D. E. Savage, B. S. Swartzentruber, and M. G. Lagally, Phys. Rev. Lett. **65**, 1020 (1990).
2. G. Medeiros-Ribeiro, A. M. Bratkovski, T. I. Kamins, *et al.*, Science **279**, 353 (1998).
3. T. I. Kamins, E. C. Carr, R. S. Wiliams, and S. J. Rosner, J. Appl. Phys. **81**, 211 (1997).
4. F. M. Ross, J. Tersoff, and R. M. Tromp, Phys. Rev. Lett. **80**, 984 (1998).
5. M. I. Alonso and K. Winner, Phys. Rev. B: Condens. Matter **39**, 10056 (1989).
6. J. Groenen, R. Carles, *et al.*, Appl. Phys. Lett. **71**, 3856 (1997).
7. Y. Chen and J. Washburn, Phys. Rev. Lett. **77**, 4046 (1996).
8. A.-L. Barabasi, Appl. Phys. Lett. **70**, 2565 (1997).
9. G. Abstreiter, P. Schittenhelm, C. Engel, *et al.*, Semicond. Sci. Technol. **11**, 1521 (1996).
10. T. I. Kamins, G. Medeiros-Ribeiro, D. A. A. Ohlberg, and R. S. Wiliams, J. Appl. Phys. **85**, 1159 (1999).
11. S. A. Kukushkin and A. V. Osipov, Usp. Fiz. Nauk **168**, 1103 (1998).

Translated by P. Pozdeev

Semiconductors, Vol. 34, No. 1, 2000, pp. 61–66. Translated from Fizika i Tekhnika Poluprovodnikov, Vol. 34, No. 1, 2000, pp. 62–66.

SEMICONDUCTORS STRUCTURES, INTERFACES, AND SURFACES

Transverse Optical Phonon Splitting in GaAs/AlAs Superlattices Grown on the GaAs(311) Surface Studied by the Method of Raman Light Scattering

V. A. Volodin*, M. D. Efremov*, V. V. Preobrazhenskiĭ*, B. R. Semyagin*, V. V. Bolotov, and V. A. Sachkov****

** Institute of Semiconductor Physics, Siberian Division, Russian Academy of Sciences, Novosibirsk, 630090 Russia*
*** Institute of Sensor Microelectronics, Siberian Division, Russian Academy of Sciences, Omsk, 644077 Russia*
E-mail: volodin@isp.nsc.ru

Submitted December 21, 1998; accepted for publication May 19, 1999

Abstract—$GaAs_n/AlAs_m$ superlattices grown on the GaAs (311)A and (311)B surfaces by molecular-beam epitaxy were studied by Raman light scattering. The form of the Raman scattering tensor allowed the TO_y and TO_x modes to be separately observed using various scattering geometries (the *y* and *x* axes correspond to atomic displacements along and across facets formed on the (311)A surface, respectively). The $TO1_y$ and $TO1_x$ modes exhibited splitting in superlattices grown on a faceted GaAs(311)A surface. The degree of splitting increased for superlattices with an average GaAs layer thickness of 6 monoatomic layers and less. No splitting was observed for superlattices grown under the same conditions on the (311)B surface, which indicates that the splitting effect is probably due to the formation of GaAs quantum wires on the faceted (311)A surface.

INTRODUCTION

An important current task in modern solid state physics is to develop methods for the obtainment of quantum wires and dots (objects with dimensions of the order of a few interatomic distances) and to study their properties. Since modern lithography offers only a restricted possibility of creating nanometer-sized objects with reproducible shapes and dimensions in the lateral directions, the considerable interest of researchers is drawn to methods based on the properties of self-organizing systems [1]. One promising approach of this type is related to application of the phenomenon of faceting (ridge formation) observed on the high-index GaAs surfaces. The faceting effect on the GaAs(311)A surface, that is, the appearance of a periodic system of microfacets (ridges) oriented in the $(\bar{2}33)$ direction (with a 32 Å period in the $(01\bar{1})$ direction), was discovered in the early 1990s by Nötzel *et al.* [2–4] and then confirmed by many other researchers [5–8]. According to the data reported, the ridge height is either 10.2 Å (which corresponds to 6 monoatomic layers in the (311) direction) [2–4] or 3.4 Å (2 monolayers) [6–8]. This point is still rather ambiguous and some researchers even reject the possibility of formation of a highly periodic ridged GaAs(311)A surface [9].

The notion about development of a periodic system of quantum wires upon the merging of microfacets in the course of a heteroepitaxial growth of ultrathin layers by the method of molecular-beam epitaxy (MBE) [2, 3] assumes that the system would exhibit anisotropy in properties of the electron and phonon subsystems. Special features of the transport of charge carriers in these structures were studied both experimentally and theoretically. In particular, Prints *et al.* [10] reported on the phenomenon of anisotropy in the conductivity along and across the direction of faceting, which was observed at temperatures up to 500 K. The properties of phonons in superlattices on the (311)A surface were studied in [11–19]. However, detailed investigations were mostly performed for relatively thick GaAs and AlAs layers, containing 12 monolayers and more [10–15], while the effect of ridged heteroboundaries is expected to be maximum in the case when the layer thickness is comparable with the ridge height. One of the few works on the Raman scattering in GaAs/AlAs(311)A superlattices with small thicknesses of the GaAs layer (8 and 5 monolayers) was performed by Armelles *et al.* [16]. It was reported that, in contrast to the theoretical calculations suggesting that the heteroboundary ridging must lead to considerable changes in the pattern of Raman scattering, the experimental Raman spectra exhibited no features that could be attributed to the faceting. The effects of faceting of the GaAs(311)A surface possessing a lateral symmetry on the phonon properties (such as the lateral phonon convolution, etc.) were also studied for superlattices formed in thick GaAs layers [14].

The purpose of this work was to study the properties of transverse optical (TO) phonons localized within a thin corrugated GaAs layer or in a GaAs quantum wire grown on the (311)A surface. An analysis of the fre-

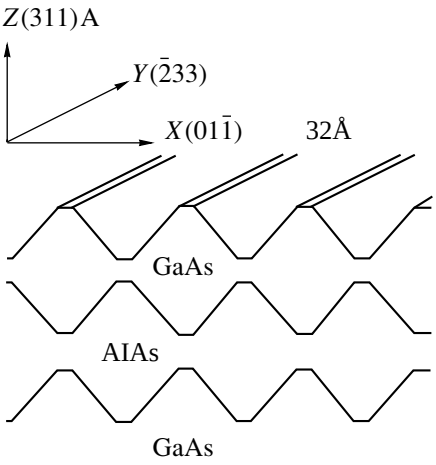

Fig. 1. Schematic diagram of a cross section of the GaAs/AlAs superlattice on a faceted (311)A surface for the model of growth with quantum wire formation.

quencies of localized TO phonons may provide additional data concerning the structure of microfacets formed on the GaAs(311)A surface. Using the quantum selection rules with respect to symmetry for the Raman scattering, we have studied the localized TO modes polarized along and across the facets formed on the GaAs(311)A surface in order to detect the phenomenon of splitting for these modes in the case of their planar localization related to the formation of a system of phonon-isolated GaAs quantum wires. We have also studied the phonon properties of GaAs/AlAs superlattices on the (311)B surface, because a comparison of the TO mode splitting on the (311)A and (311)B superlattices may reveal the effect of the GaAs–AlAs (311)A heteroboundary faceting on the phonon properties of the objects studied.

EXPERIMENTAL

The sample structures were grown by MBE on semiinsulating GaAs(311)A and GaAs(311)B substrates. The angular misorientation of substrates with respect to the (311) direction was less than 15′. The (311)A and (311)B surfaces are not equivalent because the III–V type semiconductor crystals possess no center of inversion. The (311)A and (311)B surfaces were determined by the anisotropic etching technique. Lateral superlattices grown on the ridged (311)A surface represent, according to an experimentally confirmed model [2, 3], a system of periodically repeated thickness-modulated (corrugated) GaAs and AlAs layers. The modulation period coincides with the period of microfacets (32 Å) and the amplitude of modulation corresponds to the microfacet depth. The structure of a system of quantum wires formed if the growth proceeds according to the mechanism proposed in [2, 3] is schematically depicted in Fig. 1.

Parameters and specification of $GaAs_n/AlAs_m$ superlattices

Substrate orientation		Average GaAs thickness *n*, monolayers	Average AlAs thickness *m*, monolayers	Number of periods
(311)A	(311)B			
A1	B1	12	12	100
A2	B2	10	8	100
A3		6	8	100
A4	B4	5	12	200
A5	B5	4	8	200

We have grown a series of $GaAs_n/AlAs_m$ superlattices where *n* and *m* are the thicknesses of the corresponding layers expressed by the number of monolayers (one monolayer thickness in the (311) direction is 1.7 Å). The parameters of superlattices grown on the (311)A and (311)B surfaces are listed in the table. The layer thicknesses were controlled by the MBE growth duration. The MBE process was conducted under the conditions necessary for reconstruction of the GaAs and AlAs surfaces into a highly periodic system of microfacets. These growth conditions are described in more detail elsewhere [10, 17]. To avoid artifacts, the superlattices were grown simultaneously on different surfaces, which provided for the otherwise identical growth conditions. The number of periods *L* (see table) was varied from 100 to 200. Every 10 periods of the superlattice contained a 50-Å-thick AlAs layer. All the superlattices were grown on the GaAs and AlAs buffer layers (0.1 μm thick) and then coated with a thin (40 Å) protective layer of GaAs.

The Raman spectra were recorded in a quasi-backscattering geometry. The measurements were performed at room temperature using a spectrometer based on a DFS-52 double-beam monochromator and an Ar laser with $\lambda = 488$ nm. The experiments with various polarization geometries were performed using a special device comprising a $\lambda/2$ polarization-rotating plate, a polarizing Glan's prism, and a depolarizing optical wedge.

RESULTS AND DISCUSSION

Figure 2 shows typical Raman spectra for the TO modes localized in GaAs layers of various average thicknesses. The measurements were performed using different scattering geometries for superlattices grown on the (311)A and (311)B surfaces. First, we will describe the crystallographic directions corresponding to the axes *X*, *Y*, *Z* and explain selection of the particular polarization geometries used for the scattering measurements.

The Raman scattering tensor for the longitudinal (LO) and transverse (TO) optical phonons with various

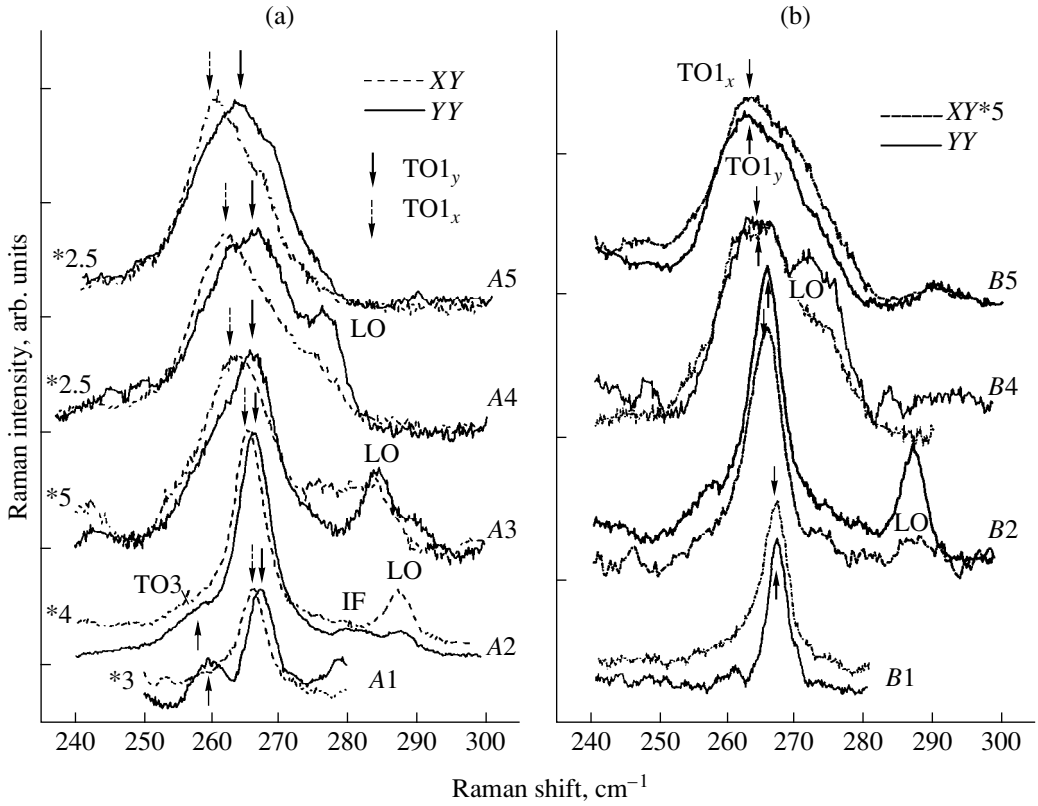

Fig. 2. Raman spectra measured in the $Z(YY)\bar{Z}$ (solid lines) and $Z(YX)\bar{Z}$ (dashed lines; for convenience, intensity is multiplied by a factor of 2.5–5) geometries for the samples grown on (a) the (311)A surface (samples A1–A5 with GaAs layer thicknesses 12, 10, 6, 5, and 4 monolayers, respectively) and (b) the (311)B surface (samples B1, B2, B4, and B5 with GaAs layer thicknesses 12, 10, 5, and 4 monolayers, respectively) surfaces.

polarizations for the backscattering from a (311) surface has the following form [13]:

$$LO - \frac{1}{\sqrt{11}}\begin{pmatrix} 0 & d & d \\ d & 0 & 3d \\ d & 3d & 0 \end{pmatrix};$$

$$TO_x - \frac{1}{\sqrt{2}}\begin{pmatrix} 0 & -d & d \\ -d & 0 & 0 \\ d & 0 & 0 \end{pmatrix};$$

$$TO_y - \frac{1}{\sqrt{22}}\begin{pmatrix} 0 & 3d & 3d \\ 3d & 0 & -2d \\ 3d & -2d & 0 \end{pmatrix}.$$

The TO_x and TO_y modes correspond to the phonon polarizations with the atomic displacements in the $X\,(01\bar{1})$ and $Y\,(\bar{2}33)$ directions, that is, across and along the facets formed on the (311)A surface, respectively (see Fig. 1). The Z-axis is oriented in the (311) direction. According to the symmetry selection rules, the scattered light intensity is proportional to the square of the product of the incident light polarization vector by the Raman scattering tensor and by the scattered light polarization vector. The vectors of polarization of the incident or scattered light are $\frac{1}{\sqrt{2}}(01\bar{1})$ (X) and $\frac{1}{\sqrt{22}}(\bar{2}33)$ (Y). Thus, the scattered light intensity for the TO_y mode in the $Z(YY)\bar{Z}$ geometry (vectors outside the brackets indicate the momentum direction, and vectors inside the brackets indicate polarizations of the incident and scattered photons) is proportional to $\left(\frac{54}{11\sqrt{22}}\right)^2 d^2$ $(\approx 1.09d^2)$. Scattering for the TO_x mode in this geometry is forbidden. For the $Z(YX)\bar{Z}$ scattering geometry, the scattered light intensity for the TO_x mode is proportional to $\frac{2}{11}d^2$ $(\approx 0.18d^2)$, and the TO_y mode of scattering is forbidden [13]. Thus, the two modes are observed in different scattering geometries and, hence, can be resolved at high precision with respect to posi-

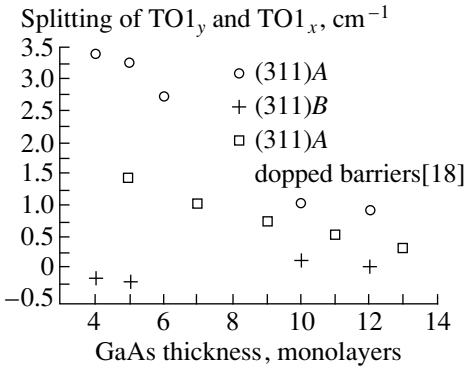

Fig. 3. Plot of the difference between the $TO1_y$ and $TO1_x$ mode frequencies versus the average GaAs layer thickness in superlattices grown on the (311)A and (311)B surfaces; open square symbols show data taken from [18].

tions of the corresponding peaks in the Raman spectra. Spectra measured in the $Z(YY)\bar{Z}$ geometry may also contain the LO modes.

Figure 2a clearly reveals splitting of the main localized modes $TO1_y$ and $TO1_x$. As the average thickness of the GaAs layer decreases, the splitting effect becomes more pronounced. In addition, the spectra of samples A1 and A2 (with a GaAs layer thickness of 12 and 10 monolayers, respectively) reveal localized TO modes of a higher (third) order. An increase in the peak width observed in the series of samples A3–A5 can be related to smearing of the AlAs/GaAs heteroboundaries on reaching a scale of the order of one monolayer. The scattering features observed in the region of 280 cm^{-1} in the spectrum of sample A2 measured in the $Z(YY)\bar{Z}$ geometry coincide in position with the GaAs interface (IF) phonons. The IF phonon position was estimated for planar GaAs/AlAs superlattices with the GaAs/AlAs layer thickness ratio 10/8. More accurate determination of the IF phonon position would require taking into account a rigid character of the heteroboundary. Therefore, assignment of the peak at 280 cm^{-1} to the IF phonon is rather an assumption. It should be emphasized that observation of the IF phonon modes under nonresonance conditions may be indicative of a ridged heteroboundary. Indeed, this feature may result from uncertainty of the wave vector q_{par} (parallel to the lateral superlattice layers), which is inversely proportional to the lateral period of this superlattice $\Delta q_{\text{par}} \approx \frac{2\pi}{d}$. For smooth superlattices, the IF phonons are not observed in the Raman spectra because of small q_{par} values. These phonons were detected in the backscattering geometry only under resonance conditions. It is also necessary to note a nonmonotonic variation of the ratio of intensities of the Raman scattering peaks corresponding to the TO_y and TO_x modes (see Fig. 2a). For example, the intensities of peaks for a lateral superlattice with relatively thick GaAs layers (A1 sample, 12 monolayers) and those with a minimum GaAs layer thickness (A4 and A5 samples, five and four monolayers, respectively) differ only by a factor of 2.5–3. As noted above for the symmetry selection rules, the relative intensities of these peaks in the spectra of bulk GaAs must differ by a factor of about six, which was actually observed in the Raman spectrum of the GaAs(311)A substrate and was also approximately valid for lateral superlattices with the GaAs layer thicknesses of ten and six monolayers (Fig. 2a, samples A2 and A3) and for the superlattices grown on the GaAs(311)B surface (Fig. 2b). Apparently, this variation of relative intensities of the TO_y and TO_x modes for lateral superlattice is related both to the mixing of various phonon modes and to a change in ratio between the sums of projections of the polarizable Ga–As bonds on the directions along and across facets as a result of the layer thickness modulation along one of the directions, in particular, $(01\bar{1})$.

In order to check whether the splitting of $TO1_y$ and $TO1_x$ modes is due to the ridge formation on the GaAs(311)A surface, we have prepared and studied superlattices on the GaAs(311)B surface with the same average layer thicknesses. Figure 2b shows the Raman spectra of samples B1, B2, B4, and B5 measured in the same geometries as those used for the samples grown on the (311)A surface. As seen from this figure, there is virtually no evidence of the TO mode splitting. The Raman scattering intensities for the $TO1_y$ and $TO1_x$ modes differ by a factor of approximately 4.5–6 for all the samples grown on the (311)B surface, in contrast to the pattern observed for superlattices grown on the (311)A surface (Fig. 2a) and close to the ratio characteristic of the bulk GaAs.

The positions of peaks corresponding to the Raman scattering in $TO1_y$ and $TO1_x$ modes were determined for all superlattices by approximating the experimental spectra with the Lorentz curves, with minimization of the rms deviation. The accuracy of determination of the corresponding vibration frequency was ±0.2 cm^{-1}. Data on the splitting of TO1 modes with different polarizations for all the samples studied are summarized in Fig. 3. As seen from this figure, the magnitude of splitting between the two different $TO1$ modes increases with decreasing average thickness of the GaAs layers in superlattices grown on the (311)A surface. The frequency of the $TO1_y$ mode, in which the atoms perform oscillations along the quantum wires, is higher than that of the $TO1_x$ mode with the atoms shifting across the quantum wires. We may suggest that this effect is actually related to the heteroboundary ridging, rather than to the mixing of TO modes with the longitudinal modes as a result of reduced symmetry of the (311) direction. Indeed, the results of calculations performed with neglect of the faceting effect indicate that the splitting

effect would be observed only for modes with the wave vectors corresponding to the middle of the Brillouin zone and greater [11]. Note that the average GaAs layer thickness for samples A5, A4, and A3 was almost equal or even smaller than the height of ridges used in one of the models used to describe reconstruction of the GaAs/AlAs(311)A heteroboundary (6 monolayers [2–4]). As seen from Fig. 3, the effect of TO_x and TO_y mode splitting for these samples sharply increases. This can be considered as indirect evidence of the (311)A surface faceting (with the ridge height of about 6 monolayers) and the GaAs quantum wire formation. According to the results of calculations performed by Castrillo *et al.* [19], no TO mode splitting takes place in a sample with an average GaAs layer thickness of 8 monolayers and a 2-monolayer-thick ridge height on the heteroboundary, while our experiment showed a significant splitting even for sample A1 with a GaAs layer ten monolayers thick.

It should be emphasized that the frequency splitting of TO_y and TO_x modes was observed only for the lateral superlattices grown on the (311)A surface. No TO mode splitting for a bulk GaAs with the (311)A was observed in experiment because these modes are degenerate for the long-wavelength vibrations symmetry allowed in the Raman spectra of bulk GaAs [13]. For superlattices grown on the (311)B surface, the splitting was either insignificant or the $TO1_y$ mode frequency was even somewhat smaller than that of the $TO1_x$ mode (Fig. 2b). This fact may be considered as evidence that the mode splitting is due to the (311)A surface reconstruction and the formation of a GaAs layer structure of the quantum wire type, rather than due to mixing of the TO and LO modes related to reduced symmetry of the (311) direction. Calculation of the frequencies of localized phonons were performed with an allowance for the coulomb interaction between cations and anions. In the case of smooth heteroboundaries (faceting neglected), the calculated magnitude of splitting between the $TO1_y$ and $TO1_x$ modes was maximum for superlattices corresponding to the minimum GaAs layer thickness ($GaAs_4AlAs_8$) and did not exceed 1.5 cm^{-1}.

Also presented in Fig. 3 (open square symbols) are the data taken from our work [18] for the samples with an AlAs barrier thickness of 27 Å (the barriers were partly doped). The superlattices were rather thin (75 periods), which led to difficulties in determination of the peak positions as a result of a considerable background signal due to scattering from the substrate and a relatively thick protective GaAs layer (250 Å). Apparently, the background signal contribution might also somewhat decrease the real mode splitting observed in [18].

CONCLUSION

We have observed the splitting of $TO1_y$ and $TO1_x$ modes in superlattices grown on a faceted GaAs(311)A surface, while superlattices grown under identical conditions on the (331)B surface exhibited virtually no splitting of these modes. This result suggests that a difference in the frequencies of TO phonons with different polarizations of the atomic displacements is related to anisotropy of the GaAs/AlAs(311)A superlattices, namely, to the formation of a periodic system of quantum wires on this surface. Dependence of the TO mode splitting on the GaAs layer thickness is indirect evidence that the height of microfacets (ridges) formed on the GaAs(311)A surface is about 6 monolayers.

ACKNOWLEDGMENTS

This work was supported the Russian Foundation for Basic Research (project nos. 97-02-18422 and 99-02-16668) and the Siberian Division of the Russian Academy of Sciences (grant No. 16 of the Competition of Young Researchers' Projects in Physics and Technology).

The authors are grateful to the Scientific Council of the Institute of Semiconductor Physics (Siberian Division, Russian Academy of Sciences) for support in the form of a Young Researcher's Grant for V.A. Volodin.

REFERENCES

1. N. N. Ledentsov, V. M. Ustinov, V. A Shchukin, P. S. Kop'ev, Zh. I. Alferov, and D. Bimberg, Fiz. Tekh. Poluprovodn. (St. Petersburg) **32**, 385 (1998).
2. R. Nötzel, N. N. Ledentsov, L. Dawerits, M. Hohenstein, and K. Ploog, Phys. Rev. Lett. **67**, 3812 (1991).
3. R. Nötzel, N. N. Ledentsov, L. Dawerits, K. Ploog, and M. Hohenstein, Phys. Rev. B: Condens. Matter. **45**, 3507 (1992).
4. R. Nötzel, N. N. Ledentsov, L. Dawerits, and K. Ploog, Surf. Sci. **267**, 209 (1992).
5. P. V. Santos, A. Cantarero, M. Cardona, R. Nötzel, and K. Ploog, Phys. Rev. B: Condens. Matter. **52**, 1970 (1995).
6. M. Wassermeier, J. Sudijono, M. D. Johnson, K. T. Leung, B. G. Orr, L. Dawerits, and K. Ploog, J. Cryst. Growth **150**, 425 (1985).
7. M. Wassermeier, J. Sudijono, M. D. Johnson, K. T. Leung, B. G. Orr, L. Dawerits, and K. Ploog, Phys. Rev. B: Condens. Matter. **51**, 14721 (1995).
8. D. Lüerben, A. Dinger, H. Kalt, W. Braun, R. Nötzel, K. Ploog, and J. Tummler, Phys. Rev. B: Condens. Matter. **57**, 1631 (1998).
9. P. Moriarty, Y.-R. Ma, A. W. Dunn, P. H. Beton, M. Henini, Phys. Rev. B: Condens. Matter. **55**, 15397 (1997).
10. V. Ya. Prints, I. A. Panaev, V. V. Preobrazhenskiĭ, and B. R. Semyagin, Pis'ma Zh. Éksp. Teor. Fiz. **60**, 209 (1994).
11. M. V. Belousov, V. Yu. Davydov, I. É. Kozin, P. S. Kop'ev, and N. N. Ledentsov, Pis'ma Zh. Éksp. Teor. Fiz. **57**, 112 (1993).

12. Z. V. Popovic, E. Richter, J. Spitzer, M. Cardona, A. J. Shields, R. Nötzel, and K. Ploog, Phys. Rev. B: Condens. Matter. **49**, 7577 (1994).
13. A. J. Shields, Z. V. Popovic, M. Cardona, J. Spitzer, R. Nötzel, and K. Ploog, Phys. Rev. B: Condens. Matter. **49**, 7584 (1994).
14. Z. V. Popovic, M. B. Vukmirovic, Y. S. Raptis, E. Anastassakis, R. Nötzel, and K. Ploog, Phys. Rev. B: Condens. Matter. **52**, 5789 (1995).
15. P. Castrillo, G. Armelles, L. Gonzales, P. S. Dominguez, and L. Colombo, Phys. Rev. B: Condens. Matter. **51**, 1647 (1995).
16. G. Armelles, P. Castrillo, P. D. Wang, C. M. Sotomayor Torres, N.N. Ledentsov, and N. A. Bert, Solid State Commun. **94**, 613 (1995).
17. V. A. Volodin, M. D. Efremov, V. Ya. Prints, V. V. Preobrazhenskiĭ, and B. R. Semyagin, Pis'ma Zh. Éksp. Teor. Fiz. **63**, 942 (1996).
18. V. A. Volodin, M. D. Efremov, V. Ya. Prints, V. V. Preobrazhenskiĭ, B. R. Semyagin, and A. O. Govorov, Pis'ma Zh. Éksp. Teor. Fiz. **66**, 45 (1997).
19. P. Castrillo, G. Armelles, and J. Barbolla, Sol. St. Electron. **40**, 175 (1966).

Translated by P. Pozdeev

Semiconductors, Vol. 34, No. 1, 2000, pp. 67–69. Translated from Fizika i Tekhnika Poluprovodnikov, Vol. 34, No. 1, 2000, pp. 67–69.

SEMICONDUCTORS STRUCTURES, INTERFACES, AND SURFACES

Dynamic Strain-Sensitive Characteristics of the Schottky-Barrier Diodes under a Pulsed Uniform Pressure

O. O. Mamatkarimov, S. Z. Zaĭnabidinov, A. Abduraimov, R. Kh. Khamidov, and U. A. Tuĭchiev

Ulugbek Tashkent State University, Universitetskaya ul. 95, Vuzgorodok, Tashkent, 700095 Uzbekistan

Submitted January 22, 1999; accepted for publication June 3, 1999

Abstract—Dynamic strain-gage characteristics of Schottky-barrier diodes of the Au–Si:Ni–Sb type subjected to pulsed uniform pressure in the range of $P = (0–5) \times 10^8$ Pa at a temperature of $T = 300$ K were studied. Studies of *I–V* characteristics of the diodes showed that, due to an additional temperature effect induced by the pulsed pressure, the dynamic parameters of the stress-sensitivity effect in these diodes were 20–30% larger than the corresponding static parameters. © *2000 MAIK "Nauka/Interperiodica".*

The rapid progress in the modern technology of machine building and, especially, of the automobile industry, requires the development of internal-combustion engines of higher efficiency with minimal expenditure of fuel. As is known, in combustion of fuel in internal-combustion engines, rapidly varying thermodynamic processes occur that are close to adiabatic processes and are accompanied by abrupt changes in pressure and temperature of gases. In connection with this, the challenge of studying the physics of the above thermodynamic processes in their dynamics and in extreme conditions is an urgent problem and, as such, requires the development of strain gages that have high sensitivity and reliability and are easy to fabricate.

There are many publications devoted to the study and fabrication of semiconducting strain gages [1]; however, these publications are concerned with pressures that are either constant or vary slowly and are close to static pressures.

The objective of this work was to study the strain-gage characteristics of Schottky-barrier diodes (SBDs) of the Au–Si:Ni–Sb type under the effect of a pulsed uniform pressure (PUP) in the range of $P = (0–5) \times 10^8$ Pa at a temperature of $T \simeq 300$ K.

In our studies, we used the SBDs fabricated on the basis of the samples of compensated silicon *n*-Si:Ni obtained by high-temperature ($T = 1100–1200$°C) diffusion of Ni from a metallic Ni layer sputtered on the *n*-Si surface [2]. The samples were of the shape of a rectangular parallelepipeds $3 \times 3 \times 1$ mm^3 in size with crystallographic orientation of (111) along the short edge. Following the diffusion of Ni, the *n*-Si samples with initial resistivity of $\rho \simeq 80\ \Omega$ cm retained their conduction type, with ρ increased to about 10^2–$10^5\ \Omega$ cm. The diodes were fabricated fabricated by sputtering of gold and antimony on the opposite faces of the sample; the area of electrodes was 3×3 mm^2.

After the current contacts were formed, the SBD samples were encapsulated with an epoxy resin in order to ensure the thermal insulation [3]. The measurements of strain-gage characteristics of SBD under a PUP were performed in a special experimental setup [4] with the use of an H-307/1 x–y plotter.

Figure 1c shows the kinetic dependence of the dynamics of the effect of PUP with the rate of increase of pressure $\partial P/\partial t = 2.5 \times 10^8$ Pa/s with the amplitude of $P = 5 \times 10^8$ Pa at an initial temperature of $T \simeq 300$ K. Kinetic dependences of the current $I(t)$ in a SBD under the PUP and for the forward-bias voltage of $U = 2.5$ V are shown in Fig. 1a; in this case, the SBD resistivity was $\rho \simeq 10^3\ \Omega$ cm. Figure 1b illustrates the temperature variations in a SBD in the course of exposure to the PUP.

As is evident from Fig. 1a, the PUP causes the SBD current to increase to a certain dynamic value I_{max} corresponding to the magnitude of the pressure applied; the rate of this increase corresponds to the rate of the pressure increase. When the pressure attains its amplitude value, the relaxation of SBD current sets in and the current decreases to its static value I_{st} ($\partial P/\partial t = 0$ and $P = \text{const}$). In the course of a decrease in pressure with the same rate as the pressure increase, the current in SBD decreases to a certain value I_{min} and, after a com-

1063-7826/00/3401-0067$20.00

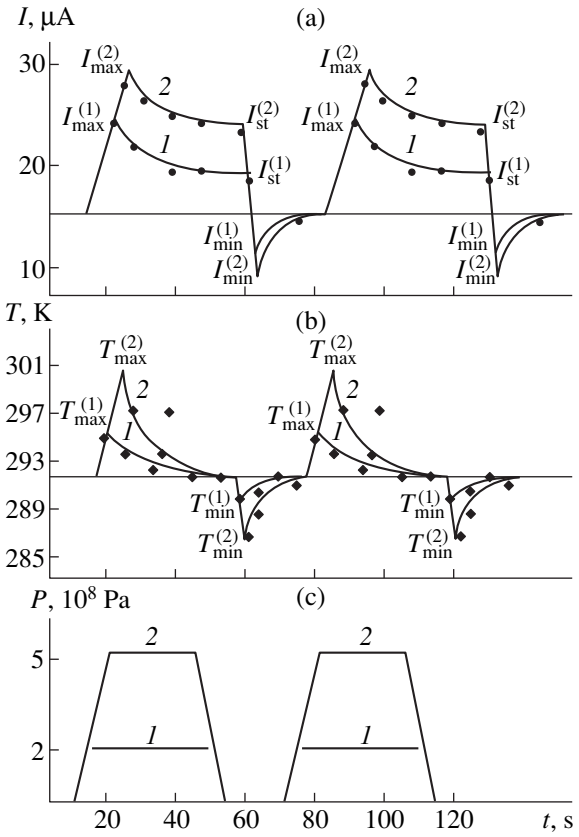

Fig. 1. Time dependences of (a) current, (b) temperature, and (c) pressure in Schottky-barrier diodes with the structure of Au–Si⟨Ni⟩–Sb for the forward bias of $U_f = 2.5$ V. The base resistivity was $\rho \simeq 5 \times 10^3$ Ω cm. The numbers at the curves correspond to the amplitude values of the pressure P equal to (*1*) 2.5×10^8 and (*2*) 5×10^8 Pa.

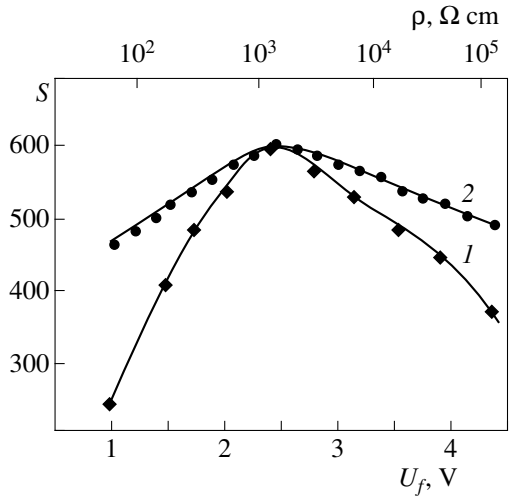

Fig. 2. Dependences of the strain-sensitivity coefficient $S = f(\rho)$ and $S = f(U_f)$ in the Schottky-barrier diodes that had the structure of Au–Si⟨Ni⟩–Sb and were subjected to a pressure of $P = 5 \times 10^8$ Pa, with $\partial P/\partial t = 2.5 \times 10^8$ Pa/s. Curve *1* corresponds to the dependence $S = f(\rho)$ for the forward-bias voltage of $U_f = 2.5$ V, and curve *2* represents the dependence $S = f(U_f)$ for $\rho \simeq 5 \times 10^3$ Ω cm.

plete relief of pressure, starts to relax and increase to its original value I_0. In this case, the greater is the PUP amplitude, the larger is an increase in current: $I^{(2)}_{max} > I^{(1)}_{max}$, $I^{(2)}_{st} > I^{(1)}_{st}$, and $I^{(2)}_{min} > I^{(1)}_{min}$ for $P_2 > P_1$.

Variations of temperature in SBD in the entire course of the PUP effect (Fig. 1b) occur similarly and synchronously to the variations of current, both qualitatively and quantitatively; i.e., with an increase (decrease) of pressure, the SBD temperature increases (decreases) to a certain value $T_{max}(T_{min})$ corresponding to the pressure amplitude. Further on, after the PUP effect reached its amplitude value (or $P = 0$), the temperature decreases (increases) to its initial value T_0.

Thus, our studies of *I–V* characteristics of SBDs subjected to PUP show that, owing to manifestation of an additional temperature effect stimulated by pulsed pressure, the dynamic parameters of the strain-sensitivity effect in SBDs increase by 20–30% as compared to the corresponding static parameters; for example, for $P = 5 \times 10^8$ Pa, the relative variation $I_{max}/I_0 = 3.2$, whereas $I_{st}/I_0 = 2.2$.

As is known [1], the basic characteristic of strain gages and sensors is the strain-sensitivity coefficient S. In connection with this, we studied the dependences of the strain-sensitivity coefficient of SBD on the resistivity ρ of its base made of *n*-Si:Ni, $S = f(\rho)$, and on the applied forward-bias voltage U, $S = f(U_f)$. The coefficient S was calculated from the following conventional formula:

$$S = [\Delta I/(I_0 E)]P.$$

Here, $\Delta I = I_{max} - I_0$ or $\Delta I = I_{min} - I_0$ is the variation of current in SBD, $E = 1.8 \times 10^{11}$ Pa is Young's modulus, and P is the amplitude value of PUP.

It is evident from Fig. 2 that the dependences $S = f(\rho)$ (curve *1*) and $S = f(U_f)$ (curve *2*) are nonmonotone; the strain-sensitivity coefficient attains a maximum ($S \simeq 600$) for the resistivity $\rho \simeq 5 \times 10^3$ Ω cm and for the forward-bias voltage $U_f \simeq 2.5$ V.

We can interpret the observed peaks of strain sensitivity in SBD subjected to PUP by making the following assumption: Since the base layer of SBD is compensated, the effect of pressure and a variation of temperature bring about a change in the concentration of majority-charge carriers; this change is due to the baric shift of the conduction band, the valence band, and the deep levels of Ni, which causes a variation of both resistivity and potential-barrier height in SBD. Apparently, the large value of the strain-sensitivity coefficient in SBD for low values of forward-bias voltage $U_f < 2.5$ V and the resistivity $\rho < 5 \times 10^3$ Ω cm is related to a simultaneous decrease in both the potential-barrier height and the base resistance, whereas, for $U_f > 2.5$ V

and the resistivity $\rho > 5 \times 10^3$ Ω cm, the role of the potential barrier becomes less important, and the strain-sensitive properties of SBD are largely defined by variations of the corresponding base resistance [5].

The results of studying the strain-sensitive properties of SBDs that have a structure of the Au–Si:Ni–Sb type and are subjected to PUP indicate that the development of strain gages based on such diodes will make it possible to "visually" observe the dynamics of the occurring thermodynamic processes and determine their physical parameters; as a result, new possibilities arise of improving such gages and enhancing their operational reliability.

REFERENCES

1. A. L. Polyakova, *Deformation of Semiconductors and Semiconducting Devices* [in Russian] (Nauka, Moscow, 1979).
2. M. K. Bakhadyrkhanov and S. Z. Zaĭnabidinov, Izv. Akad. Nauk Uzb. SSR **6**, 73 (1976).
3. O. O. Mamatkarimov, Candidate's Dissertation, Tashkent (1993).
4. A. Abduraimov, S. Z. Zaĭnabidinov, O. O. Mamatkarimov, *et al.*, Prib. Tekh. Éksp., No. 5, 229 (1992).
5. A. Abduraimov, S. Z. Zaĭnabidinov, O. O. Mamatkarimov, *et al.*, Fiz. Tekh. Poluprovodn. (St. Petersburg) **27**, 516 (1993).

Translated by A. Spitsyn

Semiconductors, Vol. 34, No. 1, 2000, pp. 70–72. Translated from Fizika i Tekhnika Poluprovodnikov, Vol. 34, No. 1, 2000, pp. 70–72.

SEMICONDUCTORS STRUCTURES, INTERFACES, AND SURFACES

Effect of the Insulator–Gallium Arsenide Boundary on the Behavior of Silicon in the Course of Radiation Annealing

V. M. Ardyshev*, M. V. Ardyshev, and S. S. Khludkov****

** Tomsk Polytechnical University, Tomsk, 634004 Russia*
*** Siberian Physicotechnical Institute, Tomsk State University, 634050 Russia*
Submitted March 29, 1999; accepted for publication June 8, 1999

Abstract—The depth–concentration profiles $n(x)$ of ^{28}Si implanted into semiinsulating GaAs (E_1 = 50 keV, $F_1 = 8.75 \times 10^{12}$ cm^{-2}; E_2 = 75 keV, $F_2 = 1.88 \times 10^{12}$ cm^{-2}) were studied by *C–V* measurements after the electron-beam annealing (P = 7.6 W/cm^2, t = 10 s). Prior to annealing, the samples were coated with protective insulating films (SiO_2:Sm; SiO_2 deposited by monosilane oxidation, or Si_3N_4) or were not coated. It was found that the implant profiles observed upon the electron-beam annealing extend to deeper layers as compared to the calculated curves or the profiles upon thermal annealing (800°C, 30 min). The profile depth depends on the type of insulating coating. The maximum "broadening" was observed in the electron-beam-annealed GaAs without insulating coating, and the minimum, in the sample with a protective SiO_2:Sm layer. The $n(x)$ curves can be divided into two parts, adjacent to and distant from the interphase boundary. The diffusion parameters and the degree of electric activation of the implanted Si atoms are greater in the second region than in the first one. The experimental results are interpreted assuming the presence of thermoelastic stresses at the insulator–semiconductor boundary in GaAs. © *2000 MAIK "Nauka/Interperiodica".*

Previously [1], we demonstrated that the radiation annealing of GaAs implanted with a ^{28}Si isotope features diffusional redistribution of the implant atoms toward deeper layers of the semiconductor. The extent of the profile "broadening" and the degree of electric activation of the implanted silicon atoms were different, depending on the presence or absence of an additional insulating layer on the GaAs surface during the sample annealing. As is known, the electrophysical characteristics of the ion-doped layers upon thermal annealing also significantly depend on the type of a protective insulating coating and the method of its formation [2, 3]. In this context, the purpose of our work was to study effects of the insulator material on the depth– concentration profiles (variation of the concentration of implanted atoms with the distance from the sample surface) of the electrically active Si atoms in GaAs upon the isothermal electron-beam annealing.

EXPERIMENTAL

The experiments were performed on (100)-oriented 400-μm-thick semiinsulating GaAs wafers with a resistivity of $\rho \geq 10^7$ Ω cm, electron mobility μ = 4200 cm^2 V^{-1} s^{-1} (300 K), and a dislocation density $N_D \leq 10^4$ cm^{-2}. The chromium impurity concentration in the material studied did not exceed $N_{Cr} \leq 10^{16}$ cm^{-3}. Prior to the silicon implantation, the wafers were etched in an $H_2SO_4 : H_2O_2 : H_2O$ mixture (1 : 1 : 10). The GaAs substrates were implanted with ^{28}Si ions in two stages: first, at an energy of E_1 = 50 keV to a fluence of $F_1 = 8.75 \times 10^{12}$ cm^{-2} and second, at an energy of E_2 = 75 keV to a fluence of $F_2 = 1.88 \times 10^{12}$ cm^{-2}. The implantation processing was performed at 300 K in a vacuum of not worse than 6×10^{-6} Pa. In order to exclude the axial and lateral channeling, the wafers were oriented with respect to the incident ion beam as described in [1].

After implantation, the wafers were cut into four parts. One part was coated with a film-forming silicon dioxide solution doped with samarium at a concentration of 2–8.0 wt % (SiO_2:Sm). Upon the solution application, these samples were dried under IR radiation at 80 and 130°C, followed by thermal degradation of the coating for 25 min at 450°C. The second part of the Si-implanted GaAs wafer was coated with SiO_2 by plasmachemical deposition (PCD) through monosilane oxidation at 400°C (PCD-SiO_2). The third part of the wafer was coated with Si_3N_4 by cathode sputtering in activated nitrogen atmosphere using a three-electrode sputter-deposition system [5]. Thicknesses of the resulting insulating layers were 110–130 nm (for both SiO_2:Sm and PCD-SiO_2 films) and 98–110 nm (Si_3N_4). The fourth part of the wafers remained uncoated. Finally, all samples were subjected to the electron-beam (EB) annealing at an electron energy of 10 keV and a radiant power density of P = 7.6 W/cm^2 for t =

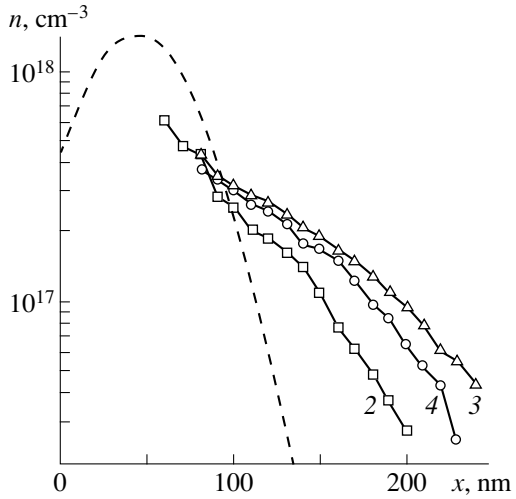

Fig. 1. The plots of electron concentration n versus depth x: (dashed line) $N_{Si}(x)$ profile calculated for ^{28}Si (see the text for details); (*2–4*) experimental profiles of $n(x)$ upon EB-annealing (see the text for conditions) for GaAs plates with various protective coatings (the number at the curve corresponds to that indicated in the table).

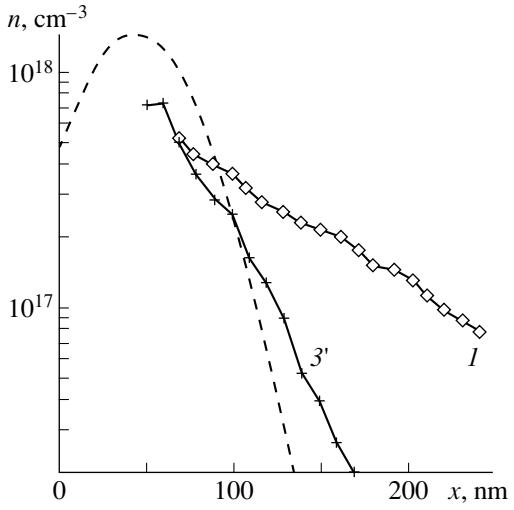

Fig. 2. Depth–concentration profiles (for notations, see legend to Fig. 1 and the table); curve *1* refers to the sample without insulating coating and curve *3*,' to the control GaAs plate with a protective film of type 3 (see table) upon thermal annealing (see the text for conditions).

10 s in a vacuum system of the "Modul" type [6]; the vacuum in the system during the annealing was not worse than 10^{-5} Pa. Control wafers with a protective 300-nm- thick PCD-SiO_2 layer were subjected to thermal (T) annealing at 800°C for 30 min in a flow of hydrogen.

After the annealing, the insulating layers were removed and the samples with 100×100 μm^2 Schottky barriers were studied by *C–V* measurements to determine the electron concentration profiles $n(x)$.

RESULTS

Figures 1 and 2 present the depth–concentration profiles $n(x)$ of EB-annealed (Fig. 1, curves *2–4*; Fig. 2, curve *1*) and T-annealed (Fig. 2, curve *3*') Si-implanted GaAs samples. Dashed lines in Figs. 1 and 2 show the profiles of implanted silicon calculated using the first two distribution moments: the mean projected range R_p and its standard deviation ΔR_p determined by the method of secondary-ion mass spectrometry (SIMS) [7].

As seen, the $n(x)$ profiles in EB-annealed samples extend to deeper layers as compared to the calculated curves and the depth-concentration profiles in T-annealed samples. The maximum redistribution of the electrically active Si implant is observed upon the EB annealing without protective insulator (Fig. 2, curve *1*). The extent of "broadening" of the implant depth-concentration profiles in the samples EB-annealed with insulating films depends on the film type, method of formation, and composition (Fig. 1, curves *2–4*). The EB-annealing of SiO_2:Sm-coated samples (Fig. 1, curve *2*) leads to the minimum redistribution of Si in GaAs as compared to the plates with other coatings. An analysis of the data showed that the experimental $n(x)$ curves can be described by a sum of two profiles:

$$n_i(x) = \sum_{i=1}^{2} n_i^{\max} \exp\left[-\frac{(x-R_p)^2}{2\sigma_i^2}\right], \qquad (1)$$

where $n_i^{\max} = \eta_i F/2.5\sigma_i$ is the maximum electron concentration, F is the total implantation dose, η_i is the degree of electric activation of the implanted Si atoms, $\sigma_i = (\Delta R_p^2 + 2D_i t)^{1/2}$ is the variance of the depth–concentration profile, D_i is the silicon diffusion coefficient, and t is the duration of annealing. In our experiments, $R_p = 44.1$ nm and $\Delta R_p = 38.9$ nm.

The values of the depth–concentration profile parameters determined from the experimental curves (Figs. 1 and 2) are summarized in the table. As seen from these data, the Si-implanted GaAs layers with various insulating coatings are characterized by different diffusion properties and degrees of implant activation. Moreover, the σ_1^2, $n_1^{\max}$, and η_1 values in the layers near the insulator–GaAs boundary (within a 100-nm-thick layer) are smaller than the analogous values at a depth exceeding 100 nm; note also that σ_1^2 is smaller than ΔR_p^2. The σ_1^2, $n_1^{\max}$, and η_1 values for the sample EB-annealed with Si_3N_4 coating are small as compared to the analogous values for the other samples. The maximum of the diffusion parameters and the degree of activation of the implanted Si atoms were observed for the sample annealed without any protective film.

Parameters of diffusion and electric activation of silicon in GaAs with various protective coatings

Coating	Depth $x < 100$ nm			Depth $x > 100$ nm			
	σ_1^2, nm^2	n_1^{max}, 10^{17} cm^{-3}	η_1	σ_2^2, nm^2	n_2^{max}, 10^{17} cm^{-3}	η_2	D_2, 10^{-12} cm^2 s^{-1}
Uncoated	1.16×10^3	2.58	0.21	1.33×10^4	3.28	0.88	5.6
SiO_2 : Sm	5.80×10^2	3.18	0.18	4.73×10^3	3.53	0.57	1.6
PCD-SiO_2	5.07×10^2	2.48	0.13	8.86×10^3	3.69	0.78	3.7
Si_3N_4	4.24×10^2	2.10	0.10	7.18×10^3	3.70	0.73	2.8

Note: σ_1, σ_2 are the variances of $n(x)$ profiles; η_1, η_2 are the degrees of implanted Si activation; n_1^{max}, n_2^{max} are the electron concentration at the $n(x)$ profile maximum.

DISCUSSION

The above results can be interpreted as follows. First, the EB-annealing of an insulator–GaAs heterostructure gives rise to thermoelastic stress fields caused by a difference in the thermal expansion coefficients of the insulator and semiconductor. Let us assume that the electric activation of the implanted Si atoms at a depth of $x < 100$ nm is limited by the diffusion of silicon atoms or gallium vacancies. We will also assume validity of the relationships $\sigma_1 \sim \exp(-E_m/2kT)$ and $\eta_1 \sim \exp(-E_b/2kT)$, where E_m is the activation energy for the migration of Si atoms (or V_{Ga} vacancies) and E_b is the barrier height for the Si–V_{Ga} interaction. Then the low σ_1 and η_1 values are explained by an increase in E_m and E_b under the action of thermoelastic stresses. According to our estimates, an increase in the E_m and E_b values relative to the sample EB-annealed without insulating film amounts to approximately kT and $0.74kT$ for the Si_3N_4–GaAs structure, $0.83kT$ and $0.48kT$ for the PCD-SiO_2–GaAs structure, and $0.69kT$ and $0.15kT$ for the SiO_2:Sm–GaAs system, respectively. On the whole, the maximum changes in E_m and E_b observed for the Si_3N_4–GaAs structure correlates with a greater difference between the thermal expansion coefficients of silicon nitride and gallium arsenide (e.g., as compared to the analogous difference for SiO_2 and GaAs).

It should be noted that the maximum effect of the thermoelastic stress fields is observed for the near-surface GaAs layers with a thickness of approximately 100 nm, which is comparable to the insulator film thickness. At the same time, the EB annealing of the sample without insulating film gives rise to a greater vacancy concentration and a greater diffusion coefficient D_2 as compared to the values observed upon annealing of the protected substrates (see table). Taking into account that vacancies in both GaAs sublattices are the centers of nonradiative recombination [8] and a high density of electron excitations in the system studied, the diffusion most probably proceeds according to the radiation-enhanced mechanism [9]. Since the increase in the migration rate is proportional to the recombination rate [10], a smaller concentration of the nonradiative recombination centers leads to the smaller diffusion coefficient D_2 observed upon the EB-annealing of samples with protective insulating layers. It should be noted that the D_2 value depends on the properties of the insulator–GaAs boundary. We may suggest that the SiO_2:Sm–GaAs boundary is a sink for the nonradiative recombination centers of both electron- and ion-irradiation origin, while the Si_3N_4–GaAs and especially the PCD-SiO_2–GaAs boundaries act as the sources of such centers for the deeper GaAs layers.

Thus the degree of electric activation of Si atoms implanted into GaAs and the implant redistribution by diffusion into deeper GaAs layers depend on the type, composition, and method of formation of a protective insulating film on the substrate surface prior to the electron-beam annealing.

REFERENCES

1. V. M. Ardyshev and M. V. Ardyshev, Fiz. Tekh. Poluprovodn. (St. Petersburg) **32** (10), 1153 (1998).
2. D. V. Morgan, IEEE Proc. A **128**, 109 (1981).
3. V. M. Ardyshev, Author's Abstr. of Candidate's Dissertation in Technical Sciences (Tomsk State University, Tomsk, 1988).
4. V. M. Ardyshev, L. A. Kozlova, O. N. Korotchenko, and A. P. Mamontov, USSR Inventor's Certificate No. 235, 899 (1 April 1986).
5. V. A. Burdovitsyn, Author's Abstr. of Candidate's Dissertation in Technical Sciences (Tomsk State University, Tomsk, 1981).
6. Yu. E. Kreindel', N. I. Lebedeva, and V. Ya. Martens, Pis'ma Zh. Tekh. Fiz. **8** (23), 1465 (1982).
7. D. H. Lee, R. M. Matbon, Appl. Phys. Lett. **30**, 327 (1977).
8. S. Y. Chiang and G. L. Pearson, J. Appl. Phys. **46**, 2986 (1975).
9. V. M. Lenchenko, Fiz. Tverd. Tela (St. Petersburg) **11**, 799 (1969).
10. L. C. Kimerling, IEEE Trans. Nucl. Sci. **5** (23), 1497 (1976).

Translated by P. Pozdeev

Semiconductors, Vol. 34, No. 1, 2000, pp. 73–80. Translated from Fizika i Tekhnika Poluprovodnikov, Vol. 34, No. 1, 2000, pp. 73–80.

SEMICONDUCTORS STRUCTURES, INTERFACES, AND SURFACES

Temperature Dependence of Residual Stress in Epitaxial GaAs/Si(100) Films Determined from Photoreflectance Spectroscopy Data

R. V. Kuz'menko*, A. V. Ganzha*, O. V. Bochurova*, É. P. Domashevskaya*, J. Schreiber, S. Hildebrandt**, S. Mo***, E. Peiner***, and A. Schlachetzki*****

** Faculty of Physics, Voronezh State University, Universitetskaya pl. 1, Voronezh, 394893 Russia*
E-mail: phssd2@main.vsu.ru
*** Fachbereich Physik der Martin-Luther-Universität Halle-Witteberg, D-06108 Halle/Saale, Deutschland*
**** Institut für Halbleitertechnik der Technischen Universität Braunschweig, D-38106 Braunschweig, Deutschland*

Submitted May 25, 1999; accepted for publication June 11, 1999

Abstract—In the temperature range T = 10–300 K, photoreflectance spectroscopy was used to study the temperature dependence of residual stress in epitaxial *n*-GaAs films (1–5 μm thick, electron concentration of 10^{16}–10^{17} cm^{-3}) grown on Si(100) substrates. A qualitative analysis showed that the photoreflectance spectra measured in the energy region of the E_0 transition in GaAs had two components. They consisted of the electromodulation component caused by the valence subband $|3/2; \pm 1/2\rangle$–conduction band transition and the low-energy excitonic component. The magnitude of stress was determined from the value of the strain-induced energy shift of the fundamental transition from the subband $|3/2; \pm 1/2\rangle$ with respect to the band gap of the unstressed material $E_0(T) - E_0^{|3/2;\,\pm 1/2\rangle}(T)$. The increase in the energy shift $E_0 - E_0^{|3/2;\,\pm 1/2\rangle}$ from 22 ± 3 meV at 296 K to 29 ± 3 meV at 10 K, which was found in the experiments, gives evidence of an increase in biaxial stress with decreasing temperature. © *2000 MAIK "Nauka/Interperiodica".*

INTRODUCTION

Nowadays, the major working elements of optical information systems are constructed on the basis of direct-band $A^{III}B^{V}$ semiconductor compounds. On the other hand, silicon is the main material of the semiconductor industry, and in the nearest future it cannot be replaced with gallium arsenide or other III–V compounds. A possible way to further develop the technology of production of optical information systems might consist in combining the advantages of III–V semiconductors with the achievements of silicon technology, i.e., combining different electronic and optoelectronic components on a common silicon chip. This might make possible the achievement of a high integration density, a high rate of signal processing, and a high reliability on the basis of a good thermal conductivity and hardness of materials. Moreover, the low cost of silicon substrates is bound to cause a sharp decrease in the price of optical information systems [1].

One of the main problems of heteroepitaxial growth technology is the minimization of residual stress in an epitaxial layer that causes the motion of nonradiative-recombination centers (point defects and dislocations) to the active region and considerably decreases the service life of a semiconductor laser [2]. It is known that stress in an epitaxial GaAs layer grown on a silicon substrate may be caused by (i) the difference of a film and a substrate in lattice constant (a_{Si} = 0.5431 nm and a_{GaAs} = 0.5653 nm [3]) and (ii) the difference of materials in the thermal expansion coefficient ($\alpha_{Si} = 2.60 \times 10^{-6}$ K^{-1} and $\alpha_{GaAs} = 5.90 \times 10^{-6}$ K^{-1} at 300 K [3]). For the GaAs/Si system, the stress caused in an epitaxial layer by the lattice mismatch is bound to represent biaxial compressive stress. However, in the region of temperatures commonly used for the epitaxial film growth (700–1100 K), this stress is completely relieved by the generation of dislocations in the interface region [4, 5]. When samples are cooled from the growth temperature to room temperature, the difference in expansion coefficient leads to the formation of biaxial tensile stress in an epitaxial layer [4]. However, as noted in [4, 6], the values of stress experimentally determined at room temperature are considerably lower than the values calculated theoretically (based on the values of thermal expansion coefficients of materials). Because of this, it is assumed that in the case where a sample is cooled from the growth temperature to a certain critical temperature T_c, the tensile stress in a film is also relieved through the generation of dislocations, and this process terminates only on the achievement of T_c.

The problem of high-accuracy determination of stress in thin epitaxial films in a wide temperature range

within the framework of one investigation method is not yet completely solved [7]. One of the most promising methods of study is the use of optical modulation photoreflectance (PR) spectroscopy. Within the framework of this method, stress is calculated by using the strain-induced change of energy of electronic optical transitions, which is determined from the energy shift of spectral features. Advantages of this method are a high spectral resolution (~1 meV) in a wide temperature range, the feasibility of studying thin layers (with thickness $d \geq 100$ nm), a high spatial resolution (down to 20×20 μm^2), and the feasibility of scanning a film in depth. In spite of these advantages, the employment of the PR spectroscopy for the determination of residual stress in (III–V)/Si heterostructures has been reported only in a few papers [8–11].

In our previous papers [12, 13], we analyzed the results of the photoreflectance measurements made at room temperature for GaAs/Si and InP/Si samples with epitaxial layers from 1 to 5 μm in thickness. When analyzing the spectra, we began with the fact that electromodulation was the dominant mechanism responsible for the formation of spectral components. To carry out a quantitative analysis of spectra, we used a model taking into account the splitting of the valence band under the effect of stress and the presence of low-energy components (excitonic components) in the PR spectrum. Our results showed that the dominant spectral contribution in the region of subband transitions corresponded to the electronic optical transition from the subband $|3/2; \pm 1/2\rangle$ ($E_0^{|3/2; \pm 1/2\rangle}$). Note that the corresponding component was measured in the medium-field mode. Because of this, the residual stress in GaAs and InP films was determined by using the energy shift with respect to the transition energy E_0 in the bulk unstressed material $E_0 - E_0^{|3/2; \pm 1/2\rangle}$.

In this work, we study the PR spectra measured for heteroepitaxial GaAs/Si samples and homoepitaxial GaAs/GaAs samples in the temperature range T = 10–300 K. To make a quantitative analysis of the spectra, we extended the mathematical model by taking into account a change of the medium-field electromodulation subband component to the low-field component due to the temperature decrease. The dependences $E_0(T)$ and $E_0^{|3/2; \pm 1/2\rangle}(T)$ obtained from the quantitative analysis of the spectra are used for the calculation of temperature dependence of residual stress $\sigma(T)$.

SAMPLE PREPARATION

The GaAs films used in the study were grown at the Institute of Semiconductor Technology of Braunschweig Technical University. They were grown on Si(100) substrates by the metal-organic chemical vapor deposition in a horizontal low-pressure reactor with arsine (AsH_3) and trimethylgallium (TMGa) used as source materials. Upon 20-min cleaning in H_2SO_4 : H_2O_2 : H_2O, silicon substrates were rinsed in deionized water. Next, we used 30-s etching in the 5% HF solution to remove possible remaining oxides and a second rinse in deionized water. Prior to the epitaxial growth, a silicon substrate was annealed in a hydrogen atmosphere (for 15 min at 950°C) to remove possible oxides. To prevent the formation of antiphase domains in the epitaxial layer in the course of cooling, a surface was exposed to 3-min treatment in an AsH_3 atmosphere at a temperature of 750°C. The growth of an epitaxial film started from the growth of a buffer layer 14 nm thick at 400°C, with B^V and A^{III} components in the gas phase being in the ratio 4 : 1. On the buffer layer produced in this way, we grew at 700°C the basic GaAs layer (the growth of a layer 2 μm thick at a pressure of 50 mbar required 60 min). In this case, the elements of the Groups V and III in the gas phase were in the ratio 80 : 1. The thickness of the basic layer in the samples under study was varied in a range of 1–5 μm. The material used for the film growth was undoped. However, the diffusion of Si atoms from the substrate caused doping of a film at the level $n = 10^{15}$–10^{17} cm^{-3} [14].

To obtain the dependence $E_0(T)$, we measured the PR of homoepitaxial n-GaAs/n^+-GaAs(100) samples with charge carrier concentrations $n = 10^{16}$–10^{17} cm^{-3} and $n^+ = 10^{18}$ cm^{-3} and epitaxial-layer thicknesses d = 2–5 μm.

EXPERIMENTAL SETUP

The experiments on PR were carried out at the Institute of Semiconductor Technology of Braunschweig Technical University and the Laboratory of Optical Studies of Martin Luther University in Halle. The spectra were measured in the energy range E = 1.20–1.65 eV with the aid of a He–Ne laser operating in the red region (λ = 632.8 nm). The laser intensity ranged from 0.01 to 10 W/cm^2. In the measurements, the modulation frequency was varied from 100 to 300 Hz. The change of reflectance ΔR was measured with the aid of an SR850 two-channel phase-sensitive amplifier. The setup provided the measurement of PR signals with amplitudes as low as 5×10^{-6}. To cool the samples, we used a helium cryostat. The sample temperature was varied in a range of 10–320 K. A spot of a probing light beam on a sample, which determined the area of a surface being analyzed, was varied in size from 100×100 to 1000×1000 μm^2. An increase in spot size caused no changes in the form of the spectrum, which provides evidence of a high uniformity of the samples. Additional potentialities of the analysis of spectra were associated with the use of the phase analysis technique [15, 16].

THEORETICAL FOUNDATIONS OF THE SIMULATION OF E_0 PHOTOREFLECTANCE SPECTRA IN THE PRESENCE OF STRESS

The features of the strain-induced PR spectra in the region of the E_0 transition should be simulated taking into account changes of the band structure. The degeneracy of the E_0 transition for GaAs in the unstressed state leads to the formation of two overlapped optical transitions from the subbands $|3/2; \pm 3/2\rangle$ and $|3/2, \pm 1/2\rangle$ in accordance with the formula

$$\frac{\Delta R}{R} = a_{|3/2;\,\pm 3/2\rangle}\frac{\Delta R^{|3/2;\,\pm 3/2\rangle}}{R_{E_0^{|3/2;\,\pm 3/2\rangle}}} + a_{|3/2,\,\pm 1/2\rangle}\frac{\Delta R^{|3/2;\,\pm 1/2\rangle}}{R_{E_0^{|3/2;\,\pm 1/2\rangle}}}, \quad (1)$$

where ΔR is the photoinduced change of the reflectance signal, $E_0 = E_0^{|3/2;\,\pm 3/2\rangle} = E_0^{|3/2;\,\pm 1/2\rangle}$ are the energies of the transitions from valence subbands, and $a_{|3/2;\,\pm 3/2\rangle}$ and $a_{|3/2;\,\pm 1/2\rangle}$ are the amplitude factors of the corresponding spectral components. The amplitude factors depend on the transition matrix element and the effective mass of charge carriers in subbands [17, 18].

The electromodulation interband PR components may have the mean-field or the low-field shapes of a spectral line. The spectral line shape is determined by the ratio of the energy parameter of transition broadening Γ to the electrooptical energy $\hbar\Omega$

$$\hbar\Omega = \left(\frac{e^2F^2\hbar^2}{8\mu_\parallel}\right)^{1/3}, \quad (2)$$

where e is the elementary charge, F is the surface electric field, $\hbar$ is Planck's constant, and $\mu_\parallel$ is the reduced electron–hole mass in the direction of the electric field. The medium- and low-field cases are characterized by $\Gamma < 3\hbar\Omega$ and $\Gamma \geq 3\hbar\Omega$, respectively.

In the medium-field mode, the interband spectral E_0 components have the fundamental peak in the region of the E_0 transition and high-energy Franz–Keldysh oscillations whose period is determined via equality (2) by the value of the surface electric field. The difference of two valence subbands in reduced effective electron–hole masses ($\mu^{|3/2;\,\pm 3/2\rangle} \neq \mu^{|3/2;\,\pm 1/2\rangle}$) leads to a small difference of electrooptical energies, which manifests itself in different transitions of Franz–Keldysh oscillations.

A mathematical model used for the description of the shape of a medium-field line should include such physical parameters as the optical-transition energy E, the electric field strength F, the penetration depth of the surface electric field d_F, the broadening energy Γ, and the depth of modulation of the surface electric field under illumination ξ ($0 \leq \xi \leq 1$). The model used by us is referred to as the generalized multilayer model, and it is described in detail in [12, 16].

In the case where the broadening energy has the dominant effect, the low-field structure has the form of the so-called third-derivative curve and is mathematically described by the third derivative of the unmodulated reflectance spectrum [19]. To simulate the low-field electromodulation components, one should know the transition energy E, the broadening energy Γ, and the phase angle φ.

In the case of biaxial strain in the [100] and [010] directions, the symmetry of the lattice of zinc blende lowers down to the tetragonal one [17]. The lattice strain lifts the degeneracy of the valence band at the point $\Gamma(0, 0, 0)$. In this case, one can calculate the energies of electronic optical transitions by the formulas [1, 20]

$$E_0^{|3/2;\,\pm 3/2\rangle} = E_0 + \left[\frac{2a}{C_{11}+2C_{12}} - \frac{b}{C_{11}-C_{12}}\right], \quad (3)$$

$$E_0^{|3/2;\,\pm 1/2\rangle} = E_0 + \left[\frac{2a}{C_{11}+2C_{12}} + \frac{b}{C_{11}-C_{12}}\right], \quad (4)$$

where $\sigma_\parallel > 0$ for the tensile stress and $\sigma_\parallel < 0$ for the compressive stress, a is the uniform-strain potential, b is the shear strain potential, and C_{11} and C_{12} are coefficients of elasticity. We used for our calculations the values of parameters from [3].

The tensile stress shifts the energies of both transitions in the direction of low energies with respect to the E_0 transition in an unstressed material. In this case, the energy shift for the transition from the subband $|3/2; \pm 1/2\rangle$ is stronger than the shift for the transition from the subband $|3/2; \pm 3/2\rangle$.

A further effect of stress on the electromodulation E_0 component in GaAs must manifest itself in a change of the ratio of amplitude factors for the components of subbands because of a change of effective masses of charge carriers in the subbands [17].

The effects listed above cause an energy shift of the spectral structure being simulated, which depends on stress, and a change of the shape of spectral lines due to a new superposition of components.

An example of simulation of the medium-field PR E_0 spectrum of GaAs within the context of the generalized multilayer model for different values of biaxial stress is illustrated in Fig. 1. The ratio of amplitudes $a^{|3/2;\,\pm 1/2\rangle}/a^{|3/2;\,\pm 3/2\rangle} = 2$, which was used in the simulation to enhance the effect of a change of spectral shape, is considerably greater than the value for the unstressed material $a^{|3/2;\,\pm 1/2\rangle}/a^{|3/2;\,\pm 3/2\rangle} = 0.5$ [21, 22]. One can see from Fig. 1 that, in the case of weak stress, the resulting spectral structure has, at first glance, the form of a one-component medium-field line (spectrum *1*) because of a small difference in transition energy E_0. In this case, the stress can be determined only from its strain-induced energy shift. For larger values of stress, the spectral structure shows not only the energy shift, but also a shoulder structure in the region of the high-energy slope of the fundamental peak, and this structure gives evidence of the presence of near-lying elec-

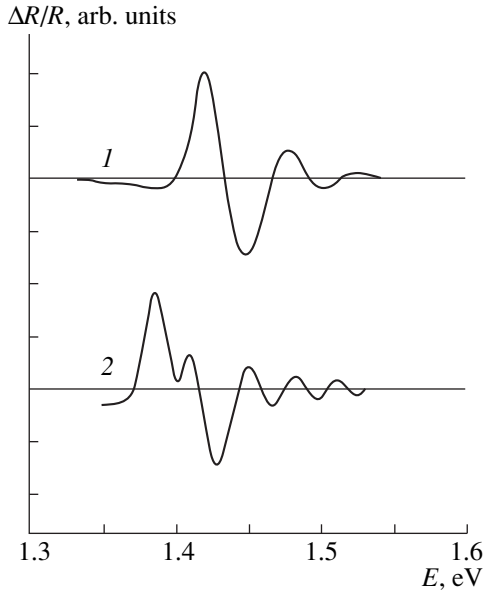

Fig. 1. Model medium-field electromodulation PR spectra calculated for biaxially stressed GaAs for the parameters $F = 4 \times 10^6$ V/m, d_F = 400 nm, Γ = 7 meV, ξ = 1, $a_{|3/2;\,\pm1/2\rangle}/a_{|3/2;\,\pm3/2\rangle} = 2$; (*1*) $\sigma_\parallel$ = 0.5 kbar, $E_0^{|3/2;\,\pm3/2\rangle}$ = 1.421 eV, $E_0^{|3/2;\,\pm1/2\rangle}$ = 1.418 eV; (*2*) $\sigma_\parallel$ = 3.9 kbar, $E_0^{|3/2;\,\pm3/2\rangle}$ = 1.409 eV, $E_0^{|3/2;\,\pm1/2\rangle}$ = 1.385 eV.

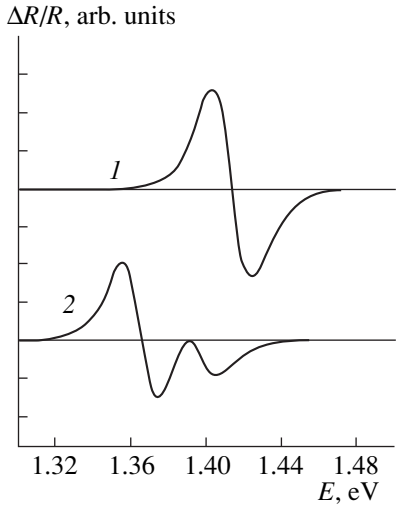

Fig. 2. Model low-field electromodulation PR spectra calculated for biaxially stressed GaAs for the parameters Γ = 20 meV, $\varphi = 50°$, $a_{|3/2;\,\pm1/2\rangle}/a_{|3/2;\,\pm3/2\rangle} = 2$; (*1*) $\sigma_\parallel$ = 1.1 kbar, $E_0^{|3/2;\,\pm3/2\rangle}$ = 1.418 eV, $E_0^{|3/2;\,\pm1/2\rangle}$ = 1.411 eV; (*2*) $\sigma_\parallel$ = 4.9 kbar, $E_0^{|3/2;\,\pm3/2\rangle}$ = 1.396 eV, $E_0^{|3/2;\,\pm1/2\rangle}$ = 1.365 eV.

tronic transitions (the "splitting structure," spectrum *2*). In this case, the position of peaks in the first approximation may be interpreted as the energy position of transitions from subbands.

In the case of low-field spectra, one should also start from the fact that the strain-induced splitting of the valence band causes the formation of two low-field components with different transition energies and amplitudes. Figure 2 shows two low-energy spectra simulated for biaxially stressed GaAs. One can see from Fig. 2 that the strain-induced splitting of the valence band manifests itself only in the case where it exceeds the splitting energy.

Our calculations show the effect of valence band "splitting" and the energy shift. However, in view of the fact that the samples under study are expected to have relatively "low" values of residual stress ($\sigma_\parallel > 3.9$ kbar) and, consequently, relatively small values of splitting, substantial "splitting structures" are not expected to appear in the E_0 spectra of GaAs/Si samples.

Because the experimental PR E_0 spectra measured for substrates or an epitaxial GaAs layer in a wide temperature range contain, as a rule, not only the electromodulation E_0 component, but also the low-energy spectral component superimposed on it, which is assigned to excitonic transitions and is well described by the Aspnes formula with parameter $n = 2$ [16, 22, 23], an adequate model for the quantitative analysis of the experimental PR spectra must also involve a mathematical formalism for its simulation. In the PR spectra simulated with allowance for excitonic effects, spectral features appear that resemble the splitting structures [13].

Thus, the problem arising because of a possible ambiguity of interpretation of the experimental spectral structures is clear. Because of this, a high-accuracy quantitative analysis of spectral structures measured on GaAs/Si samples can be performed only within the context of multicomponent fitting of the whole spectral line, which uses two electromodulation E_0 components and two excitonic components (E_{exc}) with different transition energies $E_0^{|3/2;\,\pm3/2\rangle} \neq E_0^{|3/2;\,\pm1/2\rangle}$ and $E_{\text{exc}}^{|3/2;\,\pm3/2\rangle} \neq E_{\text{exc}}^{|3/2;\,\pm1/2\rangle}$ and different amplitude factors. Moreover, to prove the presence of low-energy components in the spectrum, one should invoke an additional experimental method, e.g., the phase analysis method [15, 16, 23].

QUANTITATIVE ANALYSIS OF THE PHOTOREFLECTANCE SPECTRA MEASURED AT ROOM TEMPERATURE [13]

Figure 3 shows the PR E_0 spectra obtained for homoepitaxial GaAs/GaAs(100) samples and heteroepitaxial GaAs/Si(100) samples [13, 14].

The PR spectra of homoepitaxial samples involve, in the region of the fundamental peak, different line shapes, which are caused by the superposition of the excitonic and medium-field components. All the spectra have approximately the same positions of the fundamental peak near the transition energy for the unstressed material E_0 = 1.425 eV.

For heteroepitaxial samples, the PR spectra with medium-field electromodulation components are measured as well (their presence is evidenced by the high-energy Franz–Keldysh oscillations). These spectra are shifted to lower energies with respect to the spectra of homoepitaxial samples, which suggests that the transition energies of all their spectral components are decreased. The shift of the spectra to lower energies corresponds to the presence of residual tensile strain in the films. In the region of the high-energy slope of the fundamental peak, spectral features in the form of peaks or inflections are observed.

To elucidate the strain-induced origin of experimental PR spectra, we analyzed them within the context of the multicomponent model described above. For the simulation, we used two medium-field and two excitonic components with variable values of transition energies and amplitude factors. The results show (see Fig. 4) that the experimental spectra can be simulated by one excitonic and one medium-field component. Their superposition describes the experimental line shape in all the spectral regions. All our attempts to perform fitting with the aid of two medium-field components with the ratio of amplitude factors exceeding the value $a^{|3/2;\,\pm1/2\rangle}/a^{|3/2;\,\pm3/2\rangle} = 0.1$ failed. Thus, within the framework of the analysis performed by us, the formation of the high-energy shoulder or the splitting structures in the experimental spectra is attributed to the overlap of one medium-field component and one excitonic component. In this case, the spectral components, in accordance with their energy position and a comparison with the results of previous papers [8, 10, 12], should be assigned to the transitions from the subband $|3/2;\,\pm1/2\rangle$. The absence of noticeable contributions of the transitions from the subband $|3/2;\,\pm3/2\rangle$ is surprising to a certain extent in spite of a decrease of the amplitude factor expected for the component of the subband $|3/2;\,\pm3/2\rangle$ from model concepts, because the latter, nevertheless, is bound to remain comparable to the amplitude factor for the component of the subband $|3/2;\,\pm1/2\rangle$.

The phase analysis performed for the spectra also supports the presence of the low-energy components in the spectrum. For the case where only the electromodulation components of subbands are present in the spectrum, an experimental phase line is expected to have the form of a straight line because its formation and damping are described by the same time laws. However, the experimental phase diagram has a loop structure, which suggests that a second low-energy component with a different phase of a signal is present [15].

Starting from the results of the quantitative analysis of the experimental spectra, values of residual stress in epitaxial layers can be determined only from a change of the transition energy E_0 for the subband $|3/2;\,\pm1/2\rangle$, i.e., $E_0 - E_0^{|3/2;\,\pm1/2\rangle}$. As an average value of the transition energy E_0 for bulk GaAs, we used the value $E_0 = 1.425$ eV [3]. The quantitative analysis performed by

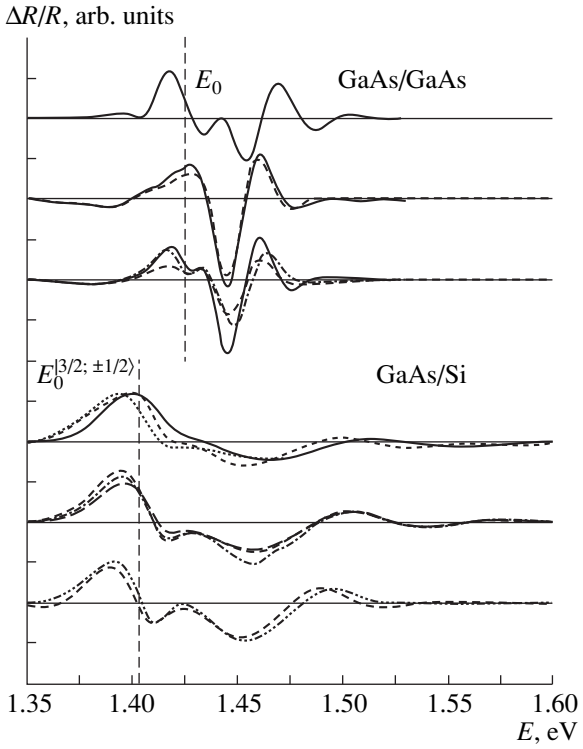

Fig. 3. Comparison of typical experimental PR E_0 spectra of homoepitaxial GaAs/GaAs samples (at the top) and heteroepitaxial GaAs/Si samples (at the bottom).

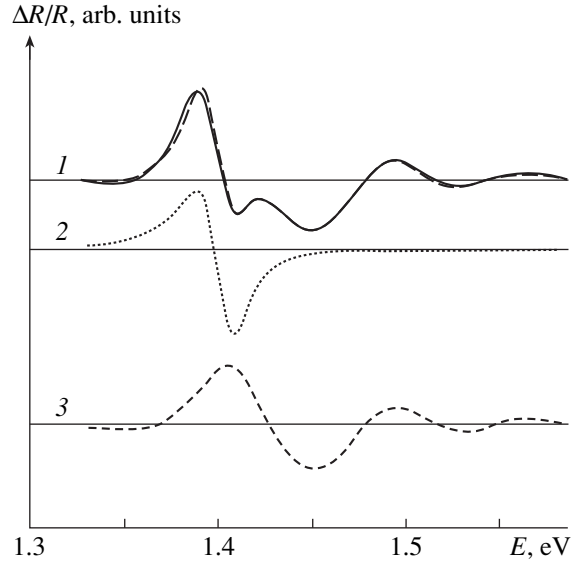

Fig. 4. Simulation of a typical PR spectrum of GaAs/Si. (*1*) Experimental PR spectrum (solid line) and its fit (dashed line) and (*2*, *3*) spectral components resolved in the analysis. (*2*) Excitonic component; $E_{exc} = 1.403$ eV, $\Gamma = 18$ meV, (*3*) medium-field component; $E_0^{|3/2;\,\pm1/2\rangle} = 1.406$ eV, $F = 9.25 \times 10^6$ V/m, $\Gamma = 14$ meV.

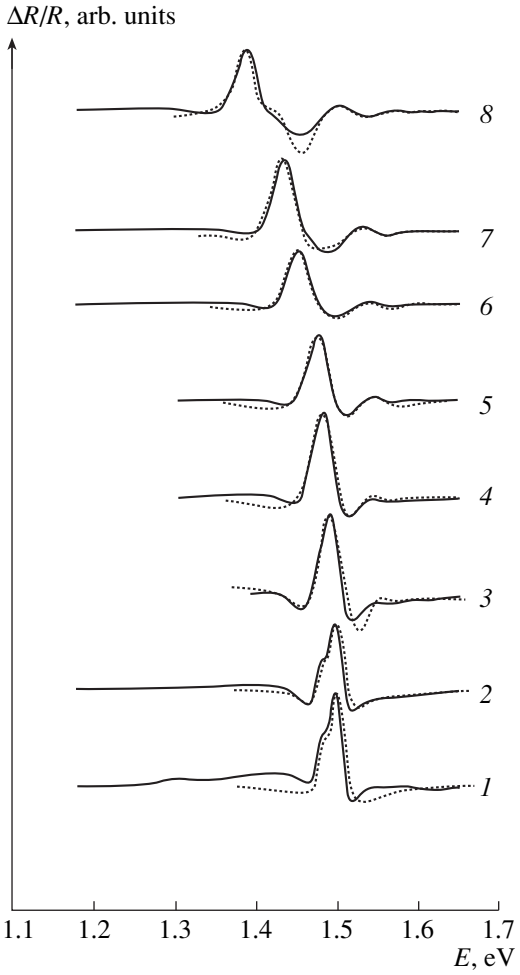

Fig. 5. Experimental temperature dependence of the PR spectrum for the GaAs/Si sample (d_{GaAs} = 2.5 μm) (solid curves) and its simulation (dashed curves). T = (*1*) 13, (*2*) 20, (*3*) 60, (*4*) 80, (*5*) 100, (*6*) 160, (*7*) 200, and (*8*) 296 K.

us for the spectra of heteroepitaxial GaAs/Si samples shows that the transition energies $E_0^{|3/2;\,\pm1/2\rangle}$ are concentrated near the value $E_0^{|3/2;\,\pm1/2\rangle} = 1.403 \pm 0.003$ eV irrespective of the GaAs layer thickness. The use of the difference of the values presented above for the calculation of stress with the aid of formula (4) yields the biaxial tensile stress $\sigma_{\parallel} = 1.88 \pm 0.16$ kbar.

PHOTOREFLECTANCE SPECTRA IN A TEMPERATURE RANGE OF 12–300 K

The measurements of PR spectra in a temperature range of 12–300 K were aimed at the determination of the temperature dependence of residual stress in GaAs samples. To evaluate residual stress from the value of strain-induced shift $E_0 - E_0^{|3/2;\,\pm1/2\rangle}$, we also needed a quantitative analysis of the PR spectra measured in the same temperature range for homoepitaxial samples.

Figure 5 shows an experimental temperature dependence of PR spectra, which is typical of the heteroepitaxial samples under study. A decrease observed for the period of Franz–Keldysh oscillations and their simultaneous damping give evidence of a decrease of surface electric field due to temperature reduction. In [24], a decrease of electric field strength with decreasing temperature for *n*-GaAs is attributed to the shift of the energy position of the Fermi level at the surface from the middle of the forbidden band in the direction of the conduction band.

The quantitative analysis made for the spectra within the context of the multicomponent-fitting algorithm shows that the E_0 spectrum of a heteroepitaxial sample retains its two-component form throughout the temperature range. However, because of a decrease of the dark surface electric field, which is caused by temperature lowering, the interband electromodulation $E_0^{|3/2;\,\pm1/2\rangle}$ component is measured at low temperatures in the low-field mode rather than in the medium-field mode. Thus, the simulation of spectra in the temperature region $T \geq 80$ K was carried out by using one medium-field component and one excitonic component, and the simulation in the low-temperature region was carried out by using one low-field component and one excitonic component. It is typical that although a temperature decrease causes a change of transition energies of both components, the energy spacing between the transition energies remains almost unchanged.

It should be also noted that the spectra of the GaAs/Si samples under study showed a large energy broadening of spectral features as compared to homoepitaxial samples even at low temperatures. It is likely that this is caused by an increased concentration of defects of the crystal structure.

The temperature dependences $E_0(T)$ and $E_0^{|3/2;\,\pm1/2\rangle}(T)$ obtained for homoepitaxial and heteroepitaxial samples from the multicomponent quantitative analysis of the PR spectra are shown in Fig. 6. The temperature dependence $E_0(T)$ is well described by the Varshney dependence. The shift $\Delta E(T) = E_0(T) - E_0^{|3/2;\,\pm1/2\rangle}(T)$ found by us is shown in the lower part of the figure. One can see from Fig. 6 that a decrease in temperature causes an increase of ΔE. However, a virtually linear increase of ΔE in a temperature range of 300–100 K slows down on passing to the low-temperature region, and ΔE tends to saturation. It is likely that this effect is caused by a decrease in the difference in the thermal expansion coefficient for GaAs and Si in the low-temperature region [3].

By using expression (4), one can use the shift $\Delta E = E_0(T) - E_0^{|3/2;\,\pm1/2\rangle}(T)$ to evaluate the temperature depen-

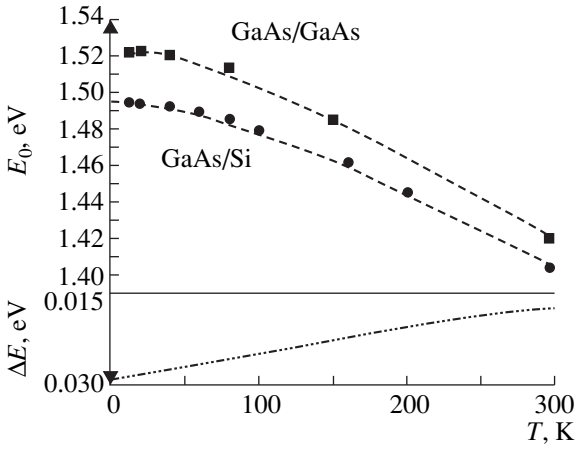

Fig. 6. Dependences $E_0(T)$ for homoepitaxial and heteroepitaxial GaAs (at the top) and the shift $\Delta E(T) = E_0(T) - E_0^{|3/2;\,\pm 1/2\rangle}(T)$ (at the bottom).

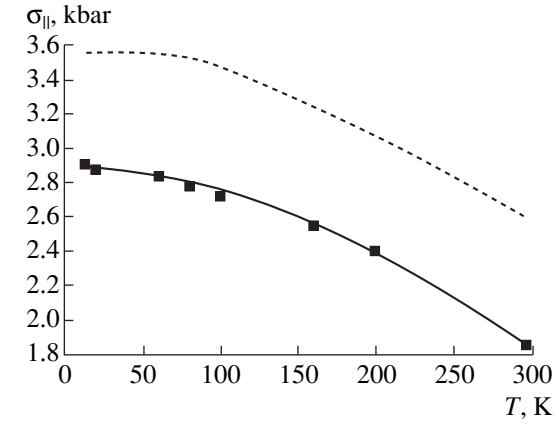

Fig. 7. The theoretical temperature dependence of residual stress $\sigma_{\|}$ in epitaxial GaAs/Si(100) films (dashed curve) and the dependence obtained from the quantitative analysis of the PR spectra (solid curve).

dence of residual stress in epitaxial GaAs layers. The dependence $\sigma_{\|}(T)$ obtained for the samples under study is shown in Fig. 7. The results of measurements on ten samples were averaged. For the samples used in the experiments, we have not observed the dependence of biaxial stress on the epitaxial-layer thickness. Although the form obtained for the temperature dependence qualitatively agrees with the behavior of residual stress in the GaAs/Si system expected from the theory and calculated from the dependences of the temperature expansion coefficients of the materials [14] (see Fig. 7), one can see that our results deviate in the direction of lower values. This disagreement is caused by the fact that the temperature of film growth from which the formation of stress set in was used in theoretical calculations as the initial temperature. Thus, the result obtained by us supports the assumption made in the literature, which states that the tensile stress in films is relieved by the generation of dislocations in the course of cooling in a temperature region above a certain critical point T_c and that the process terminates on attaining the temperature T_c. The dependence obtained by us agrees well with the experimental data presented in [14, 25].

In this work, we studied the structure of the strain-induced PR E_0 spectra obtained for the GaAs/Si semiconductor system in a temperature range of 10–300 K. The analysis of experimental spectra was performed within the context of the model accounting for a possible multicomponent structure of the spectra. The results of our analysis show that the PR spectra have the two-component form throughout the temperature range under study and represent a spectral superposition of the electromodulation interband component and the low-energy excitonic component. We showed by way of analyzing the experimental data that both components were formed with involvement of electronic optical transitions from the subband $|3/2;\,\pm 1/2\rangle$. A change from the medium-field mode to the low-field mode, which was observed for the electromodulation interband component in the course of decreasing temperature, is caused by a decrease of surface electric field.

The temperature dependence of biaxial stress $\sigma_{\|}(T)$ for epitaxial GaAs films was determined from the value of strain-induced shift $E_0 - E_0^{|3/2;\,\pm 1/2\rangle}$ found from the quantitative analysis of the PR spectra of heteroepitaxial and homoepitaxial samples. The disagreement observed for the experimental and theoretical dependences $\sigma_{\|}(T)$ supports the assumption made in the literature, which states that the generation of dislocations in the high-energy region relieves tensile stress.

ACKNOWLEDGMENTS

This work was supported by Deutsche Forschungsgemeinschaft (grants no. 9/25-1,2 and 428/3-1,2) and the Russian Foundation for Basic Research (project no. 96-15-96496).

REFERENCES

1. S. F. Fang, K. Adomi, S. Iyer, *et al.*, J. Appl. Phys. **68**, R31 (1990).
2. J. P. Van der Ziel, R. D. Dupuis, R. A. Logan, *et al.*, Appl. Phys. Lett. **51**, 89 (1987).
3. *Numerical Data and Functional Relationships in Science and Technology*, edited by K.-H. Hellwege, O. Madelung, and Landolt-Börnstein (Springer-Verlag, Heidelberg, 1984).
4. M. Sugo, N. Uchida, A. Yamamoto, *et al.*, J. Appl. Phys. **65**, 591 (1989).
5. H.-H. Wehmann, G.-P. Tang, and A. Schlachetzki, Solid State Phenomena **32–33**, 445 (1993).
6. G. Landa, R. Carles, C. Fontaine, *et al.*, J. Appl. Phys. **66**, 196 (1989).

7. F. H. Pollak, *Annual Reports, Mater. Res. Soc., Fall Meeting* (Boston, 1995).
8. T. Kanata, H. Suzawa, M. Matsunaga, *et al.*, Phys. Rev. B: Condens. Matter **41**, 2936 (1990).
9. N. Bottka, D. K. Gaskill, R. J. M. Griffiths, *et al.*, J. Cryst. Growth **93**, 481 (1988).
10. A. Dimoulas, P. Tzanetakis, A. Georgakilas, *et al.*, J. Appl. Phys. **67**, 4389 (1990).
11. M. Dutta, H. Shen, S. M. Vernon, *et al.*, Appl. Phys. Lett. **57**, 1775 (1990).
12. S. Mo, E. Peiner, A. Barteles, *et al.*, Jpn. J. Appl. Phys. **35**, 4238 (1996).
13. R. V. Kuz'menko, A. V. Ganzha, O. V. Bochurova, *et al.*, Fiz. Tverd. Tela (St. Petersburg) **41**, 725 (1999).
14. *Abschlußbericht zum Vorschugsvorhaben, "Optimierung von II/V-Si-Heterostrukturen"*, Nos. 9/25-1,2 and 428/2-1,2 (DFG, März 1997).
15. A. V. Ganzha, W. Kircher, R. V. Kuz'menko, *et al.*, Fiz. Tekh. Poluprovodn. (St. Petersburg) **32**, 272 (1998).
16. S. Hildebrandt, M. Murtagh, R. Kuz'menko, *et al.*, Phys. Status Solidi A **152**, 147 (1995).
17. G. L. Bir and G. E. Pikus, *Symmetry and Deformation Effects in Semiconductors* [in Russian] (Nauka, Moscow, 1972).
18. H. Shen and M. Dutta, J. Appl. Phys. **78**, 2151 (1995).
19. D. E. Aspnes, Surf. Sci. **37**, 418 (1973).
20. H. Asai and K. Oe, J. Appl. Phys. **54**, 2052 (1983).
21. R. A. Batchelor, A. C. Brown, and A. Hamnett, Phys. Rev. B: Condens. Matter **41**, 1401 (1990).
22. J. P. Estrera, W. M. Duncan, and R. Glosser, Phys. Rev. B: Condens. Matter **49**, 7281 (1994).
23. R. Kuz'menko, A. Ganzha, J. Schreiber, *et al.*, Fiz. Tverd. Tela (St. Petersburg) **39**, 2123 (1997).
24. C. R. Lu, J. R. Anderson, D. R. Stone, *et al.*, Phys. Rev. B: Condens. Matter **43**, 11 791 (1991).
25. H. Shen, M. Dutta, D. W. Eckart, *et al.*, J. Appl. Phys. **68**, 369 (1990).

Translated by A. Kirkin

Semiconductors, Vol. 34, No. 1, 2000, pp. 81–86. Translated from Fizika i Tekhnika Poluprovodnikov, Vol. 34, No. 1, 2000, pp. 81–85.

AMORPHOUS, VITREOUS, AND POROUS SEMICONDUCTORS

Energy Distribution of Localized States in Amorphous Hydrogenated Silicon

K. V. Kougiya*, E. I. Terukov, and I. N. Trapeznikova****

** St. Petersburg State Pediatric Academy, St. Petersburg, 194100 Russia*

*** Ioffe Physicotechnical Institute, Russian Academy of Sciences, Politekhnicheskaya ul. 26, St. Petersburg, 194021 Russia*

Submitted January 19, 1999; accepted for publication May 17, 1999

Abstract—A new method for determining the spectral dependence of the optical-absorption coefficient in amorphous hydrogenated silicon is suggested. The method is based on the analysis of spectral and temperature dependences of transient photoconductivity in this material. Energy distribution of localized states involved in recombination of nonequilibrium holes was calculated. © *2000 MAIK "Nauka/Interperiodica".*

INTRODUCTION

The constant-photoconductivity method that was suggested in [1, 2] and is still under development at the present time [3] remains one of the most convenient and rapid methods for determining the optical-absorption coefficient within a wide spectral range in photoconducting amorphous materials. A basic assumption inherent in this method is the supposition that there is a unique relation between the level of constant photoconductivity and the kinetics of its relaxation; to put it differently, it is assumed that the maintenance of a constant level of steady photoconductivity implies that the lifetime of photogenerated charge carriers is independent of the energy of the excitation-light quantum (i.e., $\sigma_{ph}(h\nu) = \text{const} \Rightarrow \tau(h\nu) = \text{const}$). Under these conditions, for small coefficients of optical absorption ($\alpha d \ll 1$, where d is the sample thickness), the photoconductivity is given by

$$\sigma_{ph}(h\nu) = en\mu = e\mu G\tau = e\mu\tau N_0(1-R)\alpha\eta, \quad (1)$$

where e is the elementary charge, n and μ are the concentration and mobility of the majority charge carriers (electrons in undoped material), G is the generation rate of electron–hole pairs, N_0 is the photon flux, η is the quantum yield, and R is the reflection coefficient. Since it is assumed that, in the case of steady photoconductivity, $\tau(h\nu) = \text{const}$ and η and R may be regarded as weakly dependent on the energy of photon, we finally arrive at

$$\alpha(h\nu) \sim N_0^{-1}, \quad (2)$$

which makes it possible to determine the spectral dependence of the reflection coefficient within a wide range.

However, as experimental data on the kinetics of photoconductivity measured under the conditions of $\sigma_{ph}(h\nu) = \text{const}$ show, the lifetime τ is not only photon-energy ($h\nu$) dependent (Fig. 1) but depends almost exponentially on $h\nu$ for $T \le 100$ K and $h\nu \le 1.9$ eV. Furthermore, at room temperature, the dependence $\tau(h\nu)$ has well pronounced features; the higher the structural perfection of the samples [4, 5], the more distinct these features are.

In this paper, we discuss the origin of spectral dependence of the kinetics of photoconductivity and develop the "kinetic-equation" method suitable both for a refined determination of $\alpha(h\nu)$ and for determination of the energy distribution of the localized-state density.

THE SAMPLES

The samples of amorphous hydrogenated Si (*a*-Si:H) studied in this work were prepared by RF decomposition of silane-containing gas mixtures in a system with capacitive coupling; the samples intended for measurements of photoconductivity were provided with sputtered contacts in coplanar configuration.

RESULTS AND DISCUSSION

We begin the discussion of experimental results with the temperature region in the vicinity of 100 K; in this region, the temperature-induced perturbations are the smallest. As shown previously, the features of photoconductivity at these temperatures can be interpreted in the context of a simple model; according to this model, the photoconductivity results from the hopping of electrons in the conduction-band tail, the holes are strongly localized and are almost at rest, and the recombination of nonequilibrium charge carriers occurs by tunneling [6, 7]. In such a model, the kinetics can be

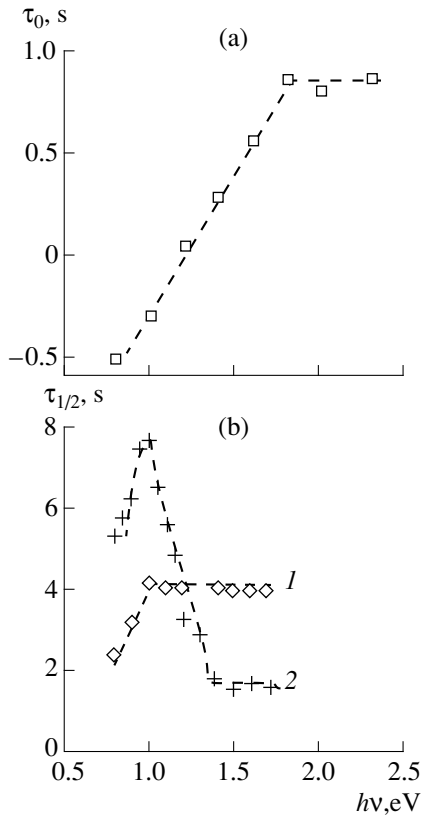

Fig. 1. Typical spectral dependences of characteristic decay times of photocurrent as measured under the conditions of constant photoconductivity: (a) T = 80 K, *a*-Si:H of unknown quality; (b) T = 293 K, with curve *1* corresponding to *a*-Si:H of "low" quality and curve *2* corresponding to device grade *a*-Si:H.

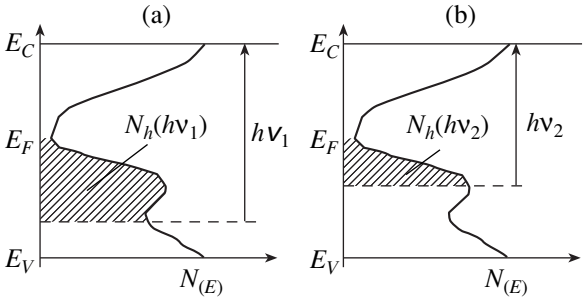

Fig. 2. Schematic diagram illustrating the origination of spectral dependence of concentration of hole localization centers ($h\nu_1 > h\nu_2$).

quantitatively evaluated with use of the equations

$$\sigma(t) = e\mu n(t) = e\mu p(t) = e\mu N_h \int_0^\infty g(r) f^{ss}(r, G) e^{-t/\tau(r)} dr, \quad (3)$$

and the steady-state photoconductivity can be calculated from

$$\sigma_{ss} = e\mu n_{ss} = e\mu p_{ss} = N_h \int_0^\infty g(r) f^{ss}(r, G) dr, \quad (4)$$

where n_{ss} and $n(t)$ are the concentrations of nonequilibrium electrons that are involved in photoconductivity and have the mobility μ, with n_{ss} corresponding to the steady state and $n(t)$ corresponding to relaxation after the illumination was switched off; p_{ss} and $p(t)$ stand for the corresponding concentrations of holes (we note that, at all points in time, we have $p = n$ according to the condition for electrical neutrality). The other notation is as follows: N_h is the concentration of centers of localization and recombination for the holes; $f^{ss}(r, G)$ is the occupancy function for these centers in the steady state; $\tau(r)$ stands for the lifetime of a hole at the specified center and is defined by the distance r to the nearest center of localization of electrons; and $g(r)$ is the distribution function for the distances r.

In the case where the distributions of localization centers for electrons and holes are uncorrelated, the following Reiss distribution [8] is valid for the function $g(r)$:

$$g(r) = \frac{3r^2}{R^3} \exp\left(-\frac{r^3}{R^3}\right). \quad (5)$$

Here, $R^3 = 3/(4\pi N_e)$, where N_e is the concentration of localization centers for electrons.

In the case of tunneling recombination, the lifetime $\tau(r)$ depends exponentially on the distance r; i.e., we have

$$\tau(r) = \nu_0^{-1} \exp(2r/a), \quad (6)$$

where $\nu_0 = 10^{12}$ Hz is the phonon frequency [9], and $a \approx 12$ Å is the localization radius for an electron [10].

Finally, for small G, the function for steady-state occupation $f^{ss}(r, G)$ is determined from the condition for the equality of the generation and recombination rates per a single localization center; i.e.,

$$G(1 - f^{ss}(r, G))/N_h = f^{ss}(r, G)/\tau(r). \quad (7)$$

As a result, we have

$$f^{ss}(r, G) = \frac{1}{1 + \dfrac{N_h}{G\tau(r)}}. \quad (8)$$

The existence of spectral dependence of the rate of photoconductivity decay from the initial constant level is equivalent to the absence of unique correlation between the level of steady-state photoconductivity and the kinetics of its relaxation. This means that there is no quasi-equilibrium in the system of nonequilibrium charge carriers; i.e., the distribution of these carriers

cannot be unambiguously described by specifying only the positions of the quasi-Fermi levels. If we take into account that the thermalization of nonequilibrium charge carriers (especially of holes, in view of the pronounced tail of the valence band) occurs very slowly at the temperatures under consideration, we may assume to the first approximation that each hole recombines from almost the same energy level at which it was generated. Consequently, there exists a dependence of concentration of the localized states involved in the process of recombination on the energy of excitation quanta, $N_h(h\nu)$; the latter function tends to increase with an increase in $h\nu$. All the aforementioned is illustrated in Fig. 2 where the schematic diagram clarifying the origin of the dependence $N_h(h\nu)$ is shown.

Under the conditions of steady-state photoconductivity, i.e., when $\sigma_{ss}(h\nu) = e\mu p_{ss}(h\nu) = \text{const}$, it follows from (4) and (8) that

$$\int_0^\infty \frac{g(r)}{1 + \dfrac{N_h(h\nu)}{G(h\nu)\tau(r)}}\,dr \sim \frac{\text{const}}{N_h(h\nu)}. \qquad (9)$$

In turn, it follows from (9) that, as $h\nu$ [and, consequently, $N_h(h\nu)$] increases, the integrand is bound to decrease, which can occur only owing to a decrease in the ratio $G(h\nu)/N_h(h\nu)$; the latter fact, as follows from a simple analysis, will cause the transient processes in photoconductivity to occur more slowly. On these grounds, it is possible to explain the fact that the rate of transient processes slows as the energy of excitation quantum increases under the conditions of constant photoconductivity. We discuss later the origin of the threshold appearing at $h\nu_{tr} \approx 1.9$ eV; above this threshold, the kinetics becomes independent of the energy of the photon.

Let us now abandon the sustenance of the constant level of steady-state photoconductivity and let us vary $G(h\nu)$ to ensure that the kinetic parameters of different processes corresponding to dissimilar energies of quanta coincide. As a result, we arrive at the "kinetics-equation" method that makes it possible to extend the ranges in which the spectral dependences of absorption coefficient can be determined, as compared to the constant-photoconductivity method. The equation of kinetics implies that it is the ratio $\sigma(t, h\nu)/\sigma_{ss}(h\nu) \equiv f(t)$ which is sustained independent of the energy of quanta; in this case, it is obvious that both the photoresponse time $\tau_0(h\nu) \equiv \lim\limits_{t\to 0} \dfrac{d\sigma(t, h\nu)}{dt}\dfrac{1}{\sigma_{ss}(h\nu)} \equiv \lim\limits_{t\to 0} f(t)$ and the steady-state lifetime $\tau(h\nu) = \text{const}(h\nu)$ are independent

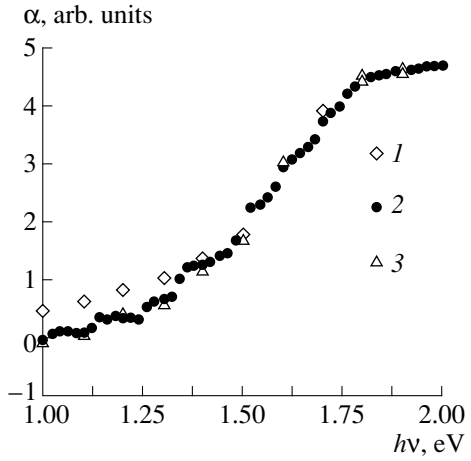

Fig. 3. Spectral dependences of the optical absorption coefficient as measured by the constant-photoconductivity method at (*1*) 293 and (*2*) 80 K and the method of equating the kinetics at (*3*) 80 K.

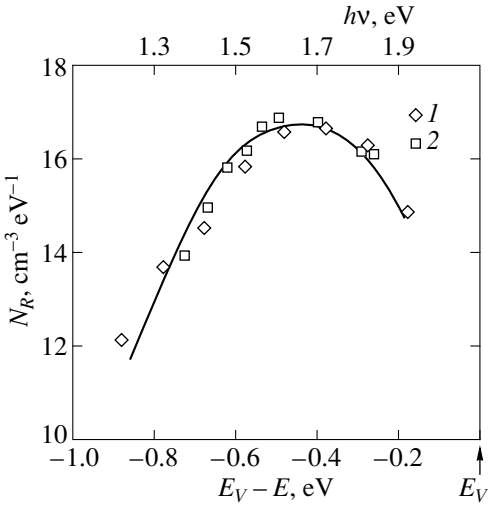

Fig. 4. Comparison of energy distributions for hole localization centers as obtained by processing the (*1*) spectral and (*2*) temperature dependences of the kinetics of photoconductivity.

of the energy of photon. Therefore, it follows from equation (1) that

$$\alpha(h\nu) \sim \sigma_{ss} N_0^{-1}. \qquad (10)$$

We emphasize that $\sigma_{ss}(h\nu)$ is the level of steady-state photoconductivity; this level should be kept such (by varying the photon flux N_0) that the independence of the rate of decay of photocurrent is ensured after the illumination is switched off.

Figure 3 shows spectral dependences $\alpha(h\nu)$ measured by the constant-photoconductivity method at 293

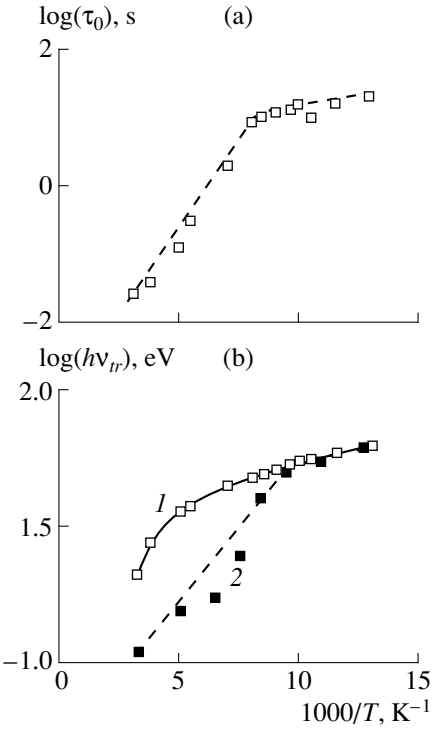

Fig. 5. Temperature dependences of (a) photoresponse time and (b) the photon threshold energy as (*1*) obtained experimentally and (*2*) calculated.

and 80 K and by equating the kinetics at 80 K, i.e., in the temperature range where the spectral dependence of photoconductivity is well pronounced. As is evident from Fig. 3, the constant-photoconductivity method yields an increase in $\alpha(h\nu)$ at 80 K, which may be erroneously regarded as indicating an increase in the density of localized states in the forbidden band. At the same temperature, the method of equating the kinetics yields results coinciding with the high-temperature data and eliminating the erroneous treatment of the data.

The second outcome of the method of equating the kinetics is found to be the possibility of determining the energy distribution of localized states available for nonequilibrium holes. In fact, the constancy of kinetics is equivalent to independence of the integrand in equation (3) [and, consequently, of the similar expression in equation (4)] on $h\nu$; thus, we may infer that, under the conditions of unvarying kinetics, we have

$$\sigma_{ss}(h\nu) \sim N_h(h\nu). \tag{11}$$

It is evident from Fig. 2 that, to the first approximation, we may assume that

$$N_h(h\nu) = \int_{E_\mu - h\nu}^{E_F} N_R(E)\,dE, \tag{12}$$

where $N_R(E)$ is the energy distribution of localization centers for holes, and E_μ is the mobility gap. Combining equations (11) and (12), we can determine the form of this distribution as

$$N_R(E = E_\mu - h\nu) = \frac{dN_h(h\nu)}{d(h\nu)} \sim \frac{d\sigma_{ss}(h\nu)}{d(h\nu)}. \tag{13}$$

The results of calculations with formula (13) are shown in Fig. 4, wherefrom it is evident that the curve of distribution of hole-related recombination centers is bell-shaped; in this case, the reference with respect to energy can be accomplished by using the value of $h\nu_{tr}$, as will be shown later.

We now direct our attention to the analysis of the threshold $h\nu_{tr}$, above which the photoconductivity kinetics ceases to depend on the energy of quanta of excitation radiation (Fig. 1). In general, the fact that the kinetics is independent of $h\nu$ for large energies of photons implies that thermalization of nonequilibrium holes occurs in two stages: following a rapid thermalization over the delocalized states and the pronounced tail of the valence band, a slow thermalization over the deeper states follows. Thus, it is expedient to assume that the value of $h\nu_{tr} = 1.9$ eV may be used to determine the mobility gap (E_μ).

It is obvious that, in the context of this approach, a decrease in the value of $h\nu_{tr}$ should occur as the temperature is elevated because the thermalization processes are promoted. As was mentioned above, such a decrease in $h\nu_{tr}$ would correlate with an increase in the rate of the corresponding processes [6]. Such a correlation is indeed observed, and an example is shown in Fig. 5.

This correlation between the quantities $h\nu_{tr}$ and τ_0 (the photoresponse time characterizing the rate of initial decay of photoconductivity) can be assessed quantitatively on the basis of a simple reasoning. To do this, it should be recalled that the photoresponse time τ_0 is controlled by depletion of the most rapid channels of recombination, whereas the value of threshold energy of photons specifies the "thermalization extent." To put it differently, the thermal emission of charge carriers from the states located at a distance from the mobility threshold of the valence band smaller than $E_\mu - h\nu_{tr}$ occurs in times shorter than the smallest recombination time. This simple reasoning shows that $h\nu_{tr}$ plays the role of a "threshold," at which the shortest recombination time (i.e., τ_0) and the time of thermal emission to delocalized states become comparable; the latter time is approximately equal to $\nu_0^{-1}\exp(-(E_\mu - h\nu_{tr})/kT)$. As a result, we arrive at the following expression relating $h\nu_{tr}$ to τ_0:

$$E_\mu - h\nu_{tr} \approx kT\ln(\nu_0\tau_0). \tag{14}$$

The results of calculation with formula (14) are shown in Fig. 5. The best agreement with the experiment is attained for the value of the mobility gap equal

to E_μ = 2.0 eV, which is consistent with the data reported in other publications [11].

Another method for "scanning" the energy distribution of localized states consists in variation of the temperature perturbation. In fact, an increase in temperature brings about a transformation of trapping centers into the recombination centers and, consequently, a decrease in the concentration of nonequilibrium charge carriers trapped at the localization centers. Thus, the temperature dependence of steady-state concentration of nonequilibrium holes can provide information about the energy distribution of localized states.

For moderately high temperatures corresponding to the generation rate of nonequilibrium charge carriers exceeding the rate of their thermal "mixing," it may be safely assumed that only the hole-localization centers, for which the specific generation rate exceeds the sum of the recombination and thermal-emission rates, are occupied; therefore, the steady-state concentration of nonequilibrium holes may be evaluated as

$$p^{ss}(T) \approx \iint g(r) N_R(E) dr dE, \qquad (15)$$

where $N_R(E)$ is the energy distribution of localization centers for holes, and the integration is performed over the region where the condition $\nu_0 \exp(-E/kT) + \nu_0 \exp(-2r/a) < G/N_h$ is satisfied.

As a crude simplification, it was assumed in (15) that the probability of thermal emission from a localized state to the valence band amounts to $\nu_0 \exp(-E/kT)$. To be more precise, this probability can be evaluated as $W(E)\exp(-E/kT)$, where $W(E)$ is the probability of transition of a hole from a delocalized state to the hole-localization center, with the use of the detailed balancing principle. For crystalline semiconductors, $W(E)$ is proportional to the cross section of trapping by the level and depends only slightly on the transition energy. In amorphous semiconductors, the wave function of a charge carrier is strongly modulated even in delocalized states; therefore, it would be more adequate to use $W(E)$ in the form suggested in [12].

Expression (15) may be further assessed as

$$p^{ss}(T) \approx \int_A^\infty N_R(E) dE \int_B^\infty g(r) dr, \qquad (16)$$

where $A = kT\ln(N_R^* \nu_0/G)$ and $B = a/2 \ln \dfrac{N_R^* \nu_0/G}{1 + (N_R^* \nu_0/G)\exp(-E/kT)}$.

For the sake of simplification, we replace $(1 + (N_R^* \nu_0/G)\exp(-E/kT))^{-1}$ with a step function, substitute expression (5) for the function $g(r)$, and finally obtain the following equation describing the temperature dependence of steady-state concentration of nonequilibrium holes:

$$p^{ss}(T) \approx \exp\left[-\left(\frac{a}{2R}\ln\frac{N_R^* \nu_0}{G}\right)^3\right] \int_C^\infty N_R(E) dE. \qquad (17)$$

Here, $C = kT\ln(N_R^* \nu_0/G)$.

Equation (17) makes it possible to calculate the energy distribution $N_R(E)$ of the hole recombination centers. In fact, introducing the notation

$$\varepsilon \equiv kT\ln(N_R^* \nu_0/G), \qquad (18)$$

we finally arrive at

$$N_R(\varepsilon) = \frac{\exp\left[\left(\dfrac{a}{2R}\ln\dfrac{N_h \nu_0}{G}\right)^3\right]}{kT\ln\dfrac{N_h \nu_0}{G}} dp^{ss}(T)/dT. \qquad (19)$$

Using the dependence $p^{ss}(T)$ obtained previously [7], we can calculate the energy distribution $N_R(E)$ for the hole recombination centers. The results of calculation are shown in Fig. 4. The obtained distribution is bell-shaped and can be matched to the distribution obtained by processing the spectral dependence for E_μ = 2.1 eV. Close resemblance between the shapes of the curves obtained by different methods and good agreement between the estimates of the mobility gap support the conclusion that the model developed here is based on consistent and self-consistent theory.

In conclusion, we dwell briefly on the spectral dependence of the kinetics of photoconductivity in the vicinity of room temperature. As is evident from Fig. 1, a well-pronounced peak is characteristic of corresponding curves in this temperature region; this fact may corrupt the data on the dependence $\alpha(h\nu)$ obtained by the constant-photoconductivity method. Unfortunately, in this case, we cannot use a correlation obtained by the kinetics-equation method because the processes occurring on different sides of the peak have dissimilar kinetics, and the corresponding kinetic parameters cannot be matched at any levels of generation. We plan to devote our next publication to comprehensive investigation of the origin of this peak.

ACKNOWLEDGMENTS

This work was supported by the International Science Foundation, grant no. 97–1910.

REFERENCES

1. M. Vanecek, J. Kocka, J. Stuchlik, *et al.*, Solid State Commun. **39**, 1199 (1982).

2. A. G. Kazanskiĭ and E. P. Milichevich, Fiz. Tekh. Poluprovodn. (Leningrad) **18**, 1819 (1984).
3. M. Vanecek, J. Kocka, A. Poruba, *et al.*, J. Appl. Phys. **78**, 6203 (1995).
4. K. Pierz, H. Mell, and E. I. Terukov, J. Non-Cryst. Solids **77–78**, 547 (1985).
5. K. V. Koughia and E. I. Terukov, J. Non-Cryst. Solids **137–138**, 603 (1991).
6. A. A. Andreev, A. V. Zherzdev, A. I. Kosarev, *et al.*, Solid State Commun. **52**, 589 (1984).
7. K. V. Kougiya, E. I. Terukov, and W. Fuhs, Fiz. Tekh. Poluprovodn. (St. Petersburg) **32**, 27 (1998).
8. H. Reiss, C. S. Fuller, and F. J. Morin, Bell Syst. Tech. J. **35**, 535 (1956).
9. V. Chech, F. Schauer, and J. Stuchlik, J. Non-Cryst. Solids (in press).
10. C. Tsang and R. A. Street, Phys. Rev. B: Condens. Matter **19**, 3027 (1979).
11. R. H. Bube, L. E. Benator, and K. P. Bube, J. Appl. Phys. **79**, 1926 (1996).
12. V. I. Abakumov, V. I. Perel', and I. N. Yassievich, Fiz. Tekh. Poluprovodn. (Leningrad) **12**, 3 (1978).

Translated by A. Spitsyn

Semiconductors, Vol. 34, No. 1, 2000, pp. 87–91. Translated from Fizika i Tekhnika Poluprovodnikov, Vol. 34, No. 1, 2000, pp. 86–89.

AMORPHOUS, VITREOUS, AND POROUS SEMICONDUCTORS

Modifications of the Structure and Electrical Parameters of the Films of Amorphous Hydrogenated Silicon Implanted with Si^+ Ions

O. A. Golikova*, A. N. Kuznetsov*, V. Kh. Kudoyarova*, I. N. Petrov, É. P. Domashevskaya***, and V. A. Terekhov*****

** Ioffe Physicotechnical Institute, Russian Academy of Sciences, Politekhnicheskaya ul. 26, St. Petersburg, 194021 Russia*
*** Elektron Central Research Institute, St. Petersburg, Russia*
**** Voronezh State Technical University, Moskovskii pr. 14, Voronezh, 394026 Russia*

Submitted June 3, 1999; accepted for publication June 8, 1999

Abstract—The influence of implantation of Si^+ ions with energies of 30, 60, and 120 keV was studied on the dark conductivity, photoconductivity, hydrogen concentration, microstructure parameter, and special features of the ultrasoft X-ray emission spectra of *a*-Si:H films that were deposited at T_s = 300°C by the dc-MASD and rf-PECVD methods and that differed in initial structural characteristics. © *2000 MAIK "Nauka/Interperiodica".*

1. INTRODUCTION

In [1, 2], the influence of implantation of Si^+ ions (T = 300 K and the dose $D = 10^{12}$–10^{14} cm^{-2}) on electrical characteristics of the films of amorphous hydrogenated silicon (*a*-Si:H) deposited by radio-frequency decomposition of silane in a glow discharge (rf-PECVD, an rf plasma-enhanced chemical vapor deposition) at a temperature of T_s = 300°C was studied. The results reported in [1, 2] indicated that there were certain similarities between the effects of ion implantation and those of long-term intense illumination of *a*-Si:H; the latter is known as the Staebler–Wronski effect. In particular, these similarities concern variations in dark conductivity σ_d, photoconductivity σ_{ph}, and also the activation energy for dark conductivity ΔE. The latter tends to the value of 0.85 eV; i.e., the Fermi level ε_F tends to the midposition within the mobility gap. It was concluded that, in both cases, the structural defects (the dangling Si–Si bonds) were formed owing to disruption of weak Si–Si bonds, rather than to disruption of Si–H bonds, the more so as the hydrogen concentration in *a*-Si:H films remained the same both after implantation and after illumination. In the films studied, hydrogen was present in the monohydride form (SiH).

The main objective of this study, as distinct from those in [1, 2], was to determine the influence of implantation of Si^+ ions with the energies of 30, 60, and 120 keV on the characteristics of *a*-Si:H films deposited by decomposition of SiH_4 in a magnetron chamber under dc conditions (the dc-MASD method, a dc magnetron-assisted silane decomposition) [3]. As demonstrated in [3], this method made it possible to widely vary the microstructure of the films (even at high temperatures T_s of deposition): silicon can be bonded to hydrogen in monohydride and dihydride forms (SiH and SiH_2), and also in the form of clusters $(SiH_2)_n$. In this case, the values of microstructure parameter R characterizing the contribution of SiH_2 bonds vary from zero to unity even for T_s = 300–400°C, which cannot be attained with the use of other known methods for deposition of *a*-Si:H.

In this work, we specially chose films prepared by the dc-MASD method (the MASD films), which were characterized by large values of the microstructure factor R = 0.65–0.75 before implantation. Previously, such films exhibited the highest stability of photoconductivity under long-term intense illumination (in fact, the Staebler–Wronski effect was not observed) [4]. Furthermore, in this paper, for the sake of comparison, we report the results of the studies of the influence of implantation on the characteristics of the films that were prepared by the rf-PECVD method (the PECVD films) and exhibited, conversely, the lowest stability of photoconductivity σ_{ph} under illumination [4].

2. EXPERIMENTAL

Implantation of Si^+ ions was performed at room temperature with the use of a heavy-ion accelerator; an SO-70 ion source was employed, and SiF_4 gaseous compound was used. In order to obtain a uniform distribution of the Si implant over the film thickness d equal to 3 μm, we used a three-stage implantation of each of the films with ion energies E = 30, 60, and

1063-7826/00/3401-0087$20.00

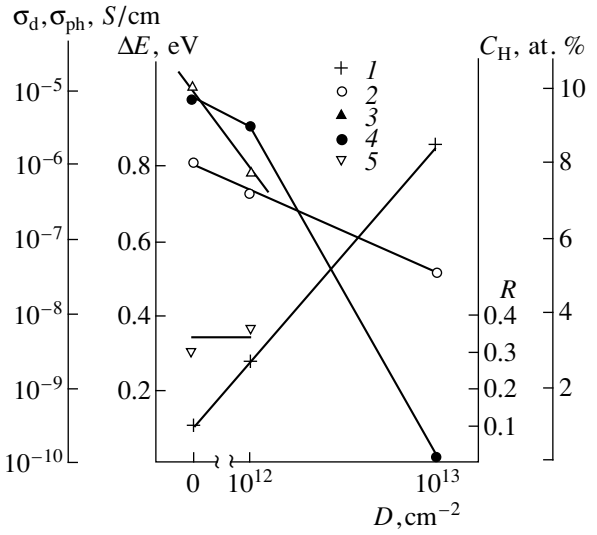

Fig. 1. Dependences of (*1*) dark conductivity σ_d, (*2*) photoconductivity σ_{ph}, (*3*) activation energy for dark conductivity ΔE, (*4*) hydrogen concentration C_H in the film, and (*5*) microstructure parameter R on the dose D of implantation of Si^+ ions for a MASD *a*-Si:H film. The values of ΔE determined at elevated temperatures (Fig. 5) are shown.

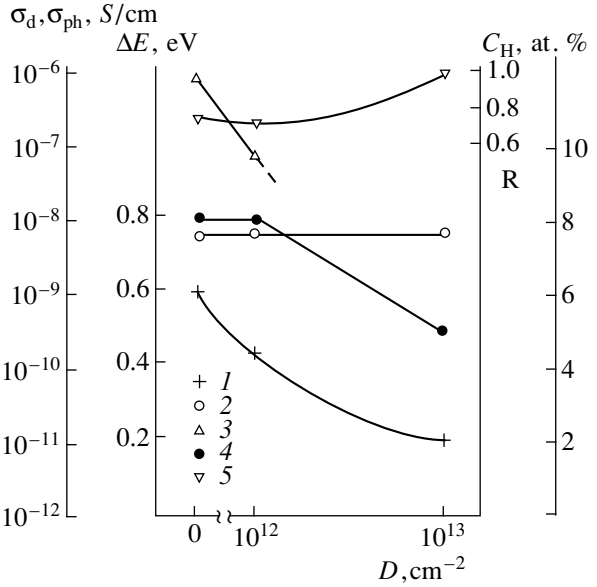

Fig. 2. The same parameters and the same symbols as in Fig. 1, but the data refer to a PECVD *a*-Si:H film.

120 keV and doses (D) varied in such a way as to ensure the required total dose D. Following the implantation, the samples were annealed in a vacuum at a pressure of $(3–4) \times 10^{-5}$ torr for 1h at 200°C [1, 2]. In this work, the total implantation doses were 10^{12} and 10^{13} cm^{-2}.

The MASD and PECVD films were deposited at T_s = 300°C. Both before and after implantation, we measured the dark conductivity in the temperature range of 250–470 K and photoconductivity at room temperature, with the photon energy of incident light 2 eV and the generation rate of photo-induced charge carriers 10^{19} cm^{-3} s^{-1}. The hydrogen content C_H in the films was determined by IR spectroscopy (the absorption band peaked at 630 cm^{-1} was analyzed). The microstructure parameter was conventionally determined from the following formula:

$$R = I_{2090}/(I_{2000} + I_{2090}).$$

Here, I_{2000} and I_{2090} are the magnitudes of absorption-band peaks at 2000 and 2090 cm^{-1}, which provide information about the concentration of SiH and SiH_2 bonds. We particularly considered the shift of the band characteristic of SiH bonds. It was done primarily to identify the $(SiH)_n$ clusters (typically, these clusters have the shape of islands or are located at the surface of voids that form a porous, so-called "grained," amorphous structure). In this case, the peak of the band characteristic of SiH bonds shifts to 2010 cm^{-1} [4]. Furthermore, if the peak under consideration shifts further to 2019–2020 cm^{-1}, the clusters are predominantly located at the boundaries of nanocrystalline inclusions [5]. To put it differently, the latter shift would strengthen the case for the existence of nanocrystalline inclusions in *a*-Si:H films.

In this work, the films were also studied by ultrasoft X-ray emission spectroscopy, both before and after ion implantation. The spectra of $L_{2,3}$ radiation of Si were measured; these spectra gave information about the partial density of all filled *s* states of Si (i.e., the states located below the Fermi level) [6]. The spectra were measured at room temperature, and the energy of electrons used for excitation was 3 keV.

3. RESULTS AND DISCUSSION

We now consider the typical dependences of dark conductivity, photoconductivity, activation energy for dark conductivity, hydrogen content in the films, and the microstructure parameter on the dose of implantation for the MASD and PECVD films (Figs. 1, 2). The parameters of the films prior to implantation (D = 0) are also shown. As is evident from Figs. 1 and 2, the initial parameters σ_d, σ_{ph}, ΔE, and C_H are almost the same for both types of films. At the same time, the MASD and PECVD films differ in the values of microstructure parameter (0.3, as compared to 0.75; see Figs. 1, 2) and in the forms of hydrogen incorporation in the films. In MASD film, the largest fraction of hydrogen (6 at. %) is in the form of SiH_2 and only 2 at. % of H is in the form of SiH, whereas, in a PECVD film, most of H is in the form of SiH (mainly, being incorporated in $(SiH)_n$ clusters) and only 3 at. % of H is in the form of SiH_2.

It follows from Figs. 1 and 2 that the effect of implantation on the parameters of a MASD film is markedly different from that of a PECVD film.

First of all, we draw attention to the fact that a PECVD film becomes completely devoid of hydrogen as a result of implantation, and, correspondingly, the film's electrical parameters change and approach the parameters of nonhydrogenated amorphous silicon; in contrast, this is not observed for a MASD film. Following the implantation with $D = 10^{13}$ cm^{-2}, about 5 at. % of hydrogen is still trapped in a MASD film. In fact, for $D = 10^{13}$ cm^{-2}, we have $R = 1$; i.e., hydrogen is incorporated in the form of SiH_2. Obviously, the SiH_2 complexes happen to be more stable than the SiH complexes; i.e., hydrogen incorporated in the form of SiH_2 features a much lower diffusivity. This conclusion is consistent with the results reported in [4, 7].

We draw attention to the fact that the Staebler–Wronski effect necessarily relies on the hydrogen diffusion that exists in *a*-Si:H at any finite temperature [8] and, for T = const and C_H = const, directly depends on hydrogen mobility. Therefore, a high stability of σ_{ph} in the MASD films with large R is caused by low mobility of hydrogen [4].

It should be also recalled that the shifts of the Fermi level to the middle of the mobility gap of *a*-Si:H are characteristic of the Staebler–Wronski effect; in this case, the activation energy for σ_d amounts to 0.85 eV. Such a phenomenon was also observed in PECVED films of *a*-Si:H after implantation of Si^+ ions [1, 2] if hydrogen in these films was predominantly in the form of SiH.

At the same time, as is evident from Fig. 1, the value of ΔE for a MASD film with initial $R = 0.75$ is constant; i.e., shifts of the Fermi level are not observed. This is also consistent with actual absence of the Staebler–Wronski effect in such films [4]. A decrease in σ_d and, especially, in σ_{ph} (Fig. 2), is then apparently caused by an increase in R, with $R = 1$ attaining the value of unity for $D = 10^{13}$ cm^{-2}; previously [3], this was also observed for unimplanted films having $R = 1$.

We now consider the results of studying the films by ultrasoft X-ray spectroscopy. We restrict ourselves to consideration of the $L_{2,3}$ Si spectra related to the valence-band states (Figs. 3, 4). As previously demonstrated [6], the shape of these spectra is extremely sensitive to the extent of ordering of the structural network of Si.

Figure 3 shows the spectra for two unimplanted PECVD and MASD films deposited at $T_s = 300$°C; the spectra are in close agreement with each other and are represented by common curve *1*. In this curve, the gently sloping principal peak of the density of the Si *s* states in the valence band for $E_v - E = 7$–9 eV (E_v corresponds to the valence-band edge); this peak is characteristic of amorphous silicon [6]. Curve *2* refers also to the implanted PECVD film of *a*-Si:H; however, this film contains nanocrystalline inclusions of Si. This was established by analyzing the Raman spectrum: in the vicinity of the TO band typical of amorphous silicon, a band peaked at 515 cm^{-1} was observed (this film was also deposited at $T_s = 300$°C and was previously studied in [5]). The data obtained by IR spectroscopy were also indicative of the presence of nanocrystalline inclusions: the peak of the band characteristic of SiH bonds was positioned at 2019 cm^{-1} rather than at 2000 cm^{-1} [5].

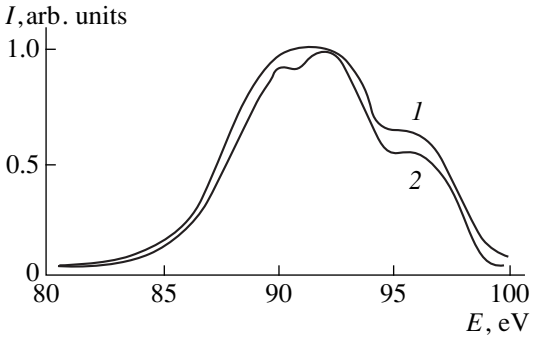

Fig. 3. X-ray emission spectra for *a*-Si:H films deposited at $T_s = 300$°C by (*1*) the dc-MASD and rf-PECVD methods (the coinciding spectra) and (*2*) the rf-PECVD method (the film contains the crystalline-Si nanoinclusions formed in the course of deposition). The films were not subjected to ion implantation.

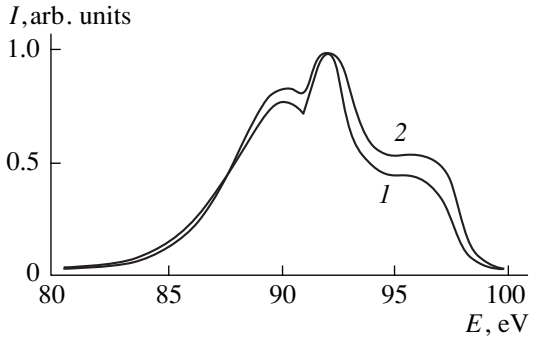

Fig. 4. X-ray emission spectra of (*1*) crystalline Si and (*2*) the *a*-Si:H film after implantation of Si^+ with $D = 10^{13}$ cm^{-2}.

On the basis of estimates obtained with the use of universally accepted methods [9], we determined the sizes of nanocrystals ($d_{Raman} \simeq 5$ nm) and their volume fraction ($X_c \simeq 10\%$); with a comparatively small contribution of crystalline phase, the X-ray emission spectrum of this film undergoes significant changes: the main peak ceases to be featureless (Fig. 3, curve *2*).

The spectrum of crystalline silicon [6] (Fig. 4, curve *1*) has well-pronounced features: the main peak splits into two peaks. It follows from Fig. 4 (curve *2*)

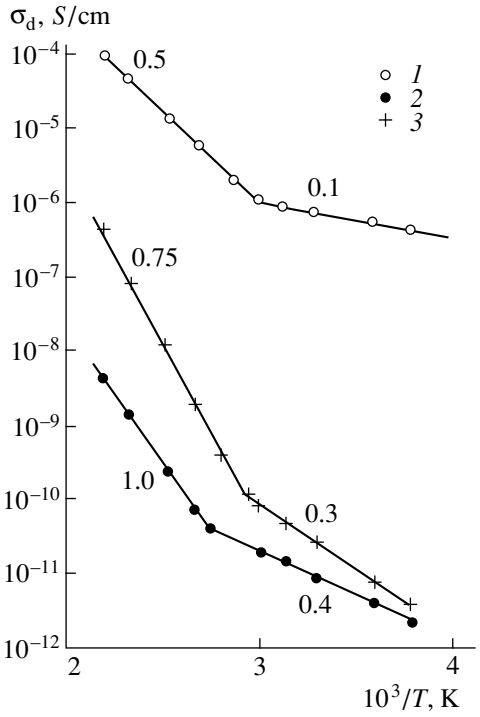

Fig. 5. Temperature dependences of dark conductivity in *a*-Si:H films after implantation of Si^+ ions ($D = 10^{13}$ cm^{-2}) (curves *1* and *2*). Curve *3* corresponds to the film containing the nanoinclusions of crystalline silicon formed in the course of deposition. Activation energies ΔE (expressed in eV) of dark conductivity in the films are indicated by the numbers at the curves.

that both the PECVD and MASD *a*-Si:H films studied in this work partially crystallize as a result of Si^+ implantation. Furthermore, by comparing the spectra shown in Figs. 3 and 4 (curves *2*), we may conclude that the role of crystalline phase in implanted films is more important than that in unimplanted films studied in [5].

We now consider the temperature dependences of dark conductivity σ_d in the films studied in this work (Fig. 5). All the curves shown in Fig. 5 feature inflection points; i.e., the activation energies of σ_d differ for lower and higher temperatures: in the former case, ΔE is appreciably smaller than in the latter case. Thus, a transition is observed from the conduction related to the existence of crystalline phase in the films to the conduction in amorphous phase. This inference is qualitatively consistent with the results reported in [9]. However, at this stage of study, it would be incorrect to perform any quantitative comparisons of the results, in particular, of the values of σ_d for comparatively low temperatures, of the activation energies of σ_d, or of the temperatures corresponding to the inflection points in $\sigma_d = f(10^3/T)$ dependences for various films. In fact, in order to perform this comparison, we would require quantitative information about (i) the role of crystalline phase and the sizes of crystalline inclusions and (ii) to what extent the distribution of these inclusions is uniform in the films.

4. CONCLUSION

In this work, we studied for the first time the effect of Si^+ ion implantation on *a*-Si:H films that were deposited by the MASD method and featured large values of the microstructure parameter $R = 0.65$–0.75. As previously shown [4, 7], films of this type do not actually exhibit the Staebler–Wronski effect and have an enhanced thermal stability, which was related to the special features of their structure: hydrogen in the form of SiH_2 is largely mainly located at the surface of microvoids that are at a considerable distance from one another; as a result, the mobility of hydrogen in the course of diffusion is drastically decreased [7].

The structure of these films may be conceived as consisting of an amorphous Si matrix involving a low amount of hydrogen in the form of SiH and incorporating the inclusions of $(SiH_2)_n$ clusters. This structural model is also supported by the results of this work; in fact, following the implantation of Si^+ into the *a*-Si:H MASD films, all hydrogen in the form of SiH_2 virtually remains in the films.

In contrast, the presence of clusters $(SiH)_n$ in the structure of PECVD films results in a complete loss of hydrogen under the effect of Si^+ implantation with a dose of $D = 10^{13}$ cm^{-2}. It should be remembered that the Staebler–Wronski effect is most pronounced for such films [4].

As compared to our previous results [1, 2], we observed here a new effect of implantation of Si^+ ions with energies of 30–120 keV on *a*-Si:H films: the formation of crystalline inclusions in the films containing the $(SiH_2)_n$ or $(SiH)_n$ clusters. This was established on analyzing the films by ultrasoft X-ray emission spectroscopy and was supported by the results of corresponding electrical measurements.

We believe that it is the $(SiH_2)_n$ or $(SiH)_n$ clusters that are responsible for the formation of crystalline inclusions; apparently, these clusters act as peculiar centers of crystallization that sets in at low energies of implanted ions. Typically, for the crystallization of amorphous silicon film to set in, implantation with ion energies of several megaelectronvolts is required [10], so that local heating sufficient for formation of small crystalline clusters (crystallization centers) is ensured.

ACKNOWLEDGMENTS

We thank R.R. Yafaev and Kh.S. Mavlyanov for their assistance in conducting this work.

REFERENCES

1. O. A. Golikova, Kh. Yu. Mavlyanov, I. N. Petrov, *et al.*, Fiz. Tekh. Poluprovodn. (St. Petersburg) **29**, 577 (1995).

2. O. A. Golikova, Fiz. Tekh. Poluprovodn. (St. Petersburg) **33**, 464 (1999).
3. O. A. Golikova, A. N. Kuznetsov, V. Kh. Kudoyarova, *et al.*, Fiz. Tekh. Poluprovodn. (St. Petersburg) **31**, 816 (1997).
4. O. A. Golikova, M. M. Kazanin, and V. Kh. Kudoyarova, Fiz. Tekh. Poluprovodn. (St. Petersburg) **32**, 484 (1998).
5. O. A. Golikova and V. Kh. Kudoyarova, Fiz. Tekh. Poluprovodn. (St. Petersburg) **29**, 1128 (1995).
6. V. A. Terekhov, Doctoral Dissertation in Physics and Mathematics, Voronezh (1994).
7. R. Zellama, L. Chahed, P. Sladec, *et al*., Phys. Rev. B: Condens. Matter **53**, 3804 (1995).
8. M. Stutzmann, W. B. Jackson, and C. C. Tsai, Phys. Rev. B: Condens. Matter **34**, 63 (1986).
9. Y. He, C. Yin, G. Cheng, *et al.*, J. Appl. Phys. **75**, 797 (1994).
10. L. A. Marques, M.–J. Caturla, H. Huang, *et al.*, Mater. Res. Symp. Proc. **396**, 201 (1996).

Translated by A. Spitsyn

Semiconductors, Vol. 34, No. 1, 2000, pp. 92–94. Translated from Fizika i Tekhnika Poluprovodnikov, Vol. 34, No. 1, 2000, pp. 90–92.

AMORPHOUS, VITREOUS, AND POROUS SEMICONDUCTORS

The Influence of Local Surroundings of Er Atoms on the Kinetics of Decay of Er Photoluminescence in Amorphous Hydrogenated Silicon

E. I. Terukov*, V. Kh. Kudoyarova*, O. I. Kon'kov*, E. A. Konstantinova, B. V. Kamenev**, and V. Yu. Timoshenko****

** Ioffe Physicotechnical Institute, Russian Academy of Sciences, Politekhnicheskaya ul. 26, St. Petersburg, 194021 Russia*
*** Moscow State University, Vorob'evy gory, Moscow, 119899 Russia*

Submitted June 25, 1999; accepted for publication June 28, 1999

Abstract—Kinetics of the decay of photoluminescence of Er impurity in the films of amorphous hydrogenated Si *a*-Si:H⟨Er⟩ was studied for the first time. The films were obtained either by cosputtering of Si and Er targets with the use of the technology of dc silane decomposition in a magnetic field (MASD) or by radio-frequency decomposition of silane. In the second case, an $Er(TMHD)_3$ polymer powder was used as the source of Er. It is shown that, at room temperature, the *a*-Si:H⟨Er⟩ films obtained by the MASD method feature the characteristic times of Er photoluminescence decay equal to 10–15 μs, which is 20 times smaller than in the case of Er-doped crystalline Si (*c*-Si⟨Er, O⟩) as measured at liquid-nitrogen temperature. For the *a*-Si:H⟨Er⟩ films obtained by radio-frequency decomposition of silane, the decay times of Er photoluminescence amount to 2 μs. The difference in the photoluminescence decay times is related to dissimilarities in the local surroundings of Er atoms in the *a*-Si:H⟨Er⟩ films obtained by different methods. © *2000 MAIK "Nauka/Interperiodica".*

1. INTRODUCTION

Interest in studies of photoluminescence (PL) of rare-earth (RE) ions in solids is motivated by the possibility of developing light-emitting diodes (LEDs) that operate at room temperature and can easily be incorporated in integrated systems based on inexpensive silicon technology. The RE ion of the most interest is the Er ion whose emission at a wavelength of 1.54 μm corresponds to a minimum of losses in an optical quartz fiber.

One of the important parameters characterizing the possibility of using a specific semiconducting material for fabrication of LEDs is the lifetime of the Er excited state.

In crystalline silicon doped with Er and O by ion implantation, the excited state of Er has a long lifetime (1–2 ms), which causes the luminescence to be saturated at relatively low levels of excitation. This fact makes it difficult to design efficient luminescent structures based on this material [1]. Recently, much attention has been given to studies of the photoluminescent and electroluminescent properties of *a*-Si:H doped with erbium [*a*-Si:H⟨Er⟩]. This material can be easily incorporated in existing silicon technology and is promising for the development of LEDs emitting at a wavelength of 1.54 μm.

Previously, we have studied the Er PL in amorphous hydrogenated silicon *a*-Si:H⟨Er, O⟩ in relation to temperature and to frequency and power of excitation. It was shown that, in this material, the intensity of Er PL decreases by a mere 20–30% when the temperature T increases from 4.2 to 300 K [2, 3]; at the same time, in crystalline Si (*c*-Si⟨Er, O⟩), PL becomes difficult to detect even at liquid-nitrogen temperature ($T = 77$ K) [4].

It is well known that Er PL in *c*-Si⟨Er, O⟩ depends on the power of excitation and is typical of systems with a finite number of emitting centers that have long lifetimes of an excited state [5]. Our previous experiments with *a*-Si:H⟨Er⟩ have shown that saturation of PL sets in at excitation intensity of about 50 W/cm^2. Such intensities exceed those characteristic of *c*-Si⟨Er, O⟩, which suggests that the lifetime of the Er excited state in *a*-Si:H⟨Er, O⟩ is much shorter than that in *c*-Si⟨Er, O⟩. Direct information about the lifetime of the excited state is typically obtained from studies of PL decay kinetics.

In this paper, we report for the first time the results of studies of the excited-state lifetime of Er in the matrix of *a*-Si:H; the data were obtained from the measurements of kinetics of the Er PL decay.

2. EXPERIMENTAL

The *a*-Si:H⟨Er⟩ films were obtained by two methods. The first method involved the cosputtering of Si and Er targets with the use of technology of silane decomposition in the dc mode (the dc decomposition) in a magnetic field. A conventional reactor designed for magnetron sputtering was employed. However, an argon–oxygen–silane, rather than an argon–hydrogen mixture, was used to prepare the films; thus, this

1063-7826/00/3401-0092$20.00 © 2000 MAIK "Nauka/Interperiodica"

method is referred to as the magnetron-assisted silane decomposition (MASD) [6]. The second method involved the radio-frequency (RF) decomposition of silane; an $Er(TMHD)_3$ powder heated to temperatures higher than 160°C served as a source of Er; this method for preparation of *a*-Si:H⟨Er⟩ films was described in detail elsewhere [7, 8].

The films were grown on the substrates of quartz and crystalline silicon.

The composition of the *a*-Si:H films (i.e., the content of Er, O, C, and H) was determined by secondary-ion mass spectroscopy (SIMS) and Rutherford backscattering (RBS). In order to find whether or not there are bonds between the atoms of the basic Si matrix and the light impurities of O, C, and H atoms and to identify the type of these bonds, we used infrared (IR) spectroscopy.

The kinetics of Er PL decay was studied with the use of excitation by the pulses of nitrogen-laser radiation with the wavelength $\lambda = 337$ nm, duration of a pulse being 10 ns, and the specific power $P = 0.01$ mJ/cm^2. The PL signal was selected by a monochromator at the maximum of the emission band. A cooled germanium detector with the time resolution of 0.3 μs was used to detect the signal.

3. RESULTS

Typical curves of decay of the PL intensity I with time t for the *a*-Si:H⟨Er⟩ samples obtained by MASD and by the RF decomposition of silane are shown in the figure. A thorough analysis showed that the decay curves could not be approximated by a single exponential function of time t. The PL decay is best approximated by the extended exponential function given by

$$I = I_0 \exp(-t/\tau)^b, \quad (1)$$

where τ is the lifetime of the excited state and b is the factor of nonexponentiality. Thus, if $b \approx 1$, the PL-decay kinetics is close to single-exponential.

Approximation of the experimental kinetics by expression (1) shows that the samples obtained by MASD feature the characteristic PL-decay times of tens of microseconds (10–15 μs) and the nonexponentiality factor $b = 0.53$. Such a value of the nonexponentiality factor can indicate that it is possible to approximate the PL-decay kinetics by two exponential functions and can indicate the presence (as in the case of crystalline Si doped with Er and O) of two different types of PL centers. The possibility that Er ion can exist with different local surroundings is supported by the data obtained by studying the Mössbauer effect and by IR spectroscopy [9, 10]. The Mössbauer spectroscopy studies have shown that, in the samples under consideration, a fraction of Er atoms exist in the configuration with the local surroundings close to Er_2O_3; other Er atoms are involved in the $ErSi_2$ configuration. The fraction of Er atoms found with local surroundings close to Er_2O_3 depends on oxygen concentration. The figure shows the results of studying the kinetics of Er PL decay in a MASD sample optimized with respect to the ratio between the oxygen and erbium concentrations; in this case, this ratio was 10 : 1.

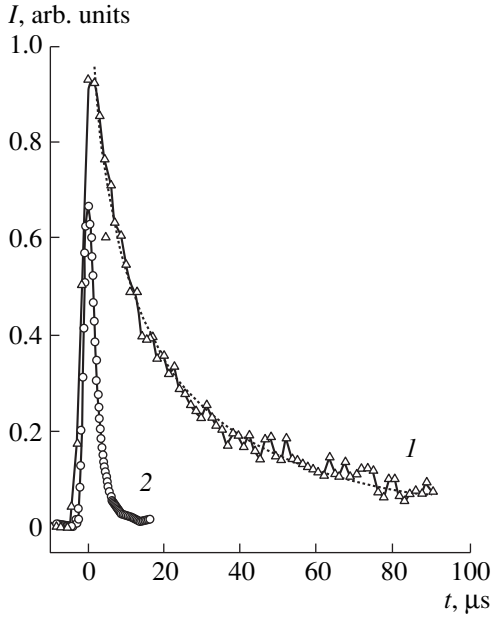

The decay kinetics of Er PL at room temperature for the *a*-Si:H⟨Er⟩ films obtained by (*1*) MASD and by (*2*) the method of RF silane decomposition. Triangles and circles correspond to experimental data. The lines represent the results of approximation by expression (1). The parameters of approximation are (*1*) $\tau = 11.8$ μs and $b = 0.53$ and (*2*) $\tau = 2.1$ μs and $b \simeq 1$.

For the (*a*-Si:H)⟨Er⟩ samples obtained by RF decomposition of silane and by doping with Er by thermal decomposition of $Er(TMHD)_3$ polymer powder, the studies of the PL-decay kinetics showed that the characteristic PL-decay times could be even shorter (~2 μs), with the nonexponentiality factor b being approximately equal to unity. The SIMS, RBS, and IR-spectroscopy studies have shown that the local surroundings of Er atoms in these samples differ from the local surroundings in the samples obtain by MASD [7, 10]. On the basis of the fact that the distribution of C, O, and H correlates with the distribution of Er and that there is no indications of formation of bonds between the atoms of the basic Si matrix and C atoms, we may assume that Er atoms have local surroundings which constitute the remainder of the polymer that was used for doping and that decomposed only partially. Apparently, Er atoms have local surroundings whose symmetry is lower than that of Er_2O_3.

4. CONCLUSION

In this work, the kinetics of Er PL decay in *a*-Si:H was studied for the first time. It is shown that the lifetimes of the Er excited state at room temperature in the *a*-Si:H⟨Er⟩ films obtained by MASD amount to 10–15 μs. These values are 20 times smaller than those obtained in crystalline silicon at liquid-nitrogen temperature.

The characteristic times for Er PL decay can be even shorter (2 μs) in the *a*-Si:H⟨Er⟩ obtained by RF decomposition of silane; this is indicative of the influence of local surroundings of Er atoms on the kinetics of PL decay.

ACKNOWLEDGMENTS

We are grateful to A.N. Kuznetsov for preparation of *a*-Si:H⟨Er⟩ films by MASD.

This work was supported by INCO-COPERNICUS, grant no. 977048-SIER.

REFERENCES

1. S. Coffa, G. Franzo, F. Priolo, *et al.*, Phys. Rev. B: Condens. Matter **49**, 16313 (1994).
2. M. S. Bresler, O. D. Gusev, V. Kh. Kudoyarova, *et al.*, Appl. Phys. Lett. **67**, 3599 (1995).
3. W. Fuhs, I. Ulber, G. Weiser, *et al.*, Phys. Rev. B: Condens. Matter **56** (15), 9545 (1997).
4. F. Priolo, G. Franzo, S. Coffa, *et al.*, J. Appl. Phys. **78**, 3874 (1995).
5. M. Kechouane, N. Beldi, T. Mohammed-Brohim, *et al.*, Mater. Res. Soc. Symp. Proc. **301**, 133 (1993).
6. V. Marakhonov, N. Rogachev, J. Ishkalov, *et al.*, J. Non-Cryst. Solids **137–138**, 817 (1991).
7. E. I. Terukov, O. I. Kon'kov, V. Kh. Kudoyarova, *et al.*, Fiz. Tekh. Poluprovodn. (St. Petersburg) **32**, 987 (1998).
8. E. I. Terukov, O. I. Kon'kov, V. Kh. Kudoyarova, *et al.*, Fiz. Tekh. Poluprovodn. (St. Petersburg) **33** (2), 208 (1999).
9. V. F. Masterov, F. S. Nasredinov, P. P. Seregin, *et al.*, Pis'ma Zh. Tekh. Fiz. **22** (12), 960 (1996).
10. V. Kh. Kudoyarova, A. N. Kuznetsov, E. I. Terukov, *et al.*, Fiz. Tekh. Poluprovodn. (St. Petersburg) **32**, 124 (1998).

Translated by A. Spitsyn

Semiconductors, Vol. 34, No. 1, 2000, pp. 95–97. Translated from Fizika i Tekhnika Poluprovodnikov, Vol. 34, No. 1, 2000, pp. 93–95.

AMORPHOUS, VITREOUS, AND POROUS SEMICONDUCTORS

Crystal–Glass Phase Transition Induced by Pulses of Electric Field in Chalcogenide Semiconductors

É. A. Lebedev*, K. D. Tséndin, L. P. Kazakova

Ioffe Physicotechnical Institute, Russian Academy of Sciences, St. Petersburg, 194021 Russia
**e-mail: kazakova@pop.ioffe.rssi.ru*

Submitted July 14, 1999; accepted for publication July 15, 1999

Abstract—It is shown that the minimum power of an electric field which induces the crystal–glass phase transition in micrometer-thick films of chalcogenide semiconductors does not depend on pulse duration τ for $\tau >$ 10 μs and increases, as τ decreases to $\tau <$ 1–3 μs. The dependence obtained is similar to that observed for crystal–glass phase transition induced by pulses of laser radiation. © *2000 MAIK "Nauka/Interperiodica".*

INTRODUCTION

It is known that application of a high electric field on the order of 10^5 V/cm to vitreous chalcogenide semiconductors (VCS) induces semiconductor–metal phase transition [1]. Depending on VCS composition, electric field strength and duration, two types of the conductivity phase transitions are possible. In VCS stable with respect to crystallization ($Si_{12}Te_{48}As_{30}Ge_{10}$ is a classical example), the reverse transition to the initial state characterized by low conductivity occurs after termination of a short voltage pulse that induced transition to the state with high conductivity. Since the state with low conductivity is semiconducting and the state with high conductivity is metallic, the aforementioned transition is named a reversible semiconductor–metal phase transition. In VCS of a composition with good crystallization properties (for instance, $Te_{81}As_4Ge_{15}$), after a sufficiently long impact of electric field, the metal-type state characterized by high conductivity is "memorized" and exists after the voltage is switched off. In this case, the semiconductor–metal phase transition which is related to structural modifications, occurs because it is known that the zone of high conductivity is a crystallized channel.

In both the aforementioned cases, a current filament of a radius of about 1 μm and filament current density of about 10^4 A/cm^2 is formed in the state of high conductivity. It is believed that, prior to the formation of the crystal channel, the metal-type state in the second case has the same nature, as in the first case. The structural glass–crystal phase transition occurs in films of a micrometer thickness usually after a voltage pulse of duration $\tau \simeq 10^{-3}$ s is applied. In this case the reversibility can be attained by application of a new sufficiently powerful pulse ($\tau \simeq 10^{-6}$ s) which, having melted the crystallized channel (memory erasure), transforms it again into the vitreous state, i.e. completes the reverse crystal–glass transition.

Evaluations show [1, 2] that during both the direct and reverse transitions, strong heating takes place in the current filament region. Thereby, the crystal–glass phase transition in memory cells is performed under conditions of high temperature existing for a short period of time ($\tau \simeq 10^{-6}$ s). In [3, 4], we described a mechanism of crystal–glass transition that takes place under the action of laser radiation pulses. The main result obtained in [3, 4] is the detection of appreciable variations of characteristics of transitions that take place under exposure to short ($\tau > 10^{-6}$ s) and long ($\tau > 10^{-5}$ s) pulses of radiation. This study is aimed at elucidating the role of the similar mechanism in crystal–glass phase transitions under the action of an electric field.

EXPERIMENTAL

The samples for investigation were thin layers of $Te_{81}As_4Ge_{15}$ in composition, with a thickness of L = 0.5–1 μm and an area of $ld = 10^{-3} \times 10^{-2}$ cm^{-2}; the layers were obtained by evaporation in a vacuum onto Pyroceram substrates and were of planar configuration with linear dimension (width) l of electrodes and length d of the film in the interelectrode gap. Gold was used as the electrode material. A thin layer of SiO_2 was applied on the VCS layers for encapsulation. In the same manner, as in [3, 4], the initial films were subject to treatment at a temperature of 540 K for 0.5–1 h; as a result of the treatment, these films transformed into the polycrystalline state and their resistance decreased from $R \simeq 10^5\ \Omega$ to $R \simeq 10^2\ \Omega$.

To study the process of the crystal–glass transition, we applied the voltage pulses of various durations to the samples.

1063-7826/00/3401-0095$20.00

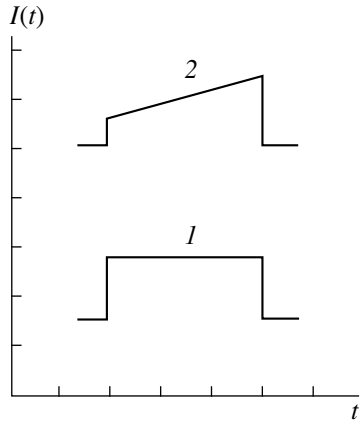

Fig. 1. The shape of the first (*1*) and the second (*2*) current pulses when applied to the sample the rectangular voltage pulses of duration 0.3 μs. *U*: (*1*) 20 and (*2*) 30 V. For the time axis *t*, we have 0.1 μs scale division; and for the current axis *I*, we have 50 mA scale division.

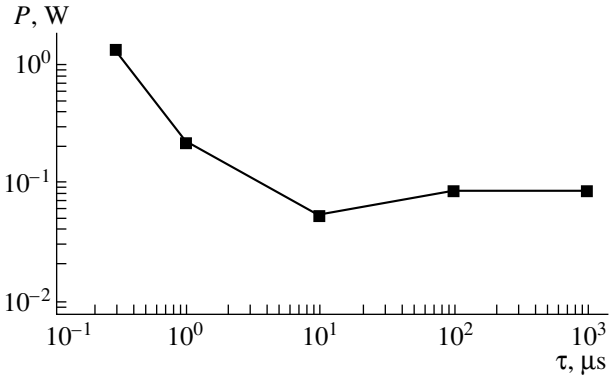

Fig. 2 Voltage-pulse duration (*t*) dependence of minimal power (*P*) of electric field pulses which results in an increase in the sample resistance

EXPERIMENTAL RESULTS AND DISCUSSION

Results of detailed investigations showed that the mechanism of the crystal–glass transition significantly depends on the voltage-pulse duration.

Pulses of duration longer than 10 μs and of a certain amplitude induce transition from initial low resistance to a high resistance of $R \simeq 10^4$–10^5 Ω. When applying voltage pulses, a rectangular current pulse whose amplitude is independent of time is recorded. The fact that the current is time-independent indicates that conductivity does not increase with temperature for the time corresponding to the current pulse duration and, hence, testifies to metal-type behavior of the temperature dependence of conductivity. With an increase in the pulse voltage *U*, current-pulse amplitude increased proportionally. The current-pulse shape *I*(*t*) was constant up to the attainment of a certain amplitude. After application of a voltage pulse of amplitude about 5 V, the sample resistance increased by 2–3 orders of magnitude. The increase in this voltage by 0.5–1 V resulted in the sample destruction. A sharp increase in the sample resistance is related to the attainment of the current magnitude that causes a temperature increase up to the melting point of the sample; therefore, a small temperature increase results in its destruction.

For short pulses of duration $t \simeq 0.1$ μs, the voltage range in which resistance variation can be observed was much wider than that for pulses of $\tau > 10$ μs and amounted to 10-20 V. As a result of the short-pulse effect, various sample resistances which increased with an increase in the pulse amplitude and duration were obtained. Thus, with the use of pulses of duration $t \simeq 0.3$ μs and a minimum power of 1 W the resistance increased only by a factor of 2–3. In this case, a change of the shape of the subsequent current pulses could be observed. The first and the second pulses are shown in Fig. 1. As seen from Fig. 1, the first pulse was rectangular and the amplitude of the second pulse increased in time.

The change of the pulse shape was related to the fact that, along with an increase in the resistance, it became dependent on temperature. Subsequent pulses induced a further increase of the resistance and enhanced its temperature dependence. Since in this case the resistance increased only several times and an increase in the resistance completely up to the initial value (as in the case of pulses of $\tau > 10$ μs) was not observed, this result indicates that, for the crystal–glass phase transition to be realized, it is important to attain the melting point as well as to provide the sufficient time of the temperature effect for transitions into the initial vitreous state of high resistance.

Figure 2 shows the dependence $P(\tau)$ of the minimal power *P* that induces an increase in the sample resistance related to the crystal–glass phase transition on the duration $P(\tau)$ of applied-voltage pulse. For $\tau > 10$ μs, this dependence looks like a plateau, and, for smaller τ, an increase in the power is observed as τ decreases.

We treat these data by assuming that a temperature, up to which the film is required to be heated to complete the crystal–glass transition, is constant and is approximately equal to the crystal melting point of $T_m \simeq 650$ K. Then, to the approximation that temperature does not depend on coordinates, the heat-conduction equation is written as

$$\rho c dT/dt = (P/V) - \lambda(T - T_0), \qquad (1)$$

where ρ is density, *c* is the specific heat, *V* is the heated volume, λ is the factor defining the external heat removal, and T_0 is the ambient temperature.

For large values of $\tau > 10$ μs, the transition takes place at a steady-state temperature and, equating the temperature derivative with respect to time to zero, we use (1) to obtain

$$P = V\lambda(T_m - T_0);$$

i.e., actually in agreement with the experiment, P is independent of τ for $\tau > 10$ μs. In case of the heat removal to the substrate across the film, the intrinsic time (τ_r) of the heat relaxation of films of thickness of about 1 μm is $\tau_r = \rho c L^2/\kappa \simeq 1$ μs, where κ is thermal conductivity of the VCS film. Considering for evaluation that, for $\tau \le \tau_r$, the adiabatic heating of the film takes place, we use (1) to obtain

$$P = \rho c V(T_m - T_0)/\tau \sim 1/\tau.$$

It is precisely this dependence that is observed in experiments for $\tau < 1$ μs (Fig. 2). Thus, we may conclude that dependence $P(\tau)$ is adequately described by equation (1) under the assumption that, for any τ, heating takes place up to the same temperature equal to T_m.

It should be noted that the dependence $P(\tau)$ is similar to the dependence of τ on the minimal power required to heat using light pulses to a constant temperature; the latter dependence was obtained for the same composition $Te_{81}As_4Ge_{15}$ in [3, 4]. Similarity with action of laser pulses manifests itself in the fact that the range of power of electric-field pulses that induce the crystal–glass transition, without sample destruction, is narrow for $\tau > 10$ μs and extends for $\tau < 1$ μs.

CONCLUSION

Thus, the study conducted has shown that crystal–glass phase transitions that occur under the action of laser radiation and electric field pulses are consistent with general relationships.

ACKNOWLEDGMENTS

The authors acknowledge the support of the Russian Foundation for Basic Research (project no. 97-02-18079).

REFERENCES

1. É. A. Lebedev, K. D. Tséndin, in *Electron Phenomena in Chalcogenide Vitreous Semiconductors* [in Russian], Ed. by K. D. Tséndin (Nauka, St. Petersburg, 1996), p. 224.
2. V. Kh. Shpunt, in *Electron Phenomena in Chalcogenide Glass-Type Semiconductors* [in Russian], Ed. by K. D. Tséndin (St. Petersburg, Nauka, 1996), p. 300.
3. É. A. Lebedev and K. D. Tséndin, Pis'ma Zh. Tekh. Fiz. **23** (12), 50 (1997).
4. É. A. Lebedev and K. D. Tséndin, Fiz. Tekh. Poluprovodn. (St. Petersburg) **32**, 939 (1998).

Translated by N. Vtorova

Semiconductors, Vol. 34, No. 1, 2000, pp. 98–103. Translated from Fizika i Tekhnika Poluprovodnikov, Vol. 34, No. 1, 2000, pp. 96–101.

AMORPHOUS, VITREOUS, AND POROUS SEMICONDUCTORS

Growth of *a*-C:H and *a*-C:H⟨Cu⟩ Films Produced by Magnetron Sputtering

T. K. Zvonareva, V. I. Ivanov-Omskiĭ, A. V. Nashchekin, and L. V. Sharonova

Ioffe Physicotechnical Institute, Russian Academy of Sciences, Politekhnicheskaya ul. 26, St. Petersburg, 194021 Russia

Submitted August 16, 1999; accepted for publication August 18, 1999

Abstract—Growth behavior of *a*-C:H and *a*-C:H⟨Cu⟩ films produced by the magnetron sputtering of a composite target consisting of graphite and copper plates in an argon–hydrogen atmosphere was studied by infrared spectroscopy, scanning electron microscopy, and ellipsometry. The introduction of copper into amorphous hydrogenated carbon films was shown to cause no marked changes in the carbon–hydrogen bonds in the matrix. In the *a*-C:H⟨Cu⟩ films ~2 μm thick, a thin uniform layer (~1000 Å) was found to adjoin the substrate; closer to the free surface, the layer acquires a columnar texture with columns oriented from the substrate to the surface. The results of ellipsometry measurements were analyzed in terms of a two-layer film model. © *2000 MAIK "Nauka/Interperiodica".*

INTRODUCTION

Films of hydrogenated amorphous carbon (*a*-C:H) represent a very well-studied object which was extensively reviewed in literature (see, e.g., [1]). The modification of *a*-C:H by various elements (metals) remains a significantly less advanced field of investigations, although at present, progressively greater attention is paid to this problem, in particular, to the introduction of metallic nanoclusters into the carbon matrix with the purpose of creating new types of electronic and magnetic media [2, 3]. When modifying *a*-C:H with copper, apart from the formation of copper nanoclusters [4] in the carbon matrix, a kind of doping of the graphite component occurs [5], which is of undoubted interest from the standpoint of creating efficient emitters for planar displays, along with the modification using nitrogen [6, 7].

The concentration of the elements that are introduced into the matrix to modify amorphous carbon may reach tens of percents; therefore, it is natural to expect the appearance of specific features in the growth behavior of such films and the effects of the modifier on the structure of the films. This follows, in particular, from the preliminary results of the investigation of the surface of a film modified by copper (*a*-C:H⟨Cu⟩) using a scanning tunneling microscope [8].

This work aims at clarifying the specific features of the growth behavior and structure of amorphous hydrogenated carbon films modified by copper and produced by magnetron sputtering of a composite copper + graphite target.

EXPERIMENTAL

The *a*-C:H films were grown by dc magnetron sputtering in an argon–hydrogen plasma (80% Ar + 20% H_2) [9].

For the introduction of copper into the amorphous hydrogenated carbon, i.e., for obtaining *a*-C:H⟨Cu⟩, copper plates (copper target) were placed onto the graphite cathode (graphite target). The total area of the graphite target was 144 cm^2. The concentration of copper introduced into the carbon films was varied by varying the area of the copper plates. In this way, samples were obtained with the area ratios between the copper target (copper plates) and graphite target (graphite surface remained uncovered with copper plates) in a range of $\Sigma = 0.02–0.14$ (2–14%).[1]

As the substrates for depositing films, we used wafers of single-crystal (100) silicon of grade KDB-20 and plates of fused quartz. Before being placed into the sputtering chamber, the substrates were annealed at 200°C. With the discharge current of 1 A and working gas pressure of ~10^{-2} mmHg, a voltage of 360 V was established across the electrodes.

Both *a*-C:H and *a*-C:H⟨Cu⟩ films were investigated using infrared spectroscopy (IR), scanning electron microscopy (SEM), and ellipsometry. The IR absorption (emission) spectra in the field of the vibrational

[1] The ratio of the atomic concentrations of copper and carbon in the films was greater than the ratio of the areas of the copper and graphite targets. The reason is both the greater rate of sputtering of copper as compared to carbon and the circumstance that some areas of the graphite target are sputtered with a smaller efficiency than others. The detailed results of the investigation of the composition of *a*-C:H⟨Cu⟩ films by Rutherford backscattering and nuclear reactions will be published elsewhere.

modes of C–H bonds was measured using a Specord 75IR two-beam spectrometer. The SEM images of the surface and fractures of the films were obtained in a Cam Scan Series 4-88 DV100 scanning electron microscope at an accelerating voltage of 15 kV with a resolution of 100 Å. The ellipsometry measurements were performed on an LÉF-3M ellipsometer using a helium–neon laser ($\lambda = 632.8$ nm) at light-beam incident angles $\varphi = 50$–$70°$.

The IR and SEM studies were performed using films deposited on silicon substrates. Polarimetric measurements were carried out using films deposited on both silicon and quartz substrates. The general pictures obtained on both series of samples were virtually the same; since we had a larger group of samples deposited on quartz substrates, in this paper we mainly give the results for films produced on quartz substrates.

The film thickness d was estimated from measurements performed with an MII-4 interference microscope, from micrographs obtained in the scanning microscope, and, more precisely, from the results of ellipsometry measurements. With other technological parameters being equal, the thickness was determined by the duration of the deposition process and did not exceed 2.2 μm in all experiments.

RESULTS AND DISCUSSION

It follows already from the technological data that the *a*-C:H⟨Cu⟩ films grow differently than the *a*-C:H films. As can be seen from Fig. 1, the average growth rate v depends strongly on the amount of copper to be introduced (Σ). (The average rate was estimated as the ratio of the film thickness obtained from interference measurements to the deposition time: $v = d/t$)

With such a strong $v(\Sigma)$ dependence, we may expect a significant modification of the structure of *a*-C:H⟨Cu⟩ films in comparison with *a*-C:H films. In order to investigate the character of changes of chemical bonds and the effect of changes caused by copper on the carbon framework ("skeleton") of the carbon film (to see whether or not these changes are catastrophic, destroying this skeleton), we measured IR absorption in a wave-number range of 3100–2700 cm^{-1}. In this spectrum range, stretching modes of the C–H bonds characteristic of *a*-C:H are observed (in the form of a wide absorption band). From the structure of this band, information on the presence or absence of bound hydrogen, the formation of various carbon–hydrogen groups (CH_1, CH_2, CH_3), the type of hybridization of atomic orbitals (sp^2, sp^3), and other features in the films can be obtained [10, 11].

Figure 2 displays optical transmission spectra of two *a*-C:H films and an *a*-C:H⟨Cu⟩ film. The films were grown under identical technological conditions. Since it cannot be ruled out that, simultaneously with the process of deposition, annealing of the film occurs, which may affect its structure, the spectra of two *a*-C:H films

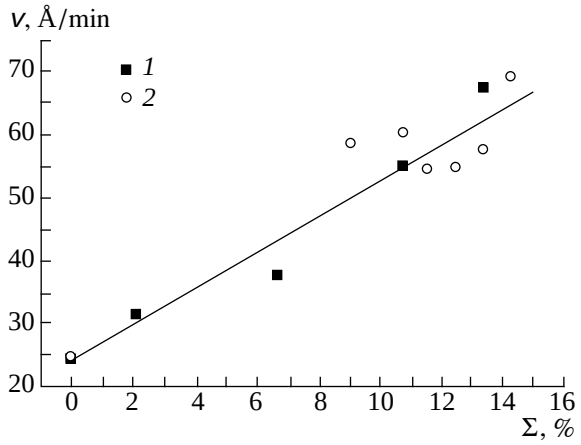

Fig. 1. Growth rate as a function of copper concentration for *a*-C:H⟨Cu⟩ films deposited for (*1*) $t = 30$ min and (*2*) 5 h.

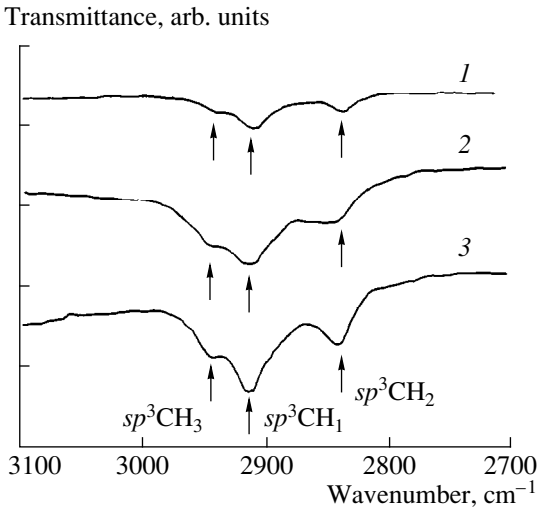

Fig. 2. Transmission spectra in the range of stretching vibrational modes of C–H bonds: (*1*) samples of *a*-C:H, $d = 0.25$ μm; (*2*) *a*-C:H, $d = 1.24$ μm; and (*3*) *a*-C:H⟨Cu⟩, $\Sigma = 13.4\%$, $d = 1.85$ μm.

of different thicknesses (with different times of deposition) are given for comparison. As follows from Fig. 2, neither the growth duration nor the presence or absence of copper affect the type of the spectrum. The observed difference in the amplitudes of the absorption bands is primarily caused by the difference in the film thickness. In all the cases, the predominant band is that corresponding to the sp^3CH_1 (2910 cm^{-1}) configuration. Bands corresponding to symmetric vibrations of C–H bonds in the configuration sp^3CH_2 (2840 cm^{-1}) and antisymmetric modes in the configuration sp^3CH_3 (2950 cm^{-1}) are also clearly pronounced. The absence of changes in the positions of characteristic absorption bands and in the ratios of their intensities suggests that the structure of chemical bonds and the relationship between the various carbon–hydrogen configuration

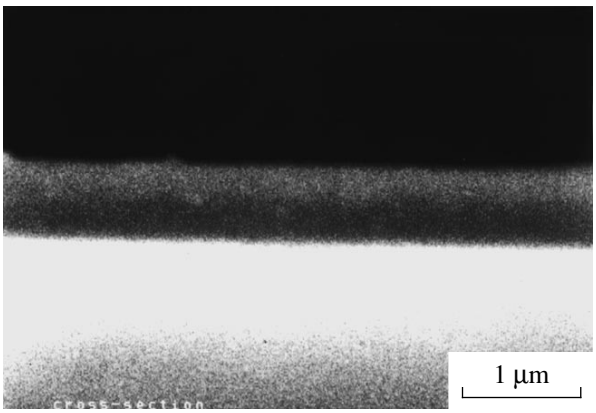

Fig. 3. SEM image of a transverse fracture of an *a*-C:H film of thickness $d = 0.8$ μm.

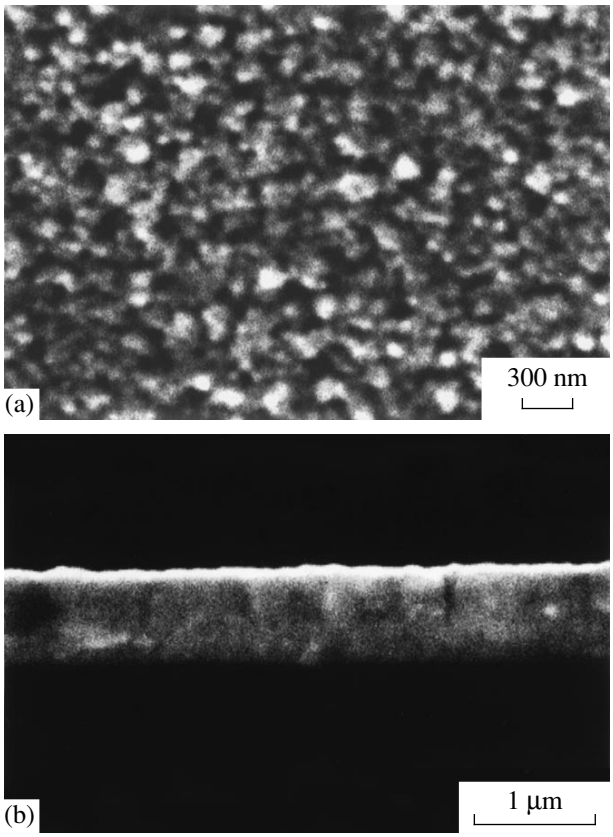

Fig. 4. SEM image of (a) the surface and (b) cross section (transverse fracture) of an *a*-C:H⟨Cu⟩ film of thickness $d = 0.8$ μm, $\Sigma = 13.4\%$.

groups in the carbon framework (skeleton) remain unaltered in the *a*-C:H films irrespective of the thickness (deposition time) as well as of the introduction of copper in concentrations of a few and even tens of percents.

Scanning electron microscopy was used to obtain information on the surface morphology and the internal microstructure of the films. Figures 3, 4a, and 4b show micrographs of cross sections (transverse fractures) of *a*-C:H and *a*-C:H⟨Cu⟩ films of the same thickness (0.8 μm) taken using the normal incidence of the electron beam on the scanned surface. In these micrographs, the disposition of the layers from bottom upward is as follows: silicon substrate, carbon film, vacuum. It is seen that the *a*-C:H film (without copper) has a smooth flat surface and its transverse fracture is uniform. The transverse fracture of the *a*-C:H⟨Cu⟩ film exhibits dark and light areas indicating the existence of inhomogeneities of submicrometer size in the bulk of the film. The surface of the *a*-C:H⟨Cu⟩ film (Fig. 4a) has a granulated structure, which manifests itself in the micrograph of the transverse fracture (Fig. 4b) as a characteristic relief of the film–vacuum interface. The average size of the granules is 150 nm, which corresponds on the order of magnitude to the size of surface nonuniformities revealed by scanning tunneling microscopy [8].

With increasing the *a*-C:H⟨Cu⟩ film thickness to 1.85 μm, the internal inhomogeneities observed on the transverse fracture transform into a pronounced columnar-like texture with columns oriented perpendicular to the substrate (Fig. 5b). The width of the vertical structural elements does not exceed 0.5 μm and frequently coincides with the dimensions of the surface granules.

In the cross section of the *a*-C:H⟨Cu⟩ film of thickness $d = 1.85$ μm, nonuniformities of the film thickness can be seen (Fig. 5b). The thin uniform layer adjoining the substrate loses its denseness with moving further from the substrate; inhomogeneities appear in it, which gradually grow wider. As can be seen from Fig. 5a, the size of granules at the surface increases to 300 nm with increasing film thickness, although the depth of the surface relief remains unaltered (cf. Figs. 4b and 5b).

The presence of a uniform layer near the substrate, the formation of nonuniformities, their widening with moving from the substrate to the free surface, the emergence of the internal inhomogeneities onto the surface with the formation of a "granulated" relief—all these features can clearly be seen in a micrograph obtained using an oblique electron beam (Fig. 6).

The in-depth nonuniformity of the film can be explained taking into account large internal stresses characteristic of the amorphous carbon films. For a thin stressed film with a sufficiently low elastic energy of the film–substrate interface, the initial growth occurs by the layer-by-layer mechanism, which causes the uniformity of the layer adjoining the substrate. However, thicker films possess larger elastic energy, which can be reduced by the formation of various internal boundaries or domains similar to the isolated growth islands in the Stranski–Krastanov growth model [12]. Self-annealing during film growth can produce a similar effect, which has already been mentioned above. Indeed, with large growth times (5 h for a film of 1.85 μm thick), it may prove to be significant that the region adjoining the sub-

strate may stay at an enhanced temperature of about 200°C (substrate temperature) for a long time. When going along the coordinate z from the substrate to the surface, this time decreases with increasing z. Such annealing appears to favor the elimination of elastic stresses. This occurs differently in different layers of the film; as a result, conditions for the formation of a uniform layer near the substrate are produced. Since the thickness of this layer is small, it does not manifest itself in the IR spectra of the films.

The micrographs of the transverse fractures of the films that were shown above do not permit us to make an unambiguous conclusion on the nature of the inhomogeneities observed. That is, we cannot determine whether this is a chemically uniform material in which a complex structural network is formed or the dark–light contrast of the image reflects the modulation of the composition, i.e., the coexistence of different phases. Note also that it would be not entirely correct to regard the contrast image of the surface as the reflection of only the geometrical relief of the surface, since the light and dark regions may also be related to the nonuniform distribution of the secondary-electron-emission coefficient over the film plane.

Previously [9], we studied the optical parameters (complex refractive index) and the growth rate of *a*-C:H⟨Cu⟩ layers on various substrates (silicon, quartz, pyroceram) using ellipsometry (at a wavelength of 632.8 nm). We found that, within the first 5 h of deposition, uniform (with a constant refractive index) layers grow at a constant rate both on silicon and quartz substrates; the difference was only in that the growth rate was greater for the quartz.

Since *a*-C:H⟨Cu⟩ films grow differently than the *a*-C:H ones, it is impossible to *a priori* consider the *a*-C:H⟨Cu⟩ films uniform merely by the analogy with the *a*-C:H films.

The measurements of the polarization parameters Ψ and Δ (see, e.g., [13]) were carried out on a series of samples with different copper concentrations deposited on substrates of fused quartz. In each technological experiment, two samples of different thickness were prepared using the same ratio between the graphite and copper targets and different deposition times (t = 30 min in the first case and t = 6–20 min in the second case). For each sample, the distributions of the experimental points in the Ψ–Δ plane depending on the angle of incidence were compared with the calculated curves obtained by solving the direct problem at the known parameters of the substrate (the refractive index of quartz n_q = 1.456). In calculations, both a single-layer model (a uniform layer with a complex refractive index $N_1 = n_1 - ik_1$ constant through the film thickness) and a two-layer model (two uniform layers, each with its own complex refractive index $N_1 = n_1 - ik_1$ and $N_2 = n_2 - ik_2$) were used. All of the sought parameters were varied, i.e., n_1, k_1, and the layer thickness d_1 in the single-layer model, and n_1, k_1, n_2, k_2, and the thicknesses of the sublayers d_1 and d_2 in the two-layer model. Finally, the characteristics of the real *a*-C:H⟨Cu⟩ layers were estimated after the best agreement between the calculation and experiment was achieved.

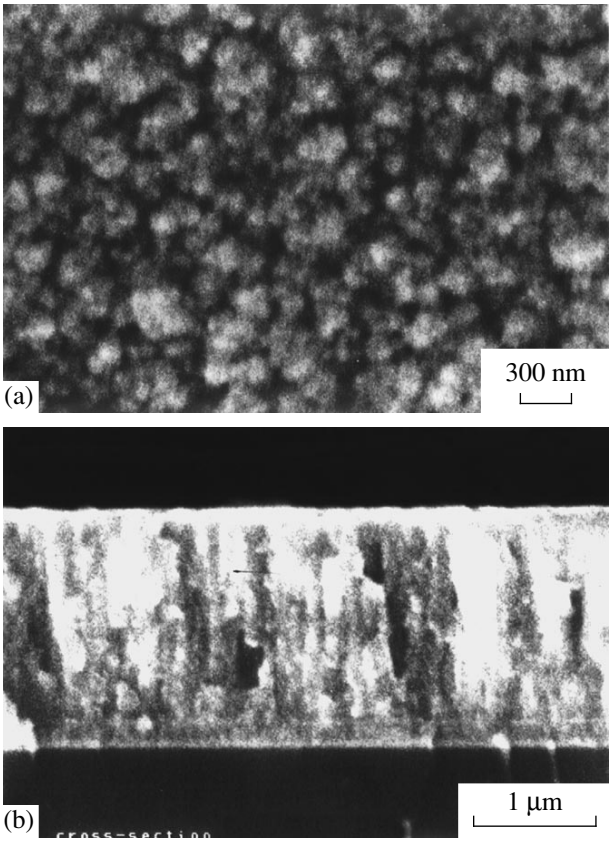

Fig. 5. SEM image of (a) the surface and (b) cross section of an *a*-C:H⟨Cu⟩ film of thickness d = 1.85 μm, Σ = 13.4%.

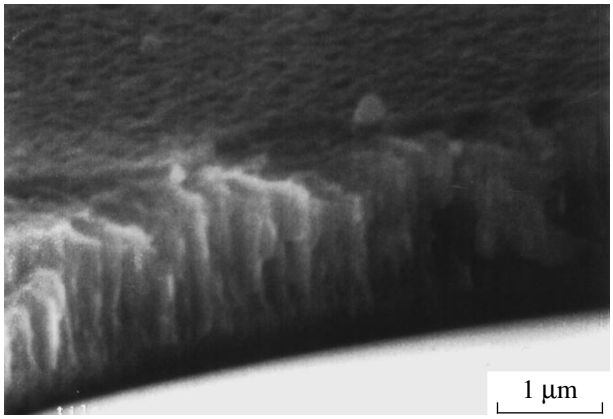

Fig. 6. SEM image of the same *a*-C:H⟨Cu⟩ film that is shown in Fig. 5 obtained using an oblique electron beam.

An analysis of the experimental data for the samples deposited for shorter times (t = 6–10 min, Σ = 2.1, 6.7, and 13.4%) shows that they well satisfy the single-layer model. The layer thicknesses are 570–680 Å and, not-

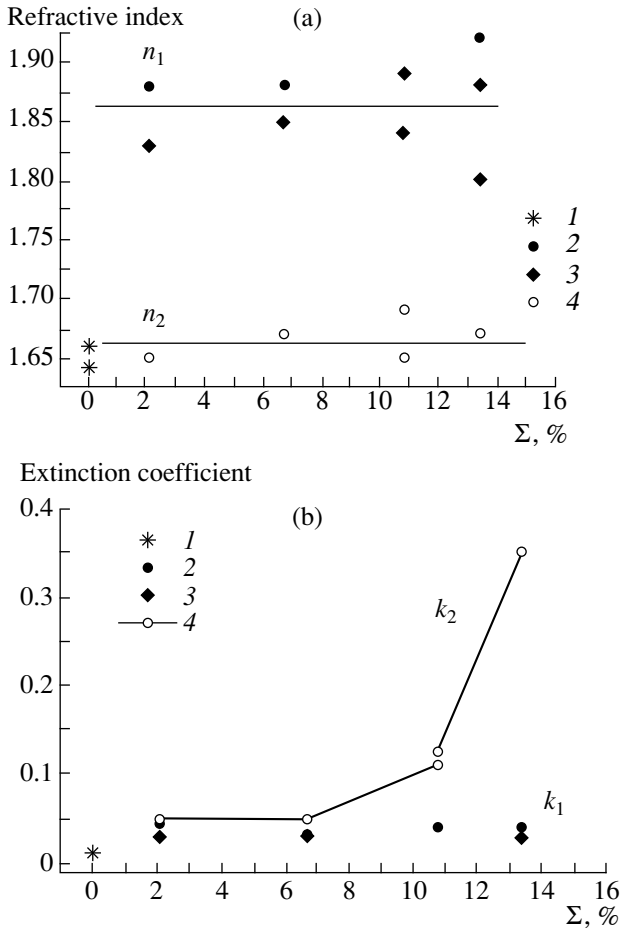

Fig. 7. (a) Refractive index and (b) extinction coefficient of *a*-C:H⟨Cu⟩ films as functions of the copper concentration Σ: (*1*) *a*-C:H (single-layer model) [9]; (*2*) "thin" *a*-C:H⟨Cu⟩ films (deposited for 6–10 min, single-layer model); (*3*, *4*) first (adjoining the substrate) and second sublayers, respectively, in "thick" *a*-C:H⟨Cu⟩ layers (deposited for 20 and 30 min, two-layer model).

withstanding the different amounts of copper used in the experiments, the layers have close refractive indices $n_1 = 1.88$–1.92 and extinction coefficients $k_1 \approx 0.3$ (see Fig. 7).

For thicker *a*-C:H⟨Cu⟩ films (deposited for $t = 20$ and 30 min), we could not even approximately describe the experimental Ψ–Δ dependences on the incidence angle in terms of the single-layer model and had to resort to a two-layer model. The starting model was constructed proceeding from the following assumptions: the first sublayer (adjoining the substrate) has optical parameters characteristic of the samples with $t = 6$–10 min, i.e., $n_1 \approx 1.9$, $k_1 \approx 0.03$ and the same or greater thickness, i.e., $d_1 \geq 700$ Å (such is the thickness of the films deposited for $t = 6$–10 min); the second sublayer has the refractive index $n_2 \approx 1.66$ (the value obtained for copper-free *a*-C:H films), and the extinction coefficient k_2 increases with increasing copper concentration (the transparency of the samples decreases with increasing copper content).

With such a two-layer model taken as a basis, we were able, by varying adjustment parameters, to obtain good agreement between the calculated Ψ–Δ dependences on the incidence angle and the experimental points for each sample, to determine in this way the optical characteristics of the first and second sublayers in the calculation model, and to construct a unified picture of the variation of optical parameters of *a*-C:H⟨Cu⟩ films depending on the copper concentration. The thus-obtained values of n_1, k_1, n_2, and k_2 are given in Fig. 7.

The results given in Fig. 7 may be summarized as follows. At the beginning of the process of co-sputtering of the graphite and copper targets, first, a layer is formed on the substrate whose optical parameters are close for all samples, i.e., are independent of the amount of copper introduced into the system ($n_1 = 1.8$–1.9, $k_1 = 0.03$–0.05), but, at the same time, differ from the parameters of copper-free *a*-C:H (in which n_1 is 1.64–1.66 and k_1 tends to zero). If we take into account that the complex refractive index of copper at $\lambda = 6328$ Å is $N_{Cu} = 0.27 - i3.417$ [14], we may assume that copper is incorporated into the framework of *a*-C:H in the form of isolated (single) atoms and changes the optical parameters of the framework itself rather than forms any second phase (foreign) species such as copper clusters. The thickness of this layer exhibits no correlation with the copper content; the adjusted value for all samples lies in the range 700–1000 Å. The thickness of the thin layer near the substrate that is observed in SEM images of the transverse fracture is of the same order of magnitude. The second sublayer is characterized by a refractive index close to that of the copper-free *a*-C:H film; the thickness of this sublayer grows with increasing copper amount. The extinction coefficient at $\Sigma < 6.7\%$ is of the same order of magnitude as in the first sublayer, but begins to grow significantly at $\Sigma \approx 6.7\%$. We may thus assume that, at $\Sigma \gtrsim 6.7\%$, the process of the atom-by-atom incorporation of copper into the *a*-C:H network saturates and inclusions of a new (metallic) phase appear (supposedly, copper or copper–graphite clusters), which leads to an increase in the extinction coefficient.

Note that the scatter of points in Fig. 7 with respect to the approximating curves for n_1, n_2, and k_1 is comparable with the error of determining these quantities as adjustment parameters. The error originates first of all from the circumstance that we cannot obtain an ideal agreement between the calculation and experiment. The most likely reason for the discrepancies is the use of a simplified model for calculations, which implies the existence of two sublayers with sharp boundaries, whereas a more realistic model should be based on the assumption of gradually changing optical characteristics. When determining k_2, the sensitivity of the calculated values of Ψ and Δ to the variation of this parame-

ter is rather large and, therefore, the error of determining k_2 in all cases does not exceed ± 0.02.

CONCLUSION

In conclusion, we emphasize that the two-layer model of the film, which permits us to interpret the results of polarimetric measurements, corresponds to a film of nonuniform thickness observed by scanning electron microscopy. A specific feature of the films modified with copper is the retention of the unaltered carbon matrix in spite of the existence of a strongly developed texture in the bulk of the film.

ACKNOWLEDGMENTS

This work was supported in part by the Russian Foundation for Basic Research, project nos. 97-02-18110 and 97-02-18340. The authors are grateful to G.S. Frolova for the measurements of the infrared absorption spectra and to V.N. Knyazevskiĭ for help in the preparation of samples for the experiments.

REFERENCES

1. J. Robertson, Adv. Phys. **35**, 317 (1986).
2. J. Jiao and S. Seraphin, J. Appl. Phys. **83** (5), 2442 (1998).
3. Th. Gabioc'h, A. Naudon, M. Jaouen, *et al.*, Philos. Mag. B **79** (3), 501 (1999).
4. V. I. Ivanov-Omskiĭ, in *Diamond-Based Composites and Related Materials*, edited by M. Prelas, A. Benedictus, L.-T. S. Lin, G. Popovici, and P. Gielisse (Kluwer Academic Publ., Dordrecht, 1997), p. 171 [NATO ASI Ser. 3, Vol. 38].
5. V. I. Ivanov-Omskiĭ and É. A. Smorgonskaya, Fiz. Tekh. Poluprovodn. (St. Petersburg) **32** (8), 931 (1998) [Phys. Semicond. **32**, 831 (1998)].
6. G. A. J. Amaratunga and S. R. P. Silva, Appl. Phys. Lett. **68** (18), 2529 (1996).
7. S. R. P. Silva, G. A. J. Amaratunga, and J. R. Barnes, Appl. Phys. Lett. **71** (11), 1477 (1997).
8. V. I. Ivanov-Omskiĭ, S. G. Yastrebov, A. O. Golubok, *et al.*, Pis'ma Zh. Tekh. Fiz. **24** (20), 28 (1998) [Tech. Phys. Lett. **24**, 800 (1998)].
9. T. K. Zvonareva and L. V. Sharonova, Fiz. Tekh. Poluprovodn. **33** (6), 742 (1999) [Phys. Semicond. **33**, 684 (1999)].
10. B. Dichler, A. Bubenzer, and P. Koidl, Solid State Commun. **48**, 105 (1983).
11. D. R. McKenzie, R. C. McPhedran, N. Savvides, and D. J. H. Cockaune, Thin Solid Films **108**, 247 (1983).
12. I. P. Ipatova, V. G. Malyshkin, A. A. Maradudin, *et al.*, Phys. Rev. B: Condens. Matter **57** (20), 12968 (1998).
13. R. Azzam and N. Bashara, *Ellipsometry. Polarized Light* (North-Holland, Amsterdam, 1977; Mir, Moscow, 1981).
14. P. B. Johnson and R. W. Christy, Phys. Rev. B: Solid State **6** (12), 4370 (1972).

Translated by S. Gorin